Lateral Pile-Soil Interaction in Liquefiable Soils

by

Suresh R. Dash

Somerville College

Michaelmas 2010

Abstract

Title: Lateral Pile Soil Interaction in Liquefiable Soils
Degree: DPhil in Engineering Science
Name: Suresh R Dash
College: Somerville college
Term: Michaelmas 2010

The $p - y$ curves are widely used to define lateral pile-soil interaction (LPSI) in a Beam on Non-linear Winkler Foundation (BNWF) model, where 'p' refers to the lateral soil pressure per unit length of the pile and 'y' refers to the lateral relative pile-soil displacement. The parameters required for a $p-y$ curve definition for normal soil condition (i.e., non-liquefied soil in this context) are well understood and have been used in practice with confidence for the last 30 years. However, these parameters for liquefied soil are still not well defined. For liquefied soil, current practice suggests a reduced strength $p-y$ curve from its non-liquefied state $p - y$ curve, which still keeps a very high initial stiffness and low stiffness at large deflection. However, in contrast, many experimental observations have shown that the initial stiffness of $p - y$ curve in liquefied soil is very small and increases significantly at large deflection.

This thesis is aimed at investigating the lateral soil-pile response in liquefiable soils and formulating a reasonable $p - y$ curve to represent this response. A detailed analysis of a set of centrifuge test results, $1 - g$ shaking table tests and numerical studies form the basis of this investigation.

The $p - y$ curve has been back calculated from the centrifuge test results of 13 pile groups. The study showed that the $p - y$ curve has very small initial stiffness which increases with increase in pile displacement. The cyclic $p - y$ curves have further been analysed to estimate equivalent viscous damping of the soil, which has shown quite high values of damping from liquefied soil, with the damping ratio going up to 50% in some cases.

To study the $p - y$ curve response directly, a set of $1 - g$ tests were carried out with plane strain idealisation of LPSI at a particular depth. The tests have shown that as the degree of liquefaction increases in the soil, the shape of the $p-y$ curve changes from strain softening to strain hardening type and the ultimate strength reduces.

Based on the above experimental observations, collated element test data on liquefied soil and numerical study, a monotonic $p-y$ curve for fully liquefied soil has been proposed. This $p - y$ curve was derived directly by scaling the stress-strain curve, and hence, retains the characteristics of the stress-strain behaviour of liquefied soil and also shows qualitative agreement with the $p - y$ curves observed in some other experiments. However, the associated limitations of this simplified $p-y$ curve model, which represents a very complex and nonlinear liquefied soil, indicates the requirement of better experiments to confirm its form and to provide more robust numerical values for its wide applicability.

To demonstrate the application of the proposed $p - y$ curve model, a well known case history of Showa Bridge pile failure in liquefiable soils was considered, which failed during the 1964 Niigata earthquake. The characteristics of the proposed $p - y$ curve were compared with the $p - y$ curve in conventional practice and its implication in capturing the failure mechanisms for pile design has been demonstrated. Although, the aim of this study was not to find the actual cause of Showa bridge pile failure, the analysis captured some major field observations of the failure by using the proposed $p - y$ curve model.

Acknowledgements

Contents

Glossary

Roman Symbols

c Coefficient of damping

C_u Strength degradation factor according to degree of liquefaction

D Diameter of pile or model pipe

D_o Outside diameter of pile

D_r Relative density

e Void ratio

E_p Young's modulus of pile

E_s Young's modulus of soil

F_d Depth of fixity

F_i lateral inertia load

F_l Severity of liquefaction

F_l Severity of liquefaction

f_n First fundamental frequency

F_p Total lateral force on model pipe

G Shear modulus

g Acceleration due to gravity

G_1 Initial secant shear modulus of soil

G_2 Critical state shear modulus of liquefied soil

G_{max} Maximum shear modulus of soil at small strain

h Depth of soil

I_p Moment of inertia of pile

K Permeability of soil

k Initial modulus of subgrade reaction

k_s Spring constant of soil

M Bending moment in pile

m Mass

M_c Critical state stress ratio in tri-axial compression

M_e Critical state stress ratio in tri-axial extension

M_p Plastic moment capacity

M_s Scaling factor for strain to deflection

M_y Yield moment

M_{ce} Factor relating ϵ_{50} with y_c of pile

N SPT value

n Scaling factor used in experimental study

N_1 SPT value corrected for overburden pressure

N_c Bearing Capacity Factor

N_s Scaling factor for stress to resistance

N_{1-60} SPT value corrected for overburden pressure and free fall hammer energy

P Axial load

p Lateral soil resistance

p' Effective confining pressure/stress

p'_{ini} Initial effective confining pressure

p_u Ultimate lateral soil resistance

P_{cr} Buckling load

p_{tl} Total lateral earth pressure of soil

p_{ud} Ultimate lateral soil resistance at deeper depth

p_{us} Ultimate lateral soil resistance at shallow depth

q Deviatoric stress

q_{max} Maximum deviatoric Stress

R_p Radius of pile in FE model

R_s Radius of soil in FE model

r_u Excess pore water pressure ratio

S_r Saturation index

s_u Residual shear strength of liquefied soil

t	Time
T_f	Transfer function
T_n	First fundamental time period
u	Hydrostatic pore water pressure
u_{ex}	Excess pore water pressure
V	Velocity of pile or model pipe
v	Specific volume
v_s	Shear wave velocity
y	Relative pile-soil displacement (or displacement of model pipe)
y_c	Characteristic pile deflection
y_p	Pile displacement
y_q	Soil displacement near quay wall
y_s	Soil displacement near pile
y_u	Ultimate relative pile-soil displacement
y_{sf}	Free field soil displacement
z	Depth

Greek Symbols

α	Reduction factor for p
$\bar{\omega}$	Forcing frequency
β	Critical depth ratio at boundary between shallow and deeper depth
δW	Incremental work
ϵ	Strain parameter
ϵ_b	Bending strain
ϵ_r	Radial strain
ϵ_a	Axial strain
η_c	Stress ratio in tri-axial compression
η_e	Stress ratio in tri-axial extension
$\frac{1}{\rho_p}$	Curvature
Γ	Specific volume of soil at critical state
γ	Engineering shear strain

γ'	Efective unit weight of soil
γ_d	Dry unit weight of soil
γ_t	Total unit weight of soil
γ_{ave}	Average engineering shear strain around pile
γ_{to}	Take off shear strain
λ	Slope of CSL in v-lnp' space
ω	Weight function
ϕ	Angle of friction of soil
ϕ'	Critical state angle of friction
ϕ_{cs}	Critical state angle of friction
ρ	Unit mass
σ	Stress parameter
σ'_1	Effective major principal stress
σ'_3	Effective minor principal stress
σ'_{vo}	Initial effective vertical (overburden) stress
σ'_v	Effective vertical (overburden) stress
σ_1	Major principal stress
σ_3	Minor principal stress
σ_u	Ultimate strength
σ_y	Yield strength
τ	Shear stress
τ_d	Static shear stress
τ_{ave}	Average shear stress around pile
τ_{max}	Maximum shear stress
ζ	Damping ratio

Abbreviations

A/D	Analog to Digital
BNWF	Beam on Non-linear Winkler Foundation
CPT	Cone Penetration Test
CSL	Critical State Line

CSSM Critical State Soil Mechanics

CVR   Critical Void Ratio

D/A   Digital to Analog

DAF   Dynamic Amplification Factor

DC   Direct Current

DEM   Discrete Element Method

EPWP Excess Pore Water Pressure

EPWPR Excess Pore Water Pressure Ratio

ERT   Electrical Resistivity Tomography

FL   Failure Line

FOS   Factor of safety

LPSI Lateral Pile Soil Interaction

MSD   Mobilised Strength Design

PI   Plasticity Index

PPT   Pore Pressure Transducer

PTFE Poly-Tetra-Fluoro-Ethylene

PTL   Phase Transformation Line

PWP   Pore Water Pressure

SPFS Soil Pile Footing Structure

SPT   Standard Penetration Test

SSL   Steady State Line

SWVT Shear Wave Velocity Test

Chapter 1

Introduction

1.1 Background

Earthquakes are natural hazards that can cause extensive damage to life and property. There are about 500,000 detectable earthquakes in the world each year, 100,000 of which can be felt, and 100 of them cause damage (USGS, 2010). Undoubtedly, the primary causalities of earthquakes are man-made structures, for example, buildings, bridges, dams, etc., and the loss of life during earthquakes is rather a consequence of the structural collapses than a direct impact. As population grows and more buildings are constructed in seismically active zones, more people are likely to be affected by earthquakes. This observation is justified by the growing number of casualties and financial losses in some recent earthquakes, for example, 26 Dec 2004 Sumatra earthquake, 12 May 2008 Sichuan earthquake, 12 Jan 2010 Haiti earthquake and 27 Feb 2010 Chile earthquake. Often, ground failures are the direct or indirect causes of the structural failures.

Liquefaction is a type of ground failure where the soil loses its strength significantly. Liquefaction occurs worldwide, mainly during earthquakes, and is of considerable importance from both safety and economical standpoints. For example, Jefferies & Been (2006) mentioned that the 1964 Niigata (Japan) earthquake caused more than $1 billion in damage where most of it was related to soil liquefaction. Liquefaction was the cause of abandonment of the Nerlerk (Canada) artificial island after more than $100 million had been spent on its construction. In 1971, Liquefaction at Lower San Fernando dam (California) required the immediate evacuation of 80,000 people living downstream of the

dam. The Aberfan (Wales) colliery spoil slide in 1966 was caused by liquefaction and killed 144 people (116 of whom were children) when it inundated a school.

Figure 1.1 shows a classic example of sinking building during the 1964 Niigata earthquake due to liquefaction of subsoil, where the foundation of the building was not able to transfer the superstructure load safely to the ground. The foundation is regarded as one of the major parts of a structure, be it a building or bridge, where it interacts with the ground. The basic purpose of a foundation is to hold the superstructure in proper position by transferring its load to the supporting ground. In the event of soil liquefaction the foundation may fail to serve the purpose of safe load transmission to the ground and lead to failure/collapse of the structure. This study is concentrated on a particular type of foundation, pile foundation in seismically liquefiable soils.

Figure 1.1: A building leaning due to liquefaction of subsoil near Niigata Station during the 1964 Niigata earthquake (JGS, 1964).

1.2 Introduction to the subject: Lateral Pile-Soil Interaction (LPSI) in liquefiable soils

Pile foundations are long slender structural members, which support heavily loaded structures such as bridges, buildings, jetties or oil platforms (See Figure 1.2 for a typical use). They are generally preferred where the soils at shallow depth are not strong enough

to bear the structural load. Piles are often considered as an all-safe solution due to their good performance in extreme loading environments such as those found offshore. However, this is certainly not true during earthquakes if the structures are in low bearing sandy soil.

In loose to medium dense saturated sand in undrained condition, moderate to strong earthquakes or other dynamic events may induce a sharp rise in pore water pressure and the sand behaves like a solid suspension. In other words, the state of the soil transforms from solid to fluid, a phenomenon known as "liquefaction," and such a soil is called "liquefiable soil". During liquefaction, the strength of soil reduces considerably. If this happens on sloping ground, the liquefied soil may also flow downhill. When a non-liquefied soil layer is present over liquefied soil, it may also crack and be carried in the same direction as the liquefied soil flow. This liquefaction induced soil flow is generally known as "lateral spreading." In some extreme events, steep slopes on liquefied soil may slip and cause landslides. Piles founded on liquefiable soil can thus be subjected to lateral force from lateral soil flow as well as that from the inertia of superstructure during seismic shaking.
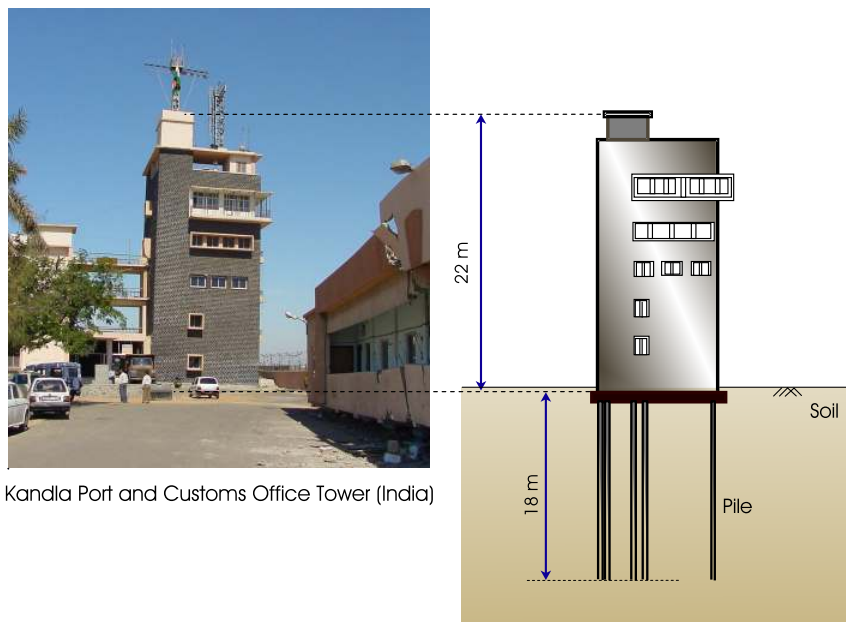
Figure 1.2: A typical use of pile foundation under a building (photograph from: NICEE, 2010). Schematic showing the slenderness of pile foundation in comparison with the superstructure.

Post earthquake observations provide many examples of pile failure in soft ground that has lead to partial/complete collapse of the structure. Often, these failures in sandy

soils were attributed to liquefaction and lateral spreading of the soil. Recent strong earthquakes continue to show similar kinds of pile failure (Figure 1.3) despite being designed with high factors of safety. This still poses a great concern to the earthquake engineering community to ensure safety of new and existing structures on pile foundations in liquefiable areas.

Figure 1.3: Failure of pile foundations during various earthquakes. (Sources: a) NISEE (2010), b) NGDC (2010), c) NICEE (2010), d) Mondal & Rai (2008), e) Photo by Daniella Escribano L.)

The aim of the present research is to contribute to the current understanding of pile-soil interaction in liquefiable soils during earthquakes, especially looking at the modelling parameters during analysis. Considering the fact that the significant loading on piles during earthquakes acts in the lateral direction, be it from lateral spreading or inertia, this study is restricted to "lateral pile-soil interaction in liquefiable soils." Figure 1.4 shows the place of this research in earthquake geotechnical engineering spectrum.
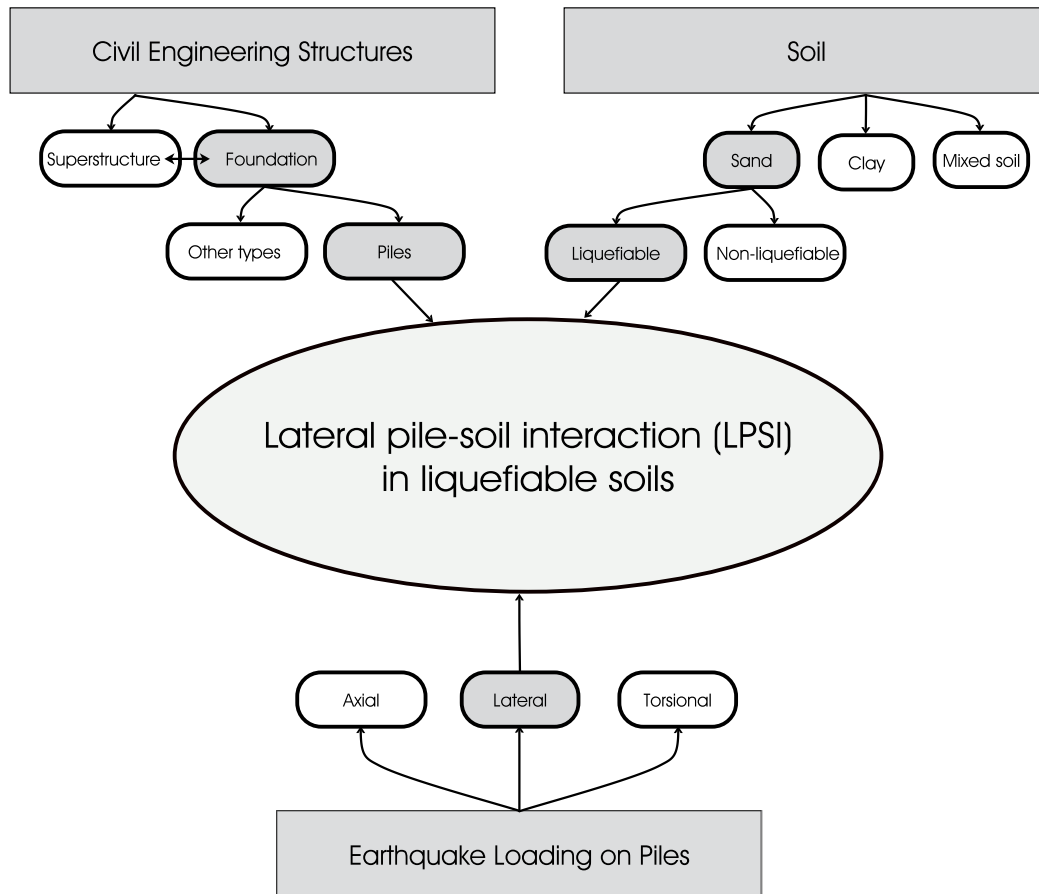
Figure 1.4: Flow diagram of the research topic.

1.3 Modelling LPSI in liquefiable soils

1.3.1 Current understanding and practice

In practice, there are many methods used to model and design the lateral response of the pile foundation and one of the widely used models is the Beam on Non-linear Winkler Foundation (BNWF) model (Figure 1.5). In BNWF model, the pile is treated as a beam and the surrounding soil is modelled as springs. The BNWF model is preferred in practice due to its simplicity, mathematical convenience and ability to incorporate non-linearity. In a BNWF model, LPSI is represented by springs with nonlinear $p - y$ curves, where 'p' refers to lateral soil pressure per unit length of pile and 'y' refers to lateral relative pile-soil displacement (Figure 1.5). The parameters required for a $p - y$ curve definition for normal soil condition (i.e., non-liquefied soil in this context) are well understood and have been used in practice with confidence for the last 30 years (API, 2000; JRA, 2002).

5

However, these parameters change for liquefied soil because the soil changes from a solid to a fluid state during liquefaction and are difficult to estimate.
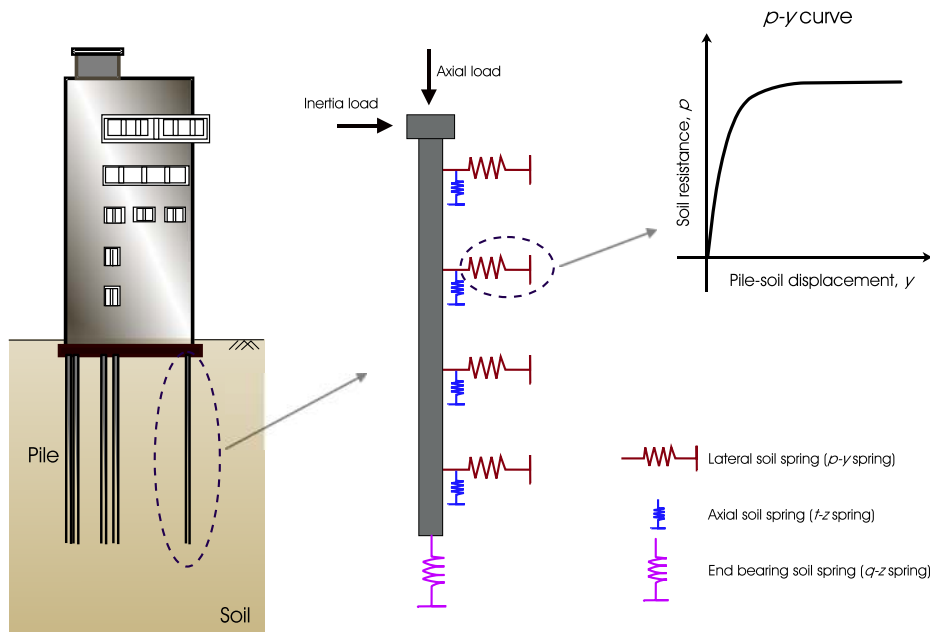
Figure 1.5: BNWF model of Pile-Soil Interaction (PSI).

Traditionally, engineers use simple fixes to tackle this complicated situation and obtain the $p - y$ curve for liquefied soil from the non-liquefied curve by using a reduction factor, α. Figure 1.6 shows a typical $p - y$ curve based on API guidelines (API, 2000) for non-liquefied soil and then a reduced strength $p - y$ curve from it for liquefied soil. Though α is not uniquely defined in literature, many design codes and researchers suggest values for practical use. For example, Brandenberg (2005) suggested the value of α that ranges from 0.1 to 0.5 depending on soil's SPT value. Dobry *et al.* (1995) suggested relationships between the degradation parameter for $p - y$ curves as a function of excess pore water pressure ratio, r_u, calibrated from a series of centrifuge model tests.

Instead of BNWF modelling, some codes of practice suggest a limiting force design approach of soil-pile interaction in liquefiable soil during large relative pile-soil displacement (e.g., lateral spreading situation). The soil springs are replaced with a limiting force that the pile is experiencing. The Japanese Code of Practice (JRA, 2002), for example, advises engineers to design piles against a lateral load of 30% of the total overburden pressure that the liquefied soil applies on the pile. This value is based on back calculation
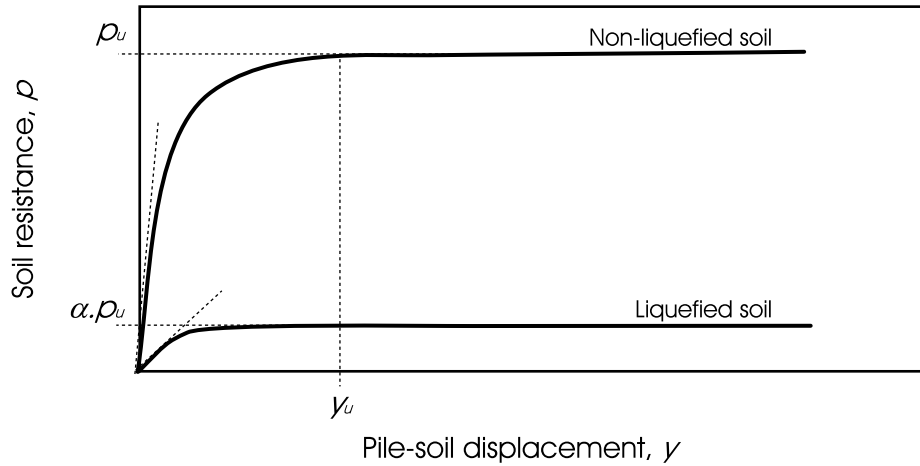
Figure 1.6: $p-y$ curve model for non-liquefied and liquefied soil.

of the case histories of structures that performed well in earthquakes, which seems very high as compared with the suggested value by the design standard for railway facilities in Japan (RTRI, 1999), which considers the strength of liquefied soil as $1/1000$ of its original non-liquefied strength.

Although, these reduced $p-y$ curve models or limiting force models capture the loss of strength behaviour of liquefied soil, they do not represent the overall pattern of $p-y$ behaviour as observed in full scale experiments as discussed in the following section.

1.3.2 Experimental observations and possible mismatch

Some recent experimental investigations show a pattern of $p-y$ curve that is completely different to that used in current practice, which could have a significant influence in the analysis. Figure 1.7 shows the observed load-deflection curve of a single pile during a full-scale test where the soil surrounding the pile was liquefied by blasting (Rollins *et al.*, 2005). The back-calculated $p-y$ curves showed a significant hardening, where the initial stiffness of liquefied soil was very small and increased with y. In contrast, the $p-y$ curves used in current practice has very high initial stiffness that decreases with y. Similar observations like the above full scale test were also made by Takahashi (2002) in $1-g$ tests and by Wilson (1998) in centrifuge tests.

7
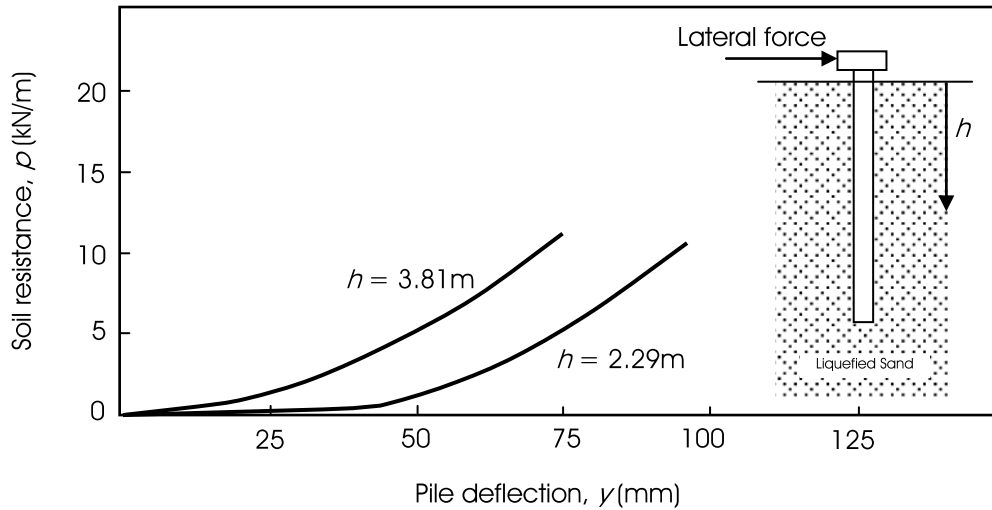
Figure 1.7: Observed $p - y$ curve from full-scale testing (Rollins *et al.*, 2005).

1.3.3   Importance of the shape of the $p - y$ curve

The main parameters of a load-displacement ($p - y$ curve) relationship are stiffness and strength. During transient vibration, the stiffness plays an important role. When the differential soil-pile movement (y) is small (i.e., the soil is not pushed to its full capacity), the soil resistance over the pile depends on the stiffness of the $p - y$ curve. In contrast, when the differential soil-pile movement is large, the resistance offered by soil over pile is governed by the ultimate strength of the $p - y$ curve. Figure 1.8 shows the soil resistance (p) for different levels of vibration for two types of $p - y$ curves, a) $p - y$ curve used in current practice and b) $p - y$ curve observed in experiments. As shown in the figure, the pile response is expected to be different for the two different shape of the $p - y$ curve. For the $p - y$ curve as in Figure 1.8a, the higher initial stiffness would induce higher bending moment in the pile and it may fail due to excessive bending. However, For the $p - y$ curve as in Figure 1.8b, the lack of initial stiffness will increase the $P - \text{delta}$ effect in the small amplitude vibration, and may promote a buckling failure of the pile. Counteracting this is the advantage that may be achieved by using the latter model (model-b) due to the higher stiffness at large differential pile-soil movement, which would prevent/delay a complete collapse of structure at large strain. The initial stiffness difference between these two models also changes the dynamic characteristics of the system significantly. The fundamental period of the model-a is smaller when compared to the model-b, which can

8

suggest a very different design criteria due to dynamic force consideration.
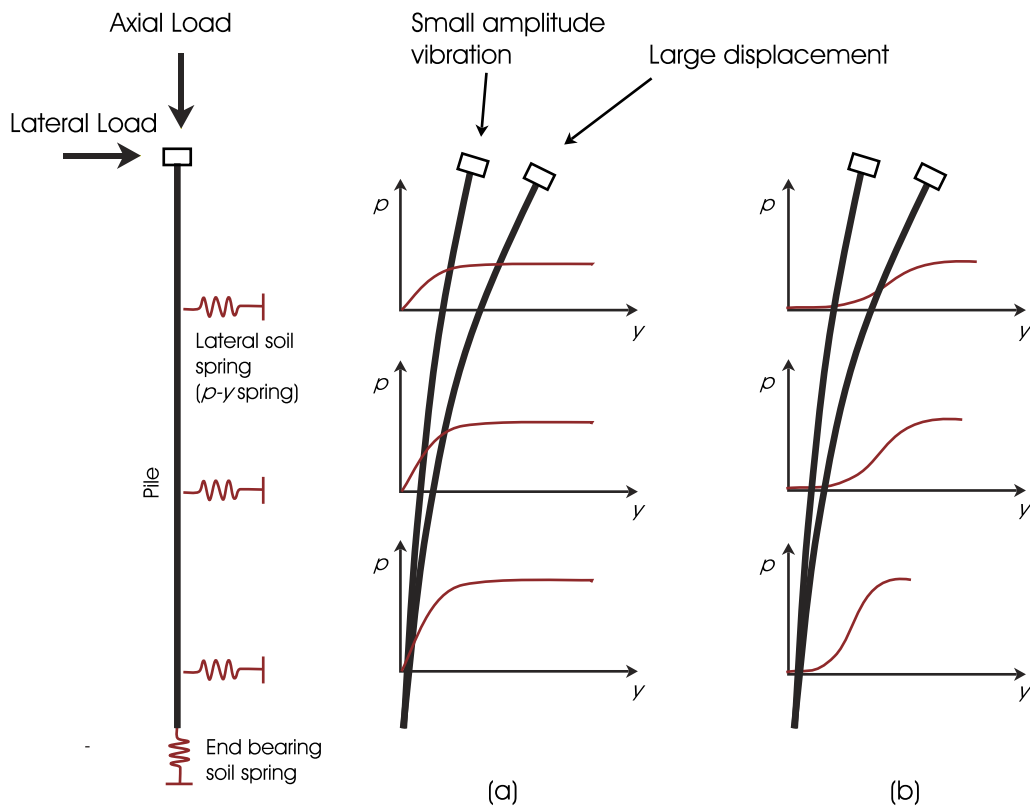
Figure 1.8: Importance of the shape of the $p - y$ curve, a) $p - y$ curve for liquefied soil in present practice, b) $p - y$ curve for liquefied soil as observed in the experiments.

1.4 Scope of present research

Soil behaviour is difficult to model, especially when the effects of liquefaction and seismic loading are taken into account. The current practice of using a strength reduction factor method does not represent the actual behaviour as observed in experiments. It also does not take into account the transient phase in the soil i.e. the soil being transformed from a solid state to a fluid state during liquefaction. Another major drawback of the present practice is that the soil has high initial stiffness even at full liquefaction (Figure 1.6) which is in contrast to many recent observations in full scale and laboratory sample tests (Rollins *et al.*, 2005, Yasuda *et al.*, 1999) that showed nearly zero initial stiffness in liquefied soil. While the $p - y$ curves for sand (under non-liquefied condition), soft clay and stiff clay are well established, the profession still lacks a promising $p - y$ curve for liquefiable soil. It must be pointed out that the correctness of the analytical solutions obtained by BNWF

model studies depends on the appropriate $p - y$ curve shape being defined. The work presented in this thesis thus concentrates on two major objectives, which are:

- Understanding the lateral pile-soil interaction in liquefiable soils at both micro and macro level.

- Defining appropriate $p - y$ curves for liquefied soils.

1.5 Organization of the thesis

This thesis presents the research carried out to achieve the above goals in seven chapters. This chapter introduces to the subject of present study. Brief outlines of the other chapters are presented below.

- Chapter 2 reviews the literature related to lateral pile soil interaction modelling in liquefiable soil.

- Chapter 3 describes the procedure to back calculate lateral resistance of liquefied soil on piles from 13 pile groups tested in centrifuge. The $p - y$ curves were estimated for fully liquefied soil and compared with the $p - y$ curves currently used in practice.

- Chapter 4 presents the $1 - g$ shaking table tests which were carried out to understand the micro level behaviour of lateral pile soil interaction.

- Chapter 5 discusses the method to characterise $p - y$ curves for fully liquefied soils from the stress-strain behaviour of soil.

- Chapter 6 presents the applicability of the proposed $p - y$ curve model by studying the well known case of Showa bridge pile failure during 1964 Niigata earthquake. The important observations from the analysis were discussed in comparison with the $p - y$ curve model of current practice.

- Chapter 7 summarizes the key findings from the experimental investigations and numerical study. The limitations of present research and its future scope are presented.

Chapter 2

Literature review

2.1 Outline of the chapter

This chapter reviews the literature related to the scope of research described in section 1.4. A brief introduction to liquefaction, behaviour of liquefied soil and its effects on pile foundations is presented. The stress-strain behaviour of liquefied soils and a theoretical framework to describe them is presented. The design philosophies for piles in liquefiable soils are reviewed. The dynamic properties of liquefied soils are discussed and the current understanding of modelling soil-pile interaction in liquefiable soils is reviewed critically.

2.2 Liquefaction

Liquefaction, in a general sense, means the process of transformation of any material from a solid to a liquid state. In soil mechanics, it is the phenomenon in which the strength and stiffness of a soil is reduced significantly during earthquake shaking or similar rapid cyclic loading.

Liquefaction can occur in saturated sands, silts, and quick clays. It can also occur in very large masses of sands or silts that are dry and loose but loaded so rapidly that the escape of air from the voids is restricted (Poulos *et al.*, 1985). High plasticity clayey soils are highly resistant to liquefaction, and so are generally avoided in liquefaction study. However, natural soil is a mixture of various types of sand, silt and clay, and the liquefaction susceptibility varies depending on the amount of each component (Boulanger & Idriss, 2006; Andrews & Martin, 2000). Although extensive research has been carried out to understand the liquefaction phenomenon in sandy soils, there is not enough data

for mixed soil to incorporate them into the main framework of liquefaction behaviour (Guo & Prakash, 1999). The discussion in this thesis is limited to the liquefaction of sandy soils.

Sandy soils are cohesion-less granular materials that offer resistance to deformation mostly due to confinement. The greater the confinement, the higher the resistance (or strength), and that is the reason why resistance to deformation in sandy soil increases with depth. Applying deformation to granular materials causes both shear and volumetric strains, and depending on the initial void ratio they may either contract or dilate. Figure 2.1 shows a typical monotonic stress-strain behaviour of loose (contractive) and dense (dilative) saturated sand obtained in a triaxial test setup.
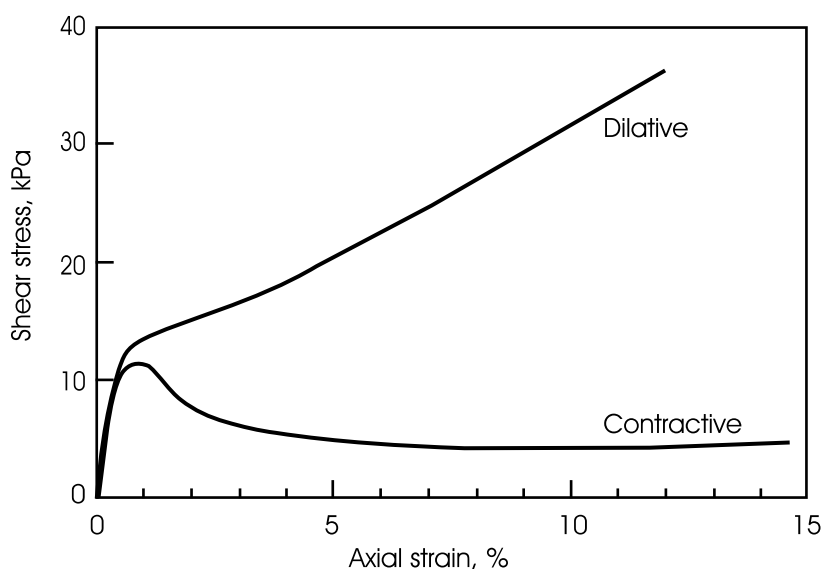
Figure 2.1: Contractive and dilative behaviour of soil as obtained from triaxial test.

The normal behaviour of contractive and dilative soils is described below.

Contractive soil: When loose sands are monotonically sheared, the sand grains move to reduce the soil volume (contract) as particles rearrange and fall into voids. When the undrained soils contract, the pore water pressure increases, decreasing the effective confinement pressure on the sand grains. Upon loosing the inter-granular contact due to the reduced confinement, the shear resistance of sand also reduces.

Dilative soil: When dense sands are monotonically sheared, the sand grains tend to increase in volume (dilate) as particles ride over each other, after a small initial decrease in volume during rearrangement. The pore water pressure decreases during dilation and

the effective confinement pressure increases, which gives rise to the shear resistance of soil.

Liquefaction, as understood by loss of strength, can only occur in the contractive soils in undrained condition. Dilative soils are not susceptible to liquefaction as their undrained strength is greater than their drained strength (Poulos *et al.*, 1985). Figure 2.2 shows schematically the concept of liquefaction and the pore water pressure response before liquefaction and at full liquefaction.
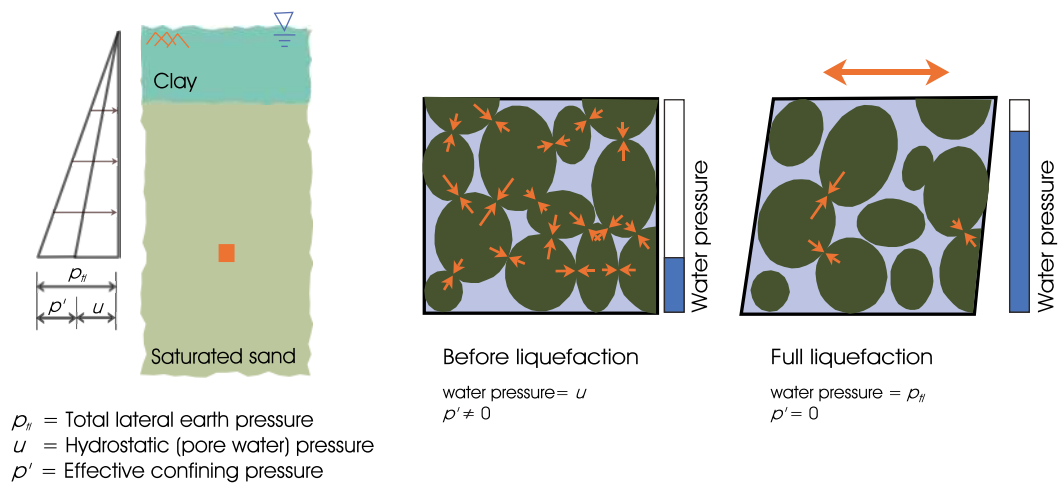
Figure 2.2: Liquefaction concept in saturated sandy soil.

The above discussion sets out three necessary conditions for liquefaction:

1. soil has to be loose: so that it can show contractive behaviour upon shearing

2. saturated and undrained: so that the pore water pressure can build up during contraction of soil

3. subjected to required level of shear stress/strain: so that the soil can contract with the driving shear stress (Poulos *et al.*, 1985 have shown that even contractive soils are not susceptible to liquefaction unless the driving shear stresses *in-situ* are large enough.)

Broadly, loose-to-medium dense sand is categorised as contractive and dense sand is dilative for normal field densities. Below depths of about 20m, evidence of liquefaction is generally not seen in past earthquakes, as the deeper soils are highly compacted by the weight of the soil layer above. The evidence of liquefaction in the field after an earthquake

is normally observed as sand boils as shown in Figure 2.3. As the pore water pressure increases in the soil during liquefaction, it tries to ooze out (to release the excess pressure) through ground cracks or fissures and looks like it is "boiling" up from the bed of sand.
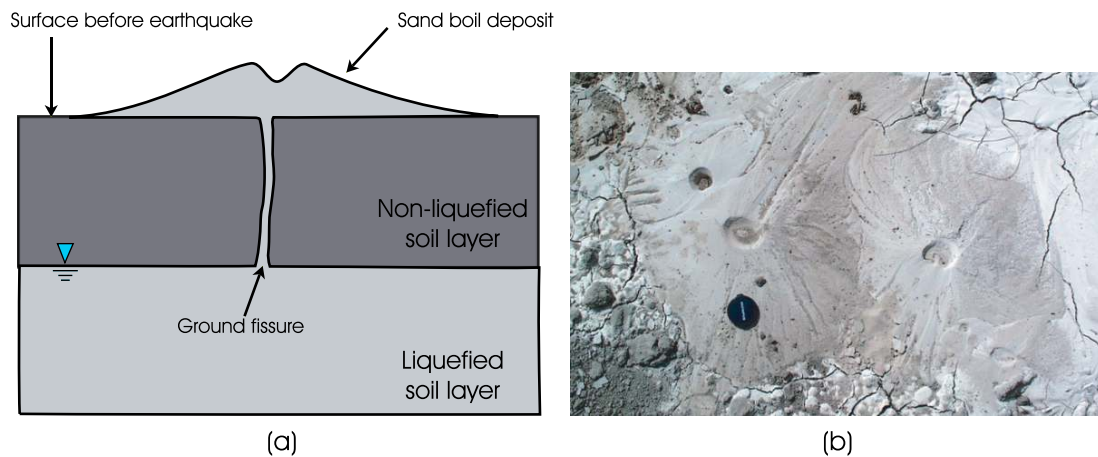
Figure 2.3: (a) Schematic of sand boil during seismic liquefaction of ground. (b) Observed sand boils during 2001 Bhuj earthquake, India. (Photograph: EERI, 2002).

2.2.1 Effects of liquefaction

Due to significant loss of strength and stiffness during liquefaction, the liquefied soil may trigger ground failures such as:

1. Soil flow

    - Landslide: when liquefied sediments are sitting on a steep slope

    - Lateral spreading: when liquefied sediments are on relatively flat terrain with a gentle slope (about $1°$ - $2°$).

2. Ground settlement

3. Cracking and breakdown of the top non-liquefied soil layer

If a pile foundation is interacting with any of the types of ground failures, it will be subjected to kinematic forces from soil deformation. Under such situations the piles may experience:

1. Loss of lateral confinement in the zone of liquefaction: The piles may deform more due to the combined action of axial and lateral loads. Lateral confinement from a

non-liquefied soil layer may also be reduced if it lies over a liquefied soil layer and subjected to cracking and disintegration during liquefaction of the underlying layer.

2. Loss of end bearing: If the pile terminates in a liquefied soil layer, it may sink due to loss of end bearing.

3. Loss of side friction: If the pile, designed as friction pile, terminates in a competent soil layer passing through liquefied soil layer, it will be subjected to additional axial resistance demand on the end bearing. If the end bearing cannot sustain the increased axial load demand, the pile may sink.

4. Additional kinematic forces: The piles in liquefied soil on slopes may get additional kinematic forces due to the movement of the soil past the pile in landslide or lateral spreading.

5. Additional load on piles due to the change in dynamic characteristics of the pile-supported structure. This is because the part of the pile in the unsupported zone (i.e., the zone of liquefaction) will now be a part of the superstructure and take part in the vibration during earthquake.

2.2.2 Evaluation of liquefaction potential

The evaluation of liquefaction potential at a site is important to determine whether the soil is susceptible to liquefaction, and if it is, will that be triggered by the design earthquake?

There are number of different ways to evaluate this, either by laboratory experiments or by field tests. The laboratory experiments that are employed consist of a) Cyclic triaxial test, b) Cyclic direct simple shear test, c) Cyclic torsional shear test and d) True triaxial shear test. The field methods used include a) Standard penetration test (SPT), b) Cone penetration test (CPT), and c) Shear wave velocity test (SWVT). These tests are used essentially to estimate/correlate the cyclic resistance ratio of the soil. The cyclic resistance ratio is then compared with the cyclic shear stress expected in the soil during the earthquakes to assess whether it will liquefy or not. A detailed discussion on the methods of evaluating liquefaction potential can be found in Brennan *et al.* (2007).

2.3 Theoretical framework of liquefaction

2.3.1 Definition

A concise definition of liquefaction has been a subject of a long continuous debate in the engineering community. Poulos *et al.* (1985) referred to Hazen (1920) as the first engineer to use the term when he stated that the Calaveras Dam in California had *"liquefied."* However, Casagrande was regarded as the first person to start detailed laboratory investigation to understand the behaviour of saturated soil and liquefaction.

In 1936, Casagrande performed a series of drained strain-controlled triaxial tests and introduced the term "Critical Void Ratio (CVR)" that is attained by both initially loose and initially dense specimens at the same confining pressure when sheared to large strains (Kramer, 1996). Performing further tests at various effective confining pressures, he obtained the critical void ratio line, which constituted the boundary between dilative and contractive behaviour of soil in drained triaxial compression. From drained triaxial tests, he hypothesized that in an undrained condition the soil above the CVR line will liquefy, but below it, it will not. However, he himself contradicted this description in his 1971 lecture to British Geotechnical Society (Casagrande, 1971) and described liquefaction as a phenomenon where the soil changes from a static structure to a flow structure.

After the 1964 Niigata earthquake and the Alaska earthquake, where there was extensive damage to structures in liquefiable soils, the study of liquefaction gained momentum throughout the world. Engineers started to look for systematic procedures to evaluate liquefaction susceptibility of the ground and to design the structures accordingly. Laboratory investigations of various types of soil at different stress conditions became one of the most used tools to understand liquefaction phenomena.

Seed & Lee (1966) defined "initial liquefaction" as a stage in a cyclic load test when 100% pore pressure developed momentarily, irrespective of the shear strength that remains after that stage is reached.

In 1969, G. Castro as part of his PhD carried out a series of stress-controlled triaxial tests in undrained samples and introduced a similar void ratio line (like Cassagrande's CVR line) known as the Steady State Line (SSL), which forms the boundary between

dilative and contractive soil. Castro & Poulos (1977) explained the SSL concept using a state diagram as shown in Figure 2.4, where the axes are void ratio (e) and effective minor principal stress (σ_3'). They described that the soil above the steady state line will be prone to liquefaction, but the soil below it will not. For example, the soil at point "A" will contract and reach a steady state void ratio (for both cyclic and monotonic loading), after which if sheared it will deform with constant void ratio and constant σ_3'. This behaviour is also called flow liquefaction to distinguish it from other definitions. The SSL liquefaction concept is different from the CVR line liquefaction concept in that the former was derived from an undrained test, but the latter was hypothesized from drained test results. Soil below SSL if loaded cyclically, as in an earthquake, may also suffer permanent deformations and lose shear strength. This is described as cyclic mobility and the term was first proposed by Casagrande in 1969 to explain progressive softening of soil. The stress path during cyclic mobility will follow D to B as shown in Figure 2.4. Although, shear strength reduction is common for both soil states (C and D) during cyclic loading, cyclic mobility should not be confused with flow liquefaction as the soil in later case will not fail after the cyclic loading ceases and will regain strength if further sheared monotonically. These two soil behaviours can be distinguished by an unstable (liquefaction) and a stable (cyclic mobility) deformation behaviour as shown in Figure 2.5.

Although liquefaction and cyclic mobility were defined as two separate concepts, the term liquefaction in conventional usage includes both. This is based on the assumption that liquefaction defines the state of soil which has suffered significant loss of strength due to the generation of excess pore water pressure (EPWP) rise. The EPWP is defined as the change in pore water pressure value from its hydrostatic value and the ratio of EPWP to initial effective overburden is defined as pore water pressure ratio. The most versatile definition of liquefaction used in the engineering community which supports the above assumption is the one defined by Seed (1979) as: "the liquefaction is a state of soil at 100% pore water pressure ratio (PWPR)."

Another advancement in understanding the behaviour of soils that was developed at the University of Cambridge and Imperial College London is known as critical state
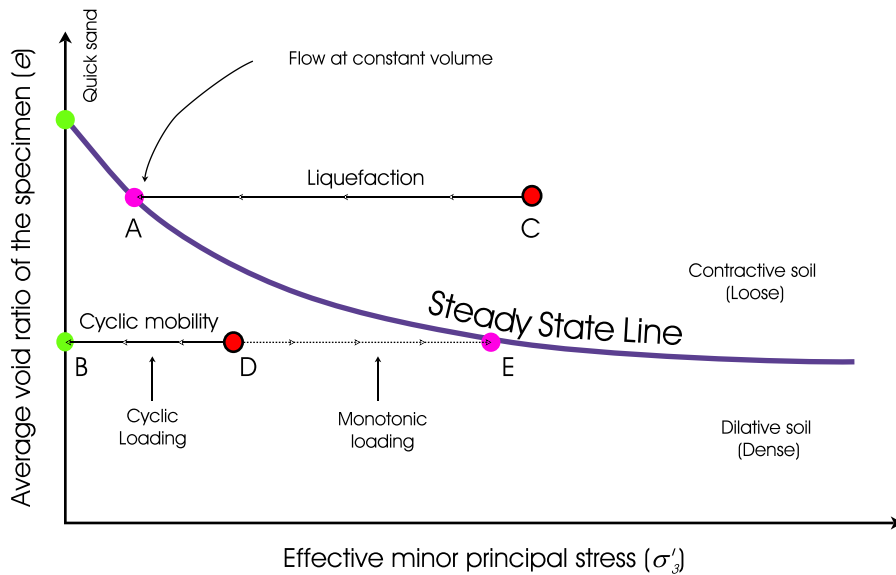
Figure 2.4: State diagram as described by Castro, redrawn after Castro & Poulos (1977).
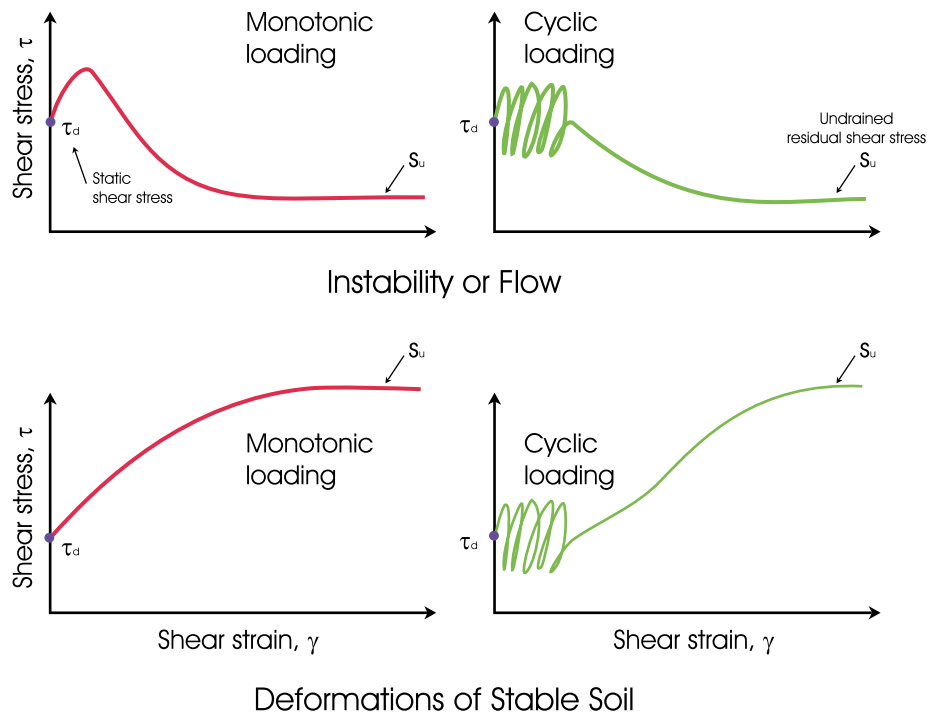
Figure 2.5: Stable and unstable behaviour of soil under static and cyclic loading, redrawn after Castro (1987).

theory of soil mechanics (Roscoe *et al.*, 1958). This is similar to the steady state concept as described by Castro & Poulos (1977), but has the advantage of describing the state of soil with a purely mathematical formulation based on plasticity theory. Using the critical state concept, Schofield (1981) defined liquefaction as a class of instability (e.g., channeling, piping, boiling, fluidising) seen in soil far on the dry side (refer Figure 2.13-c)

of critical states near zero effective stress and in the presence of a high hydraulic gradient. Details of the critical state theory for liquefied soil behaviour will be discussed later in section 2.3.4.

Ishihara (1993) defined liquefaction as *"a state of particle suspension resulting from release of contacts between particles of sand constituting a deposit. The type of soil most susceptible to liquefaction is one in which the resistance to deformation is mobilized by friction between particles under the confining pressure."*

Based on critical state concept and evidence from case histories, Muhunthan & Schofield (2000) remarked that the 100% pore pressure rise is a necessary condition for liquefaction but not the sufficient condition. The formation of openings and the presence of a high hydraulic gradient, which leads to the disintegration of the continuum into clastic blocks of soil, is another important requirement.

Although every definition discussed above has its own validity in the context it was defined, the term liquefaction is not generalised enough to describe different types of soil failure. For example, the definition by Ishihara (1993) and Seed (1979) seems reasonable in experimental tests to characterise strength loss in soil due to pore pressure rise, but, the definition by Schofield (1981) is more appropriate to the field cases of soil failure where different types of mechanism that cause the strength loss in saturated soil (e.g., channelling, piping, boiling, etc.) are of importance.

In this thesis, it is required to define the term "liquefaction" which can be studied quantitatively in experimental tests and is also valid in field applications. Hence, "liquefaction" here will be used to refer a state of soil in which the effective overburden stress (σ'_v) falls to near-zero value due to a build up of pore water pressure. The pore water pressure (u) refers to the pressure of the ground water held in the pores/gaps between soil particles and is close to the hydrostatic pressure at a no-flow condition. The excess pore pressure ratio 'r_u' is defined as the ratio between excess pore water pressure (u_{ex}) and initial effective overburden stress (σ'_{vo}) as:

$$r_u = \frac{u_{ex}}{\sigma'_{vo}} \tag{2.1}$$

Full liquefaction refers to the condition when $r_u = 1$, and no liquefaction is when

$r_u = 0$. Partially liquefied soil is characterised with r_u values ranging between 0 and 1. Partial liquefaction can occur either due to smaller driving shear stress or partially drained conditions.

2.3.2 Stress-strain behaviour of soil during liquefaction

To understand a typical stress-strain behaviour of liquefied soil, a laboratory test result of Nevada sand with the time history of excess pore water pressure at $D_r = 40\%$ is presented in Figure 2.6. The test was conducted in an undrained, anisotropic consolidated stress-controlled cyclic triaxial test during the VELCAS report (Arulmoli *et al.*, 1992) as reported in Yang *et al.* (2003). The excess pore pressure plot shows the occurrence of liquefaction in the test while the excess pore pressure reached 150kPa. The stress-strain behaviour shows the accumulation of deformation in a cycle-by-cycle pattern. The stiff curves correspond to the pre-liquefaction case, while the curves with higher deformation were at full liquefaction. Stiffness had degraded to a very low value for small strains, but, the soil became stiff again at higher strain due to reduction in excess pore water pressure.

In element tests, the stress state of soil is generally plotted in $q - p'$ space, where q is the deviator stress and p' is the mean effective confining stress. This allows one to track the stress path taken by the soil during the loading and unloading phases of the tests. The shear stress, τ, in the soil is half of the deviator stress, q. For a soil sample in a triaxial stress state, the definition of τ, q and p' can be referred to in Figure 2.7. In natural soil deposits, p' is directly proportional to the effective overburden pressure of the soil, σ'_v.

Ishihara *et al.* (1975) studied the contractive and dilative behaviour of saturated sandy soil through a series of monotonic and cyclic triaxial tests. They defined a line known as the Phase Transformation Line (PTL) in $q-p'$ space, which forms the boundary between contractive and dilative behaviour of soil during the element tests. Figure 2.8 shows the measured $q - p'$ behaviour of Fuji sand during monotonic and cyclic triaxial tests by Ishihara *et al.* (1975). All the stress paths change from contractive to dilative or vice-versa when they cross the PTL. This line lies slightly below the failure line (FL).
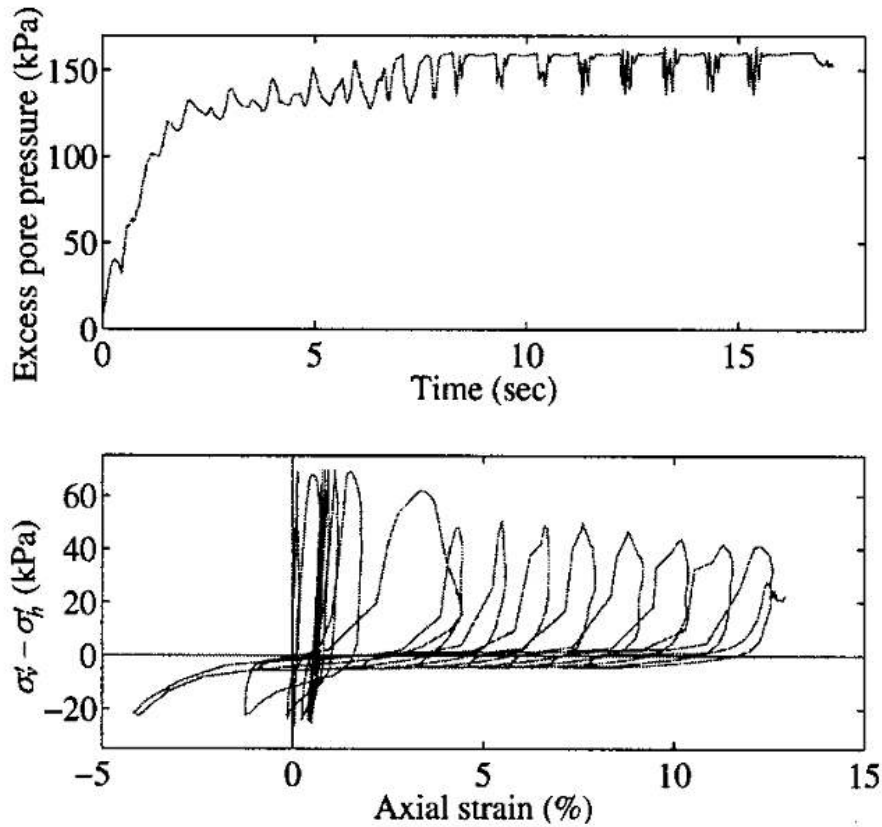
Figure 2.6: Time history of excess pore water pressure and stress strain behaviour of Nevada sand at $D_r = 40\%$ (Yang *et al.*, 2003).

τ = Shear stress = $q/2$ = $(\sigma'_1 - \sigma'_3)/2$

q = Deviator stress = $\sigma'_1 - \sigma'_3$

p' = Mean effective confining stress = $(\sigma'_1 + 2\sigma'_3)/3$
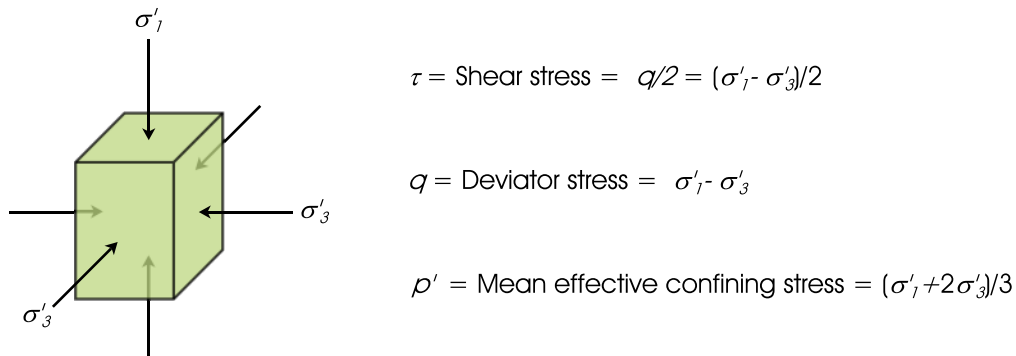
Figure 2.7: Definition of τ, q and p' in triaxial stress state in a soil sample.

The same phenomenon had been studied independently by Luong & Sidaner (1981) and they described the boundary between contractive and dilative behaviour of the soil as the characteristic state line. The characteristic state line is essentially the same as PTL. Once the soil crosses this line it dilates and then follows a path very close to the failure line.

The monotonic load path in Figure 2.8a shows an initial contraction and dilation thereafter. In the cyclic load path in Figure 2.8b, once the soil reaches a state of zero

21
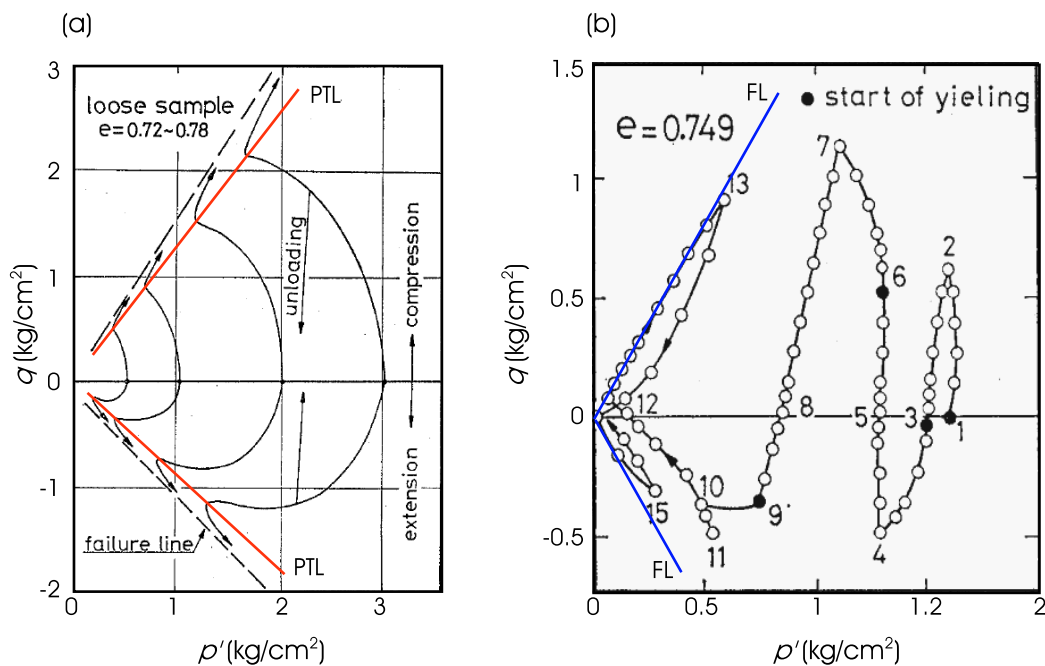
Figure 2.8: Stress path of loose Fuji sand obtained from triaxial tests subjected to (a) monotonic loading, and (b) cyclic loading (Ishihara *et al.*, 1975).

effective overburden (i.e., full liquefaction), the stress path during loading is always dilative and closely follows to the failure line (FL).

2.3.3   Post-liquefaction behaviour

The phenomenon when the zero effective stress state occurs for the first time is usually known as initial liquefaction for cyclic undrained loading, which may classify the liquefaction behaviour into two parts: pre-liquefaction and post-liquefaction. As liquefied soil has a very small strength at small strain, the large strain behaviour is often of particular interest. This is generally studied by applying a monotonic shear to the soil after initial liquefaction is achieved by cyclic loading. A schematic representation of this loading is shown in Figure 2.9.

Yasuda *et al.* (1999) carried out multi-stage triaxial tests where the soil was initially liquefied by cyclic loading and then monotonically sheared at a constant strain rate. Figure 2.10 shows the post liquefaction stress-strain behaviour of Toyoura sand at different relative densities. Similar tests had also been carried out by Vaid & Thomas (1995) on Fraser River sand at various relative densities and initial confining pressures, the results of which are presented in Figure 2.11. The tests have shown that the liquefied soil offers
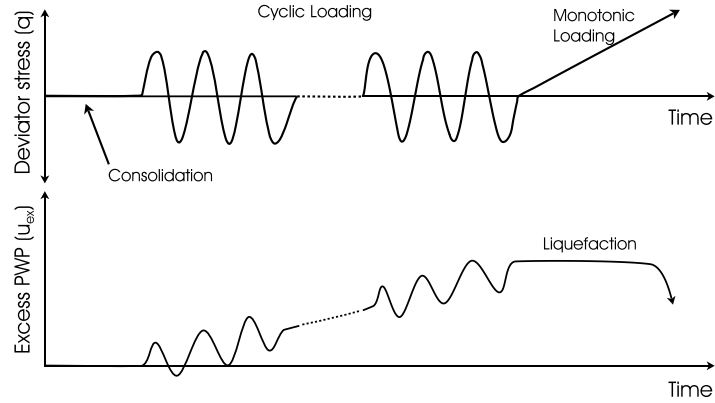
Figure 2.9: Procedure of applying cyclic and monotonic loading to study post liquefaction behaviour of liquefied soil (redrawn after Yasuda *et al.*, 1999).

nearly zero resistance for a particular amount of strain and then starts to offer resistance. The cause of this resistance was attributed to the suppressed dilation with a decrease in excess pore water pressure. The zone of zero resistance was quite large in liquefied soil as compared to non-liquefied soil, and it depends largely on initial relative density. The higher the relative densities (D_r), the lower the zero resistance zones.

Sitharam *et al.* (2009) conducted a series of cyclic triaxial tests on Ahmadabad sand (India) to investigate the influence of amplitude of axial strain, relative density and confining pressure on the post liquefaction undrained response. A typical test result at 70% relative density with different initial amplitude of axial strain to cause liquefaction is given in Figure 2.12. Similar results were also obtained by other researchers such as Shamoto *et al.* (1997), Kokusho *et al.* (2004) and Hyodo *et al.* (1998). Their tests have shown that the undrained stress path ($q - p'$ response) after liquefaction started from the origin and increased linearly irrespective of the amplitude of axial strain used to induce liquefaction.

2.3.4 Critical state theory for liquefied soil

The critical state theory of soil mechanics, devised by Roscoe *et al.*, 1958, provides a strong mathematical framework to describe the behaviour of soils. The theory states that the soil, if sufficiently distorted, will come into a well-defined critical state where it shears without any change in stress or volume (Schofield & Wroth, 1968). This state can also be
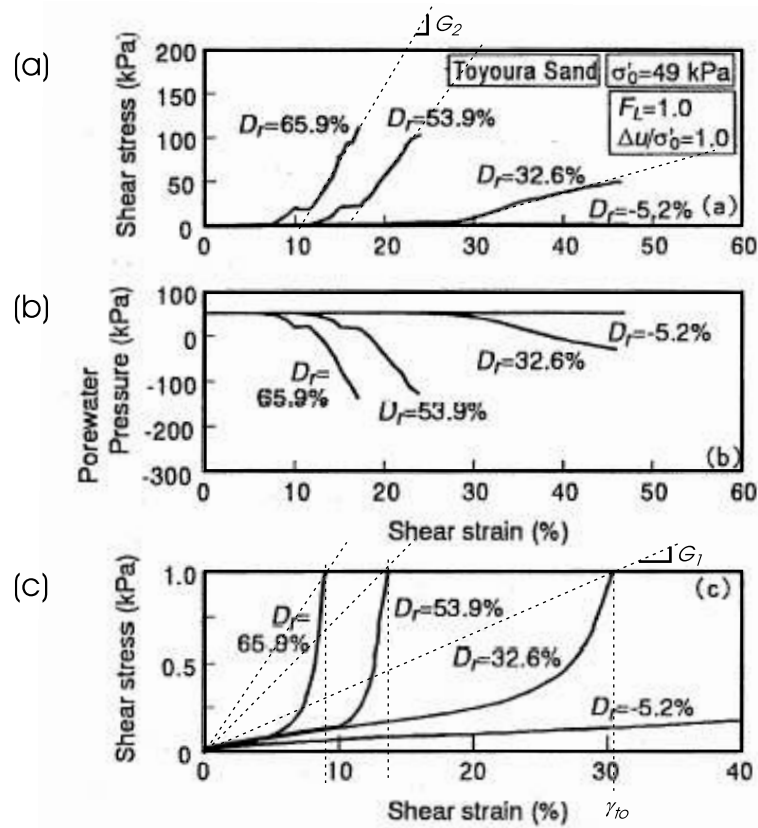
Figure 2.10: Triaxial test results by Yasuda *et al.* (1999).

understood as the end state that soil attains as it is deformed irrespective of the type of loading. The main advantage of this theory is that if the end-state is known it becomes simpler to construct well-behaved theoretical models, and you know exactly where you are going. The soil state in the critical state framework is defined by three parameters, namely:

1. mean effective confining stress, p'

2. deviator stress, q, and

3. specific volume, v.

The specific volume of the soil is defined as $1 + e$, where e is the void ratio of the soil. The critical state of the soil can be depicted as a line in $p' - q - v$ space (Figure 2.13), known as the Critical State Line (CSL). The critical state in 2D can be defined in $q - p'$ space and $e - \ln p'$ space, given by Equations 2.2 and 2.3.
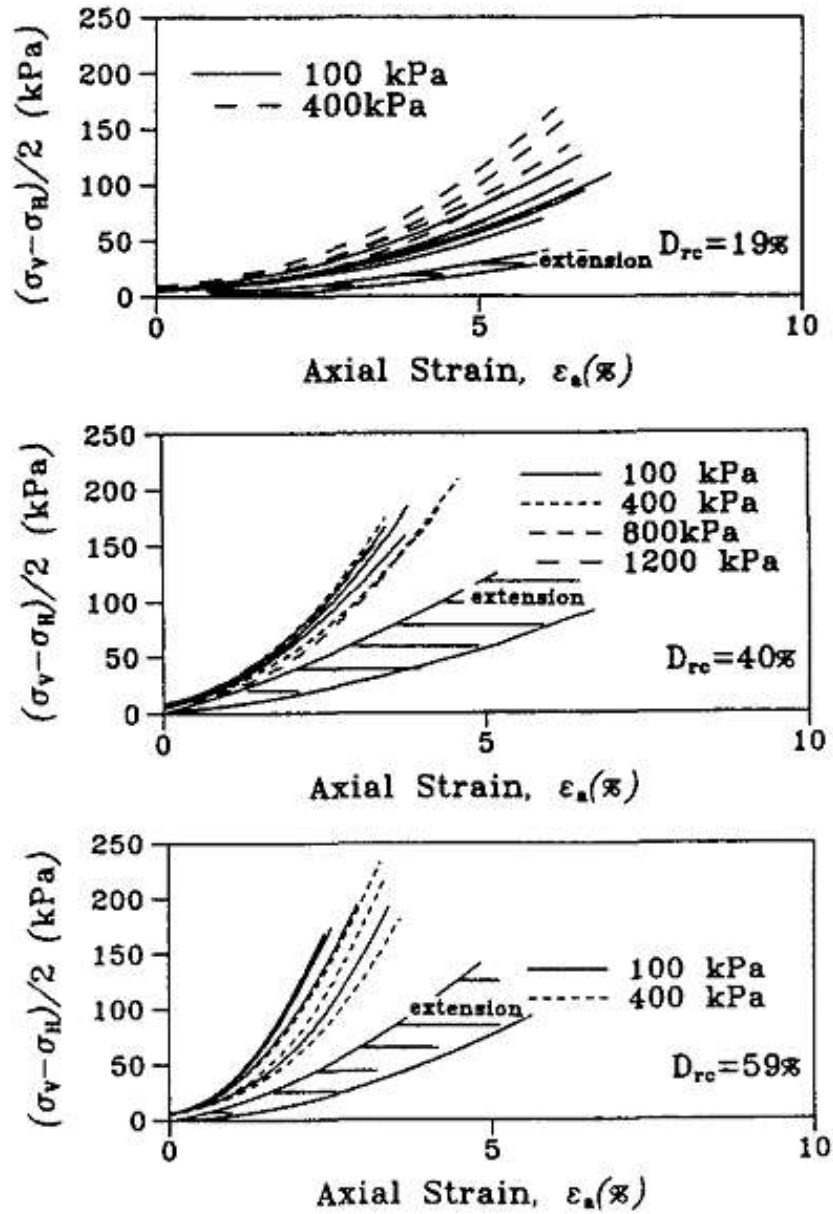
Figure 2.11: Post liquefaction monotonic response of Fraser sand (Vaid & Thomas, 1995).

$$\frac{q}{p'} = M_c \text{ or } M_e \tag{2.2}$$

$$v = \Gamma - \lambda \ln p \tag{2.3}$$

M_c and M_e are defined as the stress ratio in triaxial compression and triaxial extension, i.e., the slope of critical state line. The soil constant λ, is defined as the slope of CSL in $v - \ln p'$ space, and Γ is defined as the specific volume of the soil at critical state

25
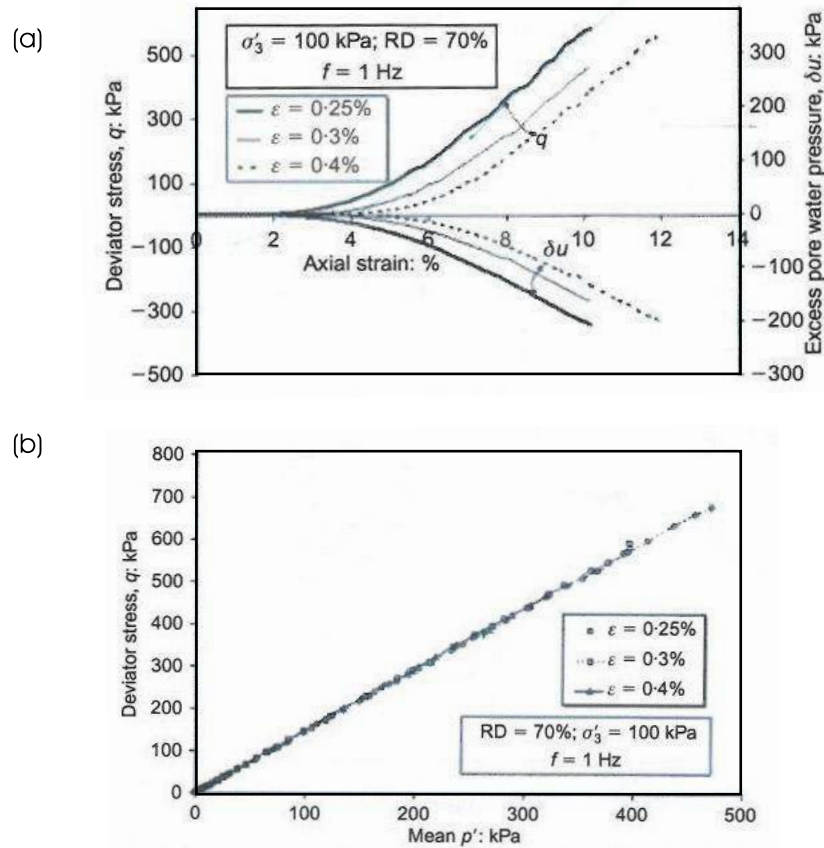
Figure 2.12: Triaxial test results at 70% D_r with different initial amplitude of axial strain to cause liquefaction by Sitharam *et al.* (2009).

corresponding to unit effective overburden pressure, p'.

In $q - p'$ space, the CSL can be defined as a straight line starting from the origin. The CSL lies very close to the failure line, just below it in the compression zone and just above it in the tension zone. A schematic representation of PTL, FL and CSL in $q - p'$ stress space is shown in Figure 2.14 along with monotonic and cyclic undrained behaviour of sand.

2.3.5 Description of element test results by critical state theory

In the framework of triaxial element test results, when the ultimate strength of the soil is mobilised, the stress ratio in triaxial compression (η_c) and in triaxial extension (η_e) can be different (MuirWood, 1990). Mathematically, η_c and η_e can be written using the Mohr-Coulomb failure criterion as (Schofield & Wroth, 1968):
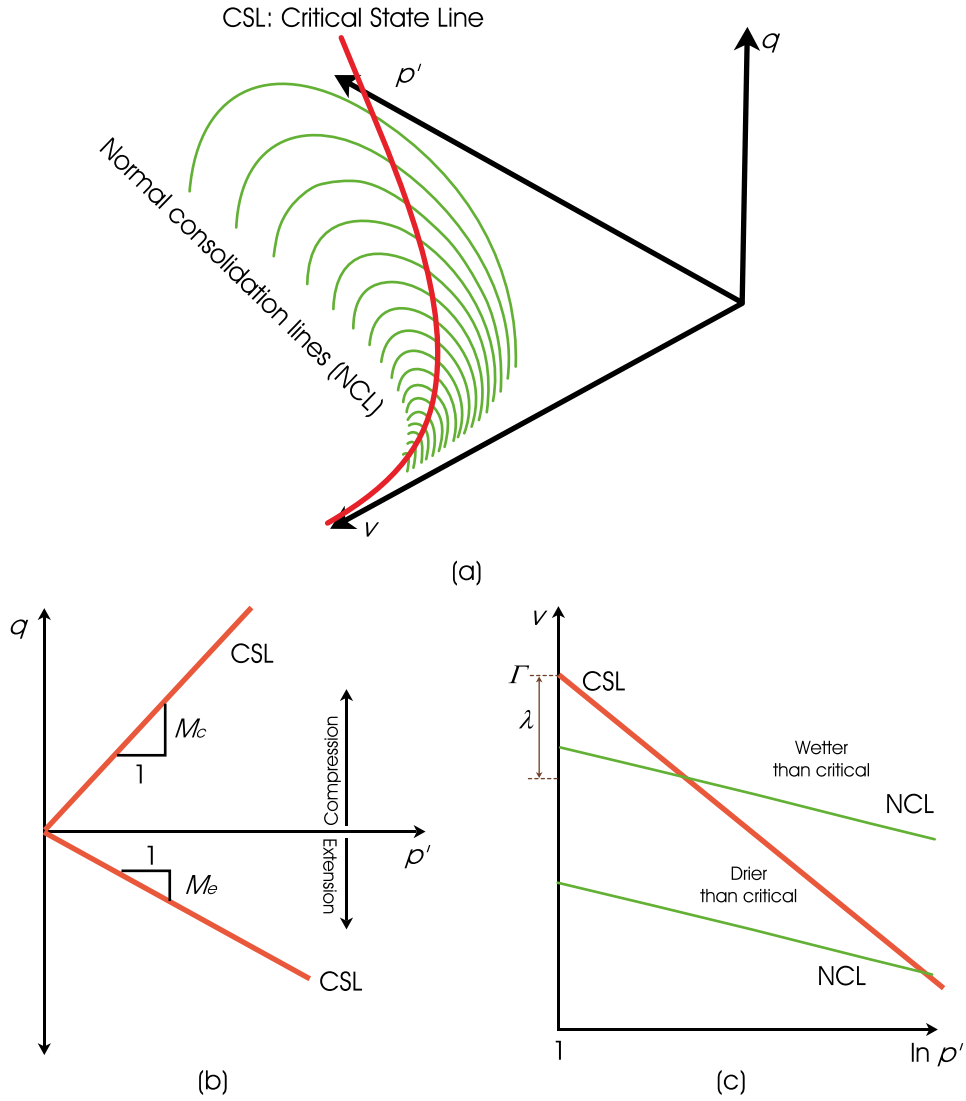
Figure 2.13: (a) Schematic representation of three dimensional view of critical state line; (b) CSL in $q - p'$ plane; (c) CSL in $v - \ln p'$ plane, redrawn after Schofield & Wroth (1968) and Muhunthan & Schofield (2000).

$$\eta_c = \frac{6 \sin \phi'}{3 - \sin \phi'} \tag{2.4}$$

$$\eta_e = \frac{6 \sin \phi'}{3 + \sin \phi'} \tag{2.5}$$

where, ϕ' is the angle of friction mobilised during shearing.

The ϕ' of a sand depends on its critical state angle of friction (ϕ_{cs}) and dilatancy behaviour. Sand dilates with shearing at a rate that increases with increasing relative density (D_r) and decreases with increasing effective confining stress (p'). The dilatancy of the soil vanishes when it reaches critical state, either due to volume change in a drained
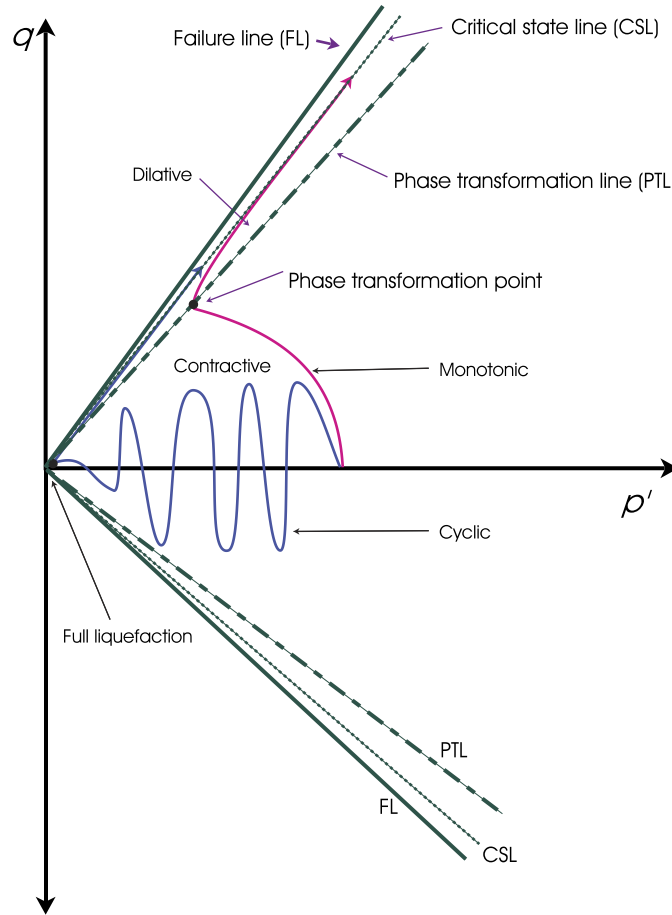
Figure 2.14: Schematic description the stress state (in $q - p'$ space) of dilative and contractive behaviour of liquefiable soil in an undrained test.

element test or, effective pressure change in an undrained element test. For liquefied soil, the post liquefaction response is always dilative, but it is suppressed due to undrained condition and follows a straight stress path on CSL upon continuous shearing. Experimental evidence (e.g., Vaid & Thomas, 1995; Sitharam *et al.*, 2009) also suggests that the post liquefaction deformation progresses with a constant stress ratio irrespective of its state of relative density. This response nearly corresponds to the critical state of the soil.

Hence, while estimating the stress ratio for post liquefied behaviour of soil in triaxial compression and extension, ϕ' can be replaced by ϕ_{cs} in Equations 2.4 and 2.5. The equation for stress ratio at critical state in triaxial compression (M_c) and extension (M_e) can hence be written as:

$$M_c = \frac{6\sin\phi_{cs}}{3 - \sin\phi_{cs}} \tag{2.6}$$

$$M_e = \frac{6 \sin \phi_{cs}}{3 + \sin \phi_{cs}} \qquad (2.7)$$

For sandy soil, the value ϕ_{cs} depends mainly on its mineralogy and the shape and size of the particle and its gradation (Atkinson, 1993; Bolton, 1986). It can also be obtained directly from the $q - p'$ plots of the element tests in which the critical state is reached. The effect of stress path on critical state friction angle, ϕ_{cs}, has been studied by several researchers, which showed that ϕ_{cs} is higher for plane strain conditions than for triaxial conditions, a good discussion on this is given by Chakraborty & Salgado (2010). Typical values of ϕ_{cs} are collated in Table 2.1.

Table 2.1: Some typical and specific values of critical state angle of friction for sandy soil.

Type of soil	Critical state angle of friction (ϕ_{cs})	Reference(s)
Typical granular soils		
River sand	32°	Atkinson (1993)
Decomposed granite	39°	Atkinson (1993)
Carbonate sand	40°	Atkinson (1993)
Specific soils		
Toyoura sand, Japan	31.2°- 34.4° (Triaxial compression) 34.5°- 38.0° (Plane shear)	Chakraborty & Salgado (2010)
Ahmedabad sand, India	35.5° (Triaxial compression)	measured from the tests by Sitharam *et al.* (2009)
Ottawa sand, Canada	28.5°	Imam *et al.* (2005)

2.4 Dynamic properties of liquefied soil

The dynamic properties of liquefied soil can be characterised by four major parameters; stiffness, strength, damping and viscosity. The next section will discuss these properties in detail.

2.4.1 Stiffness

The shear modulus (G) is normally used to represent soil stiffness. On this, Eurocode 8 says: "Due to its influence on the design seismic actions, the main stiffness parameter of

the ground under earthquake loading is the shear modulus G, given by $G = \rho v_s^2$, where ρ is the unit mass and v_s is the shear wave propagation velocity of the ground." O'Rourke & Liu (1999) collated data that quantify the stiffness of liquefied soil. They refer to Takada *et al.* (1987), who developed an equivalent soil spring to model pipes in liquefied soil, and proposed that the stiffness of the liquefied soil may range from 1/1000 to 1/3000 of that for non-liquefied soil. O'Rourke & Liu (1999) also reported that the stiffness may range from 1/100 to 3/100 that of non-liquefied soil, a finding based on model studies by Yoshida & Uematsu (1978); Matsumoto *et al.* (1987); Yasuda *et al.* (1987) and Tanabe (1988).

Yasuda *et al.* (1998) carried out a set of torsional shear tests to study post liquefaction behaviour of several sands. The sands studied included two clean sands from Japan and Turkey (Toyoura sand and Istanbul sand), one gravelly sand with fines (Masa sand) and one mixed sand (Istanbul sand with 10% silt). The study showed that the stiffness (G) of soil at full liquefaction had reduced to less than 1/1000 the initial stiffness.

More recently, Ghosh (2003) carried out centrifuge tests at Cambridge University to measure the variation of shear wave velocity 'v_s' for both pre-earthquake and post-earthquake conditions of soil, and then estimated the shear modulus G. Figure 2.15 shows the test results where v_s decreased to 15m/s at full liquefaction as compared to 150m/s at the pre-earthquake state. This implies a 100 fold decrease in shear modulus due to liquefaction.
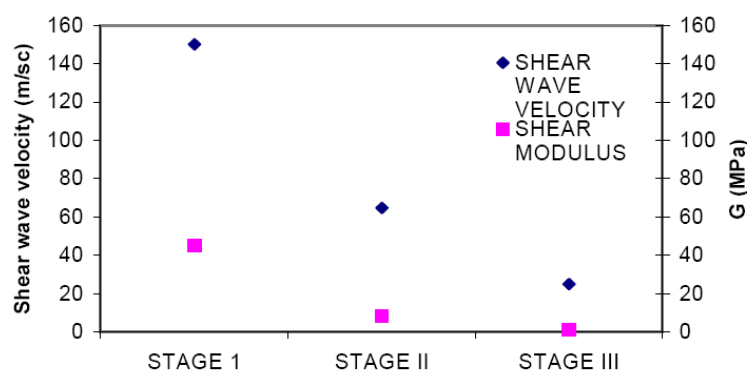
Figure 2.15: Typical stiffness degradation of saturated sandy soil during different magnitude earthquake. Stage I: Pre earthquake condition, Stage II: Medium strength earthquake, no liquefaction, Stage III: Strong earthquake that caused liquefaction.

The above discussion has shown a possible significant loss of stiffness, however, these

are mainly reflecting the small strain behaviour. The large strain behaviour is expected to yield higher stiffness as discussed in section 1.3.2.

2.4.2   Strength

Several definitions do exist that define the shear strength of liquefied soil; examples include undrained steady state strength (Poulos *et al.*, 1985), undrained residual strength (Seed, 1987) and undrained critical strength (Stark & Mesri, 1992). The definition used here is taken from Olson & Stark (2002) as it is very general and does not imply any correspondence to laboratory test conditions. It states that "the liquefied shear strength s_u is defined as the shear strength mobilised at large deformation after liquefaction is triggered in saturated contractive sandy soils."

Poulos *et al.* (1985) proposed a laboratory based procedure to estimate the *in-situ* value of s_u from undrained tri-axial test data (Figure 2.16). Kramer (1989) argued that these laboratory methods may not be a good representation as a slight error in estimating the *in-situ* void ratio during sample preparation may cause a large difference in the estimated shear strength. Poulos *et al.* (1985) also hypothesized that s_u depends solely on the void ratio after consolidation. However, studies by Vaid & Thomas (1995) showed that s_u may also be influenced by the mode of shear, the effective confining stress and sample preparation method.

In contrast, Seed (1987) proposed a relationship between s_u and SPT blow count value (N_{1-60}), which was based on back-analysis of 17 case histories of liquefaction flow failure. This was later updated by Seed & Harder (1990) and is being used as state-of-the-practice despite the uncertainties implicit in back-calculation procedures (Olson & Stark, 2002). Figure 2.17 shows the s_u values proposed by Seed & Harder (1990) for clean sand corrected SPT blow count. The figure shows that the upper bound value of strength varies between 11kPa and 32kPa, whereas the lower bound value varies between 0kPa and 25kPa. This value is very low as compared to standard strength of soil expected at site in normal conditions. We can note that Eurocode 7 (Eurocode, 1998) suggests soil having an s_u less than 15kPa is very weak and does not bear enough strength to resist lateral deflection of piles, as is evident from this clause:
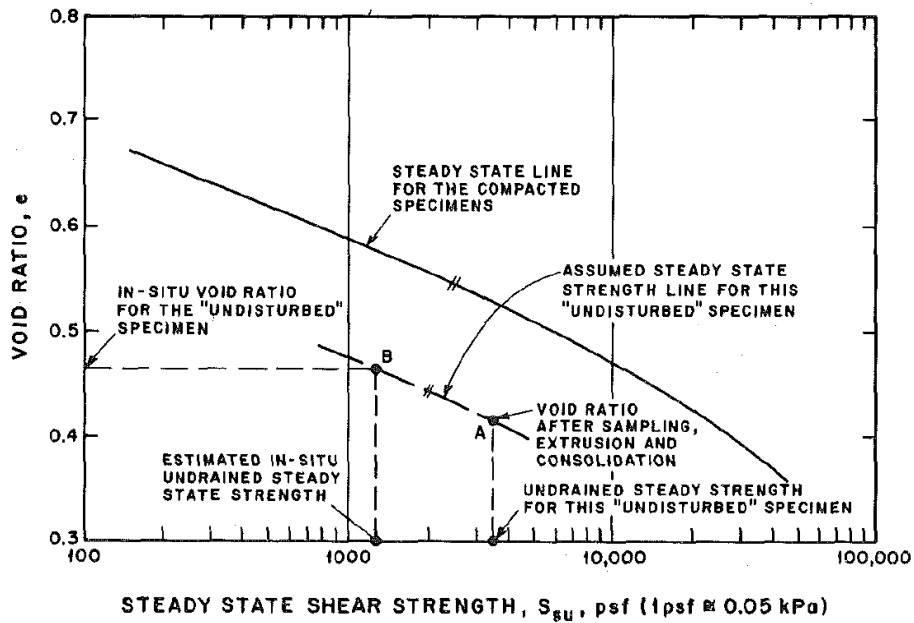
Figure 2.16: Steady state strength of liquefied soil (s_u) as proposed by Poulos *et al.* (1985).

"Slender piles passing through water or thick deposits of very weak soil need to be checked against buckling. This check is not normally necessary when piles are completely embedded in the ground unless the characteristic undrained shear strength is less than 15kPa".

Recently, Eurocode 7 (2008) has reduced the shear strength limit to 10kPa, although the reason of this reduction is not apparent in the literature.
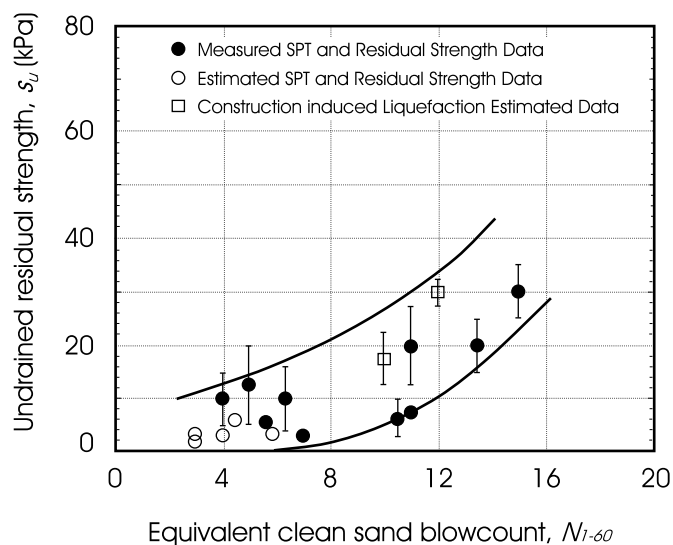
Figure 2.17: Maximum residual strength of liquefied soil obtained from case histories (after Seed & Harder (1990)).

The shear strength criterion has been further modified by Stark & Mesri (1992), and then improved by Olson & Stark (2002). The relationships proposed by Olson & Stark (2002) based on SPT blow count and CPT tip resistance are given in Figures 2.18 and 2.19, respectively.
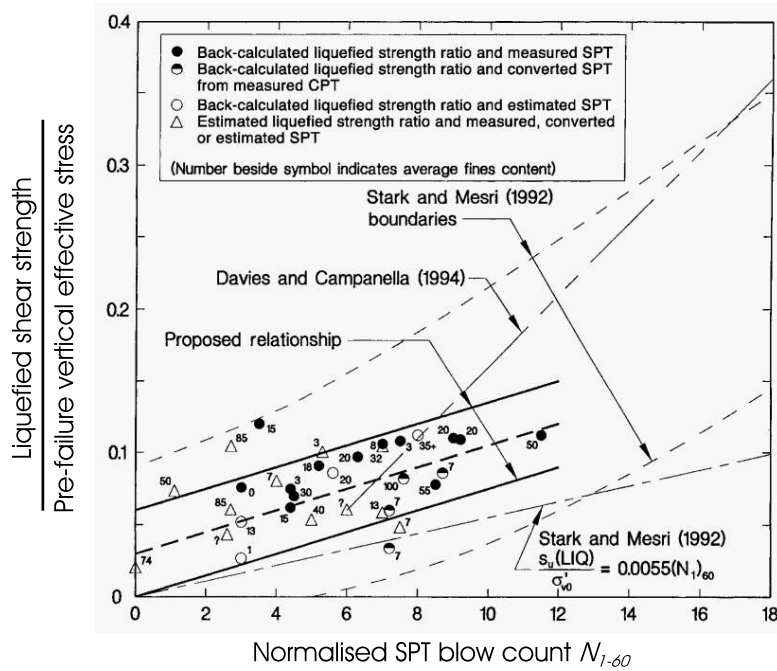
Figure 2.18: Liquefied strength ratio based on normalized SPT blow count as proposed by Olson & Stark (2002).
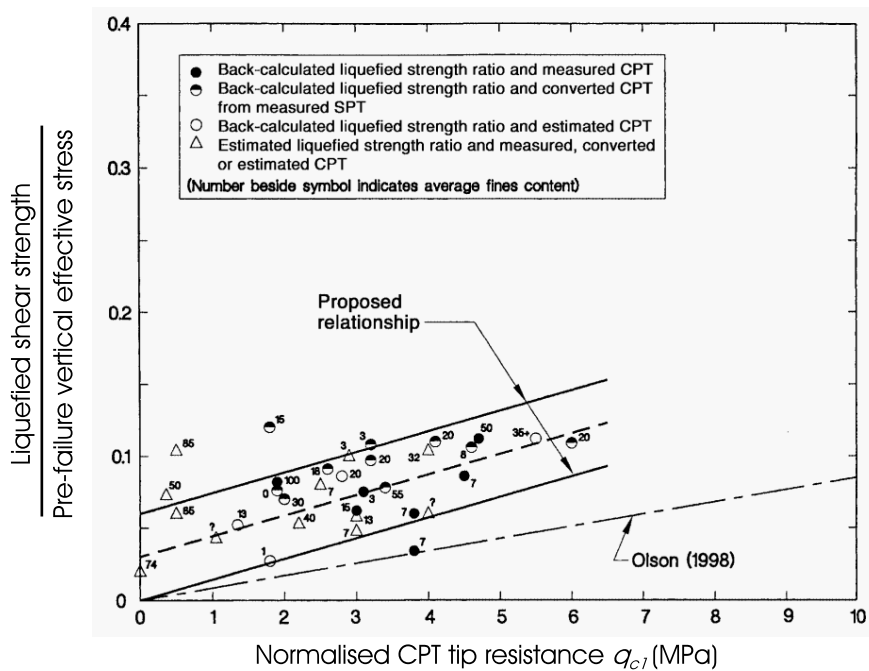
Figure 2.19: Liquefied strength ratio based on normalized CPT tip resistance as proposed by Olson & Stark (2002).

2.4.3 Damping

Damping of the soil can have significant influence on the pile-soil interaction during earthquakes or dynamic loadings. Although, extensive studies have been carried out to evaluate the damping of soil in general for shear strains not more than 1% ($\gamma < 1\%$), the literature is very limited on damping for liquefied soil subjected to large strains.

Sitharam *et al.* (2004) conducted strain controlled cyclic triaxial tests to study the effect of relative density on damping ratio for a given confining pressure. Two sand samples with relative densities (D_r) of 30% and 70% were prepared and tested under a confining pressure of 100kPa. The tests were conducted at a constant cyclic axial strain of varying magnitudes. The cyclic axial strain was sinusoidal and applied at a frequency of 1Hz. The estimated damping ratios for different levels of peak shear strain are shown in Figure 2.20. These results show that the effect of relative density on damping ratio was not very significant. However, a higher damping was observed with higher strain and the variation was nearly linear in the range of 0.1% to 5% strain in log scale. About 30% of damping was observed at 5% strain in the saturated soil sample loaded cyclically.
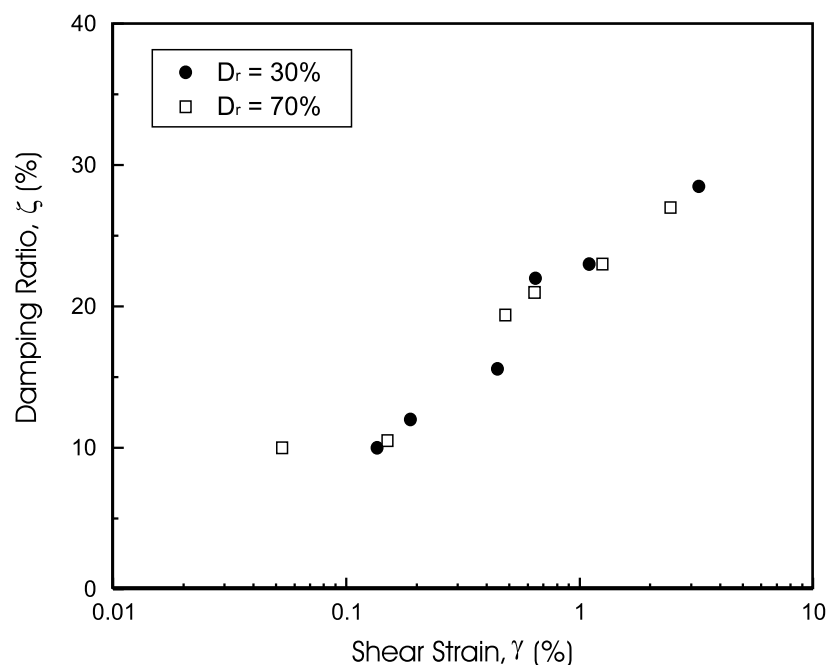
Figure 2.20: Damping from laboratory tests on saturated sand (Sitharam *et al.*, 2004).

Recently, Kamijo *et al.* (2004) conducted a series of full scale experiments of a pile-supported structure in a liquefiable sand deposit. The experiments were conducted in

a test pit back-filled with 100% water saturated clean sand. Large amplitude ground vibration was applied by mining blasts near the test pit. Figure 2.21 shows the experimental model and the measured natural frequency and damping of the structure. Using measured ground motion inputs and structural responses, dynamic properties of the soil–pile-structure system such as the natural period and damping were identified by fitting test records to the single-input-multi-output auto regression model. They observed significant decrease in fundamental period and increase in overall damping of the structure at full liquefaction as compared to the no-liquefaction case. The effective damping at no liquefaction condition (Test-1) was less than 7%, whereas, it was considerably higher with a value of about 20–40% for fully liquefied state (Test-3).
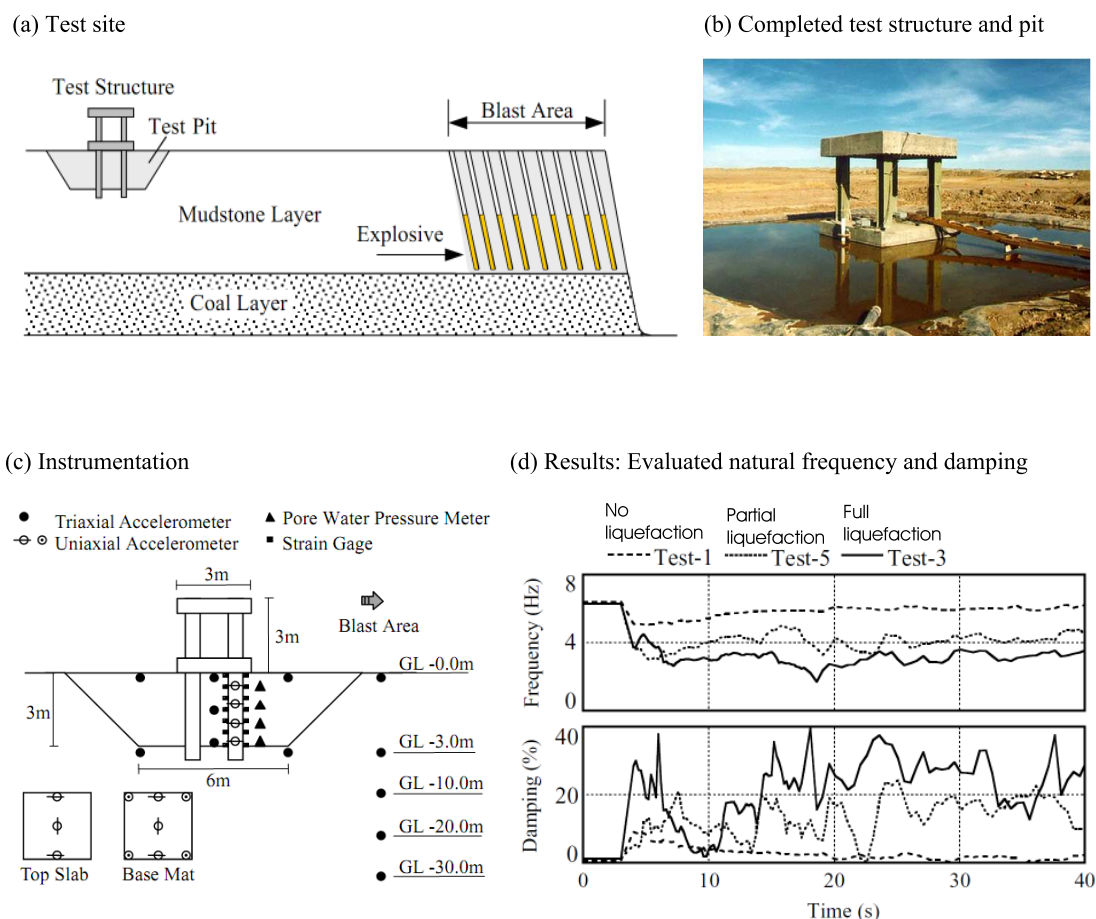
Figure 2.21: Full scale experimental setup (Kamijo *et al.*, 2004) used for dynamic soil-pile interaction study in liquefiable soils.

2.4.4   Viscosity

It has been seen that liquefied soil offers very low resistance to deformation and the sand particles are in a near suspension state. Based on this hypothesis, attempts have been made by various researchers (Towhata *et al.*, 1992; Uzuoka *et al.*, 1998 and Hadush *et al.*, 2000) to treat it as a thick fluid and many experiments were carried out to obtain viscosity of liquefied soil. They modelled the resistance of a pile in soil as the drag force in an incompressible fluid which can be estimated by knowing the viscosity of fluid, the relative velocity of the fluid and the size of the object. Hwang *et al.* (2006) collated various tests to estimate the viscosity of liquefied soil, as shown in Figure 2.22. For example, Kawakami *et al.* (1994) measured the viscosity of Toyoura sand (this sand is studied later in chapter 3 in the centrifuge test) to be about 20Pa-s. They also developed a relationship between viscosity and shear strain rate where the viscosity decreases with increase in strain rate. Uzuoka *et al.* (1998) used a fluid mechanics based model to estimate the deformation of slopes on liquefied soil and the loads applied by these flowing slopes to underground walls in shaking table tests.
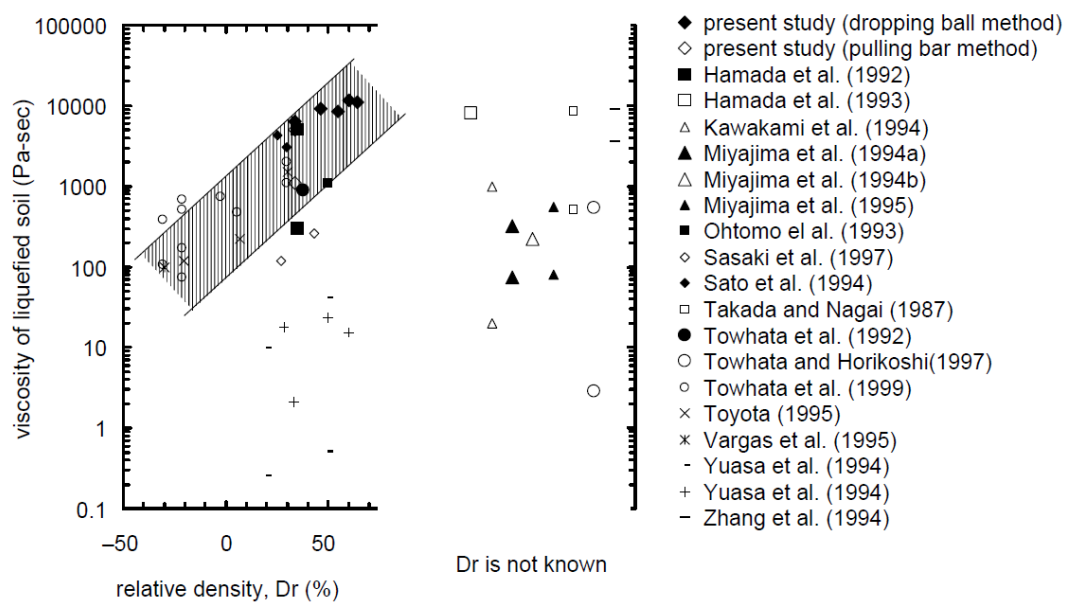
Figure 2.22: Viscosity of liquefied soil obtained by various researchers (Hwang *et al.* (2006)). [Present study in the figure refers to the study carried out by Hwang *et al.* (2006) on liquefied Jumoonjin sand]

Takahashi (2002) carried out $1-g$ experiments to study the lateral resistance of a pile in liquefied soil for different strain rates and concluded that the resistance increases with an increase in strain rates. This observation supports the hypothesis that the liquefied soil can be treated as a fluid where the loading rate affects lateral resistance. However, he argued that this assumption may not be suitable for the recent performance-based approach to pile foundations where it might be very difficult to determine the relative pile-soil velocity during the period of the shaking.

On another account, although viscous assumption of liquefied soil gives a good prediction of the drag force a pile may experience while subjected to soil flow, it cannot model the phase change behaviour of soil. Liquefied soil in an undrained condition, while subjected to large strain, can dilate and the interlocking of sand particles again makes it behave like a solid. It is not possible to represent this behaviour with a fluid mechanics assumption which considers that the material is fluid throughout the analysis.

2.5 Design philosophy for piles in liquefiable soils

The predominant loads acting on a pile in liquefiable soils during an earthquake can be classified into two categories: (a) loads from the superstructure (e.g., axial load, inertial load, etc.) and (b) loads from the soils (e.g., lateral kinematic load from lateral spreading soil, vertical kinematic load from soil settlement, etc.). The failure mechanism of a structural element is one of the prime parameters on which a design philosophy is based. Ignoring a possible failure mechanism in the design phase (i.e., ignoring a safety check for a possible cause of failure) may lead to a disaster, as has been learnt from many events in the past (Bhattacharya *et al.*, 2008).

The major school of thought considers that the pile foundations in liquefiable soils subjected to seismic shaking may fail due to:

- excessive settlement,

- shear,

- bending,

- static instability, or

- dynamic instability.

Of these mechanisms, bending due to liquefaction induced lateral spreading of the ground is often regarded as the root cause of many pile foundation failures during earthquakes, see for example: Hamada (1992a,b); Ishihara (1997); Tokimatsu *et al.* (1998); Goh & O'Rourke (1999); Abdoun & Dobry (2002); Finn & Fujita (2002). However, buckling instability has been studied recently as another possible mechanism of pile failure in liquefiable soils; e.g., Bhattacharya (2003); Bhattacharya *et al.* (2004); Kimura & Tokimatsu (2005); Knappett & Madabhushi (2006) and Shanker *et al.* (2007). The design philosophies based on these two major failure mechanics are described below.

2.5.1 Bending philosophy

In many major earthquakes where extensive liquefaction has been observed, permanent lateral deformation or lateral spreading of soil has been reported to be the main source of distress in piles (Abdoun & Dobry, 2002; Finn & Fujita, 2002). The current understanding is that lateral spreading induces bending in the pile, and the design codes check the bending moments in piles caused by lateral spreading of the ground. The movement of the superstructure can also induce bending moments in the pile.

However, Ishihara (1997) noted that during an earthquake soil liquefaction starts at approximately the instant of peak acceleration. He argues that since the seismic motion has already passed its peak, subsequent shaking will be less intense, so that the lateral force applied by the superstructure will not be significant. Therefore, the effects of inertia of the superstructure on the pile stresses are considered separately and are not combined with the lateral spreading effects.

Eurocode 8 (Eurocode, 1998) advises designers to design piles against bending due to inertia and kinematic forces arising from the deformation of the surrounding soil recommending that piles should be designed to remain elastic, but that the sections at the pile cap and at the interfaces between layers of soil with markedly different properties should have the capacity to form plastic hinges. Eurocode 8 (part 5 clause 5.4.2) also suggests that the side resistance offered by the soil layers susceptible to liquefaction shall be ignored.

The Japanese Code of Practice (JRA, 2002), for example, advises engineers to design piles against bending failure assuming there is a non-liquefied crust and the liquefied soil applies a lateral load of 30% of the total overburden pressure to the pile. Other codes, such as NEHRP guideline (NEHRP, 2000) and Indian Code IS 1893 (IS-1893, 2000), also focus on bending strength of the pile. In summary, the current philosophy of pile design simply treats them as beams and assumes that the lateral loads due to inertia and soil movement cause bending failure of the pile.

2.5.2   Buckling philosophy

Buckling instability of the pile may be regarded as static or dynamic depending on the loading condition. The main idea of the buckling mechanism is that, during liquefaction, the pile suffers a significant loss of lateral support in the liquefied zone. If the axial load is very high (i.e., near to the critical buckling load), buckling instability of an end-bearing pile may occur promoted by the actions of lateral loads and/or imperfections. Normally, this form of failure may happen if the pile is not sufficiently embedded in competent soil below the liquefiable soils, and the depth of liquefied soil is deep enough to make the pile to behave as a long slender column with high axial load.

In some cases the pile tip may rest in the liquefiable zone. This situation may pose a threat to the overall stability of the pile supported structure in a major seismic event. This form of failure has been explored through the study of the Kandla Port and Customs Office Tower failure during 2001 Bhuj Earthquake by Dash *et al.* (2009).

2.5.3   Interaction of design philosophies

When piles in liquefiable soils are subjected to an inertia load from a superstructure and/or kinematic force from a lateral spreading soil, they may be damaged structurally due to higher bending moment or shear force or may buckle due to higher axial load and lower lateral resistance from soil. It may also be possible for pile supported structures to sink in liquefied soil in level ground due to loss of bearing. Though there may not be any structural damage due to sinking, the whole structure will fail to meet the serviceability condition.

It is also recognised that the failure of piles in liquefiable soils is governed either by individual mechanisms or any of their combinations (Dash *et al.*, 2009; Dash *et al.*, 2010a and Dash & Bhattacharya, 2007). The mechanisms identified and their possible interactions are shown in Figure 2.23. Their study showed that the piles designed for individual failure mechanisms according to current state of practice may be unsafe considering the interaction of the mechanisms. A detailed numerical study has been carried out in chapter 6 to understand the interaction of two major failure mechanisms and its effect on lateral pile soil interaction.
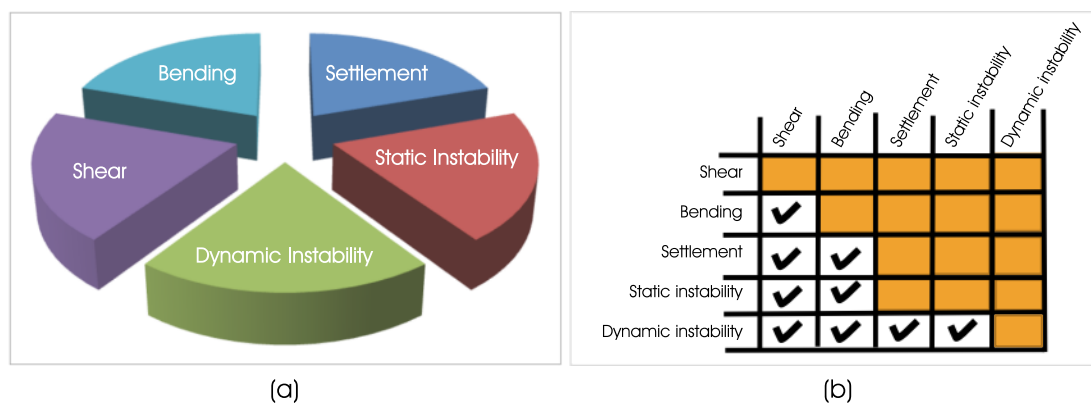
Figure 2.23: a) Schematic showing the individual mechanisms of pile failure, and b) their possible interaction.

2.6 Observations of pile failure in past earthquakes in liquefiable soils

Recorded failures of pile supported structures in liquefiable soils go back to the early 20th century, for example: failure of Salinas Bridge pier during 1906 San Francisco earthquake (USA) due to the tilting of supported pile due to soil softening (Meymand, 1998). However, only since the 1964 Niigata and Alaska Earthquakes, a significant amount of research has been carried out to understand the response of pile foundations in liquefiable soils. As earthquakes are very rapid events and most of the damage to the piles occurs beneath the ground, it is hard to ascertain the detailed pattern of failure unless deep excavations are carried out. Twenty years after the 1964 Niigata earthquake, and following the 1995 Kobe earthquake, investigations have been conducted by excavating and extracting some of the

damaged piles from the subsoil (Yoshida & Hamada, 1991). The detailed field investigations provided important information about the location of cracks and damage patterns for the piles. Figure 2.24 shows the result of one such excavation where extensive damage was observed in the piles of the NHK building that had tilted during the 1964 Niigata earthquake (Tazoh, 2007) where the site was subjected to ground liquefaction. The piles were severely damaged with the reinforcement exposed. Figure 2.25 shows details of a failed pile of the NHK building. Another pile failure of a building in liquefiable soil during 1995 Kobe earthquake is shown in Figure 2.26.

Figure 2.24: NHK Building suffered damage to its pile foundations during 1964 Niigata earthquake and tilted 76° on its long span. But, the damage pattern of pile was observed only after being excavated 20 years after the earthquake (Tazoh, 2007).

Main observations

Liquefaction and related phenomena have been responsible for large amounts of structural damage in historical earthquakes around the world. A useful collation of case histories of damage to pile foundations can be found in Mizuno (1987), Bhattacharya (2003), Finn (2005), Brandenberg (2005), Madabhushi *et al.* (2009), which mainly present the pile foundation performances from post earthquake surveys. Dash *et al.* (2010a) studied 15 well documented case histories in liquefiable soils to investigate the governing mechanism(s) of pile failure. Some of the major inferences from the above study, mainly regarding the structural nature of pile damage, can be summarised as below.

1. In some cases, the displacement of the piles was found to be in line with the horizontal displacement of the ground (Yoshida & Hamada, 1991). This could be the reason
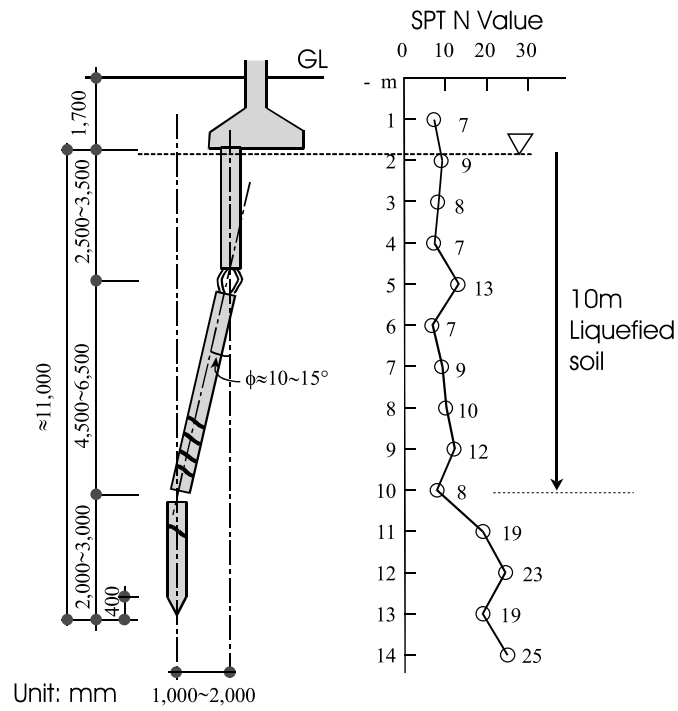
Figure 2.25: Excavated pile of NHK Building (Tazoh, 2007).
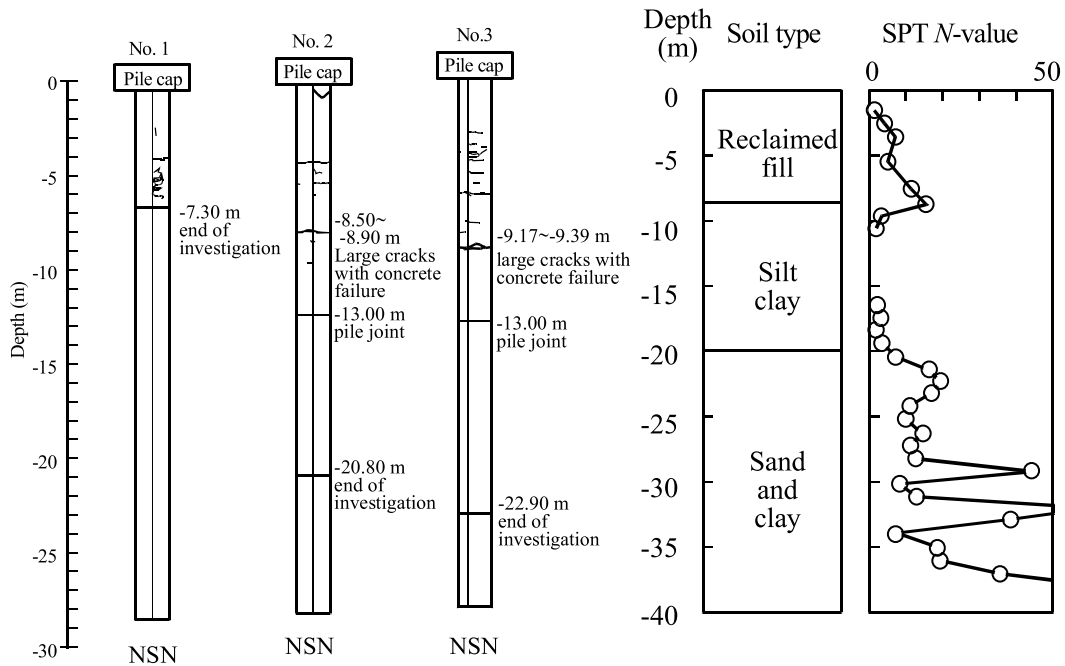
Figure 2.26: Failure pattern of a pile foundation under a building in Kobe city after 1995 Kobe earthquake (Tazoh, 2007).

to consider lateral spreading as the major cause of failure to piles in liquefiable soil, which overlooks the possibility of buckling instability as discussed by Bhattacharya *et al.* (2005).

2. Cracks in piles were observed mostly near the bottom and top boundaries between liquefied and non-liquefied layers. However, in some cases they were present at intermediate depths (see for example Figure 2.26), and in few cases at the middle of the liquefied layer.

3. Large diameter piles performed well during earthquakes. For example, the 0.5m diameter RCC piles of old jetties at Kandla port suffered damage to the upper part of the pile due to cracking during the 2001 Bhuj earthquake. In contrast, in the same area, the 1.0m diameter RCC piles on the new jetties and the concrete-filled-steel tubular piles performed well.

4. Failure of foundations not only occurred in laterally spreading ground but was also observed in level ground where no lateral spreading would be expected. This supports buckling instability as another failure mechanism of piles in liquefiable soil.

5. In some cases of moderate ground displacement, the failure can be described due to the combined effect of axial load and lateral force from soil flow.

As per the current understanding of pile design philosophies (section 2.5), the first and second observation listed above support the theory of bending. The theory of buckling is supported by third and fourth observation. However, neither bending nor buckling theory could explain the formation of plastic hinges in the pile at intermediate depths, especially in the middle of a liquefied soil layer. A better representation of pile-soil interaction in liquefiable soil is therefore necessary to investigate, which may describe the possibility of plastic hinge formation at intermediate depths.

2.7 Modelling of lateral pile soil interaction

2.7.1 Major LPSI Models

Mainly, LPSI is modelled in three ways such as:

1. **Subgrade reaction approach:** (Figure 2.27a): In the subgrade reaction approach, the stiffness of the soil is defined by a mathematical formulation and the analysis

is carried out considering a flexible pile of finite length embedded in a semi-infinite soil medium (Spillers & Stoll, 1964; Poulos, 1971; Banerjee & Davies, 1978 and Koo *et al.*, 2003). This is the most simple type and preferable for small strain analysis where the soil response is in the linear range.

2. **Continuum approach:** (Figure 2.27b): In this approach, the pile and soil are modelled as a continuum with a finite element mesh (Kuhlemeyer, 1979; Randolph, 1981; Wu & Finn, 1997 and Zhao *et al.*, 2008). This is preferable where complicated geometry and non-linearity of the system are essential modelling parameters. However, its use is limited by the large computation time and the need of specialist knowledge.

3. **Spring approach (BNWF model):** (Figure 2.27c): This approach is also known as Beam on Nonlinear Winkler's Foundation (BNWF) model. Here, soil-pile interaction is represented by independent springs lumped at discrete locations (Hetenyi, 1946; McClelland & Focht Jr, 1958; Matlock, 1970; Reese *et al.*, 1974; Makris, 1994 and Thavaraj *et al.*, 2010). The non-linearity in the interaction is assigned as a spring property. This method has gained popularity in the years over the other two methods due to its simplicity, mathematical convenience and its ability to incorporate non-linearity. Use of this model for a LPSI problem is discussed below.
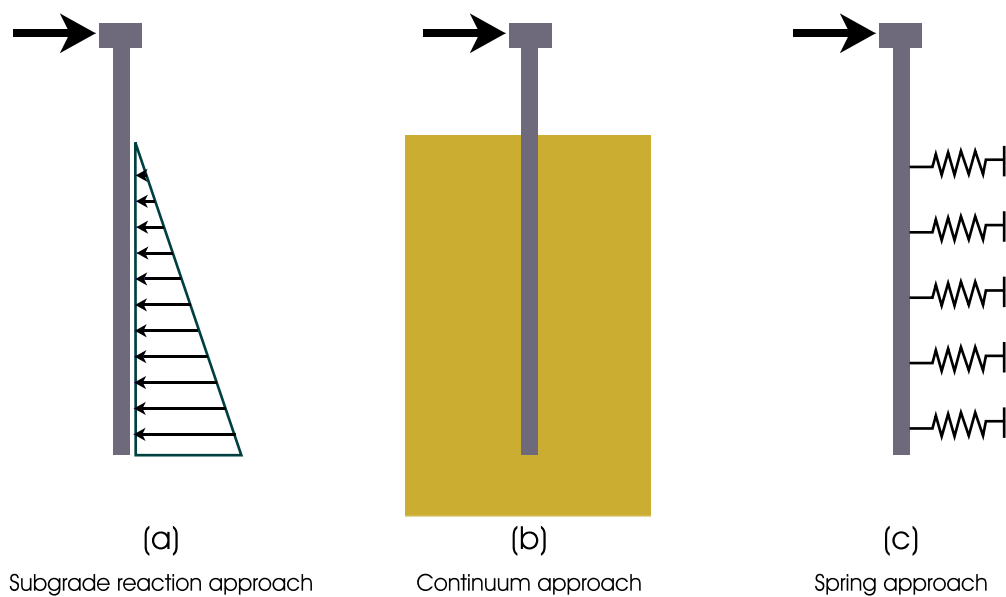
Figure 2.27: LPSI modelling techniques.

2.7.2   BNWF model for LPSI

The BNWF model for LPSI maintains the subgrade reaction idea but replaces the continuous soil reaction function by discrete point spring reactions. The finer the distribution of these discrete points, the better is the analysis result. By specifying the springs with properties that mimic the reaction behaviour observed in full-scale field tests a far more realistic depiction of LPSI in the analysis is obtained.

In seismic analysis, the BNWF model may either be pseudo-static or dynamic according to the requirements. For pseudo-static BNWF (Figure 2.28a) the dynamic seismic forces are computed and applied statically on soil-pile system. The basic differential equation of this model used by JRA (2002) for piles subjected to lateral forces is expressed as Equation 2.8.

$$E_p I_p \frac{d^4 y}{dz^4} + k_s y = F_l \qquad (2.8)$$

where, $E_p I_p$ = flexural stiffness of pile, k_s = spring constant of soil (it can be a constant value or nonlinear dependent value), and F_l= force on pile in the direction of y.

Finn (2005) suggested that the seismic analysis could be improved potentially by using a dynamic BNWF model for soil-pile interaction (Figure 2.28b). This model includes the inertia and damping behaviour of soil, which is ignored in the pseudo-static method. The governing differential equation for dynamic BNWF model can be expressed as Equation 2.9.

$$E_p I_p \frac{d^4 y}{dz^4} + m \frac{d^2 y}{dt^2} + c \frac{dy}{dt} + k_s y = F_l \qquad (2.9)$$

In BNWF model, the stiffness and the damping are two parameters that change significantly during liquefaction and can influence the pile response in liquefiable soil. Hence, their appropriate definition in the BNWF model is of paramount importance. Major discussion in this thesis is given to the stiffness parameter for a pseudo-static model for liquefied soil.
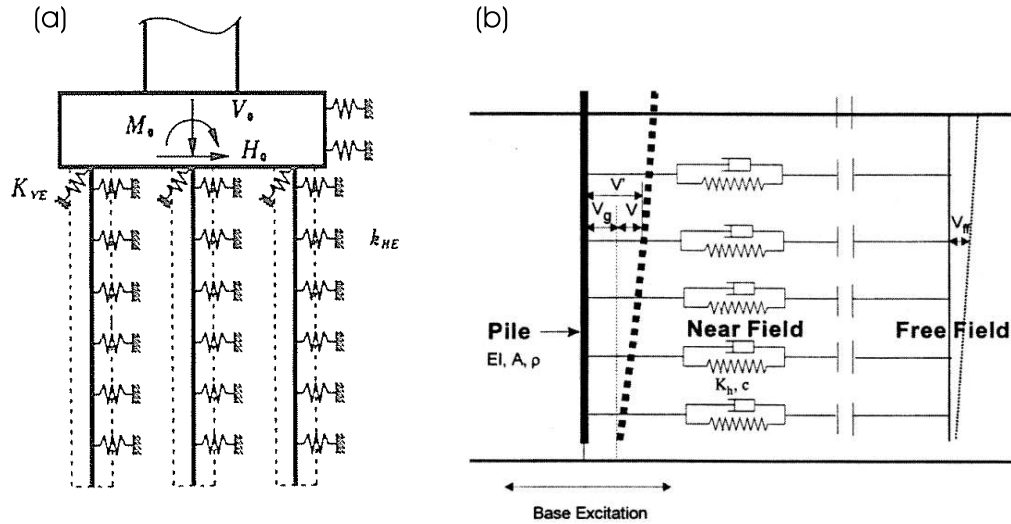
Figure 2.28: (a) Pseudo-static BNWF model (JRA, 2002). (b) Dynamic BNWF model (Finn, 2005).

2.8 Lateral spring property definition in BNWF model

As discussed earlier, the lateral pile-soil interaction (LPSI) in a BNWF model is represented by lumped soil springs with nonlinear backbone curves, called $p - y$ curves, where p refers to lateral soil pressure per unit length of pile and y refers to relative soil-pile displacement (see Figure 1.5). The following section describes the state-of-the-art understanding of $p - y$ curve models for liquefied soils followed by a brief introduction to $p - y$ curve models in non-liquefied soils.

2.8.1 $p - y$ curves for non-liquefied soils

Some codes of practice, e.g., API (2000) and JRA (2002), suggest $p - y$ curves for static loading conditions. For seismic loading conditions, these static $p - y$ curves are frequently used with little modification, as the dynamic $p - y$ curves have not yet been well established. Hence, in seismic analysis, the modified static $p - y$ curves are used with pseudo-static analysis. Tables 2.2 and 2.3 briefly present the method of $p - y$ curve construction as suggested by API (2000) and JRA (2002) respectively. While API (2000) suggests a hyperbolic $p - y$ curve, JRA (2002) advises the use of elasto-plastic $p - y$ curve.

Table 2.2: $p-y$ curve estimation as per API (2000) guidelines for non-liquefied soil.

Steps	Parameter	Computational formulation
1.	Estimate ultimate soil resistance at shallow depth, p_{us}	$p_{us} = (C_1 h + C_2 D)\sigma'_v h$
2.	Estimate ultimate soil resistance at deeper depth, p_{ud}	$p_{ud} = C_3 D \sigma'_v h$
3.	Determine ultimate soil resistance to be used in $p-y$ curve formulation p_u	Lower value from that calculated in step 1 and 2.
4.	Obtain adjustment coefficient for static and cyclic loading, A	for static loading: $\left(3 - \frac{0.8h}{D}\right) \geq 0.9$ for cyclic loading: 0.9
5.	Formulate $p-y$ curve	$p = A p_u \tanh\left(\frac{kh}{A p_u} y\right)$
	A, C_1, C_2, C_3 : Coefficients as defined in API (2000).	

Table 2.3: $p-y$ curve estimation as per JRA (2002) guidelines for non-liquefied soil.

Steps	Parameter	Computational formulation
1.	Estimate coefficient of horizontal ground reaction, K_H, and horizontal passive earth pressure, p_{up}	From fundamental soil properties.
2.	Estimate initial stiffness of $p-y$ spring, K_{HE}	$K_{HE} = \eta_k \alpha_k K_H$
3.	Estimate ultimate soil resistance p_u	$p_u = \eta_p \alpha_p p_{up}$
4.	Construct elasto-plastic $p-y$ spring	Stiffness = K_{HE}, Ultimate resistance, p_u
	η_p, α_p, η_k, α_k : Correction coefficients as defined in JRA (2002).	

2.8.2 $p-y$ curves for liquefied soils: Current practices

$p-$multiplier (α) model:

To define the $p-y$ curve for liquefied soil, the curve for the same soil in non-liquefied condition is evaluated and a strength degradation factor is used. This strength degradation factor is normally known as the p-multiplier (α) and has been defined with respect to the SPT blow count N_{1-60} by various codes of practice and researchers. Figure 2.29 shows the use of the $p-$multiplier schematically and gives different α values suggested by JRA guidelines (JRA, 2002), RTRI guidelines (RTRI, 1999) and Brandenberg (2005).

C_u- factor model:

Liu & Dobry (1995) suggested a strength degradation factor (C_u) for liquefiable soils according to the degree of liquefaction. From a series of centrifuge tests, they have arrived
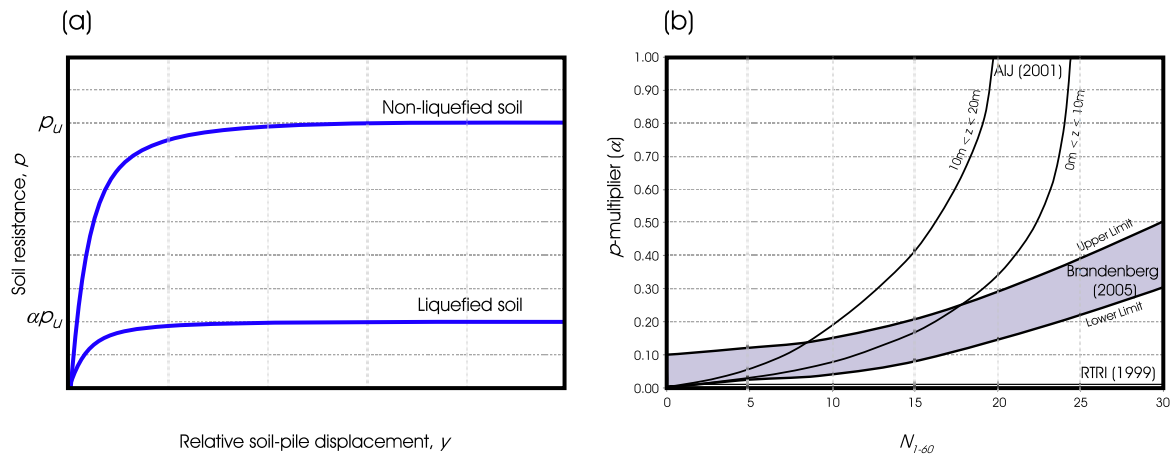
Figure 2.29: (a) $p - y$ curve for liquefied soil in p-multiplier model, (b) p-multiplier (α) values according to SPT value of soil.

at a degradation factor which varies linearly with excess pore pressure ratio (i.e., $C_u = 1 - r_u$). Figure 2.30 shows the C_u factor and its application in the $p - y$ curve model for liquefied soil.
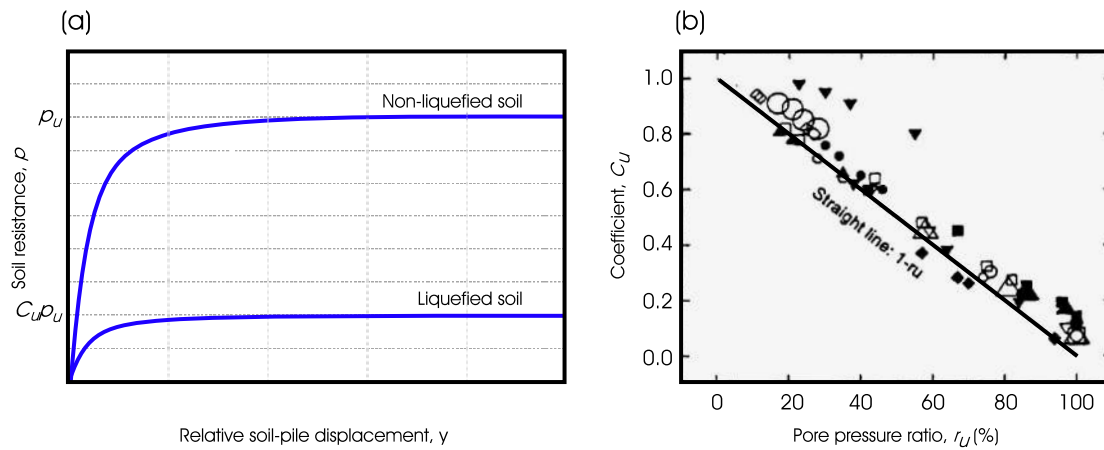
Figure 2.30: $p - y$ curve with C_u factor according to degree of liquefaction (after Liu & Dobry, 1995).

Residual strength model:

Many researchers assume that undrained liquefied soil behaves like clay. On this assumption, Goh & O'Rourke (1999) developed a normalised $p - y$ curve based on a series of FE analysis and compared them with dynamic centrifuge test results. The undrained shear shear strength of clay was replaced by the residual shear strength (s_u) of the liquefied sand. Figure 2.31 shows the proposed $p - y$ curves for both smooth and rough pile-soil

interface in liquefied soil.
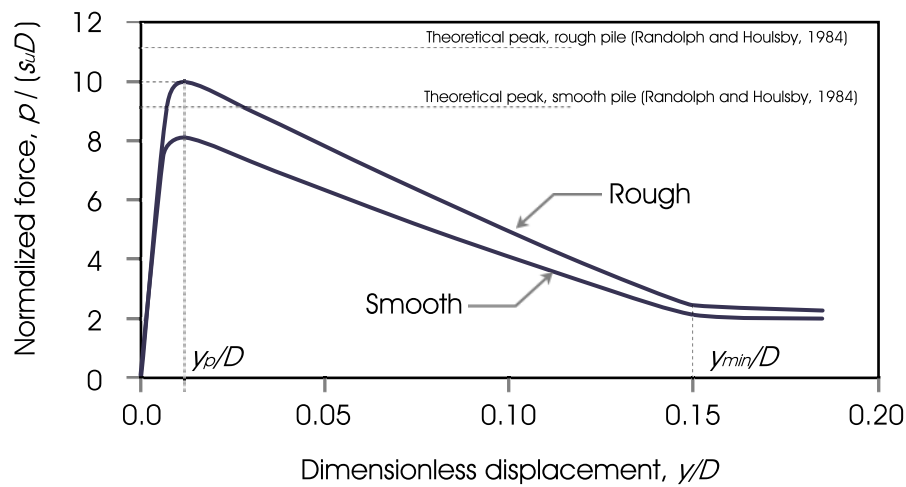
Figure 2.31: $p - y$ curve based on residual strength of liquefied soil (redrawn after Goh & O'Rourke (1999)).

$p - y - u$ model:

Haigh (2002) proposed the $p - y$ curve for liquefiable soils to be a soft type clay model, but he included the pore water pressure ratio (r_u) as another variable to construct a family of $p - y$ curves for different degrees of liquefaction (Madabhushi *et al.*, 2009). This model in fact combines the concepts of above two models, i.e., residual strength and C_u-factor models. Figure 2.32 shows the $p - y$ curves for four different degrees of liquefaction. Curves with higher shear resistance are associated with weak earthquakes which may result in low pore pressure ratios, while the lower shear resistance curves represent strong earthquakes that may result in high pore pressure ratio.

Combined dilative and residual $p - y$ model

Based on a series of centrifuge tests under liquefied conditions, Knappett & Madabhushi (2009) have suggested a $p - y$ spring model for liquefied soil as shown in Figure 2.33. This $p - y$ curve combines both dilative and residual behaviour of soil.
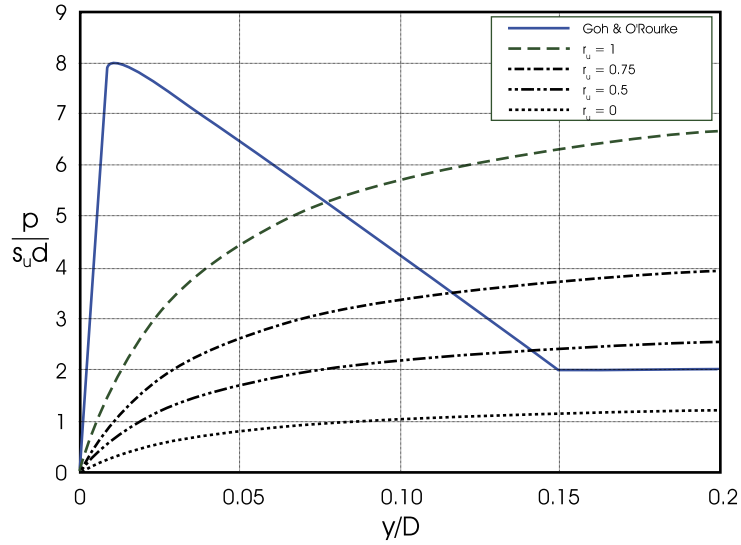
Figure 2.32: $p - y$ curve based on residual strength of liquefied soil but modified with another dependent parameter, the pore pressure ratio (r_u). (Source: Madabhushi *et al.*, 2009).
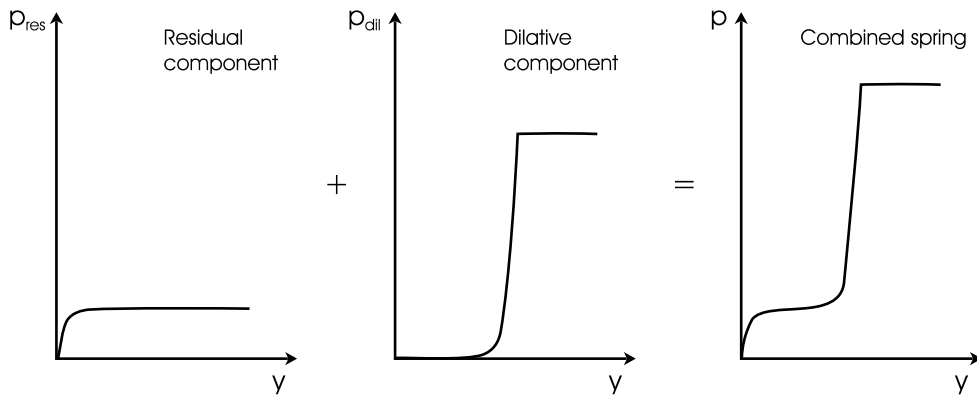
Figure 2.33: Combined dilative and residual $p - y$ curve proposed by Knappett & Madabhushi (2009).

Zero strength model:

In contrast to all the above models, in order to achieve a conservative design, some codes of practice advise ignoring the strength of liquefied soil. For example, Eurocode 8 (part 5, Sec. 5.4.2 of EC8, 1998) advises to ignore the side resistance of soil layers that are susceptible to liquefaction or to substantial strength degradation while analyzing pile foundations. Similarly, IS-1893 code prescribes that "The piles should be designed for lateral loads neglecting lateral resistance of soil layers liable to liquefy." Some researchers, e.g., Bhattacharya *et al.* (2005), also consider zero strength representation for liquefied

soil layer while analysing soil-pile interaction.

All of the $p - y$ curve models in current practice except the zero strength model assume high initial stiffness in liquefied soil, which is in contrast to many experimental observations as discussed below.

2.8.3 $p - y$ curves in liquefied soils: Experimental observations

2.8.3.1 Centrifuge test

Wilson (1998) conducted a series of centrifuge tests with liquefiable Nevada sand at two different relative densities, $D_r = 35\%$ and 55%. His experiments are considered to be the first dynamic characterisations of p–y curves in liquefied soils from centrifuge model tests (Brandenberg $et\ al.$, 2005). The test piles were instrumented with strain gauges and the recorded strains were used to back-calculate $p - y$ curves at each time step. Figure 2.34 shows the $p - y$ curves during three shaking events at two different relative densities. The results were also compared with API (2000) monotonic $p - y$ curves for the same sand for non-liquefied condition. At full liquefaction, the lateral soil resistance for the loose sand ($D_r = 35\%$) was small, even for large relative lateral displacement ($y/D \approx 0.1$). In contrast, the medium dense sand ($D_r = 55\%$) exhibited a peak resistance followed by a softening. The $p - y$ curves have shown characteristics that are consistent with the undrained stress-strain behaviour of liquefying sand (e.g., Yasuda $et\ al.$, 1999, Vaid & Thomas, 1995) (see Figures 2.10 and 2.11), including the effects of relative density, dilation, cyclic degradation, and displacement history.

2.8.3.2 Full scale field test

Rollins $et\ al.$ (2005) carried out a series of full scale tests of single piles and pile groups following blast-induced liquefaction to evaluate pile–soil–pile interaction effects. From the bending moment data along the depth of pile, $p - y$ curves were back-calculated using conventional beam theory. Figure 2.35 shows the measured load deflection behaviour for a single pile and pile group before and after liquefaction. The lateral resistance of each pile in the group was similar and about the same as that for the single pile test. Similar to the observations by Wilson (1998) in centrifuge tests, the stiffness of the back-calculated $p - y$
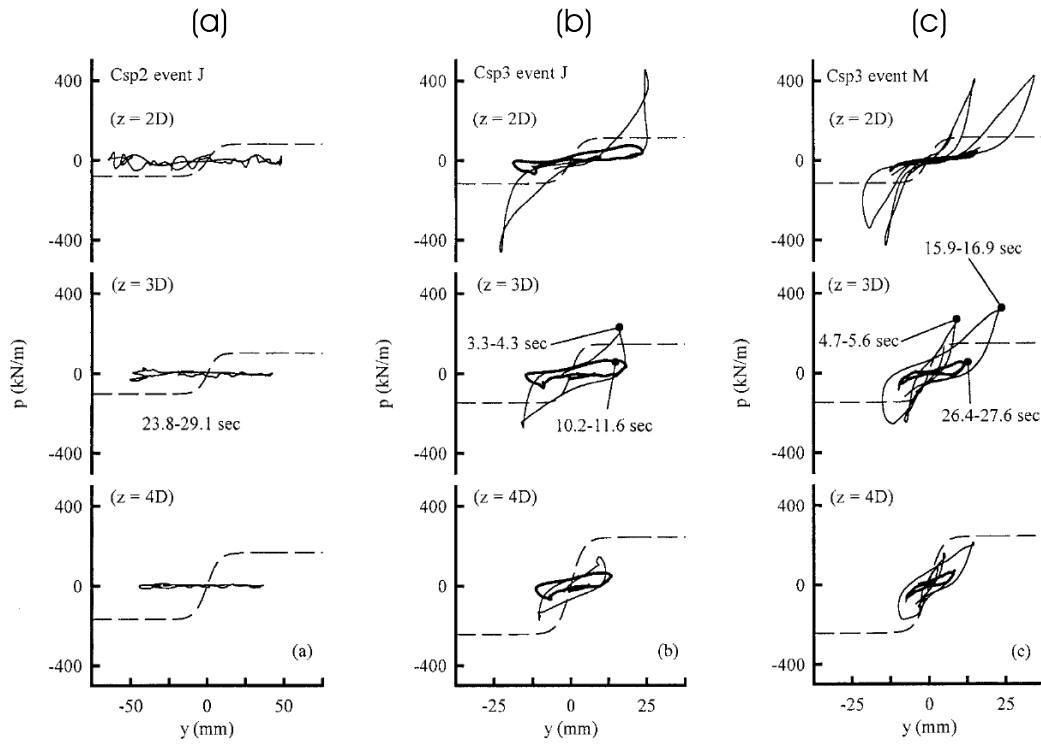
Figure 2.34: $p - y$ curve for liquefied soil back-calculated from centrifuge tests from three shaking events (Wilson *et al.*, 2000). (a) $D_r = 35\%$, Maximum base acceleration $= 0.45g$; (b) $D_r = 55\%$, Maximum base acceleration $= 0.22g$; (c) $D_r = 55\%$, Maximum base acceleration $= 0.41g$.

curves for liquefied soil was also small and it increased with pile deflection. He described this phenomenon to be related with load-induced dilation and decrease in excess pore pressure locally around the pile. For a 3×3 pile group, the $p - y$ curves at different depths are shown in Figure 2.36. The curves were observed to be much stiffer with depth. The shape of the $p - y$ curves were also similar to the shape of the post liquefied stress-strain curve as observed by Yasuda *et al.* (1999), Vaid & Thomas (1995) (see Figures 2.10 and 2.11).

From the experimental observations, he proposed an empirical equation for $p - y$ curve in liquefied soil with a power law relationship, such as:

$$p = A(By)^c \tag{2.10}$$

where, A, B and C are depth dependent constants as defined below:

$A = 3 \times 10^7(h + 1)^{6.05}$, $B = 2.80(h + 1)^{0.11}$ and $C = 2.85(h + 1)^{-0.41}$

The Equation 2.10 is only valid for soil pressure $p \leq 15$kN/m, pile deflection $y \leq$
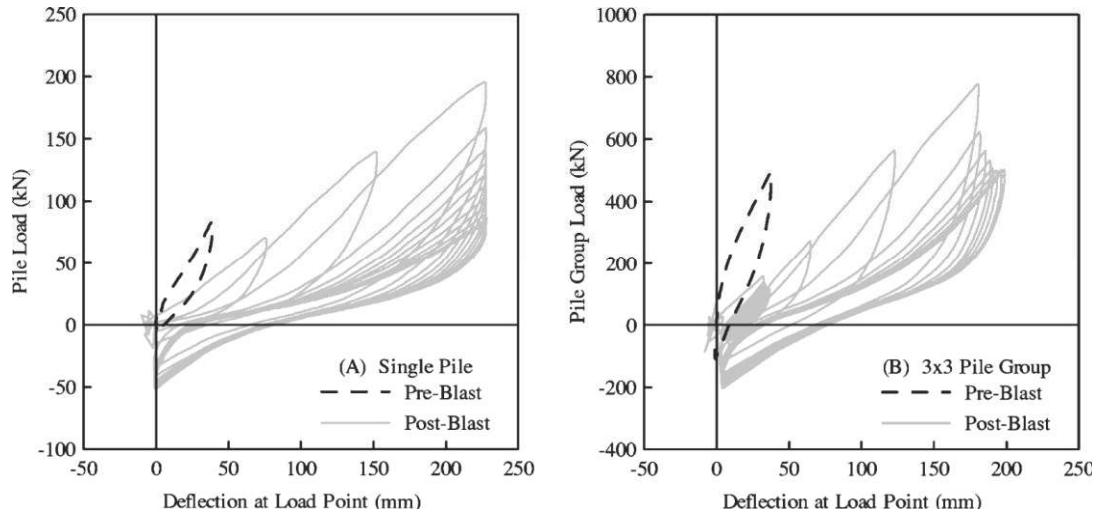
Figure 2.35: $p-y$ curve obtained from full scale testing of a single pile and a pile group subjected to blast induced liquefaction of the soil (Rollins *et al.*, 2005).
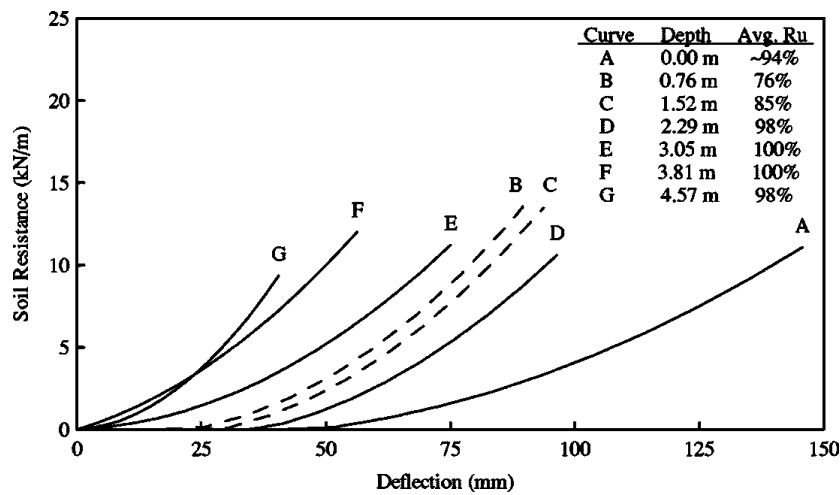
Figure 2.36: Computed p–y curves for various depths during first load series after blasting for a 3×3 pile group in liquefied soil (Rollins *et al.*, 2005).

0.15m, depth $h \leq 6$m and the relative density of sand $D_r \approx 50\%$.

2.8.3.3   1-g model tests

Many researchers have carried out $1-g$ experimental studies to investigate the lateral resistance of liquefied soil on pile foundations. Important examples include the studies by Yasuda *et al.* (1989), Sato *et al.* (1994), Towhata *et al.* (1999) and Takahashi (2002). These experiments were normally carried out by modelling the drag force on the pile at a particular depth by pulling a pipe in saturated sandy soil and liquefying the soil by either

shaking or fluidising. A typical test setup used by Towhata *et al.* (1999) can be seen in Figure 2.37.
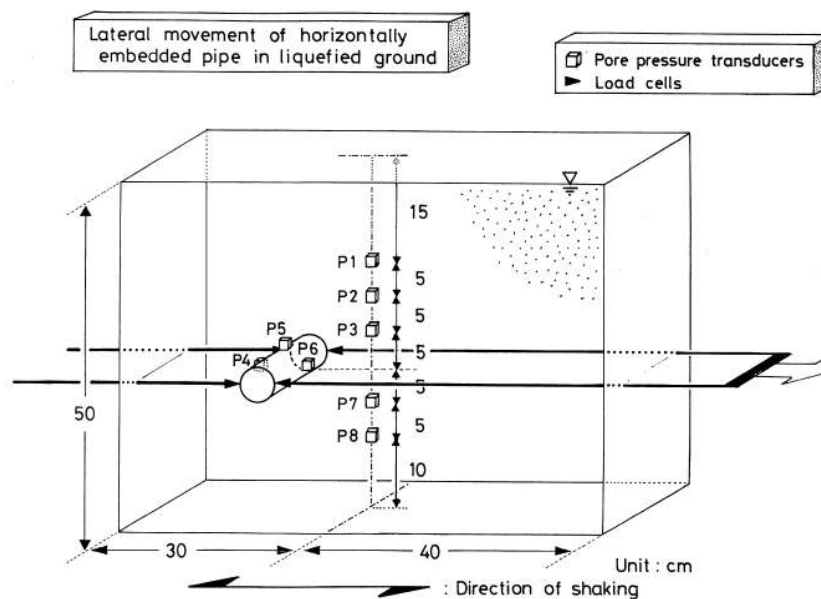
Figure 2.37: 1g test setup of pulling a pipe in liquefiable soil to investigate the lateral resistance of liquefied soil (Towhata *et al.*, 1999).

The major conclusions drawn from these studies were:

1) A drastic reduction in modulus of subgrade reaction upon liquefaction (Yasuda *et al.*, 1989).

2) The drag force on the pipe (i.e., resistance of liquefied soil) varied with the velocity leading to a viscous behaviour of liquefied soil (Towhata *et al.*, 1999).

3) The drag force on the pipe was very low at small strains but increased at large strains (Takahashi, 2002). A larger lateral resistance was mobilised as the loading rate increased. Furthermore, when the loading rate was higher, the pipe displacement required for the lateral resistance mobilisation became smaller. These trends are associated not only with the dilatancy characteristics of sand but also with the pore fluid migration around the cylinder. Figure 2.39 shows the resistance of liquefied soil for different velocity of pipe pulling tests carried out by Takahashi (2002).

4) A strain softening behaviour in non-liquefied state changes to a hardening behaviour after liquefaction but having a very large initial strain demand to offer resistance against deflection. From the test carried out by Towhata *et al.* (1999), Figure 2.38 shows

the drag force offered by saturated sand on model pipe before and after liquefaction.

These above observations with very low initial stiffness of liquefied soil are also consistent with the full scale and centrifuge test observations (section 2.8.3.1 and 2.8.3.2), but the current practice lacks a systematic representation of this behaviour.
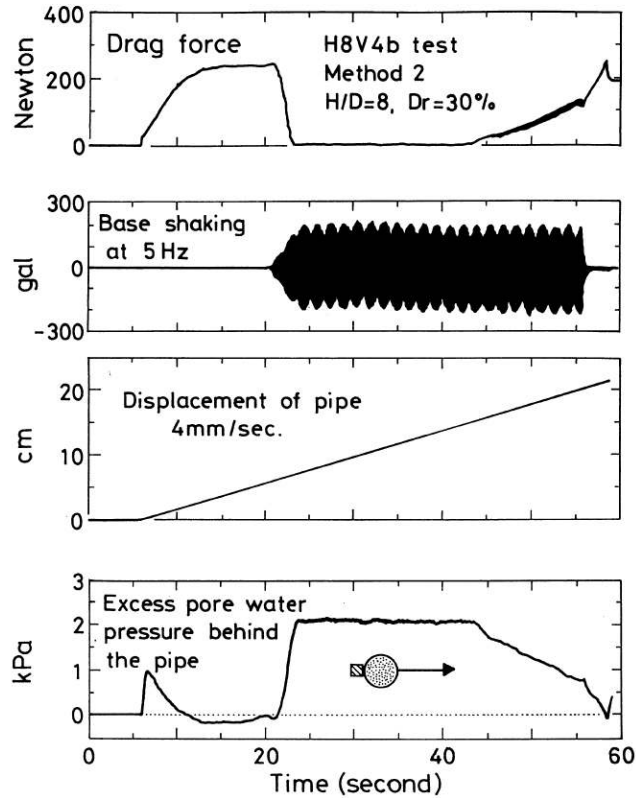
Figure 2.38: Soil-pile response for the pipe pulled in liquefiable soil ($D_r = 30\%$) before and after liquefaction (Towhata *et al.*, 1999).

2.9 Discussion

A significant difference lies between the patterns of the $p - y$ curves being used in current practice when compared with experimental observations. As discussed in section 1.3.3 the shape of the curve can be very significant in determining the response of the lateral soil-pile interaction in seismic loading. None of the $p - y$ curve models in current practice are able to reflect the very low initial stiffness behaviour of liquefied soil.

However, one may ask, why not consider the liquefied soil to have no strength and avoid any further concern of modelling it? While this seems a feasible option provided a very conservative design is sought, but the dynamic response will be affected significantly.

55
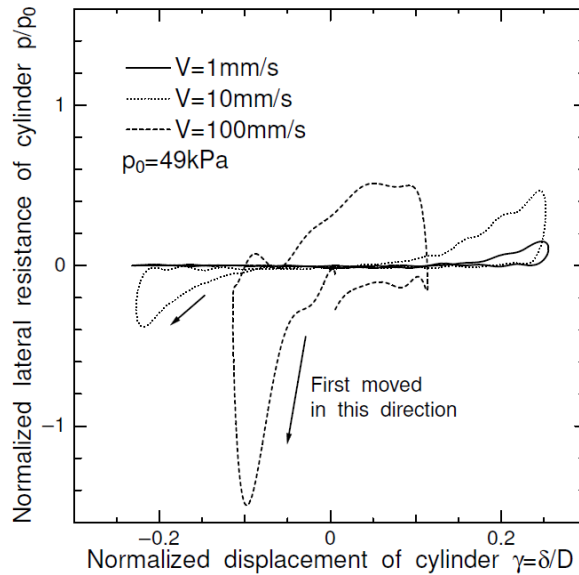
Figure 2.39: Resistance of liquefied soil for different velocities of pipe pulling (Takahashi, 2002).
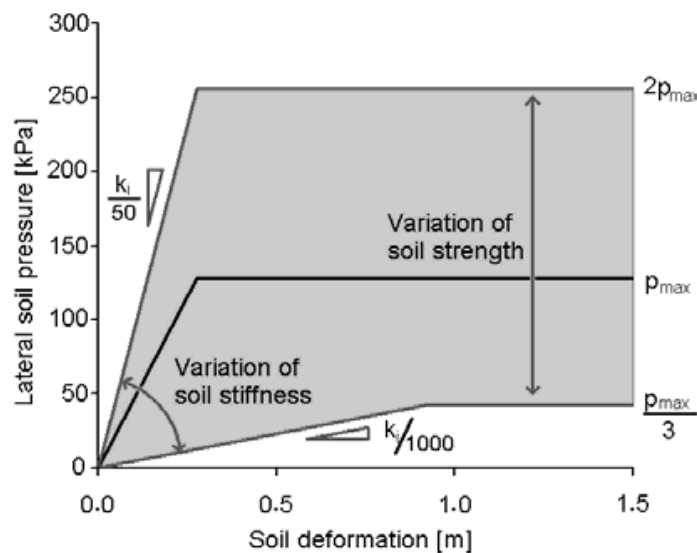
Figure 2.40: Schematic illustration of variation in the p-y relationship for the liquefied soil (Cubrinovski *et al.*, 2009).

Initial studies by Castro & Poulos (1977) and Seed (1979) and later followed by many other researchers showed that even after liquefaction many sands do retain a small amount of shear resistance under large strains. The liquefied soil offers nearly negligible stiffness at small strains, it can be very stiff at large strains if it is subjected to suppressed dilation in undrained conditions.

Cubrinovski *et al.* (2009) compared the range of variation in strength and stiffness of liquefied soil's $p - y$ curve for their numerical study, considering the uncertainties

56

associated with the stiffness and the strength of liquefied soils as shown in Figure 2.40. There is a 20 fold difference between the upper and lower bound values of stiffness and a 6 fold difference in strength.

Therefore, limitations exist for all the current approaches of the $p - y$ curves in liquefied soils being followed that do not address the issue of nearly zero stiffness at small strains and higher stiffness at large strains. As a result, designers often switch from one method to another to satisfy their needs, rather than structural safety.

Chapter 3

Experimental investigation (Centrifuge Test)

3.1 Introduction

To understand the macro behaviour of the pile-soil interaction in liquefiable soils, a set of centrifuge test data was studied. The data for this study were taken from a series of sophisticated centrifuge tests carried out at the Shimizu Corporation of Japan. Details of the tests can be found in Tazoh *et al.* (2005), where the main aim of the tests was to investigate the kinematic interaction of piles in liquefiable soils. The test data were further analysed here to investigate lateral pile soil interaction (LPSI) and to back-calculate the $p - y$ curves and damping values in liquefiable soils.

3.1.1 Outline of the chapter

This chapter includes a brief discussion of the principles of centrifuge modelling and the experimental setup for the tests under consideration. The procedure used to back-calculate $p - y$ curve and damping from the measured data is also outlined including the signal processing techniques. The calculated $p - y$ curves are compared with the available monotonic API $p - y$ curves. Lastly, from the observed $p - y$ behaviour, the mechanism of lateral pile-soil response in liquefied soil is discussed.

3.2 Centrifuge model principle and scaling

3.2.1 Why centrifuge test?

Often, in geotechnical earthquake engineering small scale model tests (under ambient gravity condition, i.e., $1 - g$ condition) cannot properly represent prototype behaviour. This is because the stress level in the soil due to self-weight is much lower in the model than that in the prototype. Generally, the behaviour of soil is non-linearly dependent on stress level. The centrifuge model under increased centrifugal acceleration is a powerful technique that enables small scale model tests under prototype stress conditions. The centrifuge test run at $n - g$ acceleration, for a $1 : n$ linear scale model, can reproduce the prototype level of soil stress in the model by increasing the self-weight due to gravity by n times. This is illustrated schematically in Figure 3.1. While the identical stress condition is achieved due to $n - g$ acceleration in centrifuge, the identical strain condition is achieved by $1 : n$ linear scale model. To demonstrate this, a deflection, δ_s is applied to the soil element of length, l_s, in the prototype scale. This induces a strain of $\frac{\delta_s}{l_s}$ in the soil element in prototype. To model the prototype in $1 : n$ scale, the soil element will be scaled to $\frac{l_s}{n}$ and the deflection will be $\frac{\delta_s}{n}$. The strain in the soil element in the model will then be $= \frac{\delta_s}{n} / \frac{l_s}{n} = \frac{\delta_s}{l_s}$, which is same as in prototype scale.
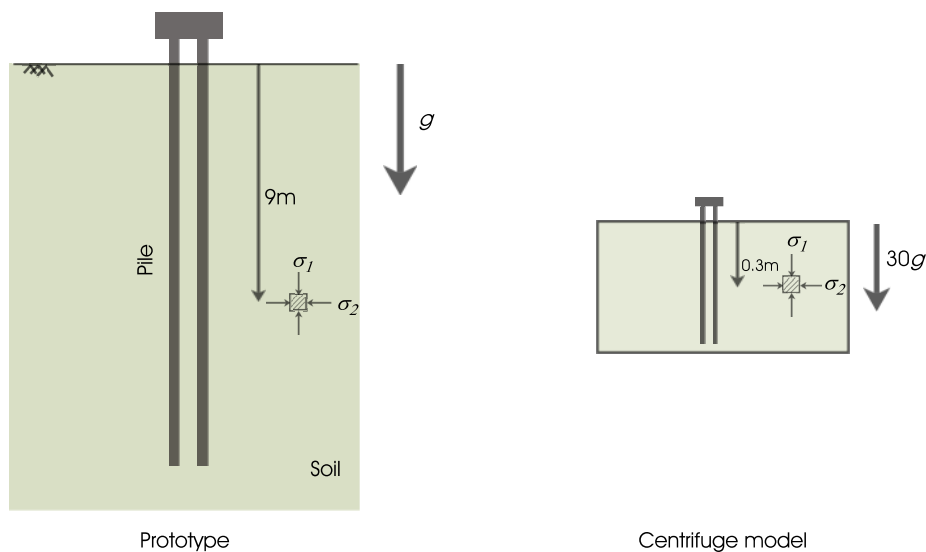
Figure 3.1: Schematic example of prototype and centrifuge model at 1:30 scale experiencing same stress level.

3.2.2 Scaling laws

The scaling parameters related to the centrifuge tests at centrifugal acceleration of $n-g$ are presented in Table 3.1. Derivations of these parameters can be found in Schofield (1981) and Chandrasekaran (2001). While modelling saturated soil media in centrifuge, one of the important parameters which need special attention is the pore pressure generation and dissipation.

In a saturated medium, the generation of pore water pressure depends on the nature of the soil skeleton and the dynamic stresses in the soil skeleton from the inertial effects during loading. The inertial effects in the model are magnified by a factor n in the centrifuge tests. On the other hand the dissipation of pore water pressure in the soil is governed by the phenomenon of diffusion and takes place much faster in the model by a factor of n^2. Chandrasekaran (2001) discussed the incompatibility between dynamic time and seepage time, which may happen if the diffusion phenomenon is not modelled properly. Hence, for proper matching of time between inertial and diffusion, it is necessary to delay the diffusion process by a factor equal to n. This may be achieved in two ways: either by reducing the permeability of the soil by a factor n by crushing the particles to a smaller size, or by increasing the viscosity of the pore fluid in the model by a factor n. The first option is not suitable as it may change the soil's constitutive behaviour (Chandrasekaran, 2001). Hence, the later is generally preferred in the tests, and was also implemented in the tests under present study.

Table 3.1: Scaling laws for centrifuge modelling at $n - g$.

Parameters	Unit	Model / Prototype
Stress (σ)	$ML^{-1}T^{-2}$	1
Strain (ϵ)	-	1
Length	L	1/n
Time (Dynamic)	T	1/n
Acceleration	LT^{-2}	n
Seepage velocity	LT^{-1}	n
Pile bending stiffness (E_pI_p)	$ML^{-3}T^{-2}$	$1/n^4$
Natural frequency (f_n)	T^{-1}	1/n

3.2.3   Non-dimensional groups for LPSI

To compare the results of the centrifuge tests as described in this Chapter, $1 - g$ tests (Chapter 4) and other analytical $p - y$ curves available in literature, non-dimensional groups were chosen to achieve a consistent comparison among the results.

Lateral resistance of soil

The lateral resistance of soil (force per unit length of pile) at a particular depth is generally normalised as a non-dimensional parameter with initial overburden pressure and pile diameter such as:

$$\frac{p}{\gamma' h D} \tag{3.1}$$

For multi-layered soil, $\gamma' h$ represents the total overburden pressure at depth h. The non-dimensional parameter is derived with the assumption that the strength of soil is linearly proportional to the confinement so the term h is in the denominator. Many researchers including Towhata *et al.* (1999); Takahashi (2002); Dungca *et al.* (2006) have used this non-dimensional parameter to represent the lateral resistance of liquefied soil in their experimental results.

However, this assumption is only reasonable if the soil is at a particular relative density and considered at a particular depth to diameter (h/D) ratio. For example, the API guidelines (API, 2000) suggest a linear relation between the effective overburden pressure ($\gamma' h$) and ultimate lateral soil resistance both in shallow and deep depth, p_{us} and p_{ud} as given in Table 2.2. Rewriting these equations in terms of non-dimensional parameters yield Equations 3.2 and 3.3.

$$\text{At shallow depth } \frac{p_{us}}{\gamma' h D} = (C_1 \frac{h}{D} + C_2) \tag{3.2}$$

$$\text{At deep depth } \frac{p_{ud}}{\gamma' h D} = C_3 \tag{3.3}$$

where, C_1, C_2 and C_3 are constants as defined by API guidelines (API, 2000) that depend on ϕ or D_r of the sand.

As per API guidelines (API, 2000), the normalised maximum lateral resistance of pile in sandy soil was estimated for a range of angle of friction (ϕ) values and is plotted in Figure 3.2. The figure shows that an increase in ϕ (or relative density, D_r) at a particular h/D ratio will produce a different amount of ultimate soil resistance and the difference becomes wider as the soil becomes denser (i.e., high ϕ or D_r). Also, for a particular value ϕ or D_r, the normalised resistance increases with increase in h/D ratio until it hits the deep depth resistance value, and thereafter remains constant. This is because the calculation of resistance at a deeper depth does not depend on h/D ratio (as can be seen in Equation 3.3). To illustrate it in another way, the normalised lateral resistance is plotted for five ϕ values at various h/D ratio of soil in Figure 3.3. It can be seen from the figure that up to a certain h/D ratio the normalised resistance increases linearly with h/D, and after that it remains constant. This depth at which a constant normalized resistance can be obtained also increases with denser soil (i.e., higher ϕ or D_r). Hence, while comparing different soils from different test conditions, the normalized lateral resistance must be used for the soils with same D_r or ϕ and same h/D ratios.
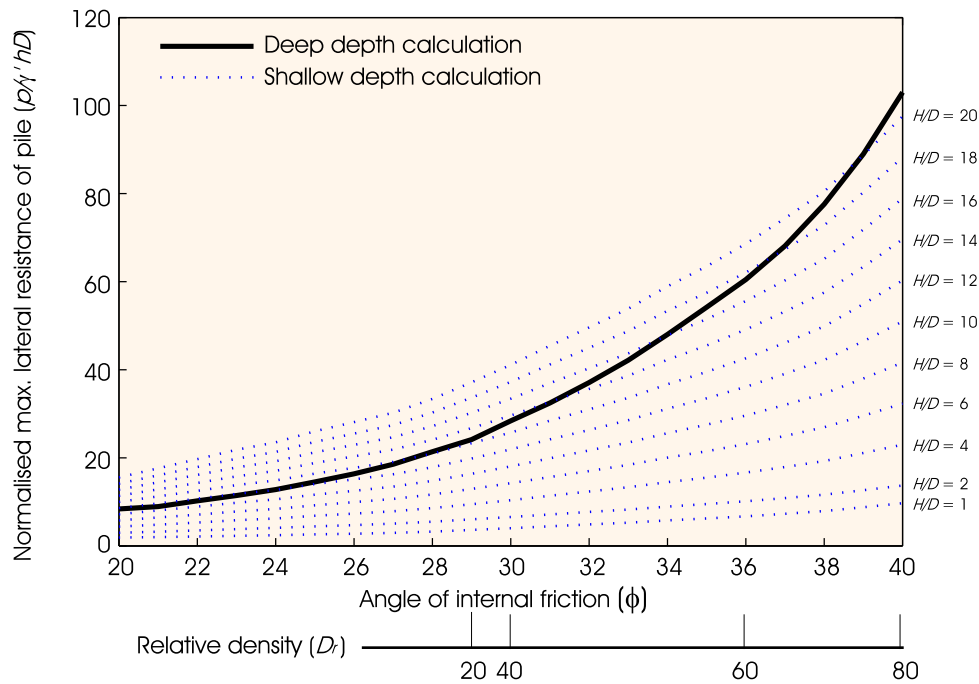
Figure 3.2: API suggested maximum lateral resistance of sand.
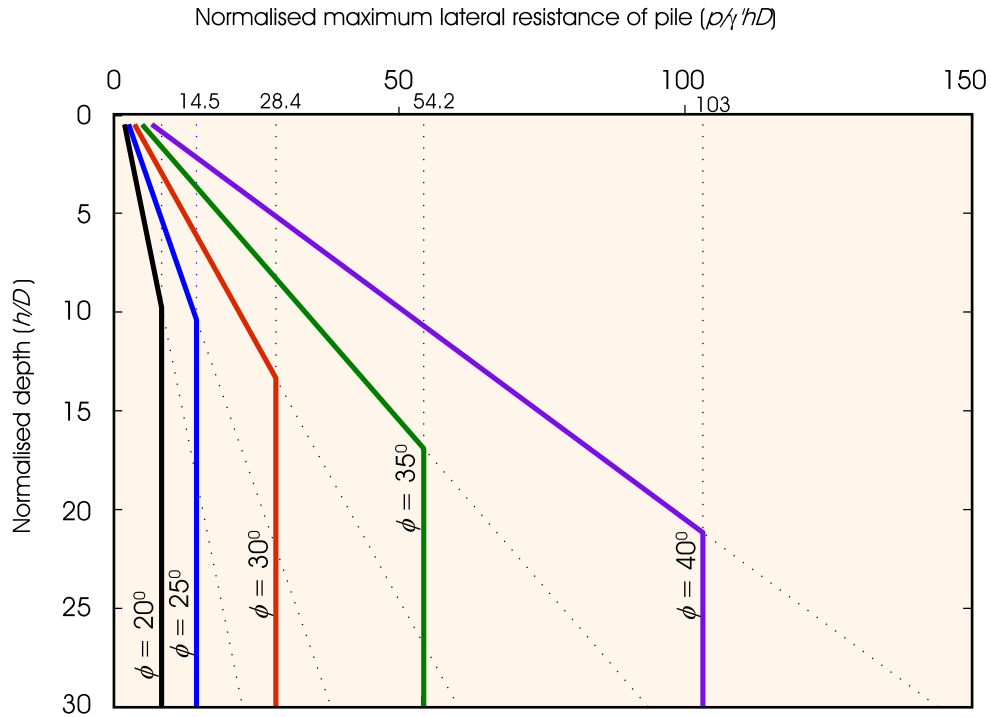
Figure 3.3: Variation of normalized ultimate lateral resistance of pile with depth of soil.

Relative pile-soil displacement

The non-dimensional group to represent the lateral relative pile soil displacement was normalized with the pile diameter as:

$$\frac{y}{D} \tag{3.4}$$

3.3   Description of experimental setup

All the tests cases considered in this study were conducted in the centrifuge facility of Shimizu Corporation, Japan. Sato (1994) has given detailed discussion of the design and operation of the centrifuge facility. The tests were carried out at a centrifugal acceleration of $30 - g$. The stress and strain parameters were modelled by a factor of unity and the linear dimensions by the scale factor of 1:n (model: prototype).

3.3.1 Test layout

Nine experimental test sets were used in the current study (see Table 3.2, CTi, i = 1 to 9). Each experimental setup consisted of two pile groups, separated by a rigid partition wall. Each pile group was composed of 4 piles fixed to the base of the container. Figure 3.4 shows a schematic of a typical test setup. So, there were 18 pile groups in total. However, 5 pile groups had battered piles (CTi-B, i = 5 to 9) and hence were not included in the present study, which is limited to the investigation of vertical piles only. The details of the 13 pile groups studied are presented in Table 3.2.
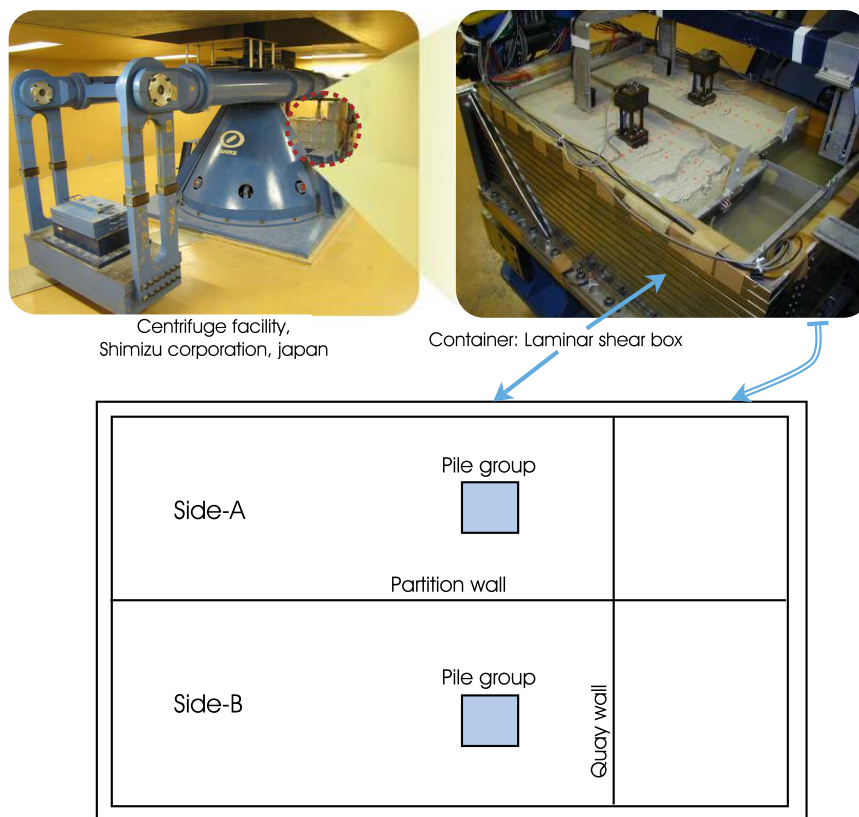
Figure 3.4: One typical test setup.

During a typical test sequence, two pile groups were modelled on each side (Side A and Side B) of the central partition wall (Figure 3.4). This kind of setup was beneficial in modelling both pile groups with the required soil/structural parameter variation while keeping all other model parameters exactly same. The arrangement of one test setup with two pile groups (CT1-A and CT1-B) before and after the test is shown in Figure

Table 3.2: Description of centrifuge tests.

Test No.	Pile Group	Description (Refer to Figure 3.8 for schematic illustration of test setups)
CT1	A	Fixed end quay wall. Distance between pile group and quay wall, b = 200mm Quay wall did not collapse during the test.
	B	Free end quay wall. b = 200mm, Quay wall collapsed during the test.
CT2	A	Fixed end quay wall. b = 100mm, Quay wall did not collapse during the test.
	B	Free end quay wall, b = 100mm, Quay wall collapsed during the test.
CT3	A	Fixed end quay wall. b = 50mm, Quay wall did not collapse during the test.
	B	Free end quay wall, b = 50 mm, Quay wall collapsed during the test.
CT4	A	Free end quay wall. b = 50mm , Quay wall collapsed during the test.
	B	Free end quay wall. b = 100mm, Quay wall collapsed during the test.
CT5	A	Free end quay wall. b = 200mm, Quay wall collapsed during the test.
	B	Batter pile group (Not included in the present study)
CT6	A	Free end quay wall. b = 100mm, Quay wall collapsed during the test.
	B	Batter pile group (Not included in the present study)
CT7	A	Free end quay wall. b = 50mm, Quay wall collapsed during the test.
	B	Batter pile group (Not included in the present study)
CT8	A	Repetition of CT7-A
	B	Batter pile group (Not included in the present study)
CT9	A	Repetition of CT6-A
	B	Batter pile group (Not included in the present study)

3.5. In the test setup, the quay wall (fixed base in Side A and free base in Side B) was modelled near to one end of the container to simulate the soil flow condition (i.e., lateral spreading). The case where the quay wall collapsed (e.g., CT1-B) can be considered as a case of lateral spreading, whereas, the liquefaction in level ground can be represented when the quay wall did not collapse (e.g., CT1-A). In each of the tests, both pile groups (A and B) were subjected to nearly identical conditions with respect to input motions and soil liquefaction.

Before test   After test
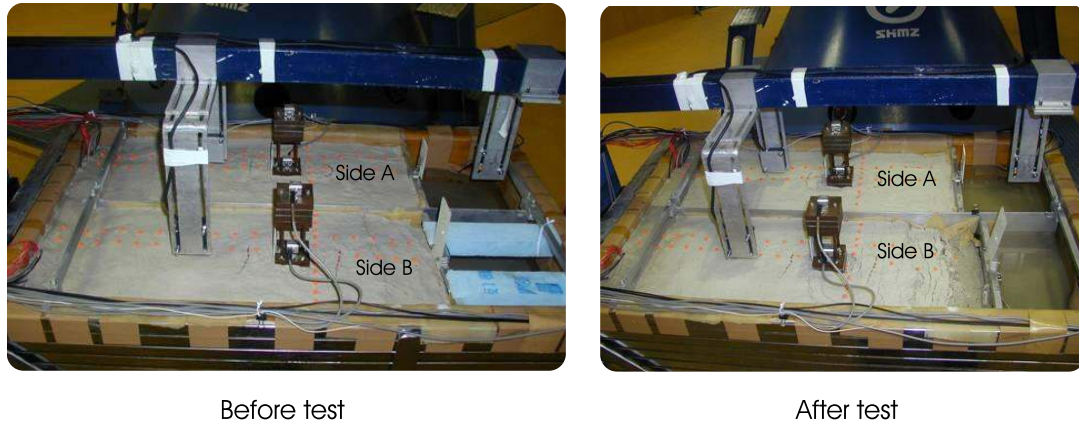
Figure 3.5: Model layout of test CT1 before and after the test.

3.3.2 Test equipments

Major parts of the facility used in this study consisted of a centrifuge, a shaking table, a laminar box and a data acquisition unit which are briefly described below.

Centrifuge

The centrifuge apparatus as shown in Figure 3.6, mainly had of a swing platform (C1), a counter weight (C2) and a rotating arm (C3) mounted on a central spindle (C4). For the dynamic tests, a shaking table and a laminar container were fitted over the swing platform. The model container was mounted on the swing platform with an adjustable counter-weight on the other side. The central spindle had the driving system (a hydraulic motor), electric and hydraulic slip-rings, fibre optic rotary joint and an in-flight balancing system. A test setup for the dynamic model could achieve an arm radius 3.11m (distance between the surface of swing platform and central spindle) at their swung-up position. Specifications related to the working range of the centrifuge facility are also given in the Figure 3.6.

Shaking table with earthquake actuator

A diagram with the specifications for the shaking table used in the centrifuge swing platform is shown in Figure 3.7. The left half of the figure shows the cross section and right half shows the side view. The movable parts are shown hatched. The shaking table was supported with 10 linear springs in two rows which allowed it to move in the

Specifications

Acceleration range: 5g~100g
(Static)
Acceleration range: 5g~50g
(Dynamic)

Max. payload : 750 kg at 100g
 (Static)
Max. payload : 300 kg at 50g
 (Dynamic)

Figure 3.6: Centrifuge facility at Shimizu Corporation.

horizontal direction. An electro-magnetic actuator was fitted at its base that can produce and control large accelerations over a wide practical range of frequencies as expected in the field during an earthquake.
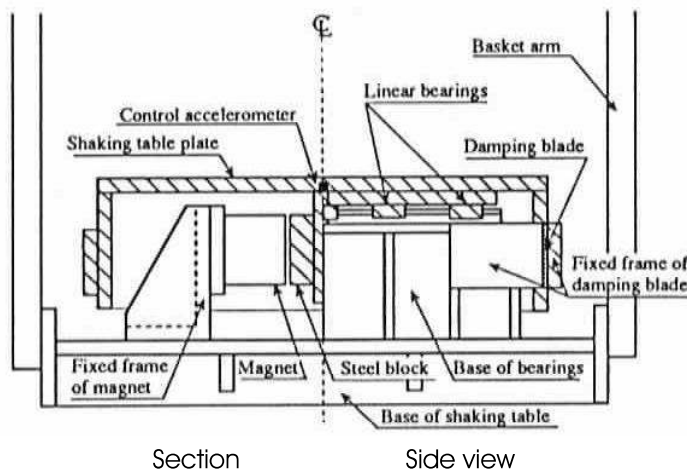
Specifications

Size:
        Length   95cm,
        Width   65cm
Frequency range: 50~350 Hz
Shaking acceleration:
        sine wave   5g
        random wave   10g
Maximum payload: 300 kg

Section   Side view

Figure 3.7: Shaking table with earthquake actuator used over swing platform in the centrifuge (Sato, 1994).

Laminar box

A laminar box used in the test had 14 rectangular frames made up of square steel tubes. The frames were connected by thin linear bearings of 2mm thickness placed in between them. The inside of the container was lined with a 1mm thick rubber membrane for waterproofing of the box and to protect the bearings from soil. The inside dimensions of the box were 805mm long, 475mm wide and 324mm high. Design details of the box can be found in Sato (1994).

Data acquisition unit

The data acquisition unit consisted of transducers, an A/D converter and a data acquisition unit. Transducers used in the tests include, accelerometers, a laser displacement transducer and pore pressure transducers.

3.3.3   Tests conditions

The model was subjected to a varying magnitude base acceleration of a 60 Hz sine wave (2 Hz at prototype scale). The magnitude of base acceleration was gradually increased to make the liquefaction process more realistic, which went up to $\sim 8g$ in 0.25s. This allowed the soil to liquefy in 5-6 cycles of loading. In contrast, many other centrifuge tests on liquefiable soils had shown a very rapid generation of pore pressure just in 1 to 2 cycles of loading, e.g., the tests carried out in the centrifuge facility at the University of Cambridge by Haigh, 2002 and Bhattacharya, 2003. The quick pore pressure generation in some cases does not represent the actual field condition, for example, NFESE technical report (Ferritto, 1997) mentions that in 1989 Loma-Prieta earthquake "liquefaction occurred after 4 to 5 cycles of shaking, about 5 seconds of strong motion".

Sometimes, real earthquakes are used to study the $p-y$ curve in liquefiable soil, as used by Wilson, 1998, which could have been used in this test. But, it was avoided here to reduce the number of nonlinear variables dependent on frequency. The site behaviour was rather represented by varying the magnitude of the base acceleration and keeping the frequency constant. A laminar shear box was used to model the flexible boundary condition. A superstructure mass was also added to the pile head to apply a reasonable amount of axial load to the piles.

3.3.4   Model details

Figure 3.8 shows a schematic of the test setup for 13 pile groups (Table 3.2). The pile groups are divided into four major categories depending on the quay wall fixity and the number of data acquisition locations (as detailed in Table 3.3). The structural properties of the pile are given in Table 3.4. A photograph of the test pile can be seen in Figure 3.9. Both the front and back sides of two piles in the pile group were instrumented with strain

gauges at the locations as shown in Figure 3.8. Two types of soil (Silica sand and Toyoura sand) were used in four layers in the model, whose geotechnical properties are presented in Table 3.5. High viscous Silicone oil was used as the pore fluid and its viscosity was 30 times that of the water to satisfy scaling requirements for the diffusion process (see section 3.2.2). The details of the material and dimensions of the model are given in Table 3.6.

Table 3.3: Pile groups studied here are broadly divided into four categories.

Category	Pile group test case (Refer to Figure 3.8)	Measurements	Quay wall fixed at base	Remarks
1	CT1-A CT2-A CT3-A	Strain measurement at 4 depths, Soil acceleration at 2 depths	Yes	Simulates liquefied soil in a level ground
2	CT1-B CT2-B CT3-B CT4-A CT4-B	Strain measurement at 4 depths, Soil acceleration at 2 depths	No	Simulates liquefied soil in a laterally spreading ground
3	CT5-A CT6-A CT7-A CT8-A,	Strain measurement at 5 depths, Soil acceleration at 3 depths		
4	CT9-A	Strain measurement at 5 depths, Soil acceleration at 3 depths, Pore pressure measurement near to pile		

Table 3.4: Structural properties of the pile.

Item	Value
Material	Steel
Pile outside diameter (D_o)	10mm
Wall thickness	0.2mm
Moment of inertia of pile (I_p)	73.95mm^4
Young's Modulus (E_p)	210GPa
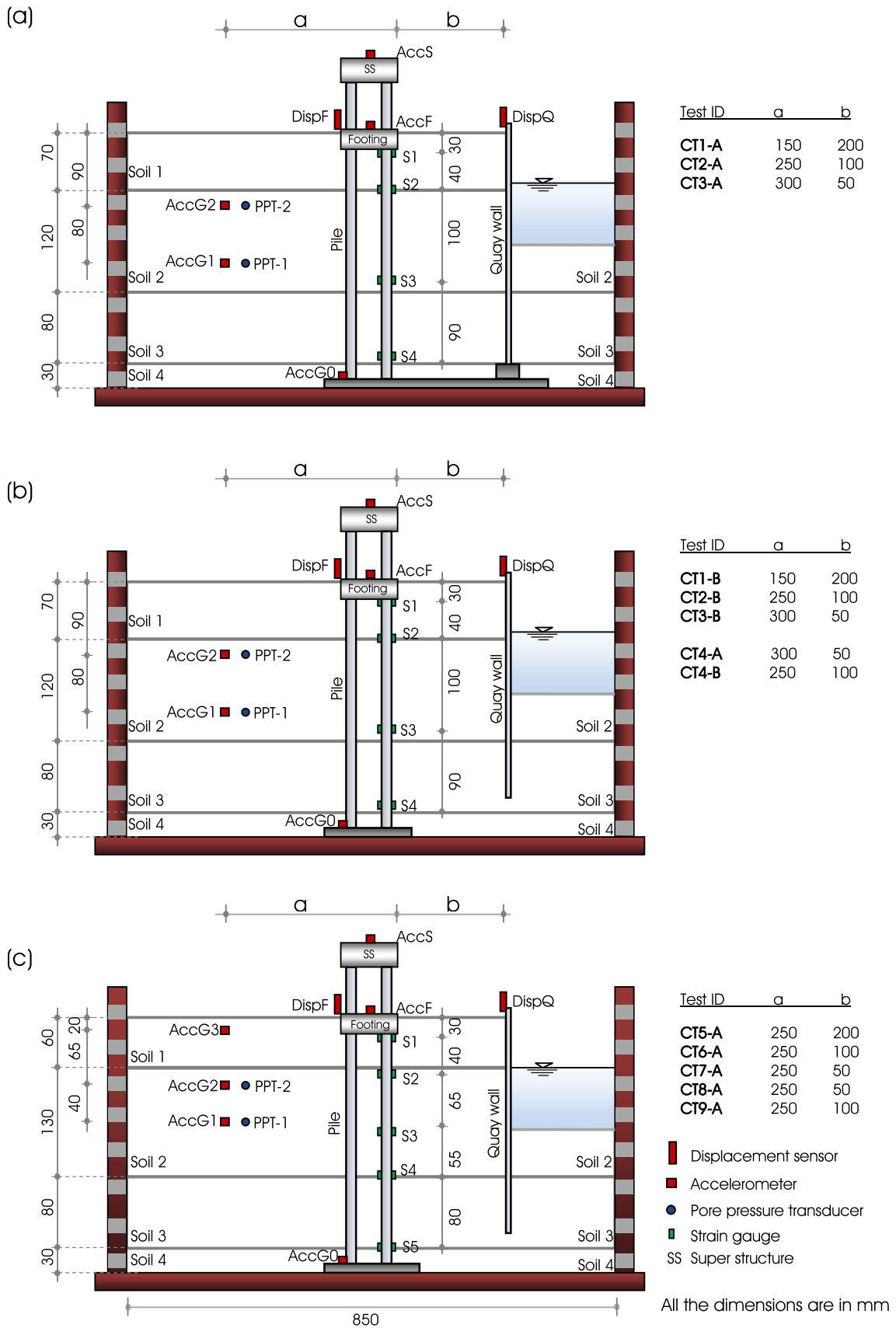
Figure 3.8: Schematic of test layout and instrumentation.

Figure 3.9: Test pile used in the centrifuge tests.

Table 3.5: Geotechnical properties of the sand used in the test.

Symbol	Unit	Soil 1 Unsaturated Silica sand No. 8	Soil 2 Saturated Silica sand No. 8	Soil 3 Saturated Toyoura sand	Soil 4 Saturated Silica sand No. 3
e_{max}	–	1.385	1.385	0.951	0.974
e_{min}	–	0.797	0.797	0.593	0.654
D_r	%	50	50	90	90
$\gamma\prime$	kN/m^3	7.652	7.652	9.908	9.496
γ_t	kN/m^3	12.851	-	-	-
S_r	%	10	100	100	100
e_{max}= Maximum void ratio, e_{min}= Minimum void ratio, D_r = Relative density, $\gamma\prime$= Effective unit weight of soil, γ_t= Dry unit weight of soil, S_r= Saturation ratio.					

3.4 Calculating the $p-y$ curve and damping from measured data: background

3.4.1 The $p-y$ curve

The $p-y$ curve is the representation of lateral pile-soil interaction, where p refers to the soil resistance and y refers to relative soil-pile displacement (details are given in section 2.8). This relative pile soil displacement is the difference between pile displacement (y_p) and soil displacement near the pile (y_s) as given in Equation 3.5.

$$y = y_p - y_s \tag{3.5}$$

Table 3.6: Materials and dimensions of the test model.

Item	Material	Size/type in model scale	Size/type in prototype scale
Laminar Box	Steel	Inner dimension L: 807mm, W: 475mm, H: 324mm	–
Partition	Aluminium	H: 305mm , L: 750mm, T: 2mm	–
Pore fluid	Silicone oil	Viscosity 30 times that of water	Water
Pile group (2 by 2)	Stainless steel	Length: 270mm Outer diameter: 10mm Wall thickness: 0.2 mm	Length: 8.1m Outer diameter: 0.3m Wall thickness: 0.006m
Footing	Steel	L: 50mm , W: 50mm, T: 20mm	L: 1.5m, W: 1.5m, T: 0.6m
Super-structure top mass	Steel	L: 50mm, W: 50mm, T: 30mm	L: 1.5m, W: 1.5m, T: 0.9m
Super-structure columns (2 by 2)	Steel	L: 60mm, Size: 6mm × 2mm	L :1.8m, Size: 0.18m × 0.06m
Sheet pile quay wall	Aluminium	Fixed base case: H: 300mm, L: 235mm, T: 10mm Free base case: H: 250mm, L: 235mm, T: 10mm	Fixed base case: H: 9m, L: 7.05m, T:0.3m Free base case: H: 7.5m, L: 7.05m, T: 0.3m
H: Height, L: Length, W: Width, T: Thickness			

The p and y_p were back-calculated from the recorded bending strain (ϵ_b) of the pile using beam theory equations. A quick review of beam theory equations is presented in Table 3.7.

Table 3.7: Beam theory equations.

Parameters	Unit	Value w.r.t. beam deflection
Beam deflection (y_p)	L	y_p
Slope	Radian	$\frac{dy_p}{dz}$
Curvature	L^{-1}	$\frac{d^2 y_p}{dz^2}$
Bending Moment	ML^{2}T^{-2}	$E_p I_p \frac{d^2 y_p}{dz^2}$
Shear Force	ML^{1}T^{-2}	$E_p I_p \frac{d^3 y_p}{dz^3}$
Distributed Loading	MT^{-2}	$E_p I_p \frac{d^4 y_p}{dz^4}$

The curvature and bending moment in the pile can be directly computed from the recorded pile bending strain by using the Equations 3.6 and 3.7. The pile deflection, y_p, can then be computed by integrating the bending moment profile of the pile twice with respect to depth, z, and dividing that by $E_p I_p$ (Equation 3.8). Similarly, p can be calculated by double differentiating the bending moment profile with z (Equation 3.9).

$$\text{Curvature} = \frac{1}{\rho_p} = \frac{\epsilon_b}{D/2} \tag{3.6}$$

$$\text{Bending moment} = M = E_p I_p \frac{1}{\rho_p} = 2 E_p I_p \frac{\epsilon_b}{D} \tag{3.7}$$

$$\text{Pile deflection} = y_p = \frac{1}{E_p I_p} \iint M dz \tag{3.8}$$

$$\text{Soil resistance} = p = \frac{d}{dz}\left(\frac{d}{dz} M\right) \tag{3.9}$$

where, D is the diameter of the pile and $E_p I_p$ is the bending stiffness of the pile.

The soil displacement near to the pile (y_s) was estimated separately from the measured soil acceleration and quay wall displacement (refer section 3.6.3 and 3.6.5).

3.4.2 Damping

The damping in soil-structure interaction can result from several mechanisms (e.g., viscous, friction and/or plastic yielding). However, it is particularly difficult to identify these mechanisms explicitly in soil testing. The most commonly used mechanism of representing soil damping is through an equivalent viscous damping model.

The $p - y$ curve, as described in the above section, is essentially a hysteresis loop under cyclic loading. The energy dissipation under $p - y$ curve can be estimated by modelling it as a viscous damper subjected to harmonic displacement. The specific damping capacity of the soil per unit depth can be defined as the energy dissipated due to one cycle of the loading (one cycle of $p - y$ curve) divided by peak potential energy, that is $\frac{W_d}{W_s}$.
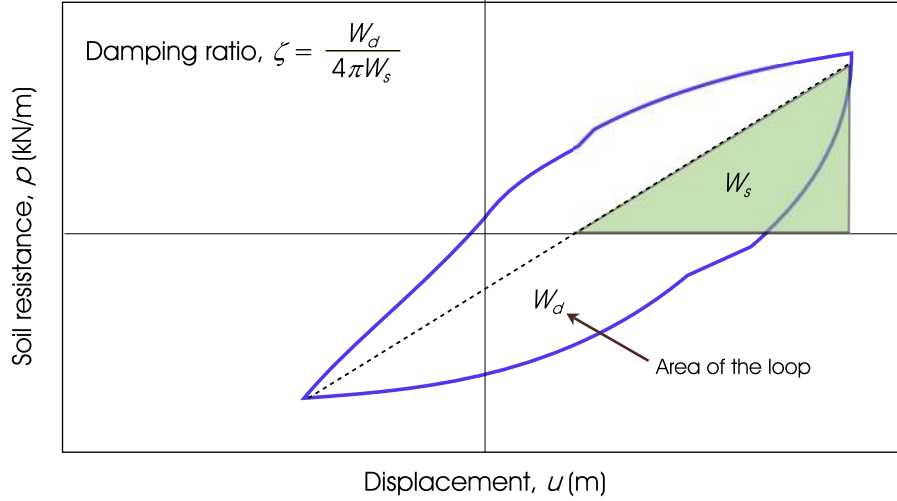
Figure 3.10: Graphical representation of damping from $p - y$ curve.

Considering an equivalent SDOF system, the energy dissipated in one cycle of hysteresis loop, W_d, (Figure 3.10) can be represented by Equation 3.10 (Kramer, 1996).

$$W_d = \pi\, c\, \bar{\omega}\, y_{max}^2 \qquad (3.10)$$

where,

$c =$ damping coefficient per unit depth

$\bar{\omega} =$ forcing frequency

$y_{max}=$ maximum relative pile-soil displacement

Further, the coefficient of damping can be calculated by Equation 3.11. Note that the unit of p is force/length (Figure 3.10) instead of force, and hence the coefficient of damping (c) is per unit length of the pile. Considering the $p - y$ response as a SDOF spring and dash-pot system, the damping ratio can be expressed as Equation 3.12.

$$c = \frac{W_d}{\pi\bar{\omega}y_{max}^2} \qquad (3.11)$$

$$\zeta = \frac{W_d}{4\pi W_s} \qquad (3.12)$$

75

3.5 Centrifuge data representation and signal processing

All the analyses presented in this thesis are at prototype scale, unless specified explicitly otherwise. The results of one test case, CT6-A, a representative case, are presented throughout the analysis procedure in this chapter to demonstrate the steps followed in the analysis. The final results are then presented for other test cases following a similar analysis procedure. Briefly, acceleration, displacement, pore water pressure and strain measurements of the tests are of interest in this study. A typical data set used in the analysis is presented in Figure 3.11 for the representative test case CT6-A.

The estimation of $p-y$ curve, as described in section 3.4.1 was involving three major steps, such as:

1. Double integration of bending moment along the pile to obtain pile deflection.

2. Double differentiation of bending moment along the pile to obtain soil resistance.

3. Double integration of soil acceleration to get displacement time history of the free-field soil.

In a continuous signal, the integration is sensitive to low frequency data and the differentiation is sensitive to high frequency data. Hence, it is important to filter both high and low frequency noise from the signal to obtain a reliable estimate during integration and differentiation of the data. As pointed out by many researchers (e.g., Han, 2003; Brennan *et al.*, 2005; Park *et al.*, 2005; Chanerley & Alexander, 2007), inappropriate filtering of the recorded data may greatly affect the estimated response of the system. A detailed sensitivity analysis was therefore performed to arrive at a reliable procedure of filtering the measured unfiltered signal prior to the back-calculation of the $p-y$ curves.

The original base acceleration and its Welch power spectral density (Welch, 1967) for CT6-A are plotted in Figure 3.12 in both model and prototype scale. The figure shows the presence of both high and low frequency noise apart from the forcing frequency of 2Hz (60Hz in model scale). Hence, a digital band-pass filter was designed to remove this from the measured data leaving the signals with the frequencies of interest. The frequencies
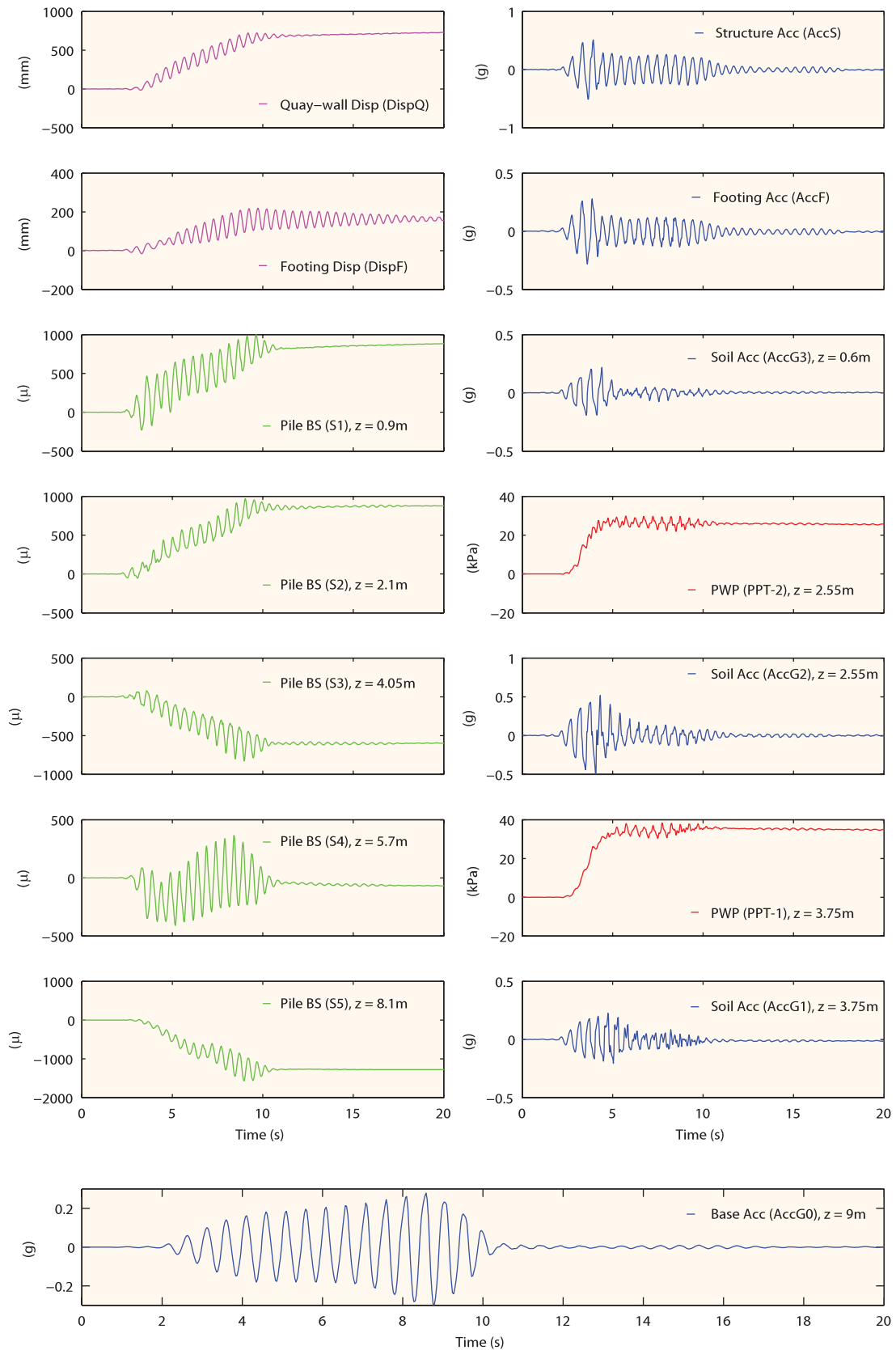
Figure 3.11: Input for test case CT6-A. (Refer Figure 3.8c for transducer labels, Depth (z) values are in prototype scale, BS: Bending strain, PWP: Pore water pressure, Acc: Acceleration, Disp: Displacement)

chosen for the filtering process are given in next section.
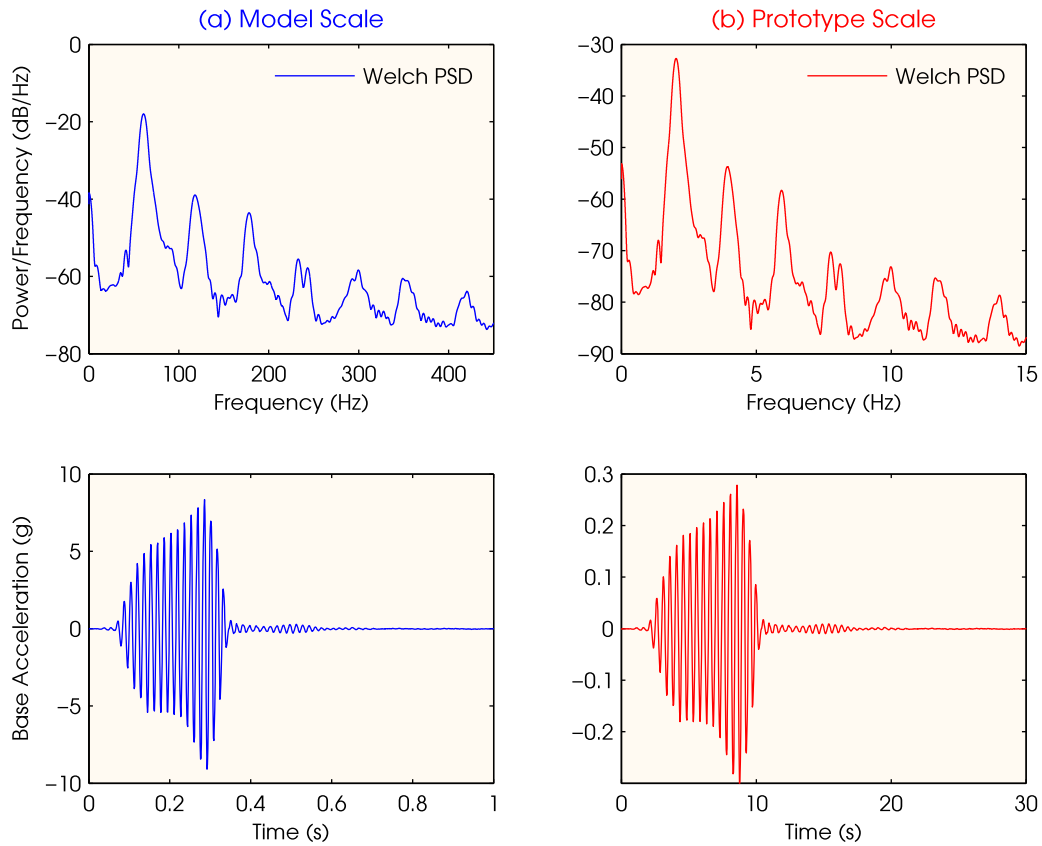
Figure 3.12: Input Base acceleration (AccG0) and it's Welch power spectral density plot (a) in model scale (first peak at 60Hz), and (b) in prototype scale (first peak at 2Hz) for the representative test case CT6-A.

3.5.1 Choosing the right filter

3.5.1.1 Pre-filtering

The best filtering option for a measured experimental data can vary from case to case depending mainly on the data acquisition system, input signal characteristics and the characteristics of the physical system being studied. A digital band-pass filter was designed for this test data and the following considerations were used to define the pass band frequencies for the designed filter.

1. The forcing frequency of base acceleration was 2Hz (60Hz in model scale) and this needs to be in the pass band of the filter.

2. The fundamental frequency of the soil-pile-footing-structure (SPFS) system was varying during the test as the soil liquefies. The first fundamental frequency of

78

the SPFS system was estimated by dynamic amplification factor analysis using the acceleration time history recorded during the test (see Appendix-A). The analysis showed that the fundamental frequency during the test was roughly varying from 7Hz (before liquefaction) to 1Hz (at full liquefaction).

3. The lower corner frequency of the pass band filter to eliminate dc offset was chosen to be no greater than the lowest frequency of interest, which was the smaller of the following two.

    (a) First fundamental frequency of the physical system before liquefaction (0.92Hz, lowest from all the test cases), and

    (b) Forcing frequency (2Hz).

4. The upper corner frequency of the pass band filter to eliminate high frequency noise was chosen to be the higher value of the following two.

    (a) First fundamental frequency of the physical system after liquefaction (8.02Hz, highest from all the test cases), and

    (b) Forcing frequency (2Hz).

5. These two criteria show that the corner frequencies for the filter are governed by the fundamental frequency of the physical system. Although, the fundamental frequencies of the system in all cases do not match with each other, with a higher margin at both ends of the filter frequency, a single frequency band was working well for all the test data.

6. For acceleration data, it is common to use Butterworth filter with higher order (Wilson, 1998) as the acceleration time history contains sharp spikes. For the present analysis, a filter order of 6 or greater gave a reasonably similar estimation of the displacement from acceleration time history. However, very high order filters with very small value of lower corner frequency had problems with instability and arithmetic overflow, which was observed with a 10th order filter with a pass band of 0.4Hz to 10Hz (Figure 3.13).
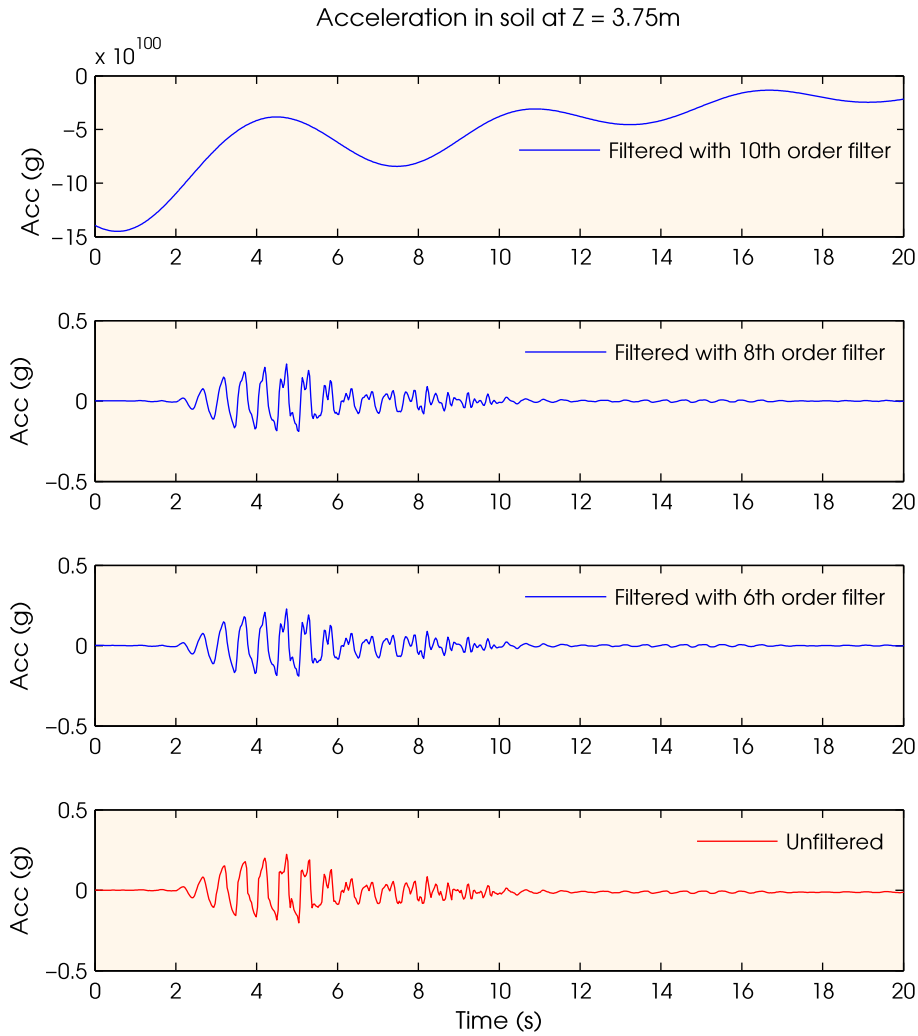
Figure 3.13: Effect of filter order for a 0.4Hz to 10Hz band-pass Butterworth filter over acceleration time history in soil (AccG1) of test CT6-A. [Acc: Acceleration]

With the above considerations, finally, a 8th order band-pass Butterworth filter was chosen with pass band frequencies of 0.4Hz to 10Hz, which gave consistent results for all the test cases. The schematic of the band pass filter with the filtered and unfiltered power spectrum density plots of one of the measured acceleration data in the soil is shown in Figure 3.14. The filtering of data was carried out using Matlab® "filtfilt" command to obtain a zero-phase distortion during filtering.

3.5.1.2 Post filtering

Post filtering of data is often necessary to remove residual low frequency components/DC offset that appears after a signal has been integrated. For the cases studied here, same
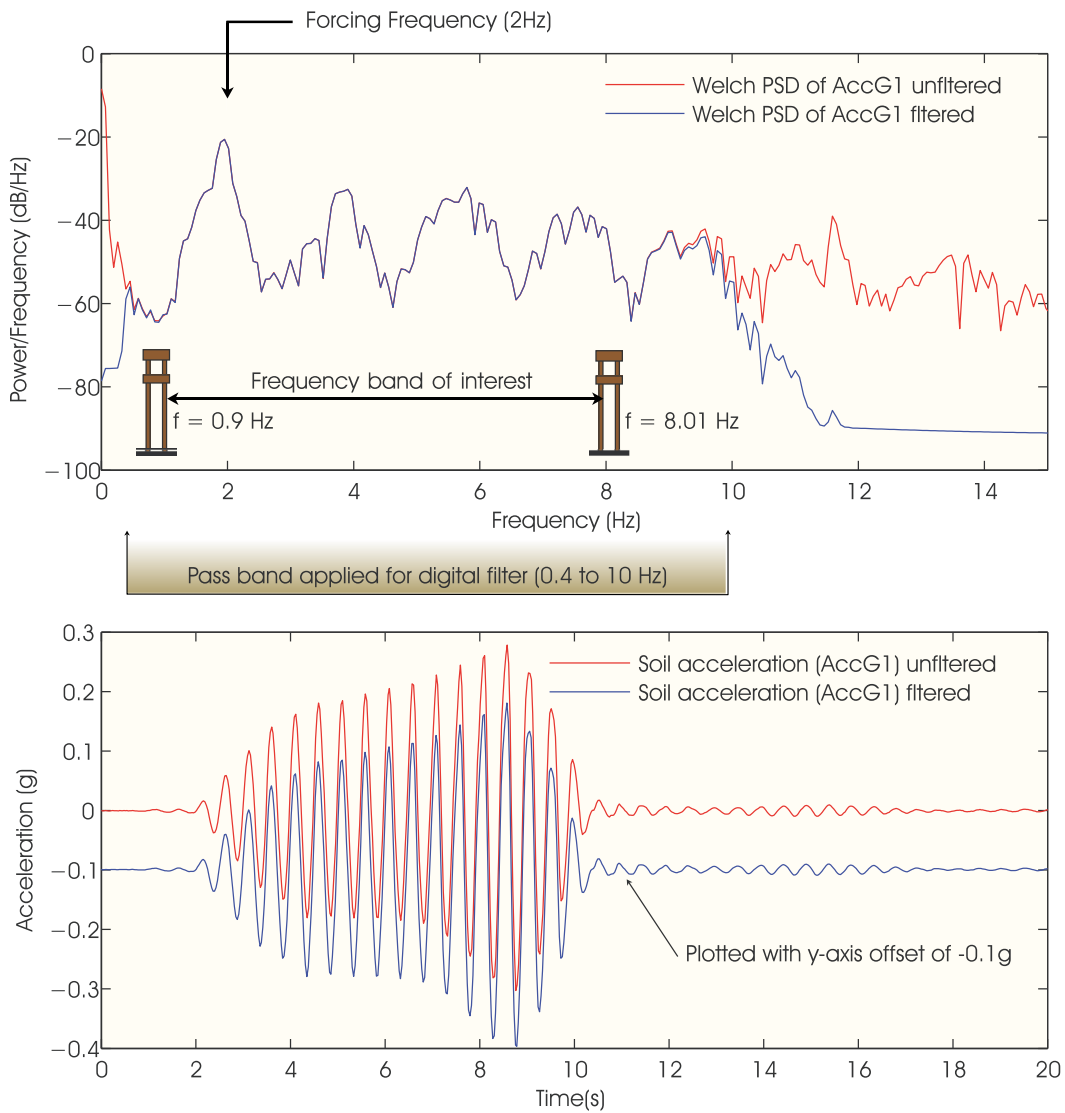
Figure 3.14: Schematic of band pass filter design showing the filtered and unfiltered Welch power spectral density for soil acceleration AccG1 for the test case CT6-A.

filter as defined above for pre-filtering was applied for post filtering as well.

3.5.1.3 Filtering acceleration data

Integration of measured acceleration data gives absolute displacements. Figure 3.15 shows the estimated displacement time history in soil by integrating the acceleration time history twice at the location of AccG1 (for CT6-A) without any data filtering. As seen in the figure, the magnitude and shape of the estimated displacement was completely unacceptable, and filtering of the recorded acceleration data was necessary. During filtering of low frequencies in the signal, any real permanent drift component of it gets unavoidably removed as noise. However, the required dynamic behaviour useful in back calculating

81

$p - y$ curve was adequately preserved.
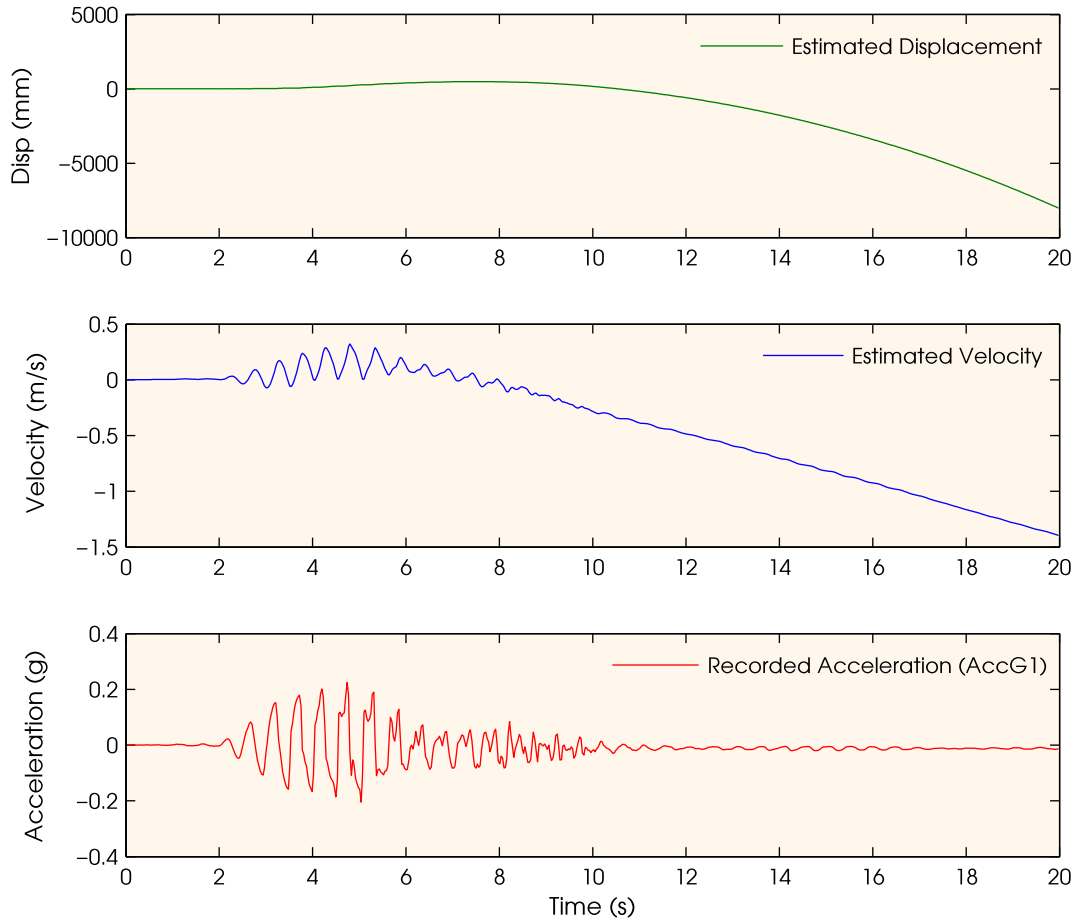
Figure 3.15: Estimation of displacement time history from measured soil acceleration data (AccG1) in test CT6-A without any data filtering. [Disp: Displacement]

For CT6-A, the soil acceleration data was filtered with the designed band-pass filter and then integrated twice to get absolute soil displacement. The integration was carried out using cumulative trapezoidal numerical integration by Matlab® command "cumtrapz." The post filter was applied to the integrated value to remove the small dc offset. Figure 3.16 shows the estimated value of the displacement time history in the soil with both pre- and post-filter applied, which gave a reasonably approximate value that can be used in further analysis.
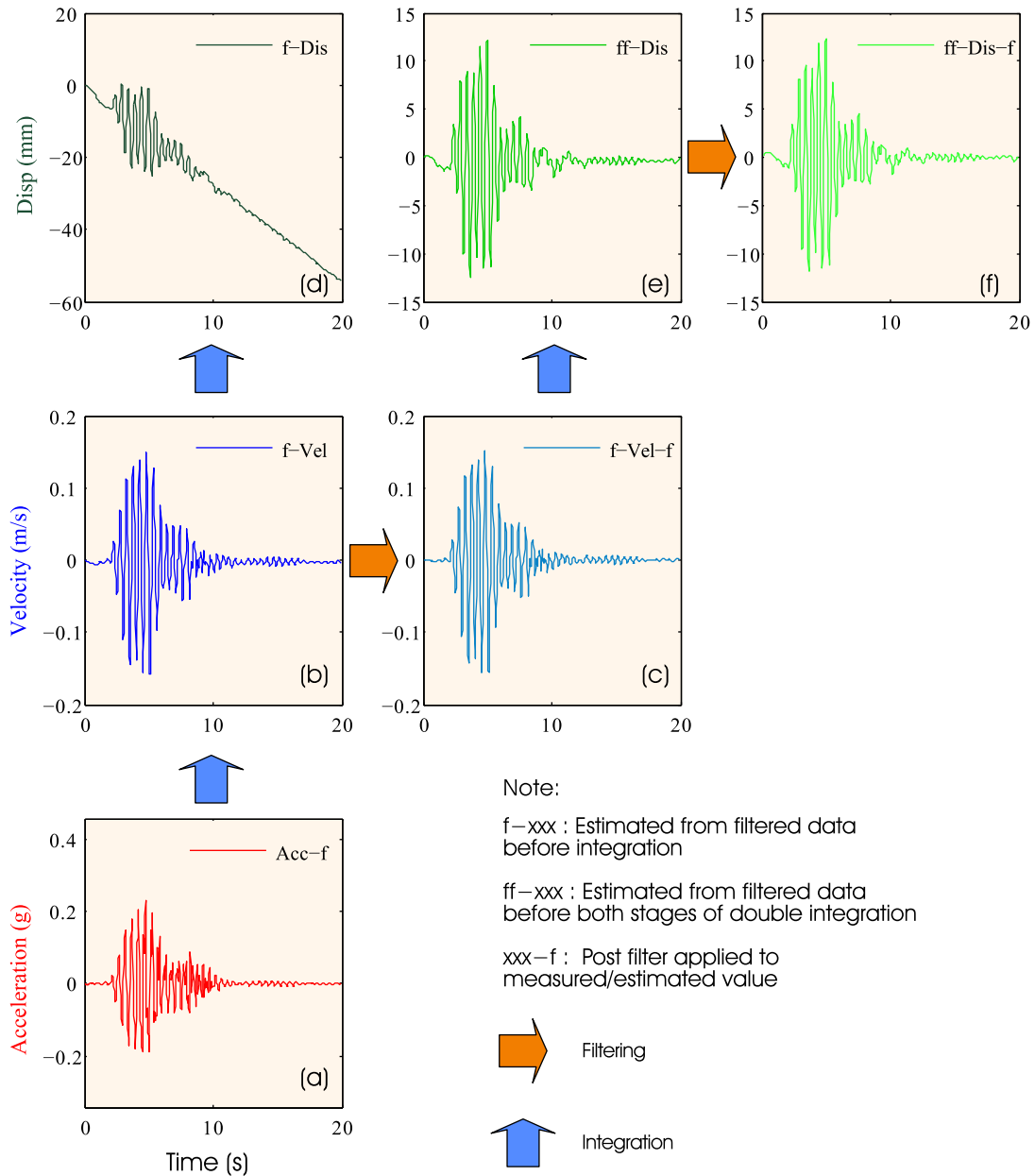
Figure 3.16: Displacement time history from acceleration time history in soil (AccG1) for CT6-A with pre- and post-filter applied to the data. Sequence of filtering process used in the present study is: a-b-c-e-f.

3.5.2 Estimation of axial and bending strain

Strain measurements were taken at both sides of the pile at the extreme fibre on the locations as shown in Figure 3.8. From the total strain measurements, the axial and bending strain components were separated as given in Figure 3.17, where ϵ_{1p} and ϵ_{2p} were total strains, measured on each sides of the pile.
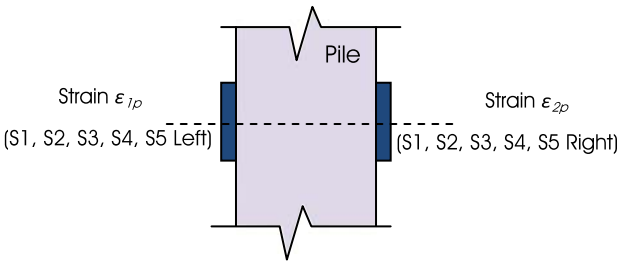
Figure 3.17: Axial and bending strain estimation from measured strain data (Refer Figure 3.8 for location of strain gauges S1, S2, S3, S4 and S5).

3.5.3 Dynamic component of bending strain

The measured strain and displacement values during the test were having a cyclic component added to a static offset. This static offset was not required to be removed in the normal condition, and the results obtained from the signal signifies a significant drift where the soil undergoes large displacement (as in CT6-A). The dynamic component can be separated from the static offset by applying a pre- and post-filter described earlier. The analysis without removing the drift component will represent the dynamic $p - y$ curve for a lateral spreading soil. However, for a better understanding of the magnitude of the $p - y$ curve and to compare it with the API monotonic $p - y$ curve, the static offsets were required to be removed (see section 3.7 for details). The unfiltered and filtered bending strains at different pile locations (obtained from strain measurements, S1...S5) are plotted in Figure 3.18.

3.5.4 Dynamic bending moment profile in the pile

From the time history of bending strain, the curvature and bending moment time histories were obtained by using Equations 3.6 and 3.7 respectively. The dynamic bending moments computed from dynamic bending strains were known only at discrete locations of the pile (Figure 3.19). Hence, an appropriate curve, fitted to the bending moment profile along the pile length, was required to be able to carry out the integration and differentiation. One of the most common ways many researchers use to fit the discrete bending moment data is by interpolation functions. The interpolation functions can be a continuous polynomial (as used by Matlock & Ripperger, 1956; Ting, 1987; Rollins *et al.*, 2005) or a segmented
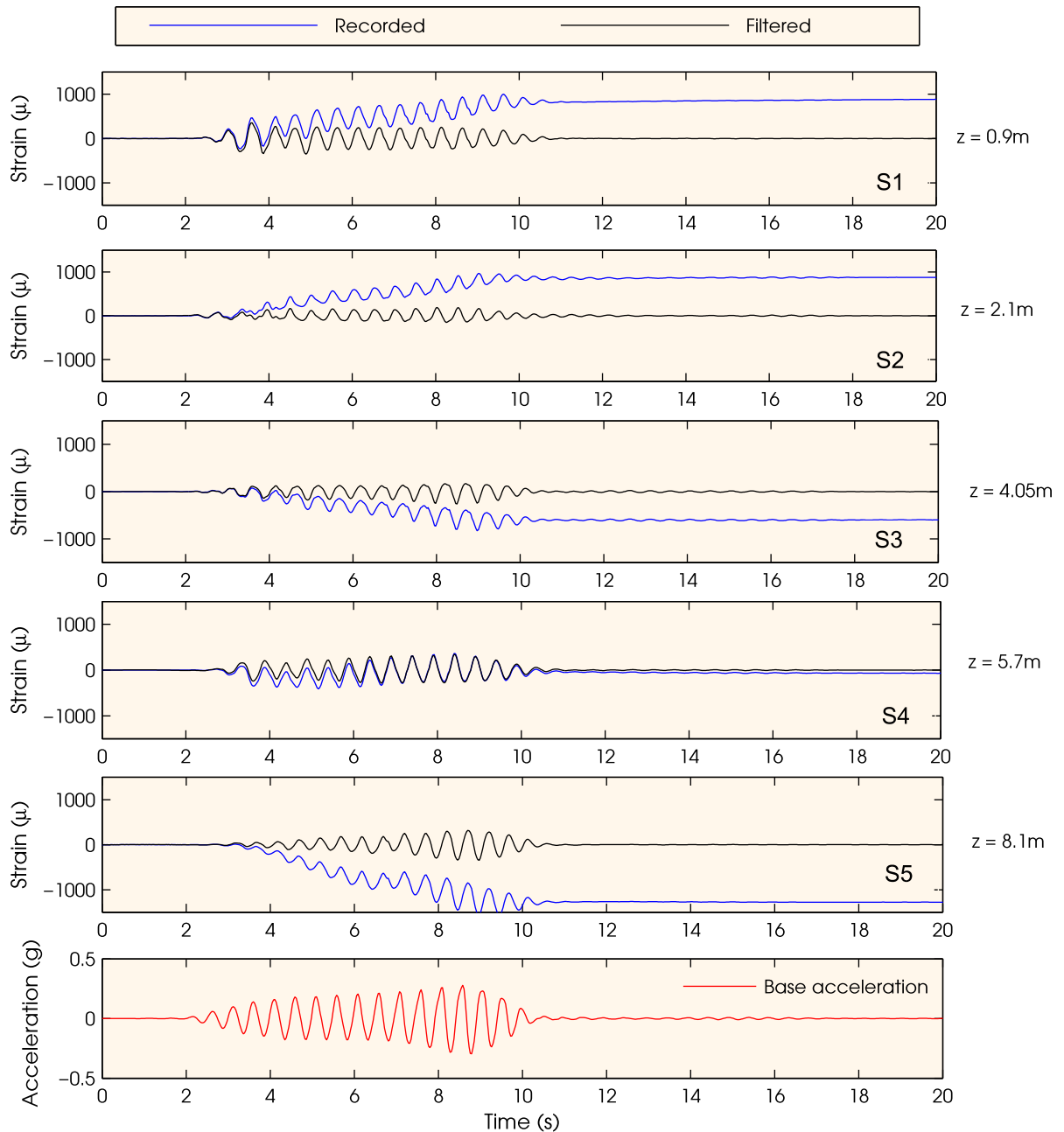
Figure 3.18: Recorded and filtered bending strain time histories from strain gauges S1, S2, S3, S4 and S5 for CT6-A.

cubic spline (as used by Dou & Byrne, 1996).

In a similar set of centrifuge tests in sandy soil, Wilson (1998) had studied three methods of curve fitting (polynomial interpolation, cubic spline interpolation and weighted residual method) to bending moment data. For differentiation purposes, the degree of agreement in results varied depending on the model container, event and the depth at which the lateral resistance (p) was estimated. He had presented the results of lateral resistance (p) using weighted residual method of bending moment fit. While calculating
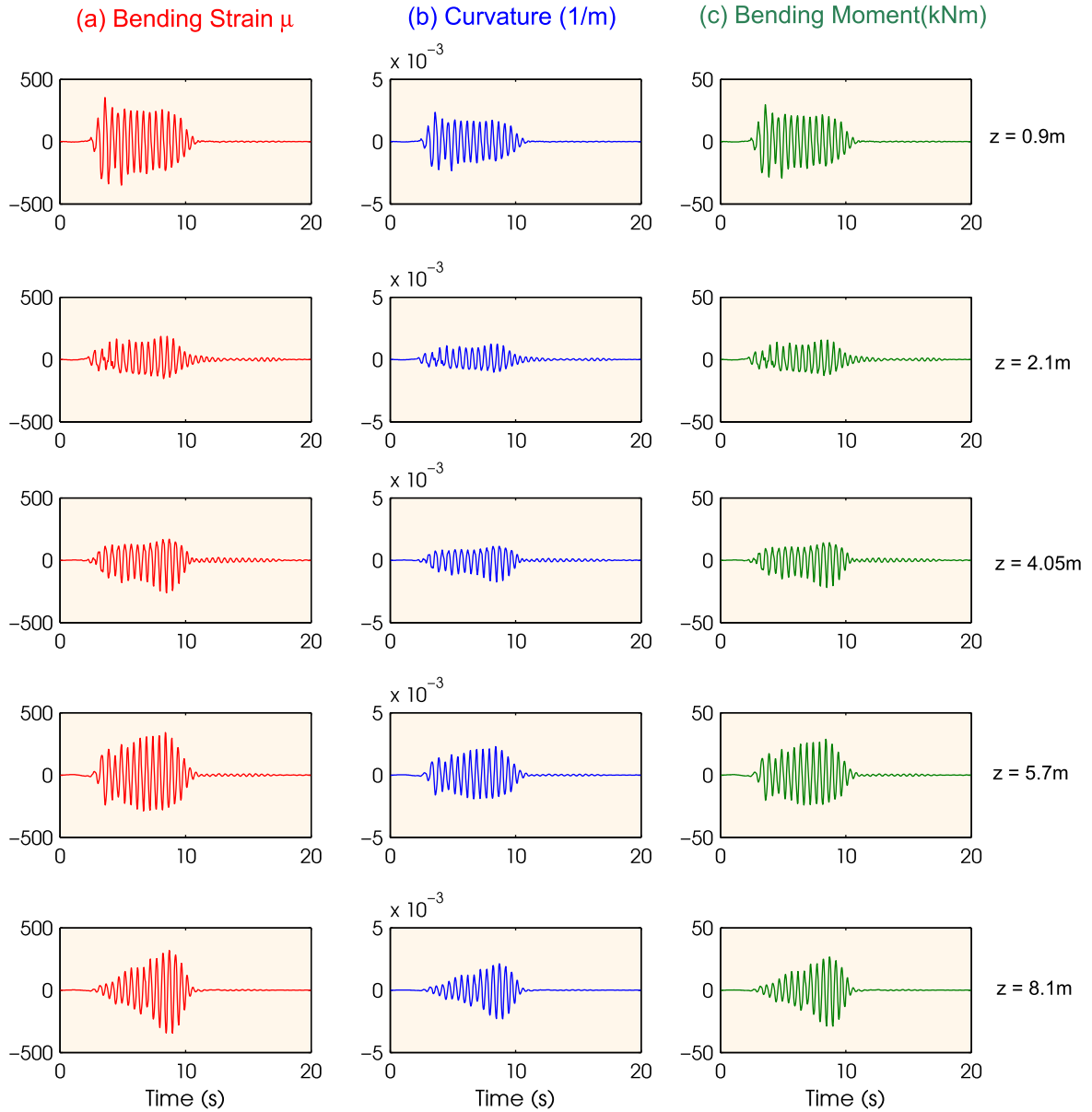
Figure 3.19: Curvature and bending moment calculated from the bending strain data.

the lateral pile deflection by integration, the bending moment fit was found to be insensitive to the interpolation function, and he used the polynomial interpolation function for computational ease. He also examined three different polynomial interpolation functions and suggested non-integer 5th order polynomial as the most appropriate for his test cases.

A similar study was also carried out by Jeanjean (2009), where he computed the $p - y$ curves for soft clays from centrifuge test data. He performed the curve fit of bending moment by three methods (6th order polynomial, Cubic spline function and Loess function) and then presented the $p - y$ curve with the average value obtained from all three methods.

In the present case, to arrive at the best curve fitting option, four different methods as detailed below were studied, where the depth was taken as the variable z.

1. Polynomial fit 1 (Poly fit-1): ($M = A + Bz + Cz^2 + Dz^3 + Ez^4$) A single 4th order polynomial was fitted to the bending moment data. As the bending moments recorded at five discrete points, the order of polynomial was limited to 4 to maintain uniqueness of the fit. The use of a continuous polynomial also eliminates the need for additional numerical differentiation or integration of the bending moment profile.

2. Polynomial fit 2 (Poly fit-2): ($M = A + Bz + Cz^3 + Dz^4 + Ez^5$) A single 5th order polynomial without the quadratic term was fitted. By leaving out the quadratic term, it computes zero lateral resistance at the surface. The coefficient of the quadratic term in bending moment fit gives a constant load after double differentiation. This consideration was also adapted by Wilson (1998).

3. Non-integer polynomial fit (NI Poly fit): ($M = A + Bz + Cz^{2.5} + Dz^3 + Ez^4$) A 4th order polynomial without quadratic term but with a non-integer term was fitted (This polynomial fit was used by Wilson, 1998 while computing p).

4. Cubic spline interpolation (CS fit): A natural cubic spline was implemented that had continuous piecewise linear second derivatives. The second derivative was considered to be zero at the end points of the data, i.e., displacement is zero at the pile tip, which was fixed at the container base.

Figure 3.20 plots the discrete bending moment values and the fitted curve for the four methods described above. All of the methods fit the bending moment data points quite well in the liquefied soil zone, 1.8m to 5.7m, where the final $p - y$ curves were back calculated. The bending moment fitting and its computed values yield similar profile irrespective of the time step of consideration. Though, all the methods of curve fitting gave similar results for bending moment, shear force and slope, the deflection profile obtained varied greatly between the methods, which could be due to higher order polynomial fits. Hence, the calculation for 'p' and 'y' were carried out with all four methods of curve fitting and the results are compared.
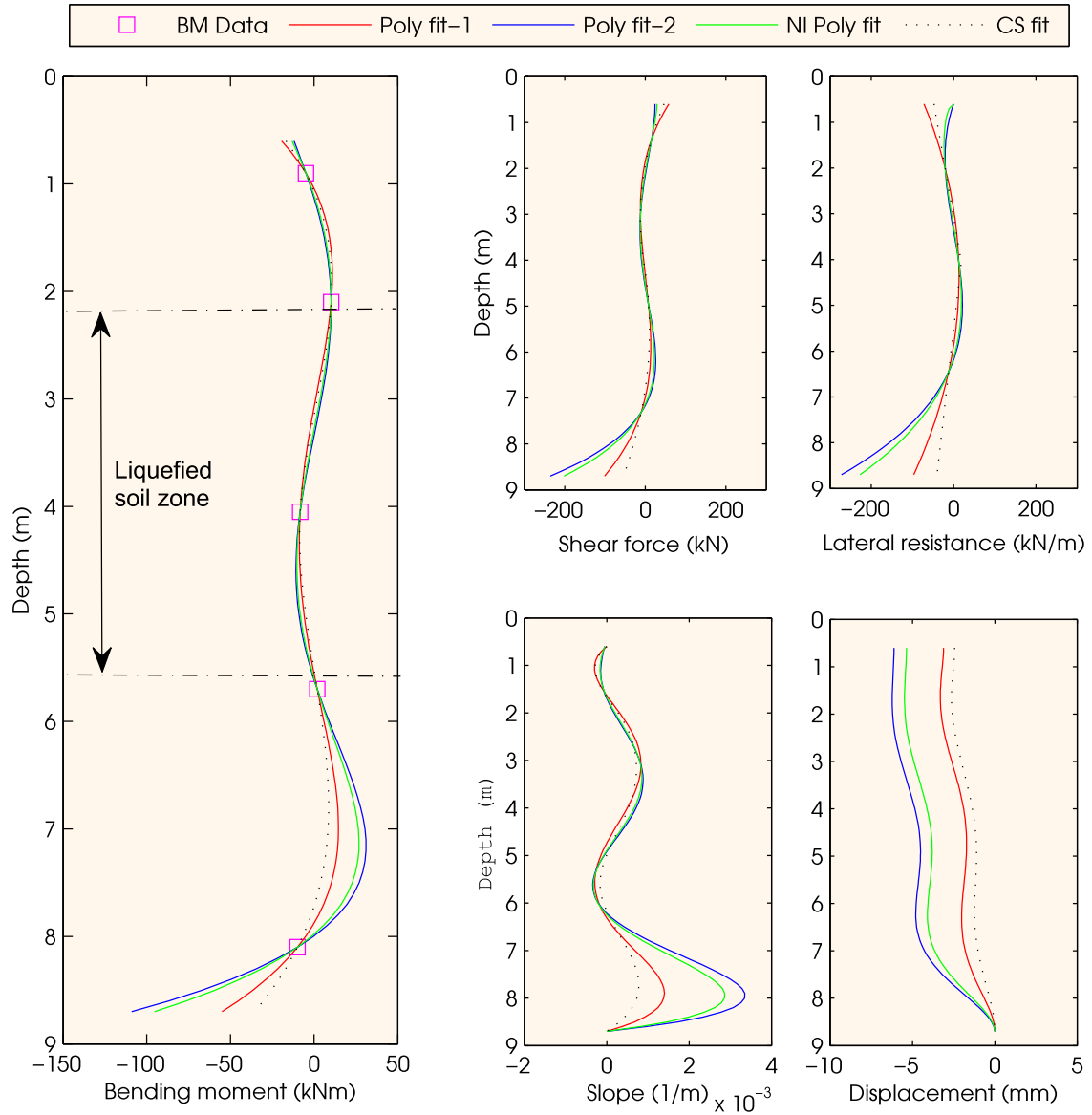
Figure 3.20: Bending moment and its fitted curve at $t = 6s$ (for case CT6-A) by four different fit, and the derived shear force, lateral resistance, slope and pile displacement. [Note: Poly fit-1: $M = A + Bz + Cz^2 + Dz^3 + Ez^4$, Poly fit-2: $M = A + Bz + Cz^3 + Dz^4 + Ez^5$, NI Poly fit: $M = A + Bz + Cz^{2.5} + Dz^3 + Ez^4$, CS fit: Cubic Spline].

3.6 Back calculation of $p - y$ curves

3.6.1 Soil resistance, p

The bending moment profile as fitted above for the discrete bending moment readings were double differentiated to obtain the lateral soil resistance (unit: force/length). Figure 3.21 shows the estimated lateral resistance from all four bending moment fits at three different depths (2.1m, 4.05m and 5.7m) for the representative case, CT6-A. Very good agreement between different fit methods was obtained at shallow depths, but at greater

depths the results varied significantly. This poor agreement shows that the data did not uniquely fit the bending moment profile. However, at the depth of consideration, (i.e., middle of the liquefiable soil layer, $z = 4.05$m), the agreement between the results of different fitting methods are comparatively better except the Poly fit-1. Hence, in further presentation of the lateral resistance, the values obtained from the CS-fit method were used.
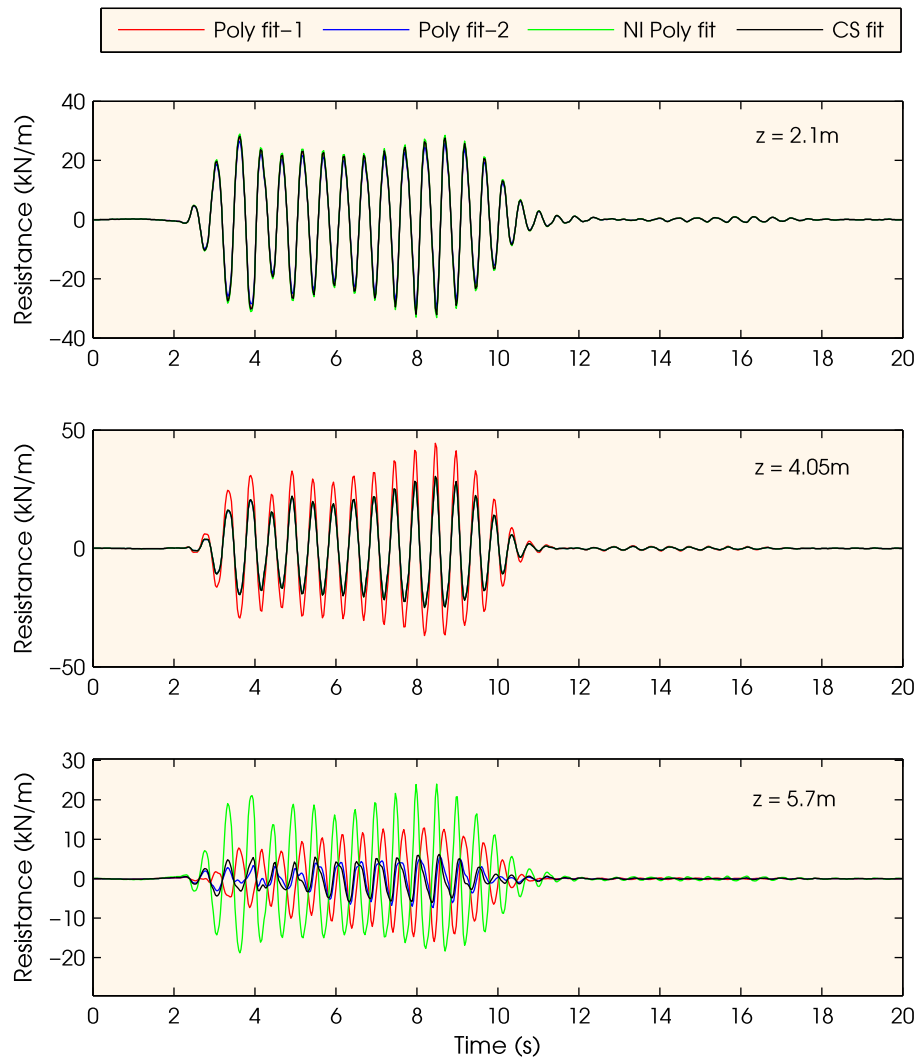
Figure 3.21: Lateral soil resistance estimated for CT6-A.

3.6.2 Pile deflection, y_p

Pile deflection was estimated by integrating the fitted bending moment profile twice. During the integration, the top and bottom boundary conditions were used. Figure 3.22 shows the schematic of the location of measured data and the boundary conditions used for

test case CT6-A. The pile deflections estimated from four bending moment fitting methods are presented in Figure 3.23. Although the deflection pattern is similar, the magnitude varied between the methods. The CS-fit, which was chosen for final representation of the soil resistance, p (Section 3.6.1), gives a lower magnitude of deflection than other three methods. For consistency in the evaluation of p and y, the same CS-fit was also chosen for estimating y.
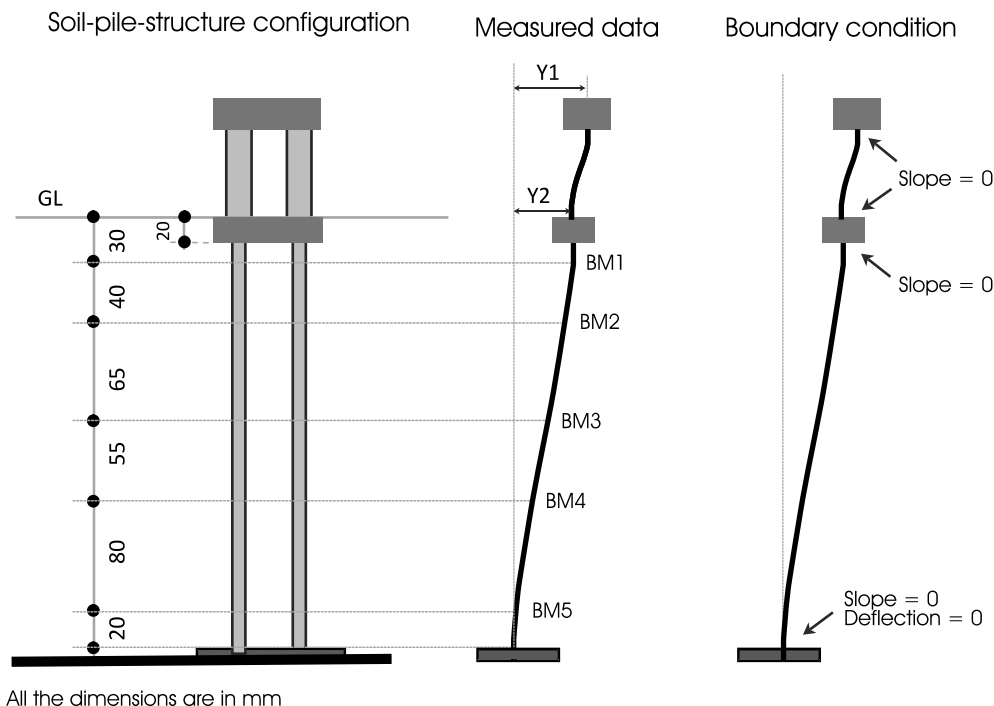
Figure 3.22: Schematic showing the details of measured data and boundary conditions for case CT6-A used in back-calculation of pile deflection, y_p.

3.6.3 Free field soil displacement, y_{sf}

The time history of soil displacement was estimated by double integrating the free field acceleration measurements (Figure 3.24) taken far from the pile group (see Figure 3.8 for the locations of acceleration measurements AccG1, AccG2, and AccG4). The acceleration data were filtered and integrated twice to give the soil displacement. Note that during the filtering process the dynamic component of the displacement was well preserved, however, any permanent component of displacement, if actually present, was removed. Surface observation (no crack formation on the surface) after the test suggests that the locations where free field measurements were taken did not experience any per-
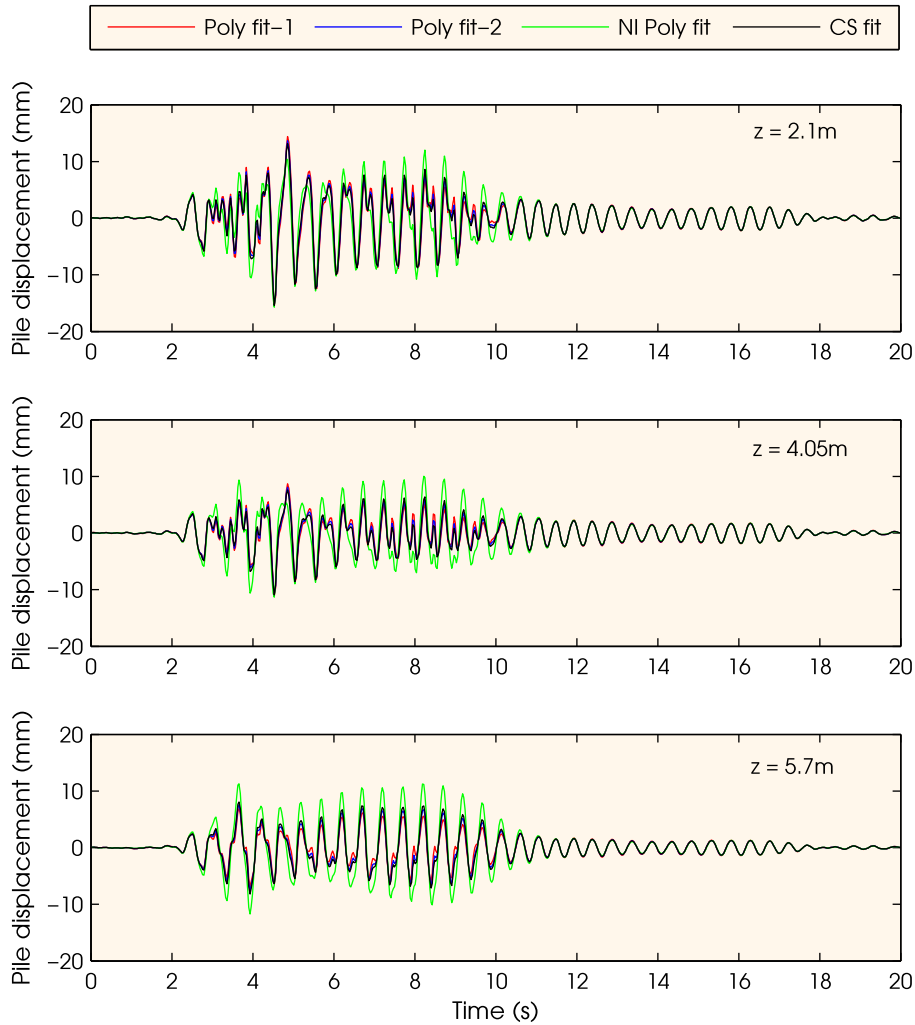
Figure 3.23: Pile displacement estimated for Case CT6-A.

manent ground deformation. Hence, the dynamic component computed here is taken with reasonable confidence in the calculation as already shown in Figure 3.16. As the integration of acceleration data gives absolute values of displacement, the displacement of soil with respect to the base of the container was obtained by subtracting the container base displacement from the estimated absolute soil displacement.

As described in section 3.3, the soil profile had four layers with both liquefied and non-liquefied soil. The soil displacement profile along depth was linearly interpolated between the measurement points but the value at the bottom of the liquefied layer was restricted to be $1/3^{rd}$ of the interpolated value to account for the continuity between liquefied soil layer and its underlying stiffer non-liquefied soil layer. Figure 3.25 shows the schematic of the free field soil profile.
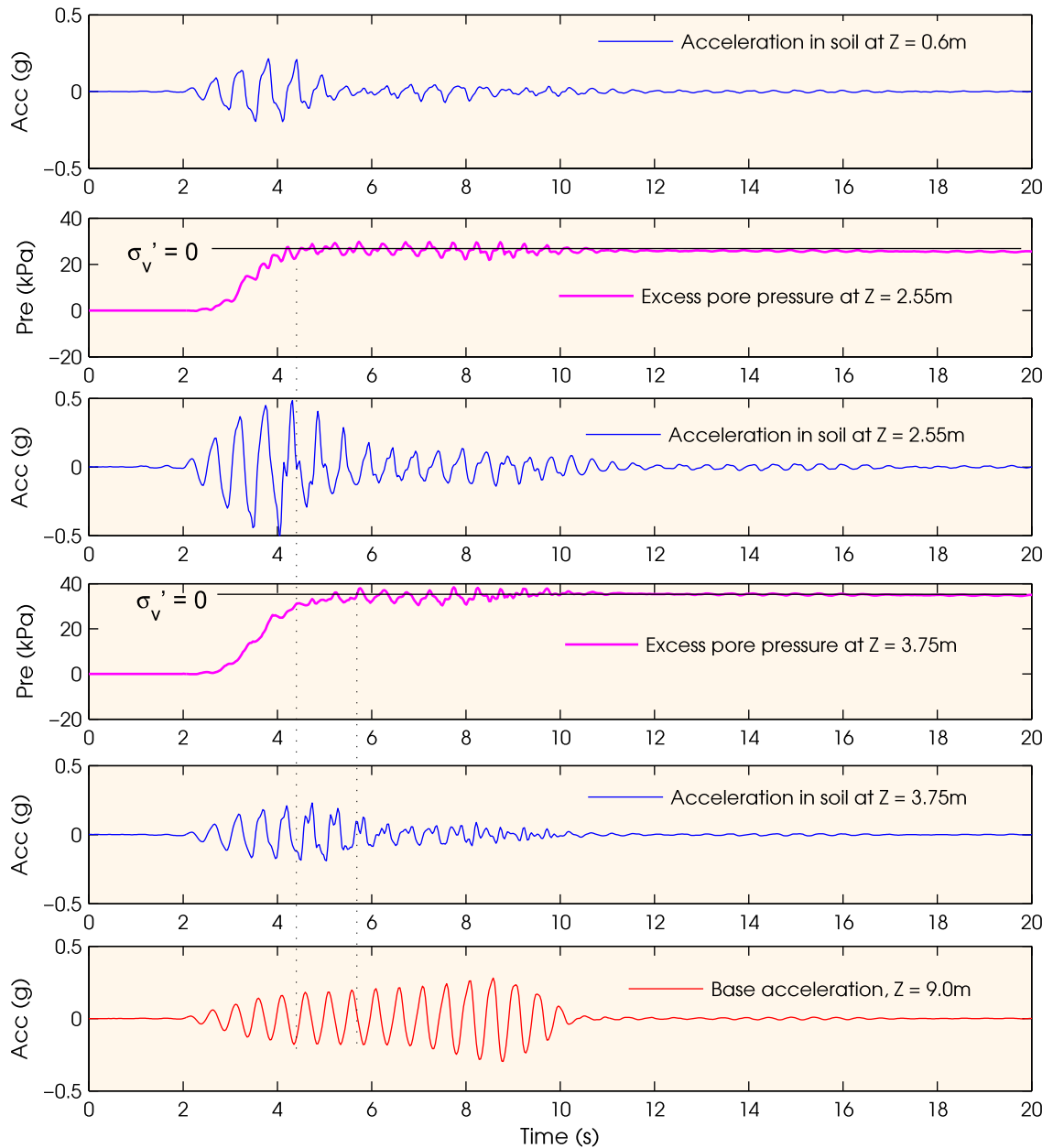
Figure 3.24: Acceleration time history and PPT readings in the soil for CT6-A in prototype scale. (Refer to Figure 3.8 for the locations of accelerometers in the model) [Acc: Acceleration, Pre: Pressure].

3.6.4 Soil displacement near quay wall, y_q

The only measurement available near the quay wall was the displacement of the top. The top 70mm of the quay wall was free on one side and supported the non-liquefied soil on the other. Hence, assuming the loading on the quay wall as a distributed force from the soil, a parabolic deflection profile has been assumed for both fixed and free end quay walls, with a maximum deflection value at the surface. The soil near to the quay wall was

assumed to deflect in the same way as the quay wall, without any gap in between.

3.6.5 Soil displacement near the pile, y_s

There was no instrumentation close to the pile that could have been used to estimate the displacement time history of the soil near to the pile. The only known soil displacement profile was available at two location on either side of the pile group, a) near to the quay wall, and b) at the free field, estimated from the recorded acceleration time history. Hence, to obtain the soil displacement near to the pile, a suitable interpolation was required between the two known displacement values. The deflection profile of the soil near the pile was linearly interpolated between the deflection profile of free field soil (y_{sf}) and the soil near quay wall (y_q), as given in Equation 3.13, which is also schematically shown in Figure 3.25. There is some potential for error because of this linear interpolation assumption, but since it can vary widely depending on many field conditions and there is no distinct way of doing this as per author's knowledge, the linear interpolation was considered simple and reasonable. Figure 3.26 shows the estimated value of soil displacement near to the pile in CT6-A at four different time steps.

$$y_s = y_q - \frac{y_q - y_{sf}}{a + b} \times b \tag{3.13}$$
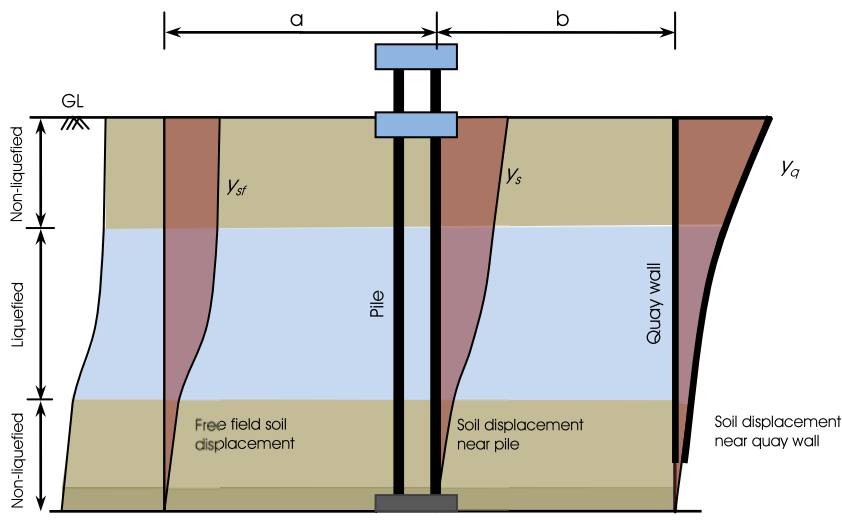
Figure 3.25: Schematic showing the method of estimating deflection profile of soil near to the pile.
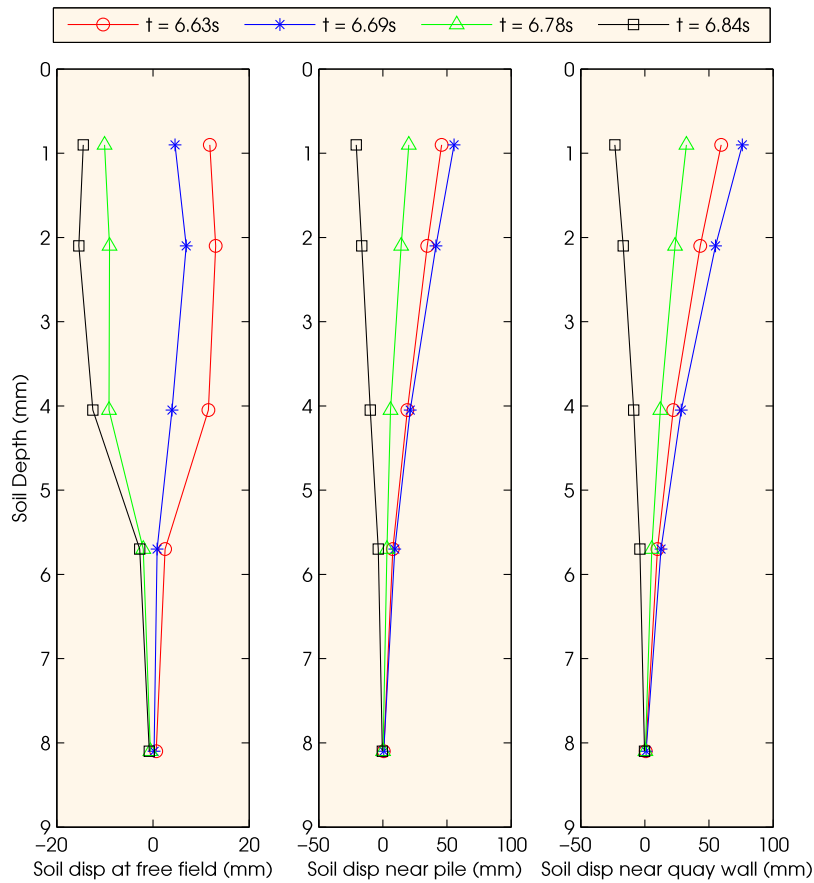
Figure 3.26: Displacement profile of soil near pile at four different time steps for CT6-A.

3.6.6 Relative pile-soil displacement (y)

Once the soil deflection near the pile and the pile deflection were computed, the relative soil-pile deflection (y) was calculated for each time step by subtracting the soil deflection from pile deflection using Equation 3.5. This relative pile-soil displacement profile was estimated at each time step for the full length of the test. Figure 3.27 shows the estimated relative pile-soil displacement for CT6-A at four time steps.

3.7 Estimated $p - y$ curves

The estimation of 'p' and 'y' was demonstrated in the above section for the representative case CT6-A. The plot between p and y at each time step constructs a dynamic $p-y$ curve. The $p - y$ curve for all other cases were carried out with the same analysis procedure as described for case CT6-A. It can be noted that some cases may give improved performance
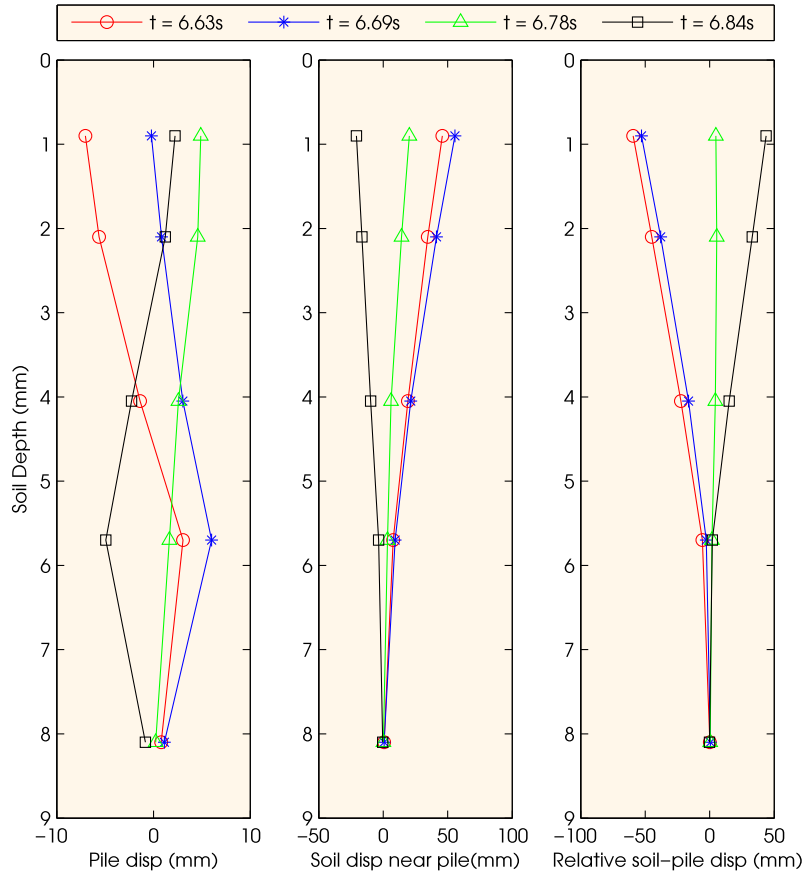
Figure 3.27: Relative soil-pile displacement at four different time steps for CT6-A.

of $p - y$ behaviour if filtering parameters and bending moment curve fitting methods are tuned, but to have a consistency among the test results, the same numerical procedure of data analysis was followed for all the test cases. The back-calculated $p - y$ curves were compared with API recommended monotonic $p - y$ curves for sand for the non-liquefied condition. The API curve was scaled down to 10% to obtain a reasonable comparison between them within the scale of the axis, which is also one of the current practice of modelling $p - y$ curves in liquefied soil as suggested by AIJ (2001). The $p - y$ curves were plotted with normalized values as defined in section 3.2.3. The damping of soil from dynamic $p - y$ curves were also estimated which will be discussed in section 3.8.

3.7.1 $p - y$ curves for no lateral spreading cases (level ground condition)

Tests CT1-A, CT2-A and CT3-A had a non failing quay wall with no large lateral soil flow. Hence, these cases were considered as liquefiable soil without lateral spreading. Figure 3.28 shows the $p - y$ curves estimated for these three cases at full liquefaction (6-10 sec) at two depths (top and bottom of the liquefied soil layer). They were also compared with 10% monotonic API $p - y$ curves for non-liquefiable soils, marked in red lines in the figure. The difference between the magnitudes of the $p - y$ curves in three cases are mostly due to the distance of the pile group from the quay wall, where CT1-A was 200mm, CT2-A was 100mm and CT3-A was 50mm (in model scale) away from the quay wall. The nearer the quay wall, the higher was the resistance due to the stiff boundary, which is seen as a higher magnitude $p - y$ curves in CT3-A as compared to other two $p - y$ curve. Although, the magnitudes differ for the three cases, it varies in the range of 2 to 5% of the API $p - y$ curve for non-liquefied soil.

3.7.2 $p - y$ curves for lateral spreading cases

All other cases except above three cases discussed in section 3.7.1 had a free base quay wall, which failed during the test. Figure 3.29 (a) shows the $p - y$ curves obtained from the CT6-A during the test (0-20 sec) at top, middle and bottom of the liquefied soil layer. As expected, the $p - y$ curves calculated are off centered, which were due to the lateral spreading of the soil as the quay wall failed and the soil experienced a permanent displacement. To get a better comparison with the API recommended monotonic $p - y$ curves, the lateral spreading component was removed from the soil deformation and the $p - y$ curves thus obtained is presented in Figure 3.29 (b). The $p - y$ curves at top of the liquefied soil show more resistance (18 % of non-liquefied API value) than the $p - y$ curves at the bottom part (4% of non-liquefied API value). However, the magnitude of the $p - y$ curves should usually be higher at deeper depth. In the present case, this observation could be due to higher y at shallow depth.

To note that, the $p - y$ curves shown in Figure 3.29 are back-calculated with some inherent limitations on accuracy due to the limited number of strain measurement points,
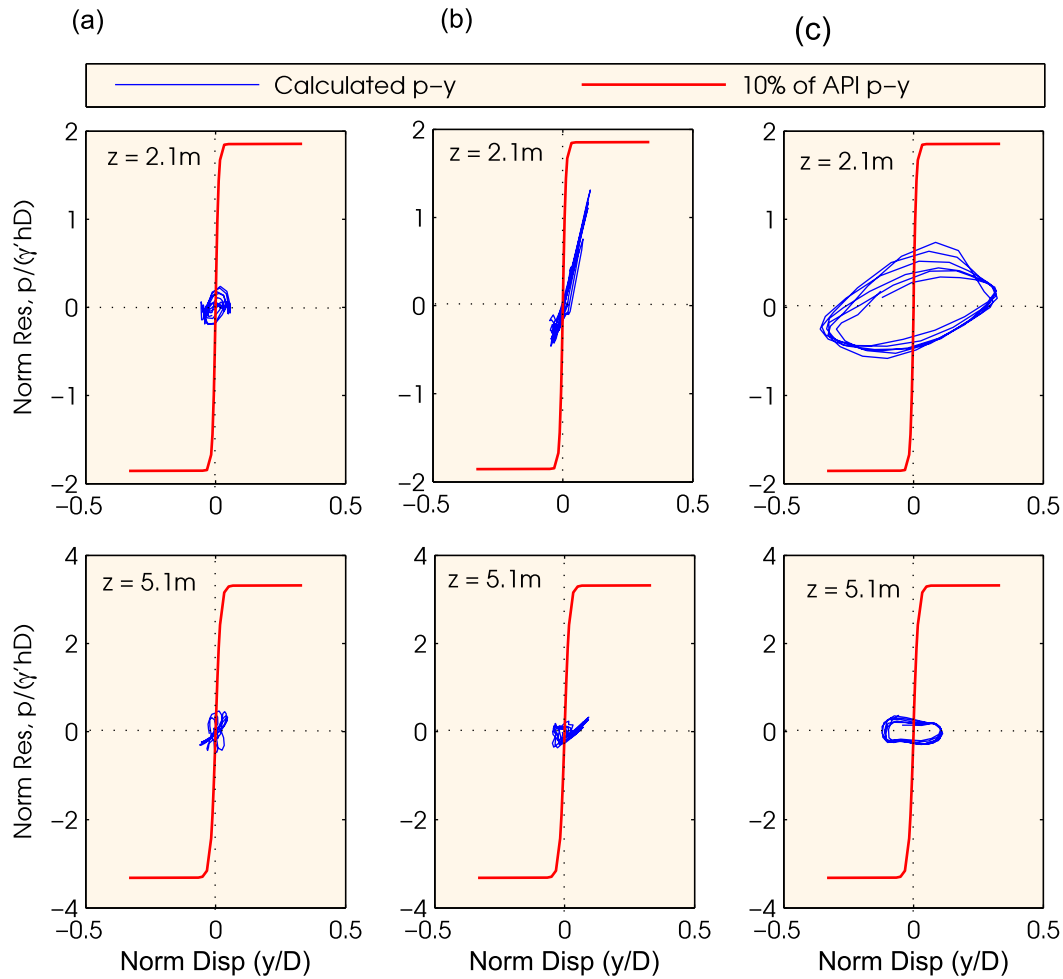
Figure 3.28: $p - y$ curves for cases (a) CT1-A (pile group 200mm away from quay wall), (b) CT2-A (pile group 100mm away from quay wall) and (c) CT3-A (pile group 50mm away from quay wall), where there was no lateral spreading of the soil.

curve fitting method for bending moment data and soil deformation measurements from acceleration time history. However, the pattern of the $p - y$ curves obtained is reasonably good at the lower level of the liquefied soil layer than the upper level. One of the reason may be the inability of filtered accelerometer data to capture the actual displacement in the soil after full liquefaction as evident from Figure 3.24. The final results for the $p - y$ curves are presented at two levels for tests CT1, CT2 and CT3 and at three levels for other test cases in the liquefied soil layer. The $p - y$ curves were also compared with the 10% API recommended $p - y$ curves for saturated sand at corresponding depths after removing the drift components. Figures 3.30, 3.31 and 3.32 show the $p - y$ curves obtained for the lateral spreading cases at fully liquefied state (6-8 sec). The observation of a higher strength at top of the liquefied layer than the bottom layer was observed consistently. Some of the
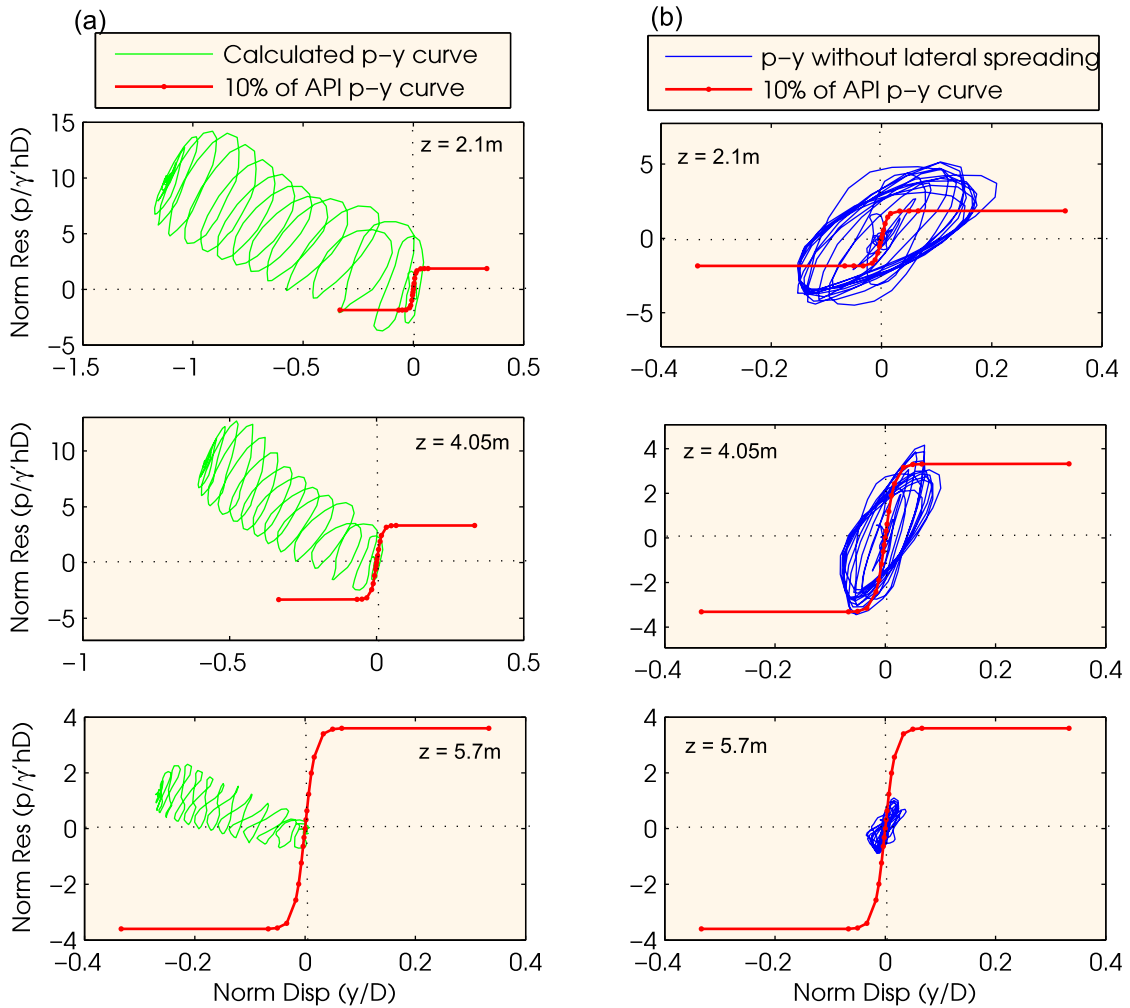
Figure 3.29: $p - y$ curve in liquefied soil for CT6-A at three depths, $z = 2.1$m, 4.05m and 5.7m, (a) with lateral spreading, and (b) without lateral spreading (i.e., only dynamic component after removing the permanent drift component).

$p - y$ curves have shown unexpected hysteresis loops, *e.g.*, in CT3-B at z = 2.1m and CT6-A at z = 5.7m, which could have resulted from the limitations in the experimental data and numerical processing methods.

3.7.3 Comparison of lateral spreading case near to and far from the quay wall

Cases CT4-A and CT4-B were in the test CT4 but the pile groups were positioned at different distances from quay wall, CT4-A was at 100mm and CT4-B at 50mm (in model scale). Both pile groups were subjected to lateral spreading due to the failure of quay wall. The $p - y$ curves obtained for both the cases including the lateral spreading component are shown in Figure 3.33. In these cases, as the magnitude of soil movement towards right
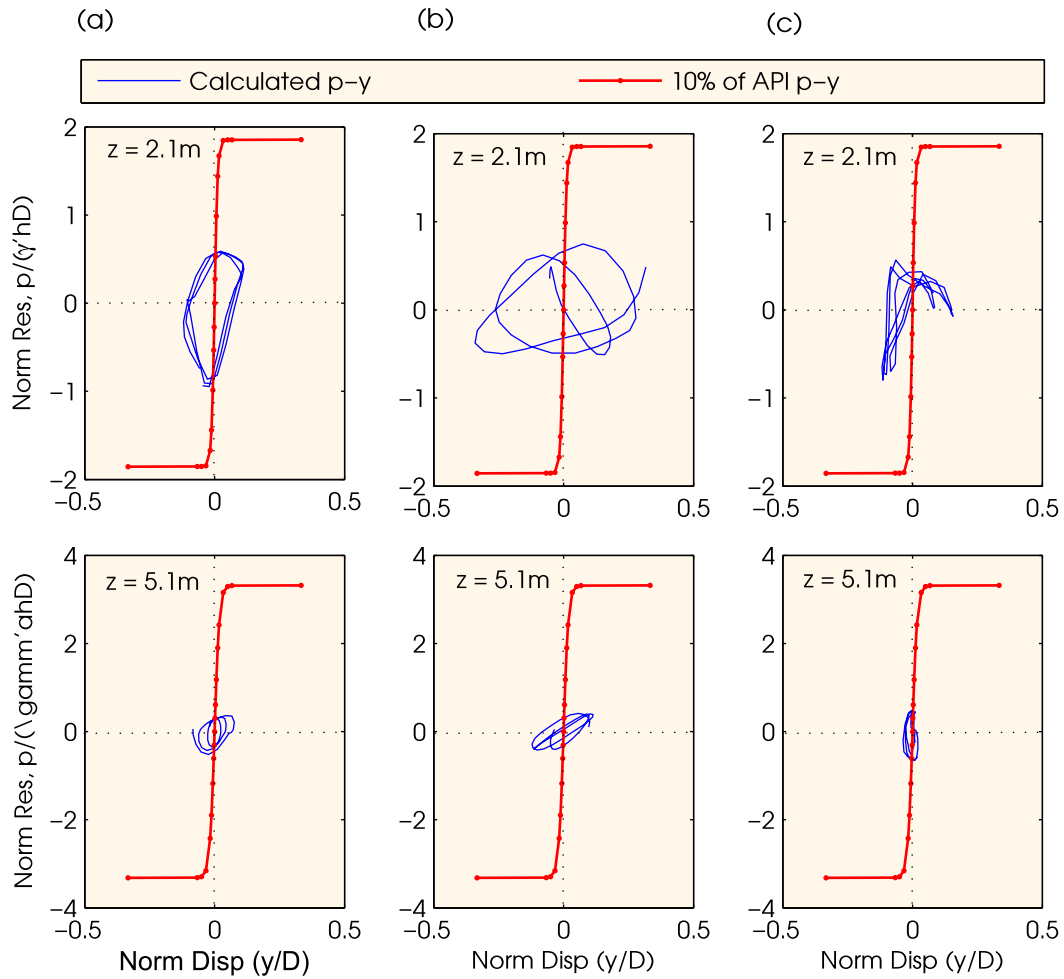
Figure 3.30: Back calculated $p - y$ curves for (a) CT1-B (pile group 200mm away from quay wall), (b) CT2-B (pile group 100mm away from quay wall) and (c) CT3-B (pile group 50mm away from quay wall) in fully liquefied soil at two depths and compared with 10% monotonic API $p - y$ curves.

was more than the pile movement, the relative pile-soil displacement was negative. Hence, the progression of $p - y$ behaviour is on the negative side in Figure 3.33. Comparing the $p - y$ curves for both cases, they were very similar in pattern, but the magnitudes were different. To get a better comparison of the magnitudes, the permanent displacement component had been removed as shown in Figure 3.34. The strength of liquefied soil was about 10% of API non-liquefied value at the top layer, which was about 2% of API value at bottom of the liquefied soil layer.
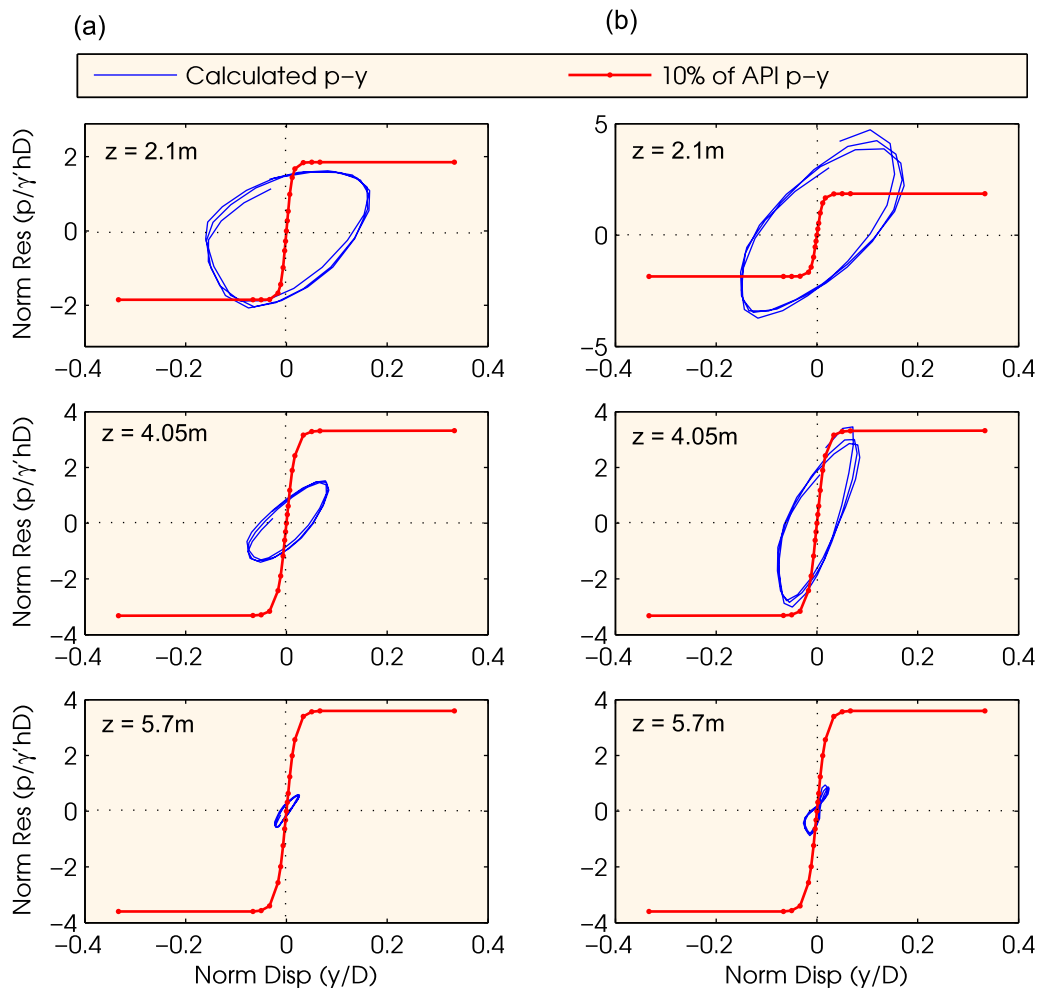
Figure 3.31: Back-calculated $p-y$ curves for (a) CT5-A and (b) CT6-A in fully liquefied soil at three depths and compared with 10% monotonic API $p-y$ curves.

3.7.4 Comparison of lateral spreading and non-lateral spreading cases under identical test conditions

Tests CT1, CT2 and CT3 had both lateral spreading (Side-A) and non-lateral spreading (Side-B) model subjected to identical test conditions. The $p-y$ curves for CT1-A, CT2-A and CT3-A can be compared with CT1-B, CT2-B and CT3-B from Figures 3.28 and 3.30. The results show no significant change in pattern and strength of the liquefied soil for these three tests.
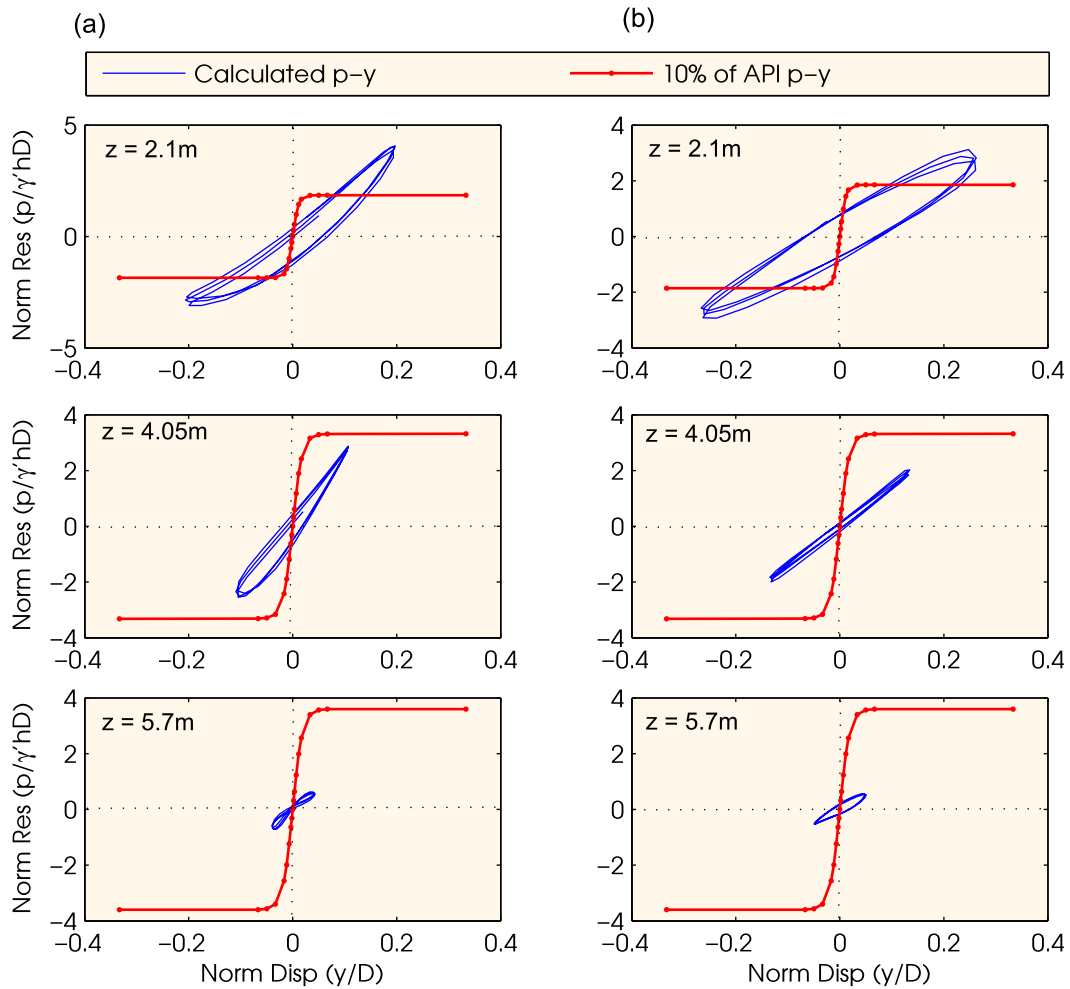
Figure 3.32: Back-calculated $p - y$ curves for (a) CT7-A and (b)CT8-A in fully liquefied soil at three depths and compared with 10% monotonic API $p - y$ curves.

3.8   Estimated damping from the $p - y$ curves

From the dynamic $p - y$ curves (i.e. drift removed), each hysteresis loop was separated at the zero crossings of the displacement time history. The equivalent viscous damping was then estimated for each hysteresis loop (section 3.4.2) and presented as a single calculated value at the middle of the considered time band. The frequency and velocity dependent behaviour on the $p - y$ curve was not available in the data, and hence the possibility of hysteresis type damping model was not explored. The damping ratios (with equivalent viscous model) estimated during the test CT8-A at three depths are presented in Figure 3.35. Other test cases too yield a very similar pattern and magnitude of damping ratio. The variation of damping ratio with the average shear strain in front of the pile is plotted in Figure 3.36, considering the average shear strain as proposed by Klar (2008) as given
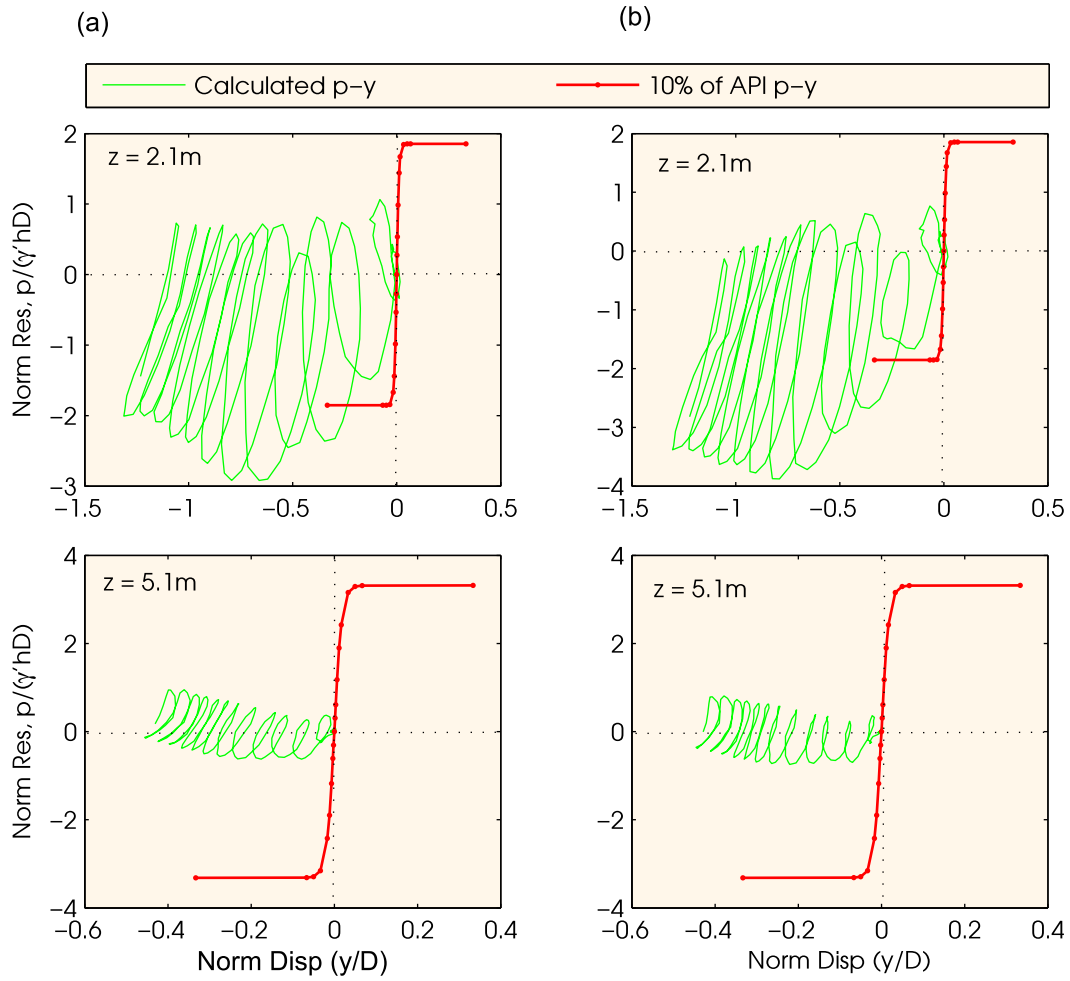
Figure 3.33: Back calculated $p-y$ curves for (a) CT4-A and (b) CT4-B subjected to lateral spreading.

in Equation 3.14. The results have shown that higher damping is associated with small strain vibration as the proportionate energy dissipated is large compared to large strain vibration. This was due to the cyclic strength degradation of the soil and change in shape of the hysteresis loop with strain.

$$\gamma_{avg} = 2.6\frac{y}{D} \tag{3.14}$$

where, γ is defined as the average engineering shear strain around a pile due to relative pile-soil displacement, y.
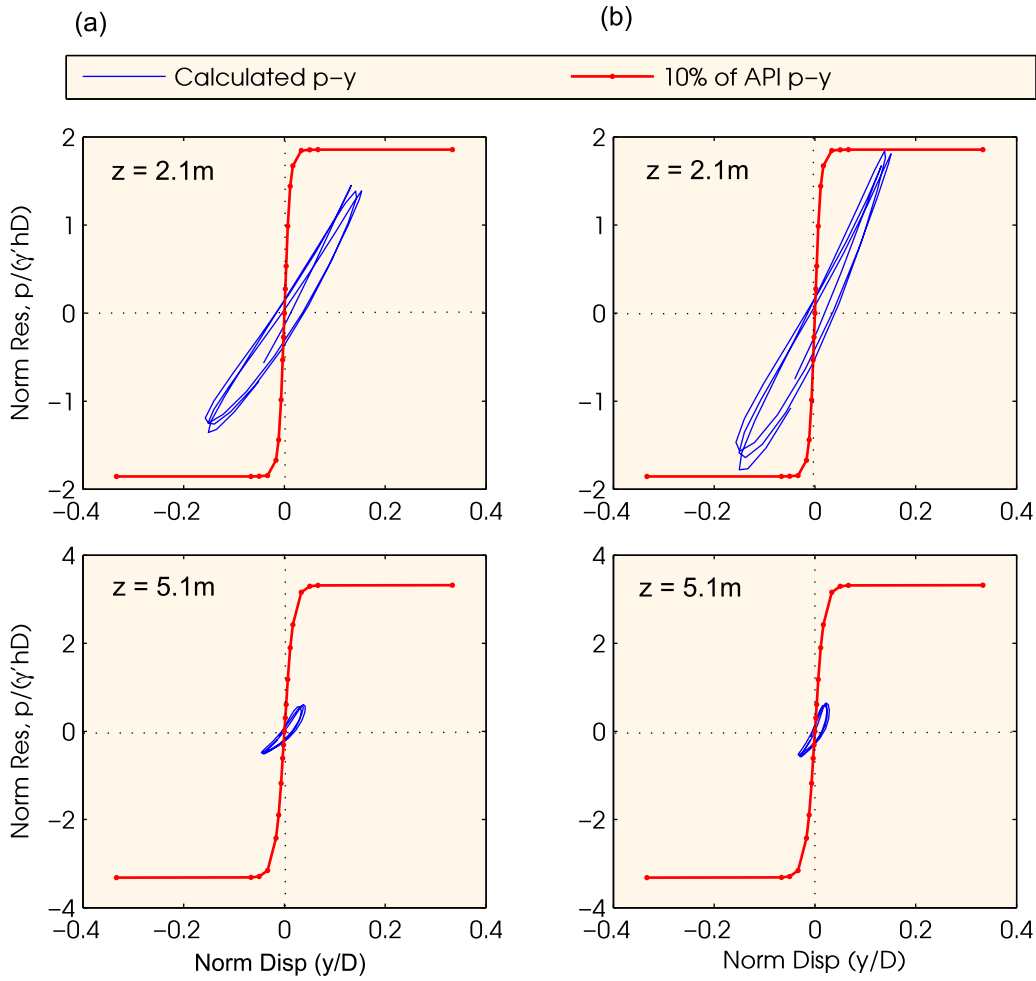
Figure 3.34: Back calculated $p - y$ curves for (a) CT4-A and (b) CT4-B after removing the lateral spreading component (i.e, removing the permanent drift).

3.9 Peak bending moment along depth during the process of liquefaction

Figure 3.37 plots the bending moment at 5 depths during test case CT6-A. Before liquefaction, the soil had sufficient lateral confinement and the depth of fixity lay within the top non-liquefied soil layer. This, hence, causes the bending moment to be maximum near to the pile head. When the intermediate liquefiable soil layer was fully liquefied, the lateral soil strength reduced significantly causing the location of maximum bending moment to move towards bottom of the liquefied soil layer. This can be seen in Figure 3.37. During the pore pressure generation phase (till 5sec), the maximum BM was occurring at the top measurement point, i.e., at $z = 0.9$m. However, it went down to the bottom of the liquefied soil layer to the measurement location of $z = 5.7$m at full liquefaction.
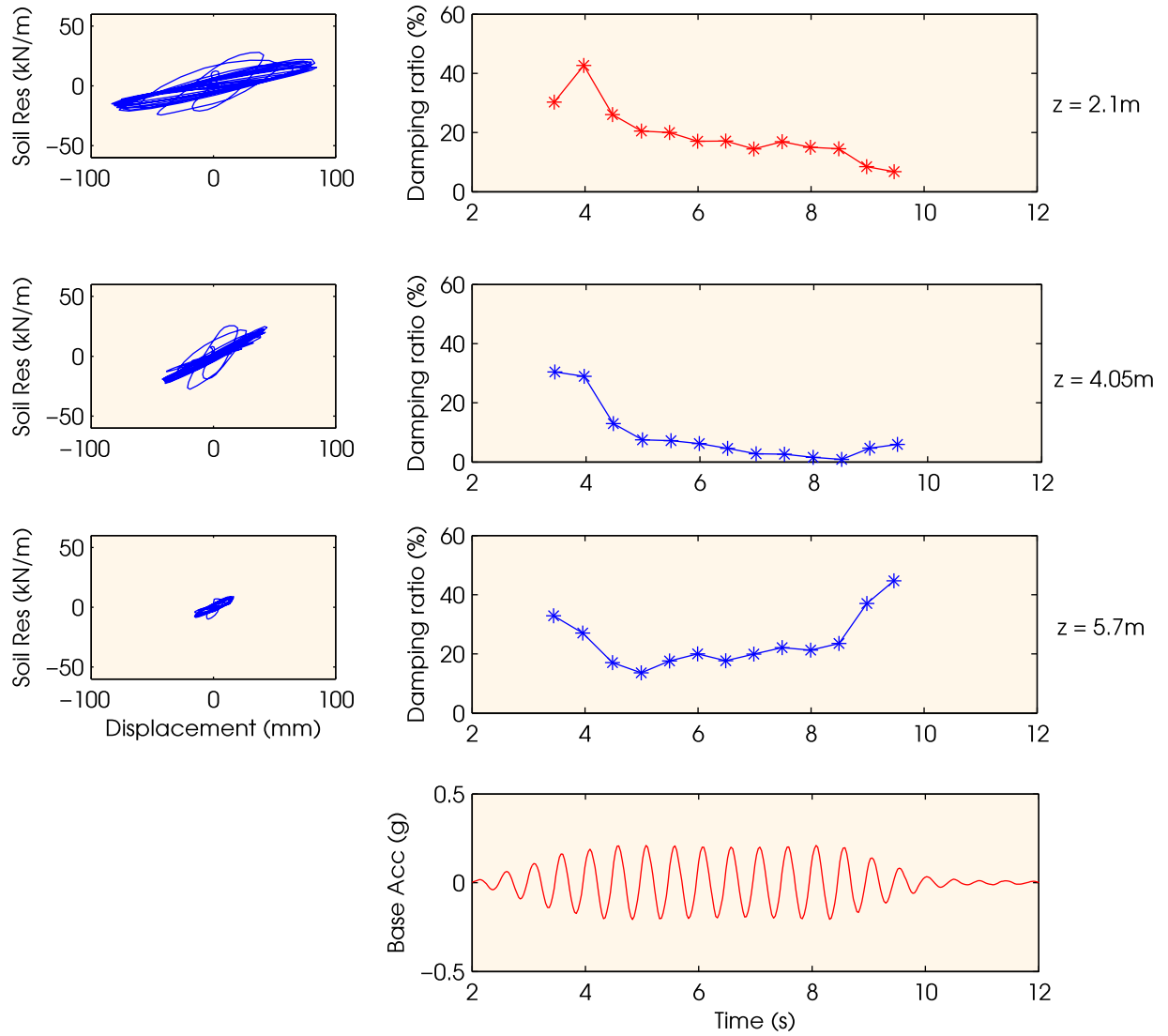
Figure 3.35: Damping ratio (ζ) as obtained from dynamic $p - y$ curves for CT8-A.

The non-liquefied soil at the base is also expected to reduce strength due to cyclic shear. This was observed as the location of bending moment went even below the bottom of the liquefied soil to the non-liquefied soil layer during continual cyclic loading after liquefaction. This can be seen in the Figure 3.37, during 7.5 to 10.5 sec. The transition of top of liquefied soil layer to bottom of liquefied soil layer was quick enough that did not show the location of maximum bending moment at intermediate level of liquefied soil layer. However, this could be a possibility when the development of excess pore water pressure is slow depending on geophysical and earthquake characteristics.
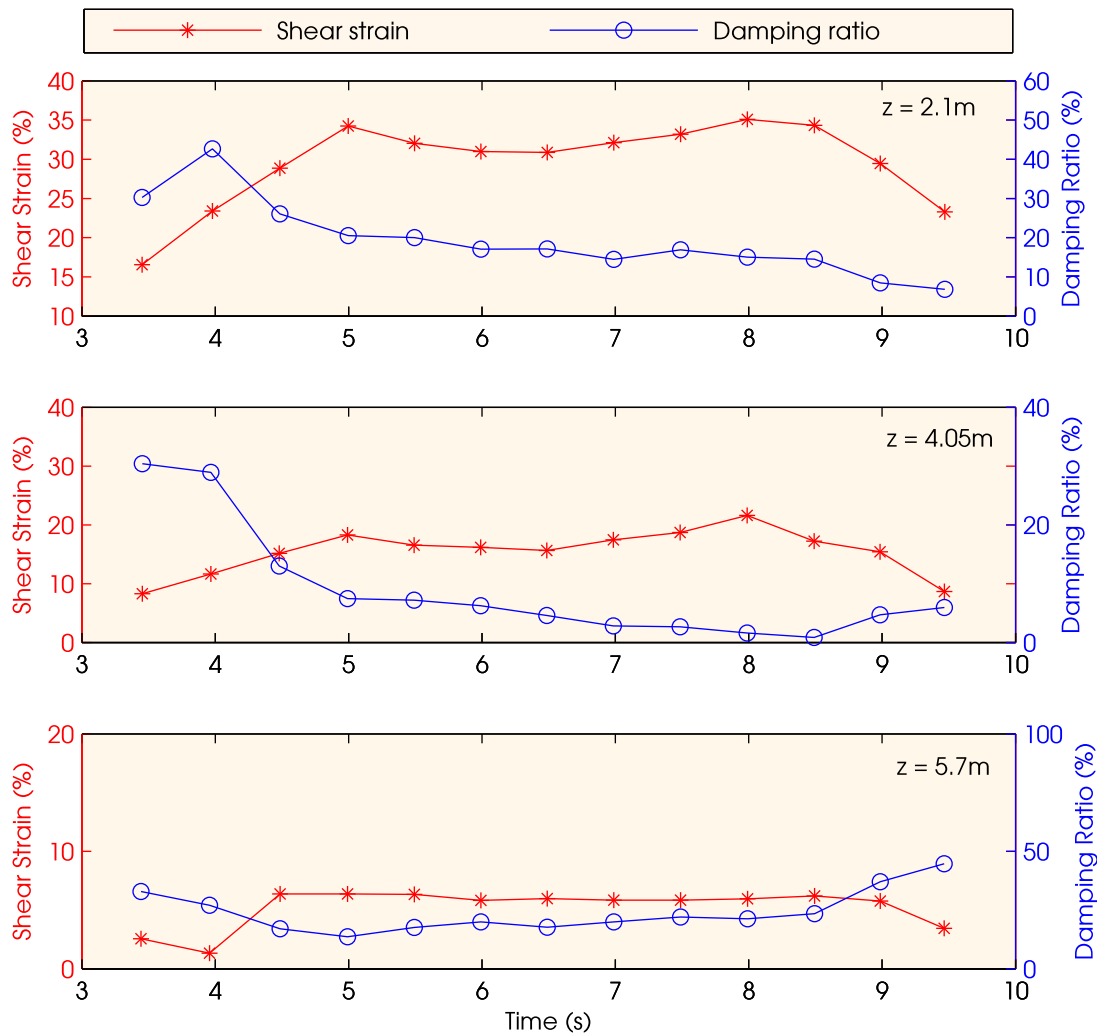
Figure 3.36: Damping ratio (ζ) versus average engineering shear strain for case CT8-A.

3.10 Pore pressure distribution: near to pile *versus* far field

Figure 3.38 shows the excess pore water pressure (EPWP) near the pile and at the far field during the test CT9-A. The near pile pore pressure observation was made behind the pile during the test. The value of EPWP, being a stress parameter, remains same for both prototype and model scale in the centrifuge test. But, the time axis changes with a scale of $1 : n$, model:prototype (as mentioned in Table 3.1). The results here are presented in prototype scale. Figure 3.39 shows $p - y$ curves at different times during the test. Viewing Figure 3.39 in conjunction with Figure 3.38 shows that the resistance of liquefied soil subjected to shear was partly attributed from the decrease in EPWP. This behaviour
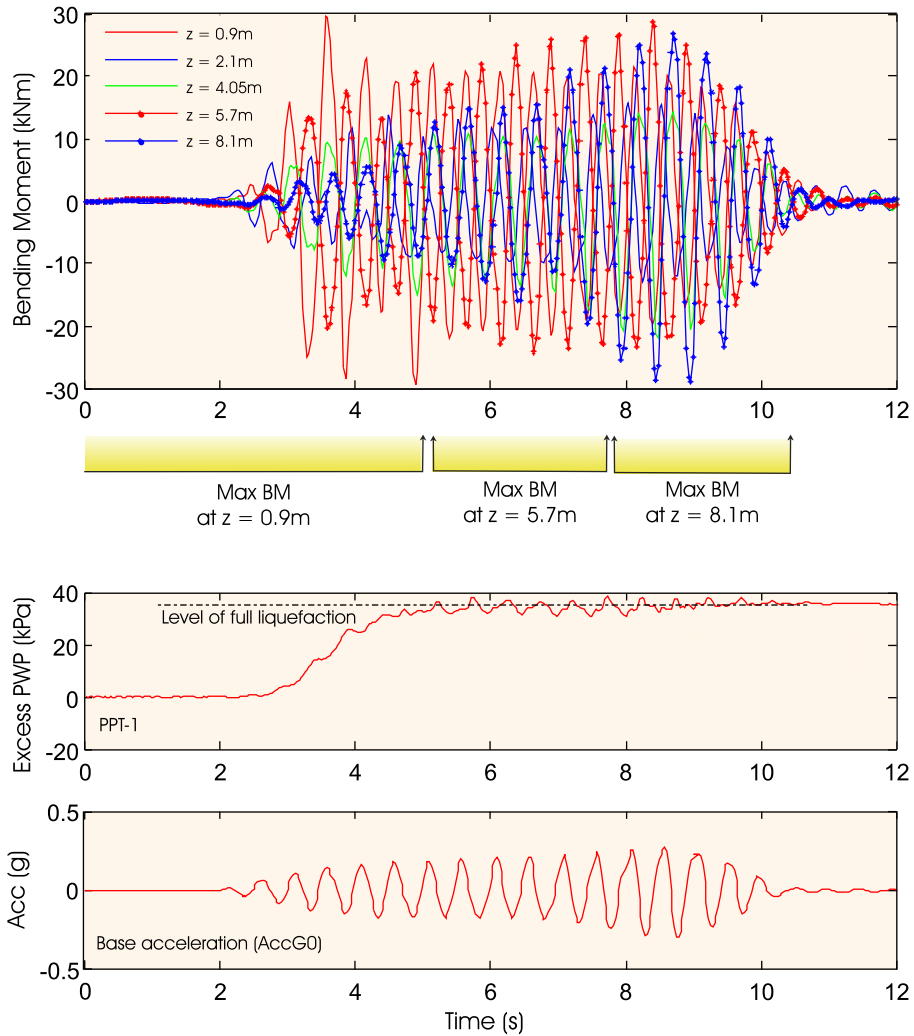
Figure 3.37: Location of peak bending moment in pile in test CT6-A.

is similar to that observed in the laboratory element tests during monotonic shearing of liquefied soil, for example: Yasuda *et al.*, 1998, 1999; Sitharam *et al.*, 2009. In the initial phase of loading, free field pore water pressure reached a maximum value (that corresponds to $\sigma'_v = 0$) in 3 to 4 cycles. But near to the pile, development of pore water pressure was dependent on pile vibration, and in each cycle the pore pressure dissipation was also happening due to pile movement. Though, excess pore pressure near to the pile could be the governing parameter of soil resistance, it is hard to characterize the expected value of it in a field condition, as it depends on many parameters including the shear loading, pile dimension, gap formation near to pile that facilitates easy dissipation of EPWP. Hence, the lateral resistance of liquefied soil at soil-pile interface is normally characterized by the degree of liquefaction expected in the soil at the site without considering the influence of
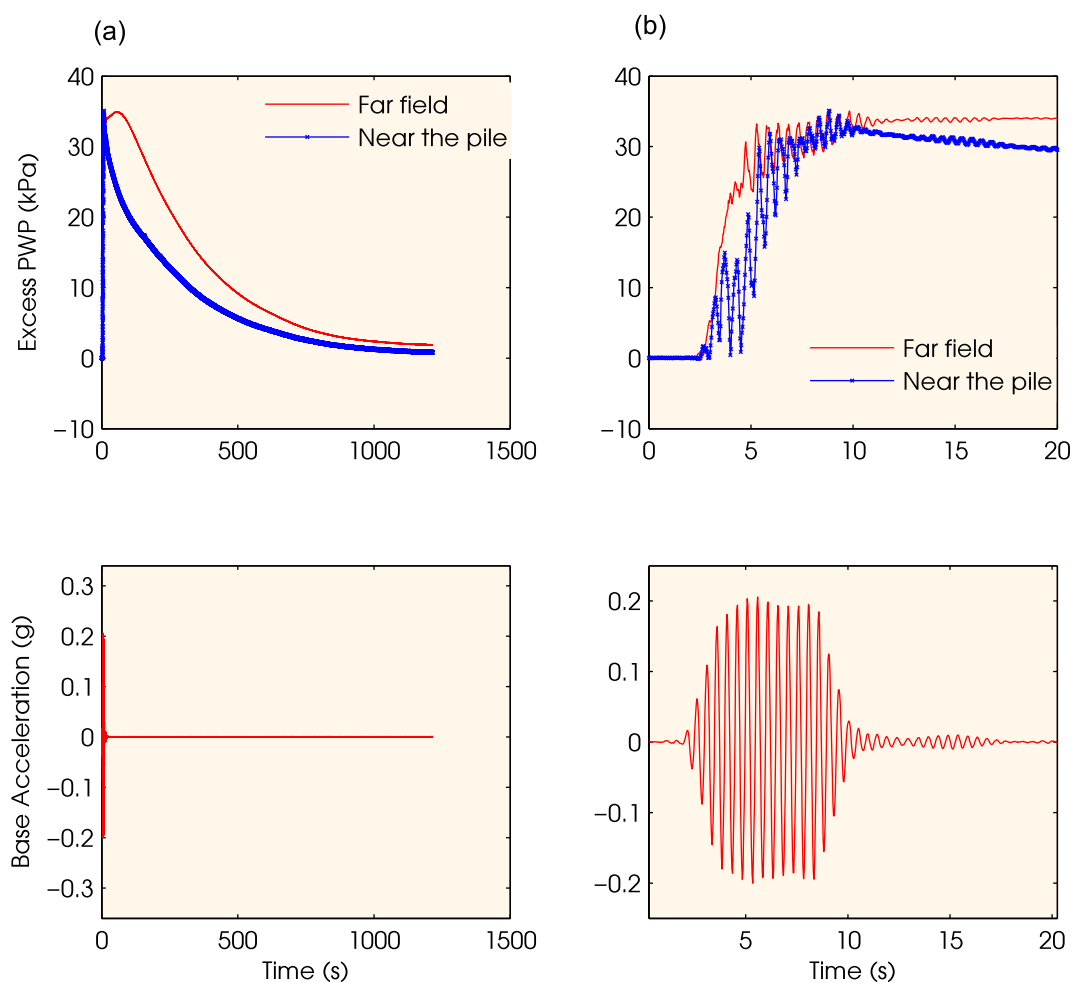
pile.

Figure 3.38: Comparison of excess pore water pressure near to the pile and at the far field, (a) full time history, (b) only during the base acceleration input in the test CT9-A.

3.11   Summary of conclusions

Thirteen pile group results from centrifuge tests have been investigated in this chapter. The $p-y$ curves have been back calculated from the recorded bending strain of the pile and soil acceleration data. From the above study, the following conclusions can be made.

- The shape and magnitude of the back calculated $p-y$ curves were having qualitative agreement across the tests for a particular depth of consideration. Most of the cases from the 13 test cases showed very similar pattern of $p-y$ curves.

- Some of the tests also have shown nearly un-drained behaviour. For example at
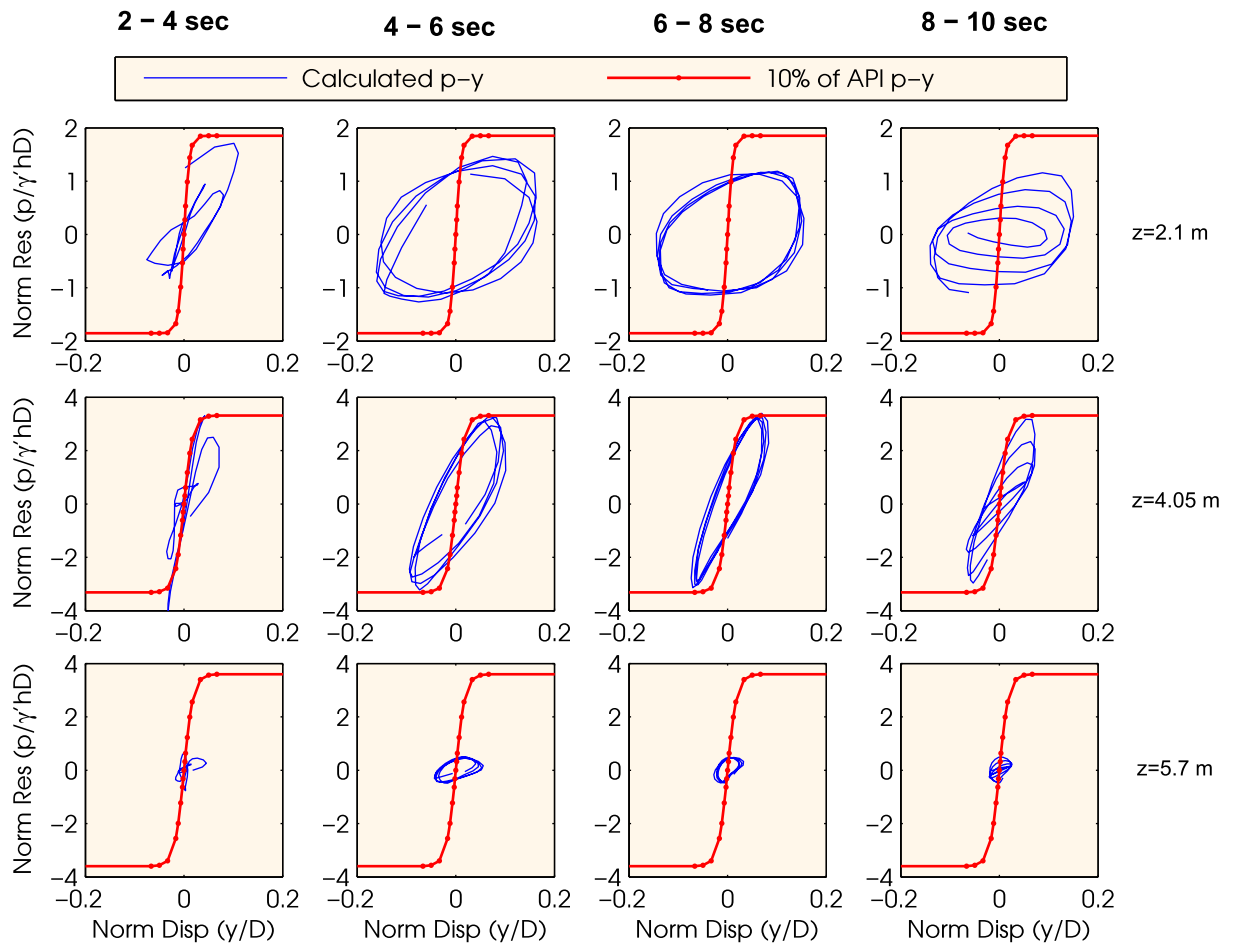
Figure 3.39: $p - y$ curves at different time range during test CT9-A.

the bottom of the liquefied soil layer in CT4-A and CT4-B, the initial stiffness of the $p - y$ curves were very low and increased with large pile-soil displacement (see Figure 3.34).

- Results from all the test cases showed that the lateral resistance of loose to medium dense soil (Relative density, $D_r = 50\%$ in this study for liquefied soil) can normally range from 1-10% of API suggested value for non-liquefied soil. This is with the consideration of a mean and more representative value of lateral resistance at the middle of liquefied soil layer. But in some cases the results at the top of the liquefied soil layer were influenced by the overlaying non-liquefied soil layer which showed larger resistance as compared to other cases. For example, in Case CT6-A the resistance at the top of the liquefied soil layer was about 18% of the API suggested value for non-liquefied soil. This higher resistance was also due to the large value of y at shallow depth.

- The higher lateral resistance was associated with the decrease in excess pore water pressure near to pile as seen in CT9-A.

- The cyclic $p-y$ curves as back calculated from centrifuge tests were used to estimate damping ratio in the liquefied soil layer. The results have shown that the damping ratio in liquefied soil could be very high, up to 50% in some cases. The higher damping values were associated with small strain vibrations, which reduced during large strain vibrations.

- Comparison between lateral spreading and non-lateral spreading ground in liquefied soil showed that the strength of liquefied soil did not change much in the lateral spreading case than in the non-lateral spreading case. These two cases of the $p-y$ curves are differentiated in literature as (a) lateral spreading case where the soil flow past pile, and (b) non-lateral spreading case where pile vibrates in liquefiable soil. From the author's knowledge, this is the first set of tests that directly compares lateral spreading and non-lateral spreading cases under an identical test condition.

- As the present analyses were involving differentiation, integration and curve fitting of experimentally observed data, there were possibilities of error in these processes. Hence, a detailed signal processing for the dynamic experimental data set was carry out to be able to meaningfully analyse them. However, it must be mentioned that some tests have shown better performance by minor adjustments in filter parameters during signal processing, but this was not done in the interest of keeping the processing consistent across all the tests.

- Some of the $p-y$ curves have shown unexpected hysteresis loops, which could have resulted from the limitations in the experimental data and numerical processing methods. Some other limitations of this analysis include: a) the sudden stiffness changes in the soil layers that have affected the $p-y$ curves in liquefied soil due to the imposed curve fitting of the bending moments in the pile, b) insufficient instrumentation in the soil to measure deflection profile of soil more precisely, and c) the assumed linear interpolation of the free field soil displacement and the soil displacement near the quay wall to obtain the soil displacement profile near the pile.

- Regardless of the above limitations, the analyses were very useful as the $p - y$ curves look reasonable except few cases, and as expected, they also show comparatively low initial stiffness in fully liquefied soil in line with other experimental results.

Chapter 4

1g model test

4.1 Introduction

In chapter 3, the macro behaviour of pile-soil interaction in liquefied soil (in particular the $p - y$ curve) was investigated through a set of centrifuge tests. While the shape and ultimate strength of the $p - y$ curve could be qualitatively ascertained, its global behaviour was governed by many factors including inertia, dynamic and kinematic interaction and model complexities such as: soil layering, quay wall position, large lateral soil flow, pile head footing and superstructure. Those $p - y$ curves are also not a direct observation, rather a back-calculated value to fit the recorded bending behaviour of the test pile. In addition, the liquefaction during the centrifuge tests occurred so quickly that the $p - y$ curve for different degrees of liquefaction could not be studied. Hence, a set of $1 - g$ experiments were designed to study the $p - y$ behaviour directly in liquefiable soils. These experiments were carried out at the BLADE laboratory of the University of Bristol.

4.1.1 Outline of the chapter

This chapter describes the $1 - g$ experiments carried out to investigate the resistance offered by liquefiable soils when a large relative soil-pipe displacement is applied. The model setup, instrumentation and control for the test rig are described in detail. From the tests, the $p - y$ behaviour was measured at different degrees of liquefaction and at various rates of loading. Finally the test results and the summary of observations are discussed.

4.2 Test procedures and conditions

4.2.1 Test procedures

This test setup was based on a plane strain idealisation of pile-soil interaction at a particular depth/overburden pressure. In this, a pipe was pulled horizontally at different velocities through saturated sand. Essentially, a section of the pile at a certain depth was modelled as a buried pipe. The base of the test box was attached to an actuator to liquefy the soil through base shaking by developing excess pore water pressure (EPWP). The analogy of using a horizontal pipe rather than a vertical pile is explained in Figure 4.1. This idealisation is widely used by many researchers (Towhata *et al.* (1999); Takahashi (2002); Dungca *et al.* (2006)) to study resistance of liquefied soil on piles. In the present study, the tests were carried out with the following objectives:

1. To understand the change in EPWP in liquefiable soils near to the pile during the pipe movement as compared to the far field EPWP.

2. To directly investigate the $p - y$ curve at different degrees of liquefaction and at different pipe velocity.

| Site condition | Plane of consideration A-B | Plane strain idealisation |
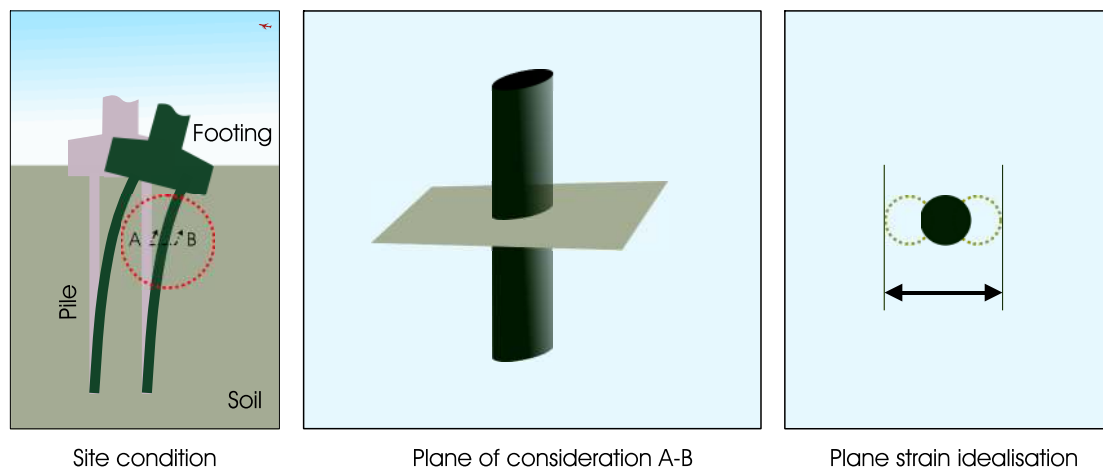
Figure 4.1: Plane strain idealisation of pile-soil interaction in the shaking table test.

4.2.2 Test conditions

A series of twenty tests were carried out, from which five representative cases are described here (see Table 4.1). The other fifteen tests were repetitions of the given five tests; in some

cases there were small variations in model input parameters, and thus are not discussed here. Some preliminary tests were carried out before the main tests to characterise the ambient conditions. These are described in section 4.6.2. The requirements of the test conditions were as listed below.

1. The test box had to be water tight and filled with fully saturated sand.

2. The sand needed to be liquefied before starting the pipe pulling test.

3. An instrumented pipe was required to move in the soil with a desired velocity.

4. Instrumentation to measure the soil resistance over test pipe and also to record any PWP variation at the front and back of the pipe during the test.

4.3 Scaling laws

It is difficult to extrapolate the $1-g$ test results to macro behaviour due to the low stress levels, unless proper scaling laws are implemented. The present study was primarily investigating the phenomenological mechanics of lateral resistance of liquefied soil. The results were analysed in model scale with following non-dimensional parameters derived to compare the test results with other available test results.

Lateral resistance of soil

The lateral resistance of soil was scaled to normalised p as mentioned in section 3.2.3. The normalised p in terms of measured total lateral force on the model pipe (F_p) can be written as in Equation 4.1.

$$\frac{F_p}{\gamma' h L_p D} \tag{4.1}$$

where, γ', h, L_p and D are defined as effective unit weight of soil, depth of consideration, length of the model pipe and diameter of the model pipe respectively.

Pipe displacement

Similar to the normalised pile deflection as mentioned in section 3.2.3, the test pipe displacement (y) was normalised with pipe diameter (D) as Equation 4.2.

$$\frac{y}{D} \qquad (4.2)$$

Velocity of pile vibration

The velocity of the model pipe (V) in liquefiable soil was normalised by the permeability of soil (K) as Equation 4.3.

$$\frac{V}{K} \qquad (4.3)$$

4.4   Model description

A typical test setup is shown in Figure 4.2, different parts of which are referred to as the superscripts in the text. The container[f1] filled with saturated sand was placed over two slider beams[f4] and connected to an actuator[f6] at the base. The plane of pile-soil interaction at a particular depth was modelled with plane strain idealisation by a pipe[f5] of 60mm diameter. The pipe was held in place with two stainless steel rods[f10] hanging from the top sliding platform[f2]. Two load cells were connected to these rods to measure the nett lateral force on the pipe from the soil. The pipe was moved back and forth by an actuator[f3] mounted on top of the container. The top sliding platform[f2] was designed to connect to the actuator and also to hold the pipe at required level inside the container. Real time movement of the pipe and top actuator was measured by a position transducer[f9] fitted on top of the container.

The working principle of the test setup is schematically demonstrated in Figure 4.3. While the base shaking was causing the sand to liquefy, the top actuator was making the pipe to move in a desired velocity. The pipe was instrumented with two pore pressure
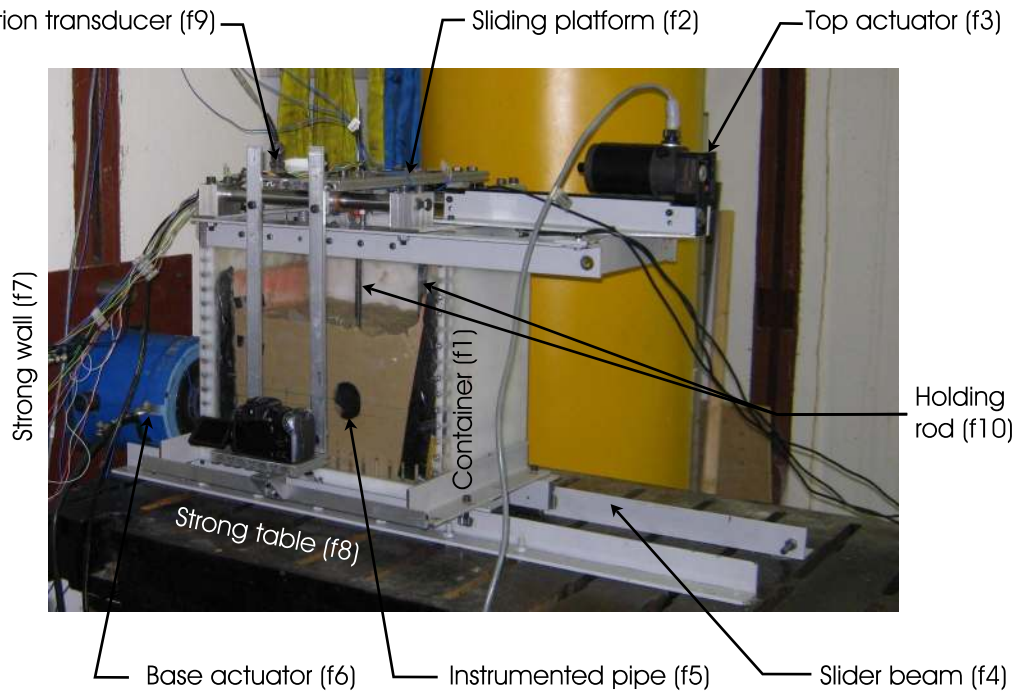
Figure 4.2: A typical $1 - g$ test setup used in the pile-soil interaction study.

transducers at its front and back. Two sets of electrodes were also fitted to it to measure density change around it by electrical resistivity tomography (ERT). The details of the application of ERT in experiments are given by Dash *et al.* (2010b). The results of ERT are not within the scope of this thesis. The pipe was positioned in the container 120 mm from the bottom. A water supply unit was fitted at the bottom of the container with an inlet at the top. Deionised water with 0.1% NaCl (99.8% pure salt) was used to saturate the sand. The salt was added to the water to have a better electrical conductivity, which was useful for ERT measurements. Table 4.1 presents the test conditions for the five considered test cases. The major components of the test setup are described below in detail.

4.4.1 Sand

In all the tests, Red Hill Amber (RHA) sand was used. This was a sub-rounded silica sand with average grain size of 216 microns whose geotechnical properties are presented in Table 4.2. The grading curve of this sand is plotted over the grain size distribution plot for liquefiable soils, as shown in Figure 4.4. The figure shows that the RHA sand falls
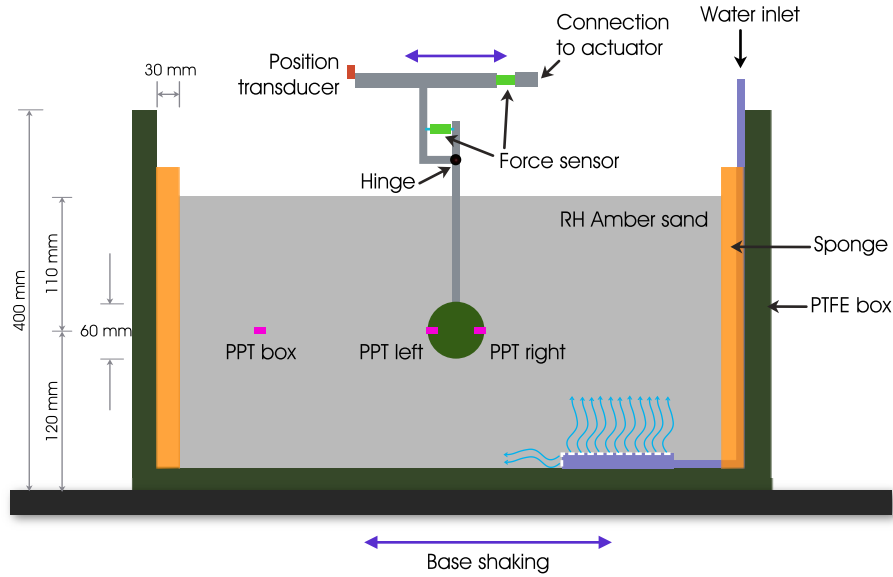
Figure 4.3: Schematic of the test setup and instrumentation.

Table 4.1: Test conditions for lateral resistance of liquefied soil to pipe pulling (Negative r_u value means generation of negative pore water pressure).

Test ID	Base Shaking	Velocity of pipe pulling (V)	Normalised pipe velocity (V/K)	Max (+ve and -ve) $r_u(\%)$	Initial D_r of soil, (%)	Effective unit weight of soil, γ' (kN/m³)
STT1	No	4mm/s	2.7e3	0	54.3	7.895
STT2	Yes	100mm/s	6.7e4	55 to -30	45.3	6.158
STT3	Yes	100 to 180mm/s	6.7e4 to 1.2e5	25 to -25	47.5	6.291
STT4	Yes	225 to 270mm/s	1.5e5 to 1.8e5	50 to -45	58	8.704
STT5	Yes	270 to 280mm/s	1.8e5 to 1.87e5	45 to -45	50.4	6.494

within the zone of most liquefiable soils and therefore considered suitable for this study.

Table 4.2: Geotechnical properties of RH Amber sand.

Property	Symbol	Value
Specific gravity	G_s	2.65
Friction angle	ϕ	30°
Maximum void ratio	e_{max}	0.91
Minimum void ratio	e_{min}	0.63
Densest bulk density	ρ_{dense}	1630 kg/m³
Loosest bulk density	ρ_{loose}	1390 kg/m³
Permeability with water	K	$\sim 1.5 \times 10^{-6}$ m/s
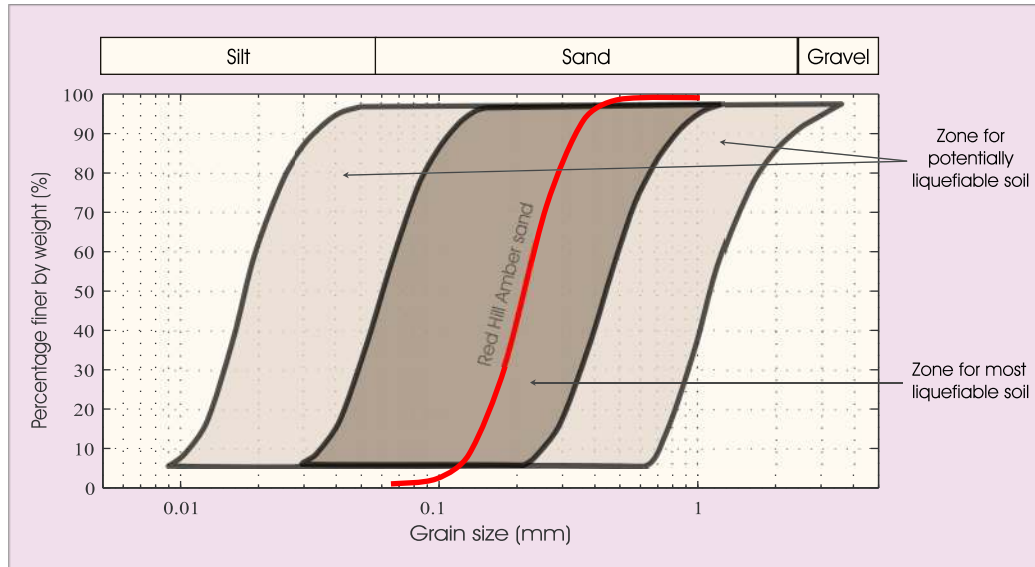
Figure 4.4: Grain size distribution for liquefiable soils suggested by Tsuchida, 1970 (Source: Xenaki & Athanasopoulos, 2003). Grading curve for Red Hill Amber sand is shown in red.

4.4.2 Container

The model container used in this study was a watertight box with inside dimensions of 450mm (width), 240mm (breadth) and 400mm (height). The front face of the box was made up of a transparent Perspex sheet (25mm thick) to observe the soil flow around the pipe during the test. All other sides of the box were PTFE (poly-tetra-fluoro-ethylene) sheets of 25mm thick. Both the materials used in the box are strong, light weight and good electrical insulators. The design of the container was rigid, so flexible boundaries were installed on two inner side walls of the box as described in section 4.4.6 to increase the shear strain in the soil to liquefy it.

4.4.3 Actuators

Two electro-mechanical actuators ($f3$ and $f6$ in Figure 4.2) were used in the test setup. Close up photographs of both actuators are shown in Figure 4.5. The base actuator[1] was capable of high frequency and low amplitude vibration, whereas, the top actuator was capable of low frequency and high amplitude vibration. The top actuator was N-series

---

[1]Being an old actuator it's manufacturer information was not available.

electric cylinder[2] type with maximum thrust of 977N. Both the actuators work in DC. The maximum voltage rating for the bottom actuator was 24V, and for top actuator was 160V.

(a) Base actuator

(High frequency Smaller stroke length)

(b) Top actuator

(Low frequency longer stroke length)
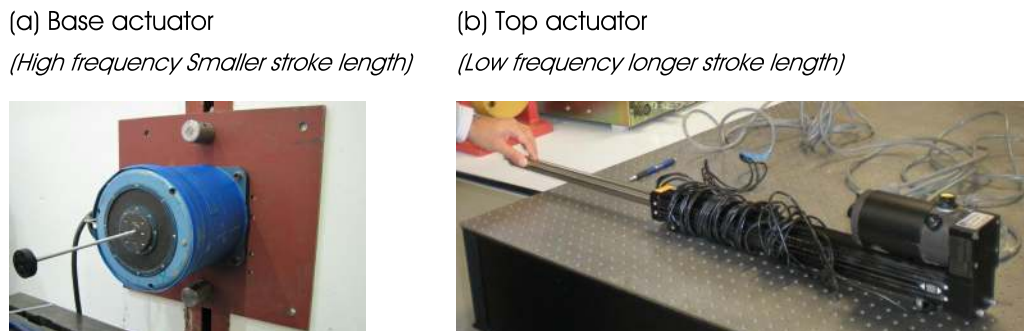
Figure 4.5: Base and top actuator used in the test.

4.4.4 Top sliding arrangement

A sliding arrangement was designed to hold the instrumented pipe in position and allow it to move horizontally by the top actuator. Figure 4.6 shows the sliding arrangements in detail. The arrangement uses three points bearing over two side rods to avoid a bearing jam in the event of slight misalignment. The instrumented pipe was hanging down from the sliding plate with two stainless steel rods. These rods were covered with electrical insulation tapes to avoid interference with ERT measurements during the test. Two force sensors were fitted to the holding rods that measured the soil resistance on pipe during the test. Calculations for the total force on the pipe from force sensor readings are described in section 4.6.2. A position transducer was attached to the container and used to measure the movement of the sliding plate, which was same as the pipe movement.

4.4.5 Instrumented pipe

A nylon pipe of 60mm external diameter and 6mm thick was instrumented with two pore pressure transducers, one at front and one at back, and two sets of electrodes. Figure 4.7 shows the left side of the instrumented pipe, where six electrodes and a PDCR 80 (PPT-Left as in Figure 4.3) can be seen. On the other side of the pipe, another PDCR 80 was

---

[2]IDC (Industrial Device Corporation, Novato, CA, www.idcmotion.com) Electric Cylinder Model, NH-105B, IND006, Serial No: 9809 023265, Rated Voltage 160V, Rated Current 8A.
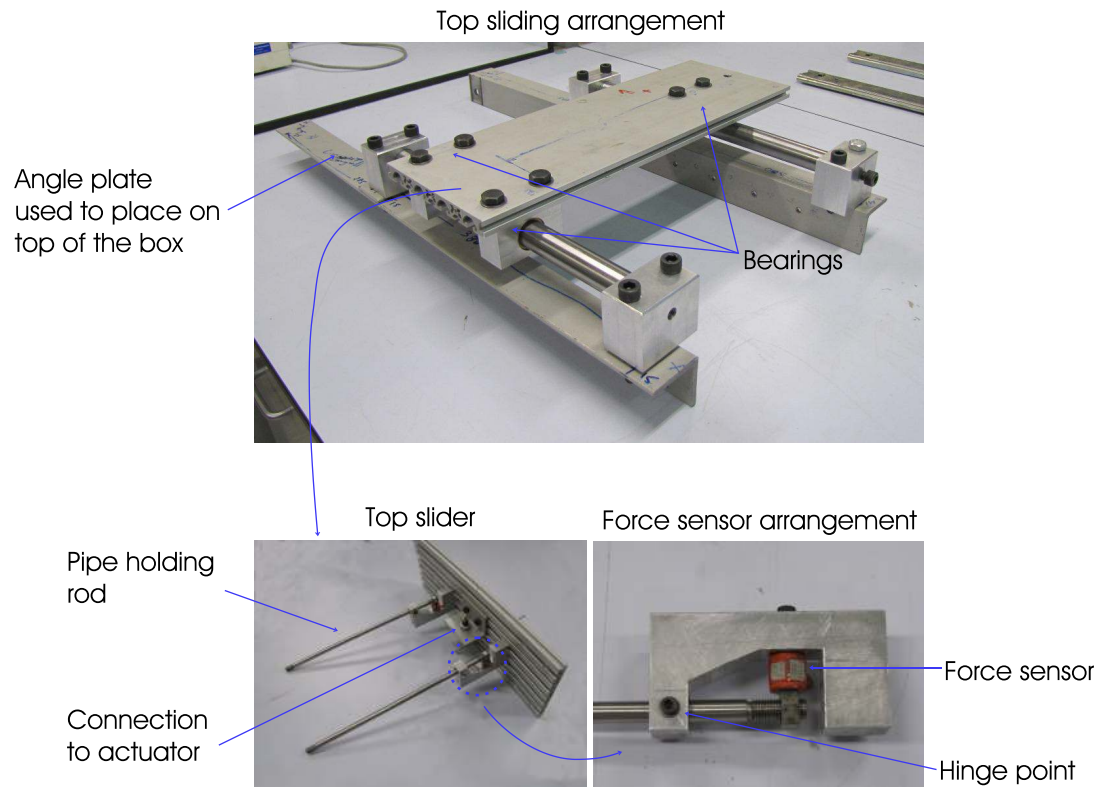
Figure 4.6: Top sliding arrangement.

there at the centre and a set of six electrodes as shown in the Figure 4.7. The non-metallic pipe material was chosen to avoid interference with electrical resistivity measurements at the surface of the pipe. Foamed neoprene sheets were put on both ends of the cylinder for soft and sticky contact with the side of the container (see the black neoprene sheet visible at the end of the pipe in Figure 4.2). The pipe ends were flush to the inside walls of the container. These neoprene sheets were used here to prevent sand particles and water migrating from one side of the pipe to other during the test through the gap between pipe and side walls of the container.

4.4.6 Boundary modelling

Boundary conditions are highly important in physical models in soil, and especially during wave propagation problems where the boundary can seriously alter the wave field in the soil. In practice, three types of containers are generally used in model tests, such as: (a) laminar shear box, (b) equivalent shear beam (ESB) container, and (c) rigid box with shock absorbing materials at the end. Although each method of modelling the soil
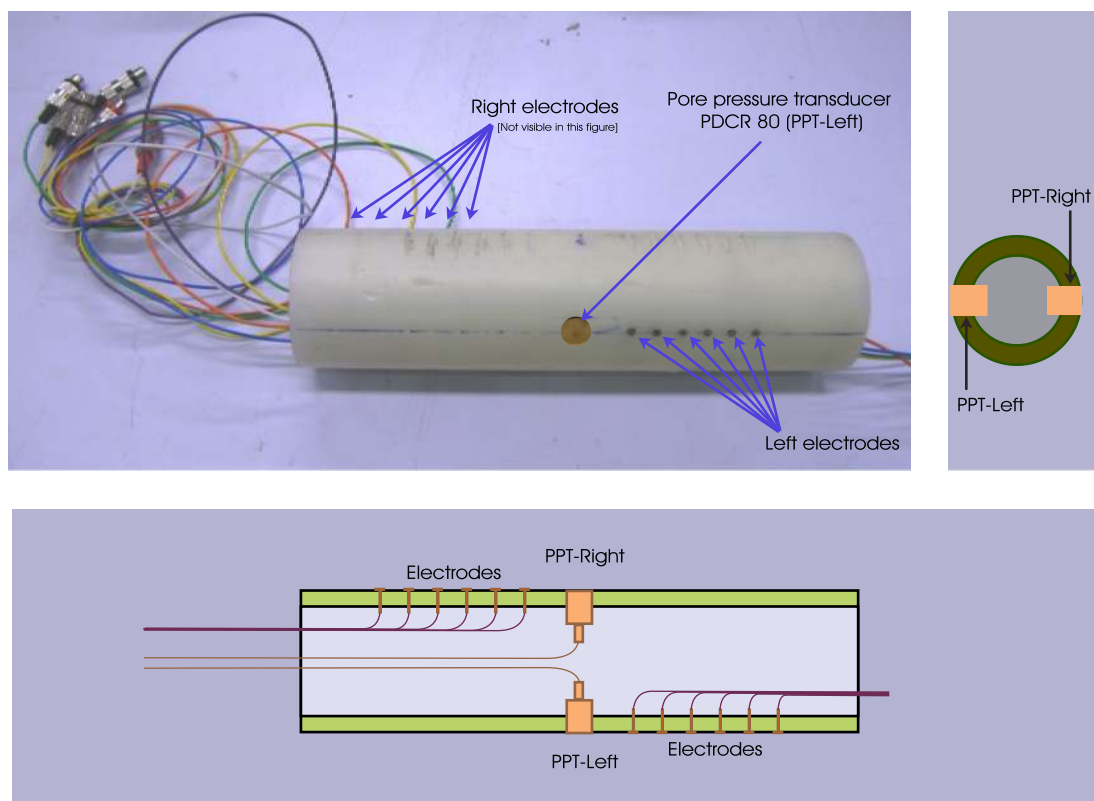
Figure 4.7: Instrumented Pipe.

boundary has certain limitations, they are used in experiments according to the test requirements. In the present study, the third method was adopted.

Initially the rigid box was used without any shock absorbing materials at the ends. Preliminary tests on the container with saturated sand of $D_r \approx 50\%$ showed that the shear induced due to base shaking was not sufficient to cause liquefaction of the sand due to the rigidity of the boundary. Hence to add shear deformation at the boundaries, two sponge pieces were attached to each of the shorter-dimension sidewalls. The sponge on each side was 3cm thick at top and 6cm at bottom in the empty tank, which became about 3cm thick throughout the depth once the tank was filled with sand (Figure 4.3). A similar use of sponge at the ends of a rigid container was also implemented by Ha *et al.* (2011) during liquefaction study on shaking table tests.

4.5 Instrumentation

4.5.1 Accelerometer

A high sensitivity general purpose ICP® (Integrated Circuit Piezoelectric) accelerometer[3] as shown in Figure 4.8(a) was installed at the bottom of the container to measure base acceleration. The accelerometer sensitivity was 100mV/g and it could measure up to 50g.

4.5.2 Position transducer

A precision cable-extension position transducer[4] as shown in the Figure 4.8-b was used to measure the displacement of test pipe. The transducer signal was also used to control the top actuator using a closed feedback loop, which will be discussed later in section 4.6.1. The transducer had a full stroke range of 0 - 635mm. It had been calibrated with a straight line fit to the data points of known displacement inputs. The linear region of the fit gave the calibration constant for the transducer as 28mV/mm.

4.5.3 Force sensor

Three force sensors[5] as shown in Figure 4.8c were used in the setup. Two were fitted to the pipe holding rods (Figure 4.6) to measure the force on pipe. The third was fitted in series with the top actuator (Figure 4.3) as a safety feature to prevent the actuator exceeding it maximum capacity. These sensors could measure up to 2.224kN in compression and tension, and their sensitivities were 2.36mV/N for the front rod sensor, 2.329mV/N for the back rod sensor and 2.341mV/N for the actuator sensor.

4.5.4 Pore pressure transducers

Two Druck® PDCR-80 miniature Pore Pressure Transducers (PPTs) were used at the front and back of the instrumented pipe to measure positive and negative pore water pressures. The measured values were used to represents the state of liquefaction around

---

[3]Manufactured by PCB Piezotronics, Serial no: 26285
[4]Manufactured by Celesco®, model no. PT101
[5]Manufactured by PCB Piezotronics ICP®, model no: 208C30
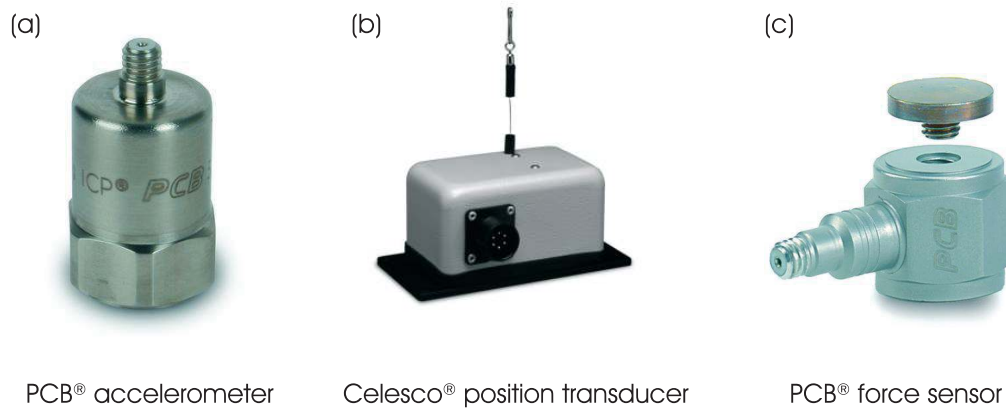
Figure 4.8: Accelerometer, position transducer and force sensor used in the test setup.

the pipe. These PPTs were flush to the pipe surface so as to cause minimum disturbance to the soil flow around the pipe.

The PPTs were rated with 17.24 kPa (2.5 psi) range for a maximum input of 10V. A typical PDCR-80 PPT and its dimensions are shown in Figure 4.9. The pore water pressure is measured by the flexible silicon diaphragm present in front of the PPT. The diaphragm is protected from the surrounding soil by a ceramic filter at its front that allows only the pore fluid to get into the PPT. If there is any entrapped air in the top ceramic filter it will give erroneous readings. To avoid this, the PPTs were saturated and calibrated prior to their installation in the saturated soil. A complete saturation prior to their use was very important to get reliable measurement of negative pore water pressure (Take & Bolton, 2002).

A schematic showing the procedure and experimental setup for PPT saturation is presented in Figure 4.10. This was carried out in a small airtight chamber as suggested by Take & Bolton (2002). This procedure involved two major steps; a) taking out the entrapped air completely from the PPT, and b) saturate it fully with pore fluid (de-ionised water in this case). The PPTs were prepared as follows.

Both PPTs were placed in a single airtight saturation chamber as shwon in Figure 4.10b. The saturation chamber had been half filled with de-ionised water and connected to a vacuum pump (for schematic see Figure 4.10a, Step-1). Initially, the transducers were kept above the water level. A negative pressure of 15kPa was applied to the chamber by a
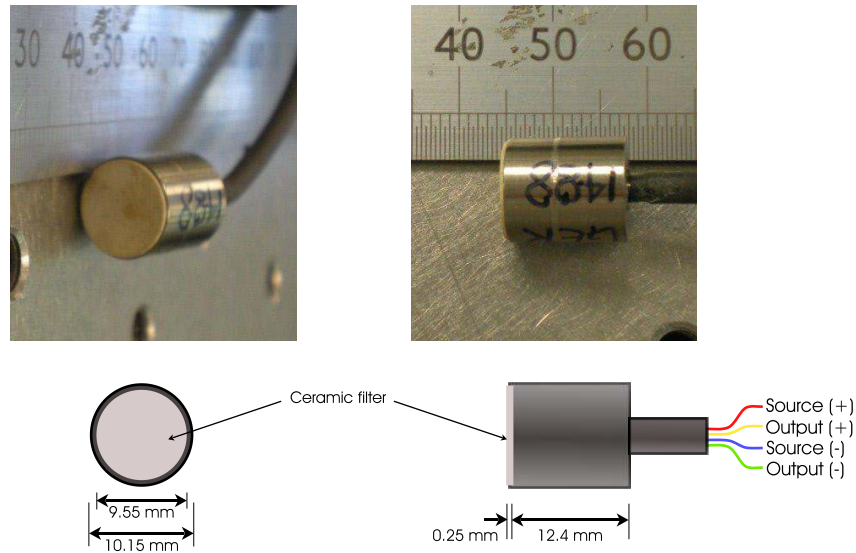
Figure 4.9: Schematic of PDCR 80 Pore Pressure Transducer.

vacuum pump and the PPT readings were amplified by a DC amplifier and continuously monitored using a signal monitoring unit. The PPTs took about 15 minutes to attain a constant pressure reading, which ensured that the ceramic filter and the gap between it and the diaphragm was almost air free. The saturation chamber was then tilted 90° allowing the transducers to be immersed in the water while it was still under negative pressure (for schematic, see Figure 4.10a, Step-2). This allowed the water to enter the void spaces of the transducer. The transducer readings were continuously monitored. It took about two and half hours to attain complete saturation.

After saturation procedure, the same setup was used to calibrate the transducers. Known negative pressures were applied (within 15kPa range) using the vacuum pump and positive pressures were applied by a static water head (for which the vacuum pump was turned off). The calibration curve between the applied pressures and the PPT readings was found to be linear and repeatable both in the positive and negative zones, which confirms that the PPTs were in good condition. The PPTs were then installed on the test pipe under water and kept in water until they were mounted in the sand box (this was to keep the PPTs saturated). The pressure ranges of the PPTs (17.5kPa) covered the range of pore water pressures expected to be measured during the tests.

Another general purpose PPT, PDCR-830, was used to measure pore water pressure of the soil away from the pipe (see Figure 4.3). This PPT did not have a porous stone,

instead, it was fitted with a stainless steel filter cap. Hence, it did not require presaturation before installation. The reading measured by this PPT was considered as the far field PWP measurement.
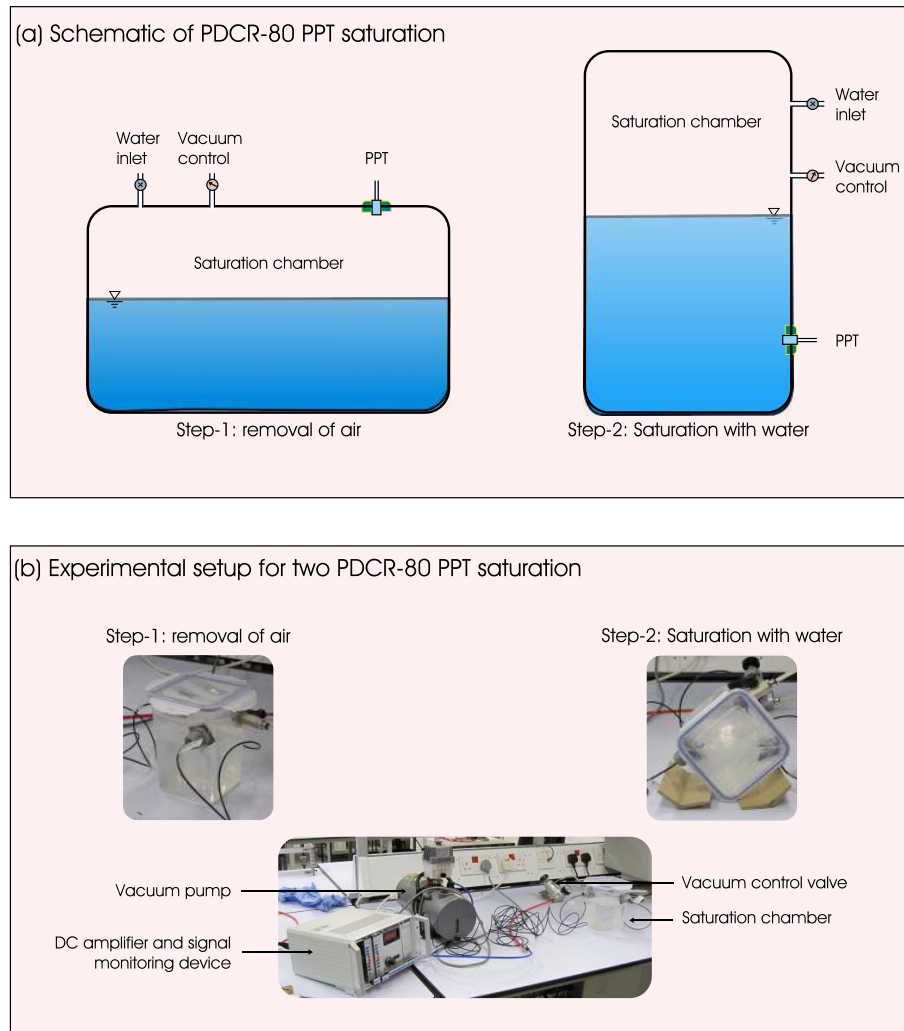
Figure 4.10: PPT Saturation procedure, (a) Schematic and (b) experimental setup.

4.5.5   Signal conditioning and data acquisition system

An independent data acquisition and test control setup was prepared for this experiment. A dSpace® board fitted to a computer was used with Simulink® for data logging and also to control the actuators. For the execution of real-time testing, a Simulink model was prepared and controlled by an interface software environment called ControlDesk®. A 20 channel A/D and 8 channel D/A connector was used for establishing connections between instruments and the dSpace® board. Figure 4.11 shows the data acquisition and test

control unit used in the test. DC amplifiers were used for force sensors, accelerometer, pore pressure transducers and displacement transducer to amplify the recorded signal and to minimize the noise.
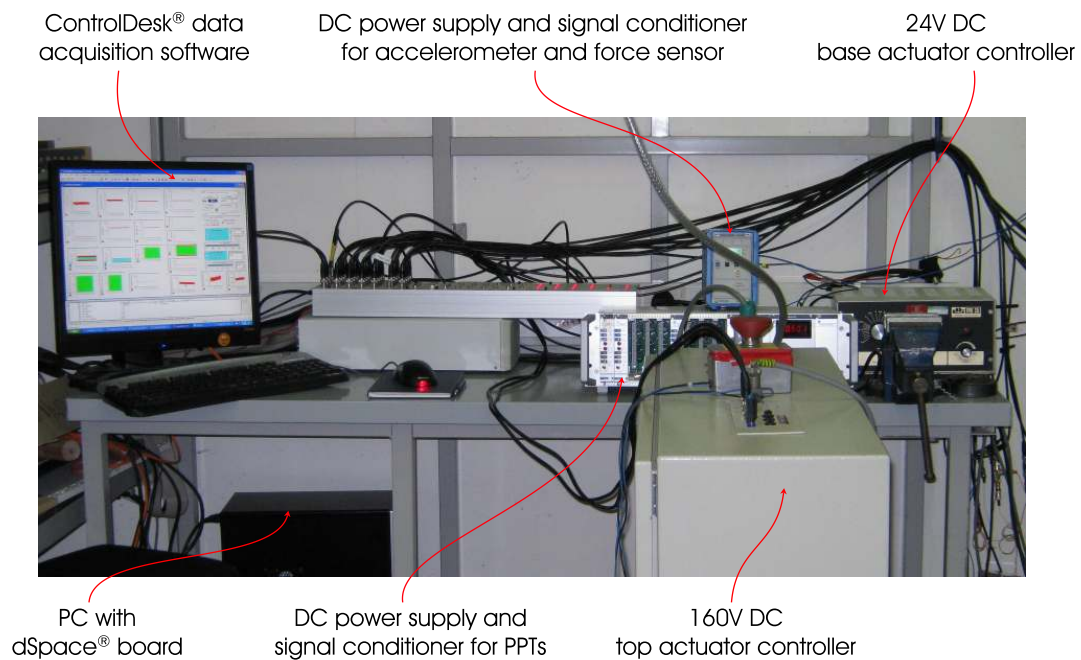
Figure 4.11: Data acquisition and signal conditioning system.

4.6 Test control

4.6.1 Actuator control

The lower actuator, used to induce base shaking, was controlled by an independent 24V DC power supply unit which was capable of changing the amplitude and frequency of the input signal.

During the cyclic loading of the pipe by the top actuator, symmetrical triangular waves were applied to achieve a constant velocity of pipe. The velocity of the pipe movement, V, was ranging from 100mm/s to 280mm/s. During slow monotonic loading of the pipe by the top actuator, the velocity of pipe was 4mm/s.

The upper actuator displacement, which had to be precise as it directly controls the pipe movement, was controlled by the dSpace® board with a real-time closed loop feedback circuit. The feedback circuit received the actuator position at each time step obtained externally from the position transducer. Figure 4.12 shows a typical desired

versus obtained value of displacement and velocity from the top actuator. It is very difficult to obtain the exact match between desired and obtained values, however, the precision obtained was considered acceptable for the tests. Over tuning of the actuator was avoided, which could have produced local oscillation and affected the smooth transition of velocity direction.

The upper actuator was fitted with an elastomeric spring inside to avoid potentially damaging actuator jams, which sometimes arises when the motor of the actuator is accidentally commanded to move towards a hard end stop. The position transducer, which was monitoring the actuator displacement, was used as an additional safety measure to prevent this situation. The position transducer reading was used to decelerate the actuator movement when it crosses the set safety limit, which was within the maximum and minimum possible shaft position of the actuator.

Another safety measure was implemented by installing a force sensor in front of the actuator. If any condition, either due to jam of the top sliding unit or very high resistance to pipe movement, that imposes more thrust to the actuator that it can bear, the motor of the actuator can get damaged. To avoid any such situation, the force sensor reading was used to stop the actuator if it was subjected to higher force than allowed.

4.6.2   Test sequence

After the test setup was instrumented but without sand in the box, the model pipe was installed and a few pre-test runs were performed. As the ends of the test pipe were flush to the container walls, resistance due to friction on both ends of the pipe was expected. The total end frictional resistances (F_{sp1}+ F_{sp2} in Figure 4.14) were measured for various velocities of pipe movement. The measurements were obtained at intermediate cycles, after leaving few initial cycles of pipe movement, to obtain consistent values over a number of cycles. The pipe ends were wetted to get the best possible estimation of end resistance that would arise during the test when container was filled with saturated sand. Figure 4.13 shows the measured total side resistance for different pipe velocities. The higher was the pipe velocity, the lower was the end frictional resistance, and it was varying between 4 to 10% of the total force on pipe. A power curve trend-line was fitted to the measured
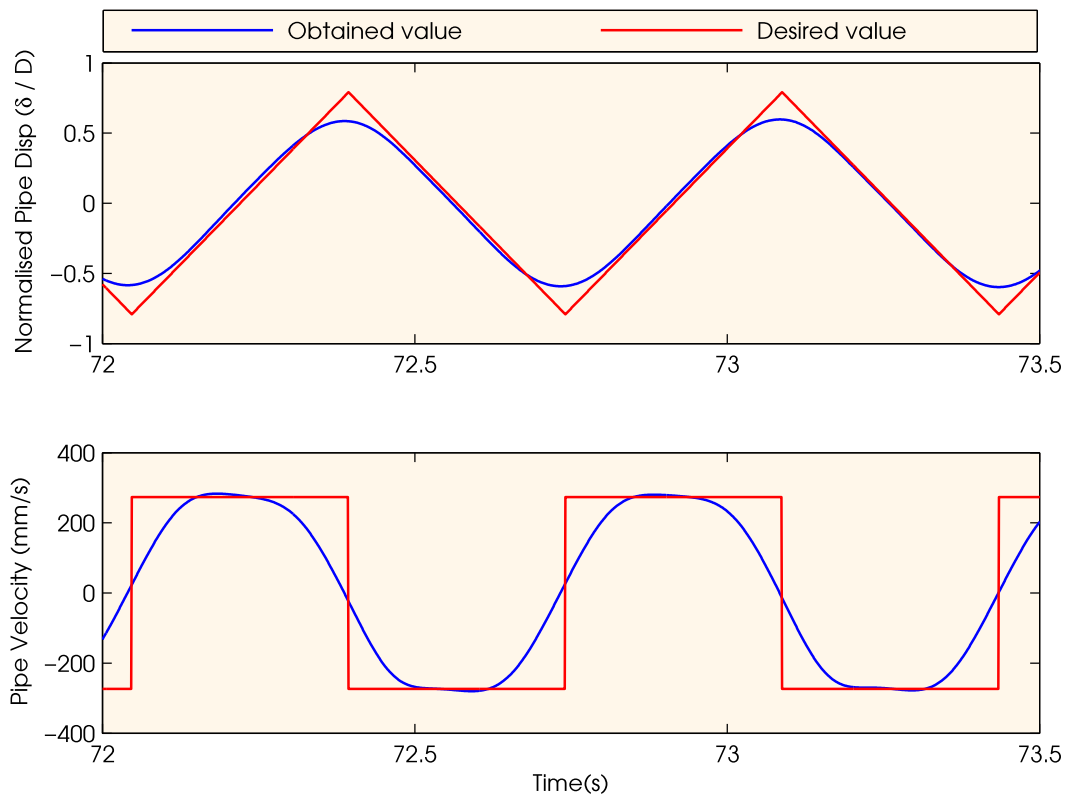
Figure 4.12: Typical top actuator performance, desired value versus obtained value of pipe velocity and displacement from Test STT-5.

data which allowed carrying out interpolation and extrapolation.
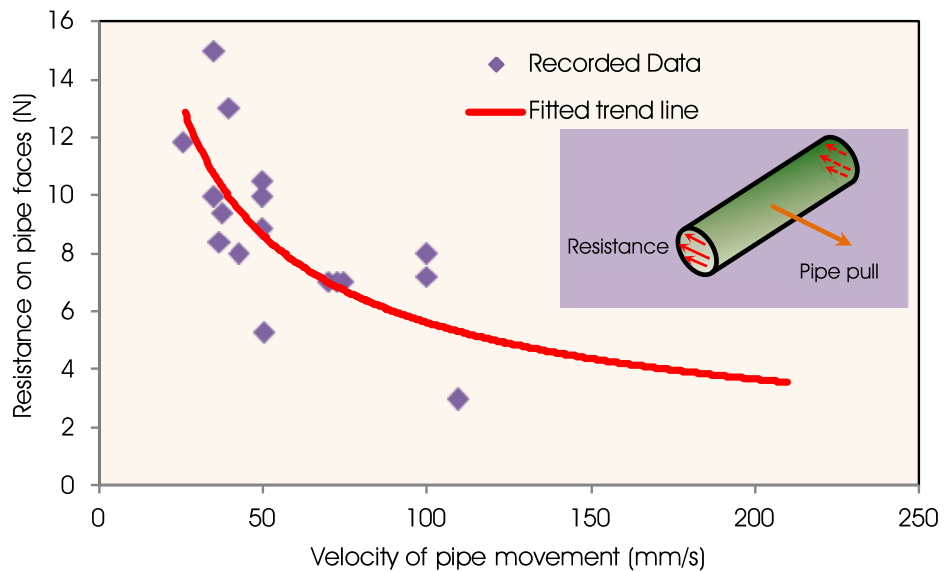
Figure 4.13: Ambient frictional resistance of the pipe from inside wall of the box ($F_{sp1} + F_{sp2}$).

After the pre-test runs, the model pipe was taken out of the container and instru-

mented with two sets of electrodes and the two PDCR 80 PPTs. The instrumented pipe was then kept under water until its installation inside the container. The container was then filled in two phases. Initially, dry sand was poured in the box loosely to a level 120mm above the base. Water was then slowly fed into the sand though feed pipes from the base of the container. Once the soil was saturated, the instrumented pipe assembly was taken out of water and fitted into position. Then the next section of the container was filled with loose sand and saturated with the water supplied through the base. Once the container was filled with saturated sand, a small amplitude base shaking was applied for 2-3 seconds to ensure that the sand did not contain any entrapped air. This, however, did densify the sand slightly but not significantly. The average initial values of effective unit weight and relative density of the sand in the container during each test were estimated and are given in Table 4.1.

A few tests were then carried out to check the development of pore pressure in the box for different frequencies and amplitudes of base shaking. The tests had shown better performance in terms of generating pore water pressure and maintaining it with a base acceleration of about $0.3g$ at 4Hz frequency. As the test setup allows drainage at the surface, pore water pressure dissipation was very quick and hence the tests could only sustain fully liquefied condition for a very short time, only about 2-3s. However, with continual base shaking at different amplitude, a range of partially liquefied soil was simulated.

4.6.3 Measurement of soil resistance

During the tests, the total force on the pipe was measured using the two force sensors. The estimated end friction was deducted from the total force measured to obtain the sand resistance, F_p. Equation 4.4 was used to obtain this.

$$F_p = (F_{s1} + F_{s2}) \times \frac{l2}{l1} - (F_{sp1} + F_{sp2}) \qquad (4.4)$$

where, F_{s1} and F_{s2} are the forces recorded with force sensor 1 and 2 respectively. $F_{sp1} + F_{sp2}$ are the average expected resistance over two pipe faces for the considered velocity of pipe movement. The procedure of obtaining F_p has been shown schematically

in Figure 4.14.
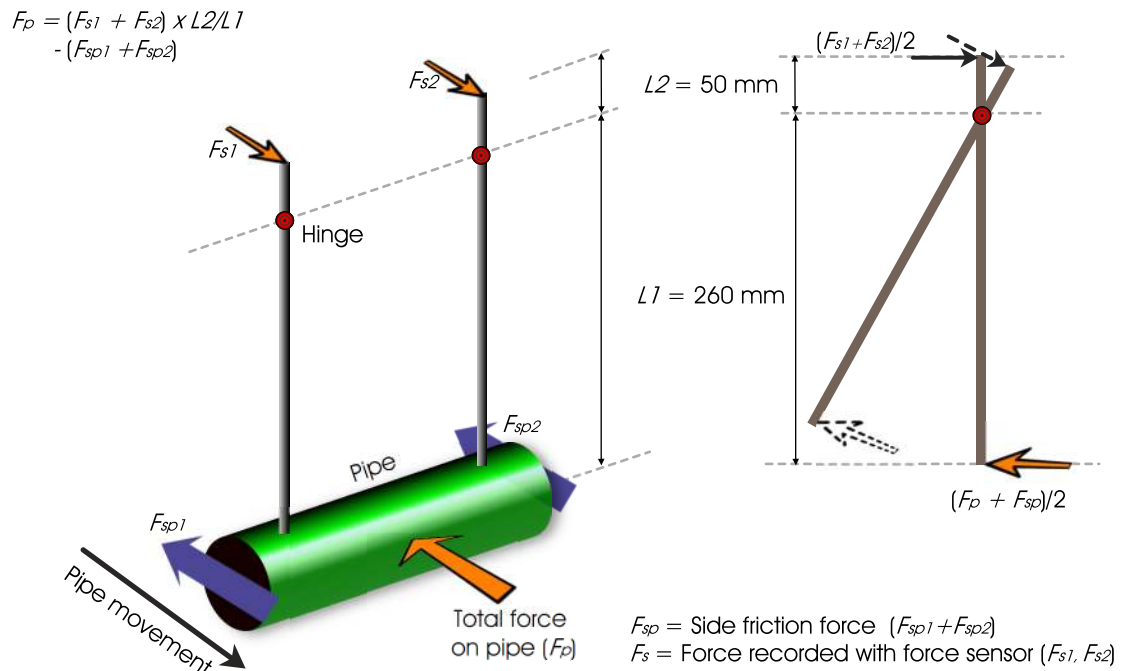
Figure 4.14: Schematic showing estimation procedure of total soil resistance on pipe.

4.7 Test results

The soil resistance for various rate of pipe movement was recorded and normalised as discussed in section 4.3. To avoid unwanted high frequency noise from the recorded signal, a low pass filter was used with a cut-off frequency of 20Hz.

The degree of liquefaction is represented by the excess pore water pressure ratio (EPWP) ratio, r_u, as defined in section 2.3.1. The tests showed different values of EPWP near to the pipe and in the far field. To characterise the soil resistance for different r_u, the value near to the pile was chosen to be more representative of the situation. As the r_u values were different at front and back of the pipe, both r_u values were used to represent the state of liquefaction for the corresponding cycle of pipe displacement, for example see the legends of the Figures 4.17 to 4.20.

4.7.1 Change in pore water pressure around the pipe and in the free field

Figure 4.15 shows the results of the monotonic pipe pulling test (see STT1 in Table 4.1) in saturated soil without base shaking. When the pipe was pulled, it compressed the soil at its front and in turn generated pore water pressure, which can be seen in the figure as PPT-Left. At the rear of the pipe, in contrast, no pore water pressure was generated initially, which can be seen in the figure as PPT-Right. Due to the presence of the dissipation boundary at the soil surface, the pore pressures generated at the pipe front was not sustained for long and began to dissipate after 8 seconds. The pore pressure continued to decrease even below the initial overburden pressure, which can be seen as negative r_u, after 10 seconds. The pore pressure generated at the far field was lower than that near to the pipe as the only source of pore water pressure generation was pipe displacement. The soil in front of the pipe was compressed and resulted in heaving of the ground, which caused the r_u to be even lower than the initial pore pressure ratio at the front of the pipe due to increased overburden.

For cyclic pipe displacement as shown in Figure 4.16 for test STT2 (see details of the test in Table 4.1), the pore pressure difference between front and back of pipe was more or less similar but opposite in sign. It was very difficult to carry out cyclic pipe pulling test in non-liquefied soil due to its very high lateral resistance, which the top actuator was not capable of applying. Hence, the cyclic pipe pulling test was carried out with base shaking. The pore pressure generation and dissipation near to the pipe was due to both base shaking and cyclic pipe displacement. The pore pressure in the soil away from pipe was observed to be more than that near to the pipe. This could be due to the rod holding the pipe providing a dissipative route. While the pore pressure was being generated at the front of the pipe, at the back it was being dissipated, often reaching negative values. At this point, it could not be determined whether the compression at the front of the pipe was the main contributor to the soil resistance or the negative pressure at the back of the pipe or both.

For both monotonic and cyclic loading, the free field pore water pressure showed a very similar pattern to that of the pore water pressure close to the surface of the pipe on
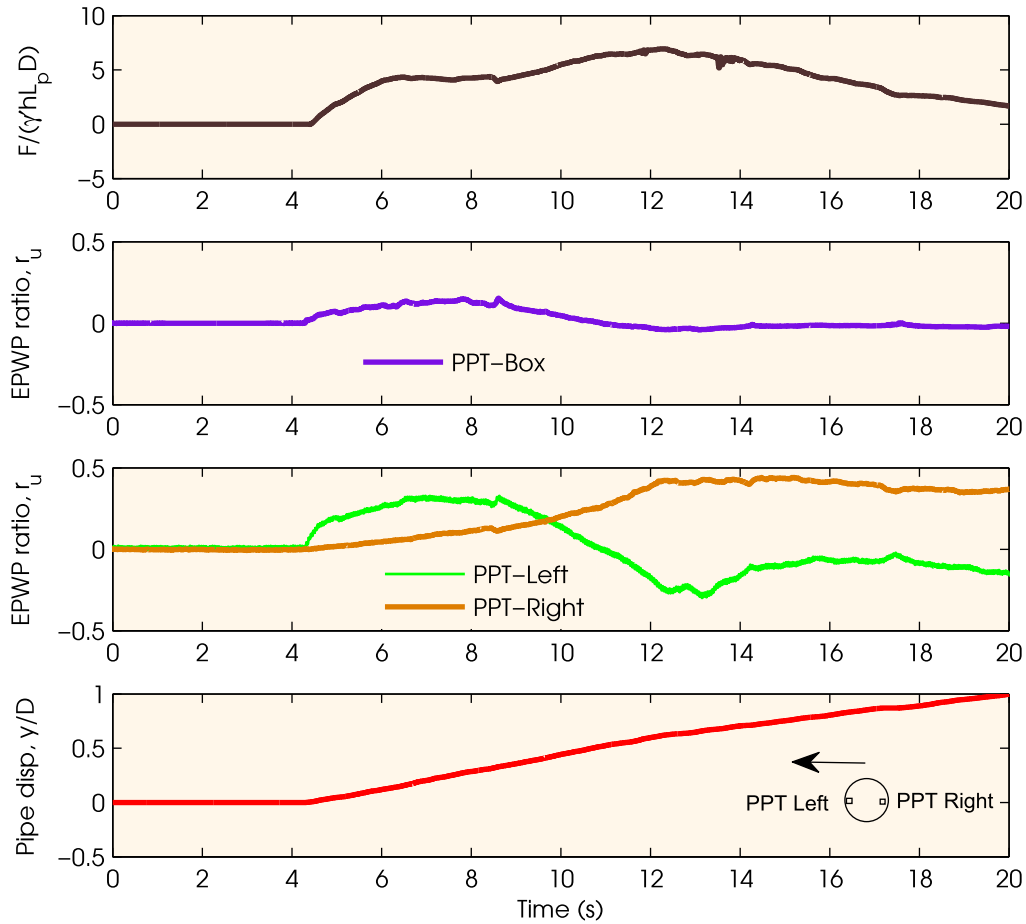
Figure 4.15: Pore water pressure distribution in the front and the back of pipe during monotonic pulling test STT1 (velocity = 4 mm/s).

the same side (PPT-Left).

4.7.2 Effect of degree of liquefaction on $p - y$ curve

In test STT2, the pipe was vibrating at nearly constant velocity of 100 mm/s and the pore pressure was varied by varying the amplitude of base shaking. Figure 4.17 shows the normalised soil resistance versus normalised pipe displacement for different degrees of liquefaction in the sand. This figure essentially represents $p - y$ behaviour in partially liquefied soil in a vertical drainage condition. As expected, the higher the degree of liquefaction the lower was the ultimate lateral resistance of sand. At 20% liquefaction the non-dimensional ultimate resistance was about 6.5 which further reduced to a value of 5 at 25% liquefaction and 3 to 4 at about 50% liquefaction. As the degree of liquefaction
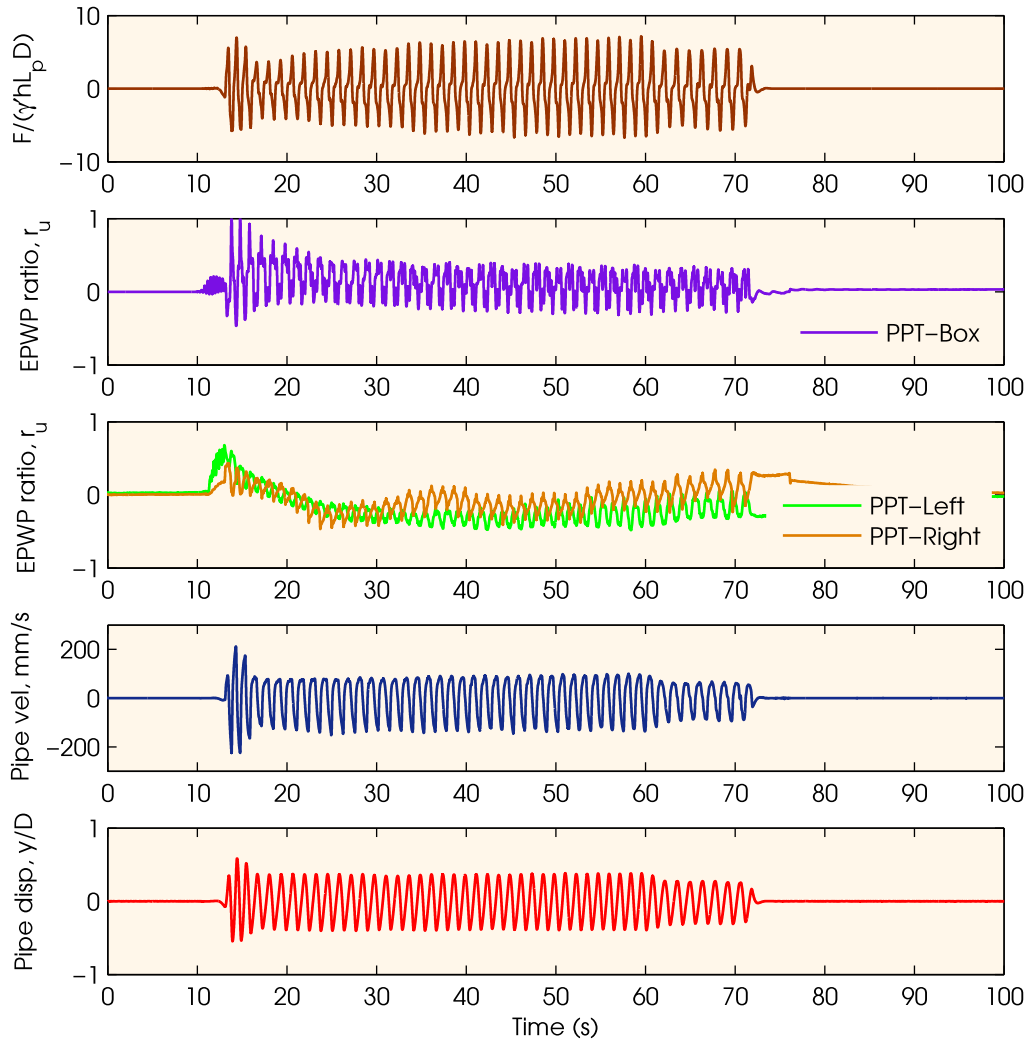
Figure 4.16: Pore water pressure distribution for cyclic pipe pulling test with a constant velocity of 100mm/s during 20s to 60s of test STT2.

increases, the displacement at which soil strength gets mobilised becomes larger. Also the pattern of $p - y$ curve is strain hardening in contrast to the conventional use of a strain softening $p - y$ curve (see section 1.3.1). The API (API, 2000) recommended design value of monotonic $p - y$ curve for non-liquefied soil is plotted in the same figure for comparison. The observed maximum soil resistances for partially liquefied soils were lower than the API suggested value for non-liquefied soil. At 20% liquefaction ($r_u = 20\%$), the observed and API values of maximum soil resistances were quite close, however, the observed initial stiffness was quite small compared to the API curve.
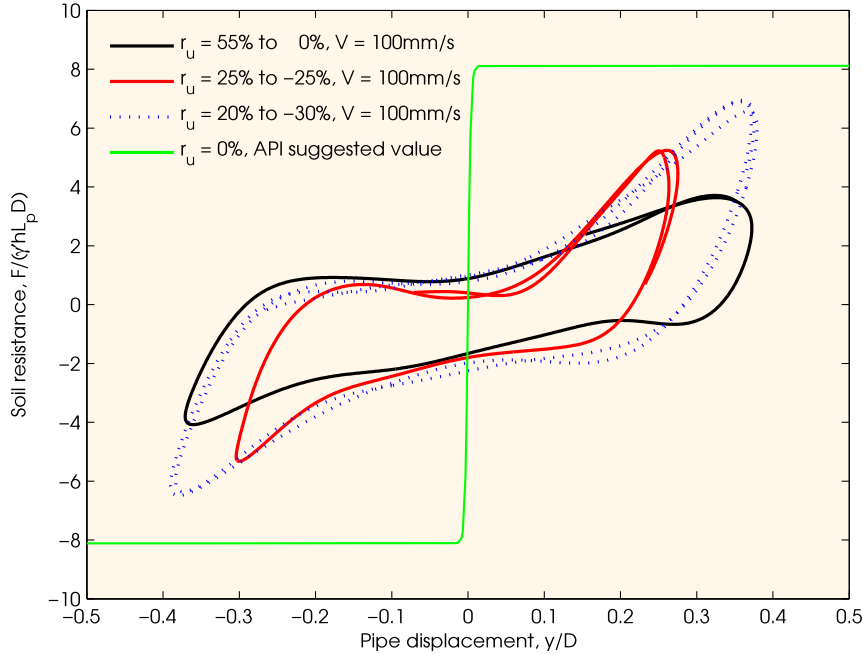
Figure 4.17: Normalised $p - y$ curves with different degrees of liquefaction in test STT-2, $D_r = 45.3\%$.

4.7.3 Effect of loading rate on $p - y$ curve

The rate of loading has been a topic of long discussion in academia due to its implication in whether to consider the liquefied soil as a thick fluid or a loose solid. A set of fast triaxial and model pile tests by Holscher *et al.* (2008) have shown that the loading rate effect is very small, about 5% for the bearing capacity of the saturated and dry sandy soil. However, for fully liquefied soil, Towhata *et al.*, 1999, Takahashi, 2002 have shown that an increase in loading rate increases the strength of the soil significantly. Hence, they have characterised the fully liquefied soil like a thick fluid where a higher rate will give greater drag force. However, for partially liquefied soil, the effect of loading rate could vary depending on the degree of liquefaction. Figure 4.18 shows the normalised $p - y$ curve for partially liquefied soil with 25% degree of liquefaction (r_u) for variable speed of pipe. Although, the r_u near the pipe was changing due to the change in the speed of pipe, its magnitude was not very significant ($< 4\%$) due to this change. At this level of liquefaction the soil was still behaving more like a solid and the change in the pipe velocity had very little influence on the shape and magnitude of the soil resistance. For the change in velocity from 100mm/s to 180mm/s, the difference in normalised maximum

soil resistance was only about 7%.
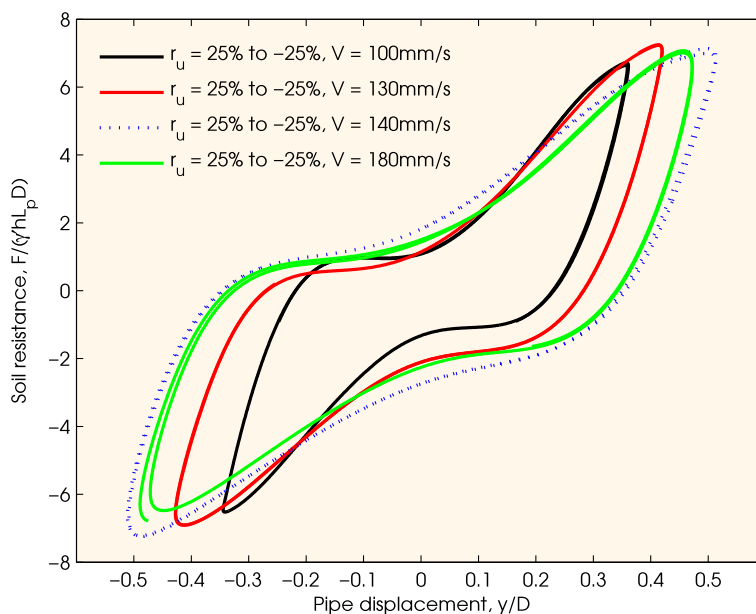
Figure 4.18: Normalised $p-y$ curves for partially liquefied soil with different pipe velocities in test STT-3, $D_r = 47.5\%$.

4.7.4 Effect of both loading rate and degree of liquefaction on $p - y$ curve

In tests STT-4 and STT-5 both degrees of liquefaction and loading rates were varied during the tests. The normalised $p - y$ curve for these cases are presented in Figures 4.19 and 4.20 respectively. These results also show a similar behaviour to Figure 4.18, where the velocity had little influence on the resistance of soil. In Figure 4.19 at an r_u of 30% the loading part of the curve is very similar to API monotonic $p - y$ curve but the mobilizing displacement for full soil strength, 0.4 y/D in this case, is about 4 times larger than API value ($\sim$0.1 y/D). The initial stiffness of $p - y$ curve decreased with increasing liquefaction, however, the stiffness and strength at large displacement were not affected.

4.7.5 Effect of relative density on $p - y$ curve

The normalised $p - y$ curves at different relative densities from tests STT2, STT4 and STT5 were compared as shown in Figure 4.21. The results show that the stiffness of $p - y$ curves both at small and large deflection increases with increased relative density
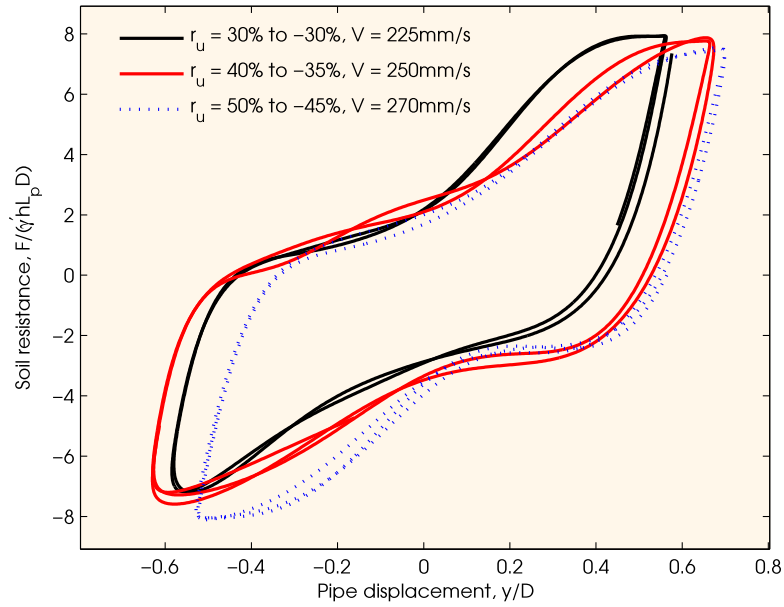
Figure 4.19: Normalised $p - y$ curves with variable degrees of liquefaction and different pipe velocities in test STT-4, $D_r = 58\%$.
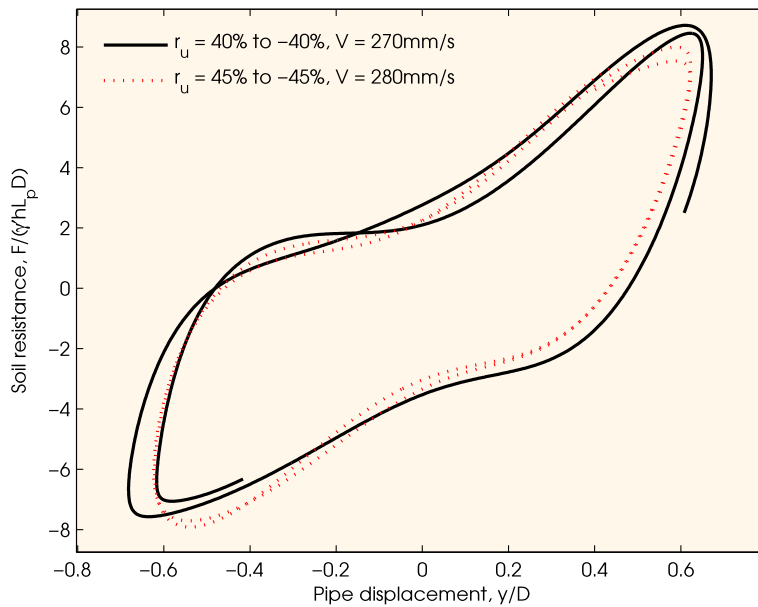
Figure 4.20: Normalised $p - y$ curves with variable degrees of liquefaction and different pipe velocities in test STT-5, $D_r = 50.4\%$.

for comparable levels of liquefaction. At large relative pipe-soil displacement, i.e. about 0.5D, the $p - y$ curve attained the ultimate possible strength as can be seen in the figure for D_r=58%, with the occurrence of flat plateau. However, other two cases, $D_r = 50.4\%$ and $D_r = 45.3\%$, may have required higher levels of displacement to mobilise their full strength.

135
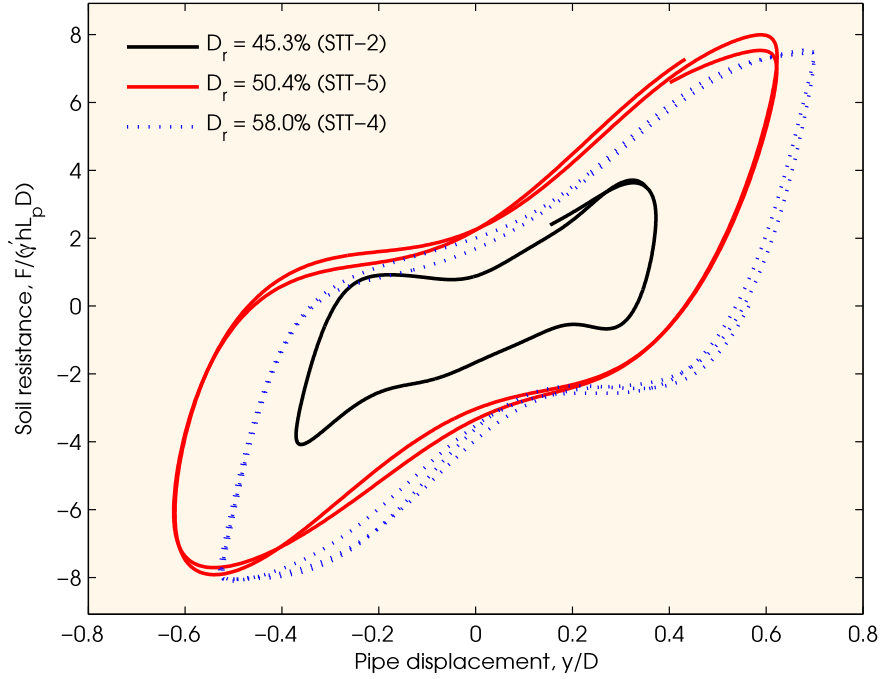
Figure 4.21: Normalised $p - y$ curves for different relative densities at $r_u \simeq 40 - 50\%$.

4.7.6 Maximum resistance of $p - y$ curves with respect to r_u

The normalised maximum soil resistance at different degrees of liquefaction (for positive values of r_u only) for the test cases STT2, STT4 and STT5 are plotted in Figure 4.22. These values are also compared with the design value of maximum soil resistance suggested by API guidelines (API, 2000). From a series of centrifuge tests, Dobry *et al.* (1995) obtained a linear strength degradation pattern for liquefiable soils at different degrees of liquefaction (see Figure 2.30), which is also presented in the figure for comparison. The present test results show degradation in maximum soil resistance for increasing degree of liquefaction (r_u), which are in line with the findings by Dobry *et al.* (1995). For case STT2, the figure shows that at 50% liquefaction the strength degradation is nearly half of the non-liquefied strength suggested by API guidelines (Figure 4.22a). For tests STT4 and STT5, the pattern of reduction in maximum resistance with r_u is also apparent in the Figure 4.22b, however, the magnitude is smaller compared to the API suggested value with Dobry *et al.*'s (1995) linear degradation pattern. To note, the API suggested values are design values and meant to be conservative and generic for all sandy soils in field. The data scatter in Figure 4.22b can partly be attributed to the variations in the mobilised

136

strengths that were achieved in the tests. For example, STT4 seems to have mobilised the full strength, whereas, others did not.
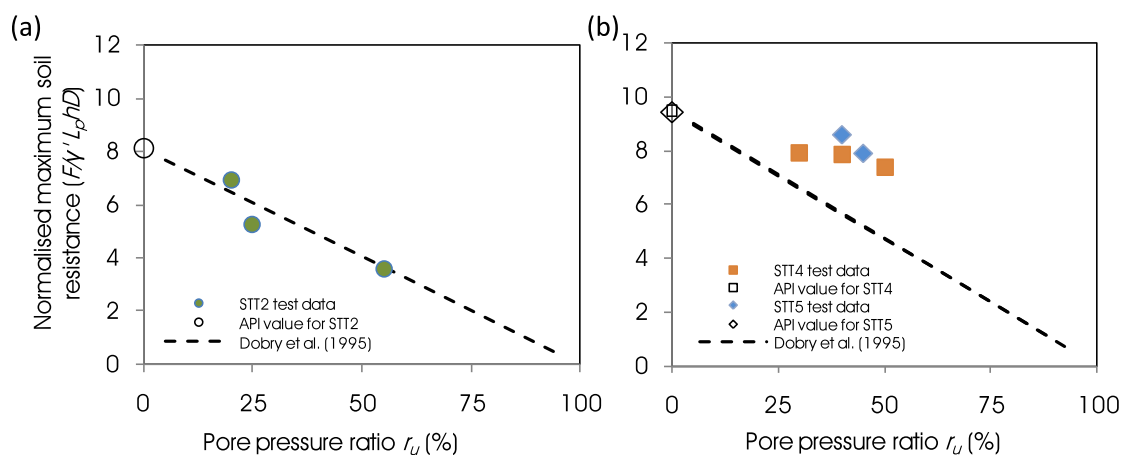
Figure 4.22: Maximum soil resistance for different degrees of liquefaction for tests (a) STT2 ($D_r = 45.3\%$), and (b) STT4 ($D_r = 50.4\%$) and STT5 ($D_r = 58\%$).

4.8   Summary of conclusions

The variation of ultimate soil resistance and the pattern of $p - y$ curve have been studied through a series of $1g$ tests in liquefiable soil, where the pile-soil interaction at a particular overburden pressure was modelled as a horizontal pipe with plane strain idealisation. Although, in field conditions a pile may be subjected to transient flow in the axial direction due to upward dissipation of excess pore water pressure and axial shaft resistance from liquefied soil, these effects are generally very small compared to the effects of lateral loading and as a result the plane strain approach used here was considered satisfactory.

This chapter investigates the change in degree of liquefaction in the soil surrounding the pipe when large relative pile-soil displacement is applied. The tests were carried out at different degrees of liquefaction and different velocities of pipe pulling. The specific conclusions obtained from this study can be summarised as below.

- From the observations in partially liquefied soil (50% liquefied) for different velocities, it can be concluded that the loading rate effect on $p - y$ curves in the tested range of pipe velocities (100mm/s to 280mm/s) was not very significant.

- The observations also confirm that the $p-y$ curve in liquefied soil is strain hardening. All the tests have shown that the initial stiffness is small and it increases with higher pipe displacement. The initial stiffness also reduces with increase in the degree of liquefaction, however, the stiffness at large displacement does not get affected by it.

- The present test results in liquefiable soils show degradation of maximum soil resistance with increasing degree of liquefaction (r_u).

- There is significant difference in EPWP near the pipe and far field, the soil resistance is more representative of the state of liquefaction near to the pipe. However, in a practical situation, estimation of EPWP near to the pile foundation could be quite difficult and hence the design guidelines generally recommend soil resistance based on expected level of PWP in the soil at site without considering pile.

- The experimental setup needs further improvement in terms of higher depth to simulate greater stress level in soil and a better base actuator system that can generate and sustain full liquefaction in soil for required time.

Chapter 5

Stress-strain to $p - y$ curve for fully liquefied soil

5.1 Introduction

Element tests are one of the most important methods used in practice to obtain stress-strain behaviour of soils. From many of these tests on liquefied soil available in the literature we have acquired considerable understanding on liquefied soil's stress strain behaviour. The lateral soil springs (defined by $p - y$ curves) are essentially load deformation characteristics of the soil. Fundamentally, the $p - y$ curves ought to be related to the stress-strain behaviour of the soil, however, current practice does not include this in constructing the $p - y$ curve (Dodds & Martin, 2007; Dash *et al.*, 2008). The $p - y$ curves used in current practice for both non-liquefied and liquefied soils have higher initial stiffness that degrades with increasing displacement (see Figure 1.6). For liquefied soil, this may not be a conservative design approach if compared with the observed $p - y$ curve behaviour in the full scale study by Rollins *et al.* (2005), where initial stiffness is very small and increases with increasing displacement.

Hence, the present understanding of the behaviour of liquefied soil from element tests, $p - y$ curve from some model studies and the similarity between them (see section 2.8.3) has prompted the investigation of establishing a rational $p - y$ curve for fully liquefied soil derived from its fundamental stress-strain behaviour in this chapter.

5.1.1 Outline of the chapter

Initially, a brief historical note on the evolution of $p-y$ curves is presented to justify the importance of this study. A pool of well-documented element test results providing stress-strain behaviour of post liquefied soil are collated and analysed critically with respect to various dependent parameters. The rate effect on the behaviour of liquefied soil has been investigated through a collaborative study on element tests carried out at the University of Yamaguchi, Japan. With the current state of understanding, a simplified monotonic stress-strain model is proposed that can be used in field cases where actual stress-strain behaviour of the soil is not readily available. The method of deriving a $p-y$ curve from the shear stress (τ) - shear strain (γ) curve is discussed. This method relates p with τ and y with γ using two scaling parameters N_s and M_s. The values of N_s and M_s are investigated through finite element analysis by using COMSOL (COMSOL, 2009) and suitable values for fully liquefied soils are proposed. At the end, the construction of the proposed $p-y$ curve has been demonstrated with two solved examples and compared with available experimental $p-y$ curves.

5.1.2 Brief evolutionary history of $p-y$ curve and justification of this study

The concept of $p-y$ curve was first developed by McClelland & Focht Jr (1958) where they obtained discrete load deflection parameters (p and y) from the strain-gauge measurements on a full- scale test pile. To note, this was a similar kind of exercise to that carried out in chapter 3 to obtain $p-y$ curves from the centrifuge test data. Their work introduced the so called $p-y$ curves that have become the backbone curve for soil springs when analyzing laterally loaded piles using BNWF models.

Since the initial work of McClelland & Focht Jr, 1958, numerous studies have been carried out to establish appropriate formulations for $p-y$ curves based on experimental studies and theoretical models. A list of important developments in this respect are listed in Table 5.1. In the last 50 years, the $p-y$ curve has evolved to a state ready to be used in practice, and it has been used with confidence for soil at service condition. However, an appropriate $p-y$ curve for liquefiable soil is still not available. As mentioned in chapter

1, the recent observations of $p - y$ curves in liquefiable soils in many model-scale and full-scale tests have shown loose correlation with current practice and strong correlation with the stress-strain behaviour of soil. This supports the idea of investigating the procedure of obtaining the $p - y$ curves form soil's stress-strain behaviour, and especially its application for liquefied soil.

5.2 Different stages of LPSI in liquefiable soils during earthquake

Figure 5.1 shows a typical soil-pile interaction and corresponding stress-strain behaviour of liquefiable soil during earthquakes. The interaction is broadly classified in three phases, such as:

1. Phase -1: Earthquake loading before liquefaction:

   During first few cycles of earthquake the amount of excess pore water pressure (EPWP) developed is very small and the soil is generally described as non-liquefied. Although, the soil stiffness degrades with each cycle of loading, this is quite small and the pile-soil interaction is practically treated as if the pile is vibrating in a non degraded soil.

2. Phase - 2: Development of full liquefaction:

   With continuing earthquake loading, the EPWP continues to rise and the soil reaches a state where its effective confining pressure becomes nearly zero. The soil is then described as fully liquefied and looses considerable strength and stiffness.

3. Phase -3: At full liquefaction:

   Once the soil is fully liquefied by development of the maximum possible EPWP, it normally remains liquefied for a few seconds to a few minutes depending on field drainage conditions and earthquake characteristics. Two types of lateral pile soil interaction may be visualised in this phase:

   (a) Cyclic: Pile vibrates cyclically in fully liquefied soil due to base shaking and it interacts dynamically with the liquefiable soil.

Table 5.1: Major contributions in the evolution of the $p - y$ curve.

Reference (s)	Development of $p - y$ curve	Remarks
McClelland & Focht Jr (1958)	Concept of $p - y$ curve was first developed from a series of full scale pile test data.	Experimentally calibrated model
Matlock (1970)	Constructed $p - y$ curve for clay from a series of field tests with static, cyclic and subsequent reloading conditions.	Experimentally calibrated model
Reese *et al.* (1974, 1975)	Suggested step by step procedure for constructing $p - y$ curve for clay and sand based on pile and soil properties, and then adjusted for full scale experimental test data.	Semi-empirical model and modified to agree with experimental results
Kagawa & Kraft (1980)	Proposed dynamic $p - y$ relationship for an elastic system from fundamental properties of soil.	Equivalent linear elastic model
O'Neill & Murchison (1983)	Collated available well documented full scale test data and modified the $p - y$ construction method of Reese *et al.* (1974) and Reese *et al.* (1975).	Semi empirical and modified to agree with experimental value
Ashour *et al.* (1998)	Proposed $p - y$ curve based on strain wedge model relating soil's stress-strain behaviour.	Semi-empirical model
Goh & O'Rourke (1999)	A clay type $p - y$ curve model for liquefiable soil was proposed based on undrained shear strength of the sand.	The shape of $p - y$ curve is similar to that of clay with high initial stiffness.
API (2000)	American Petroleum Institute (API) included O'Neill & Murchison (1983) recommendations in the subsequent edition of API RP-2A-WSD in 1987. API guideline does not provide any guidance for $p - y$ curves in liquefied soil.	This semi-empirical model is still used in practice.
AIJ (2001), Brandenberg *et al.* (2005)	A reduced strength $p - y$ curve for liquefied soil from API suggested non liquefied soil's $p - y$ curve. The strength reduction coefficient is correlated with the SPT value of soil.	The shape of $p - y$ curve remains similar to that of non-liquefied soil.
Haigh (2002)	Modified the $p - y$ curve formulation for soft clay including excess pore pressure as a variable to construct $p - y$ curve in liquefied soil.	The shape of $p - y$ curve is similar to that of clay with high initial stiffness.
Tokimatsu & Suzuki (2004)	Based on three large scale shaking table tests (nearly full scale) of piles in liquefiable soils, suggested that the shape of $p - y$ curve for liquefied soils have a strain hardening behaviour, completely different than the dry soil's $p - y$ curve (strain softening).	The shape of the $p - y$ curve is in line with the observations made in element test in liquefied soils.
Rollins *et al.* (2005)	Suggested $p - y$ curves for liquefied soil from a series of full scale pile tests. These are applicable for the soil up to 6m deep with $D_r \simeq 50\%$ and $y \leq 150$mm.	Experimentally calibrated model with very limited applicability
Klar (2008)	An upper bound solution of elastic strain field due to pile displacement was carried out. The solution uses mobilised strength design (MSD) approach to relate stress-strain curve with $p - y$ curve.	Its usage is limited to deeper depths of clayey soil. In liquefiable soil the applicability is not verified

142

(b) Monotonic: An unidirectional interaction is achieved if the pile deflects mono-tonically in liquefied soil, or if the liquefied soil flows past pile. Examples will include buckling of pile and lateral spreading of ground.

The pile response during phase-1 and phase-3 are two extreme cases both of which should be considered during the analysis. Phase-2 can sometimes become very important due to its dynamic consideration. As the soil goes into liquefaction, the lateral stiffness reduces and consequently the natural frequency of the structure drops. Hence, there is a possibility of resonance if the natural frequency of the structure crosses the dominant frequency of the earthquake, and the bending moment could amplify. However, the amount of amplification would also depend on the change in damping of the soil. In this chapter, the emphasis is given to monotonic pile-soil interaction in fully liquefied soil, as described above in phase-3b.

5.3 Post liquefied monotonic stress-strain behaviour of soils from element tests

5.3.1 Collation of already available test results

Various element test data available for liquefied soil's monotonic stress-strain behaviour are collated and tabulated in Table B.1, Appendix B. A typical post liquefaction stress-strain behaviour of Toyoura sand at different relative densities can be referred in Figure 2.10. This collation also includes the present test results which are described in section 5.3.2. For consistent comparison across these test results, the following terms are defined.

Take-off shear strain (γ_{to}): Shear strain at which the shear strength of the liquefied soil exceeds a very small amount of shear strength (about 1kPa) while subjected to monotonic shearing without drainage.

Initial shear modulus (G_1): Secant shear modulus in the initial stage of straining when take-off strain is attained.

Critical state shear modulus (G_2): Tangent shear modulus, a nearly constant value, while the soil is continuously shearing following the Critical state line.
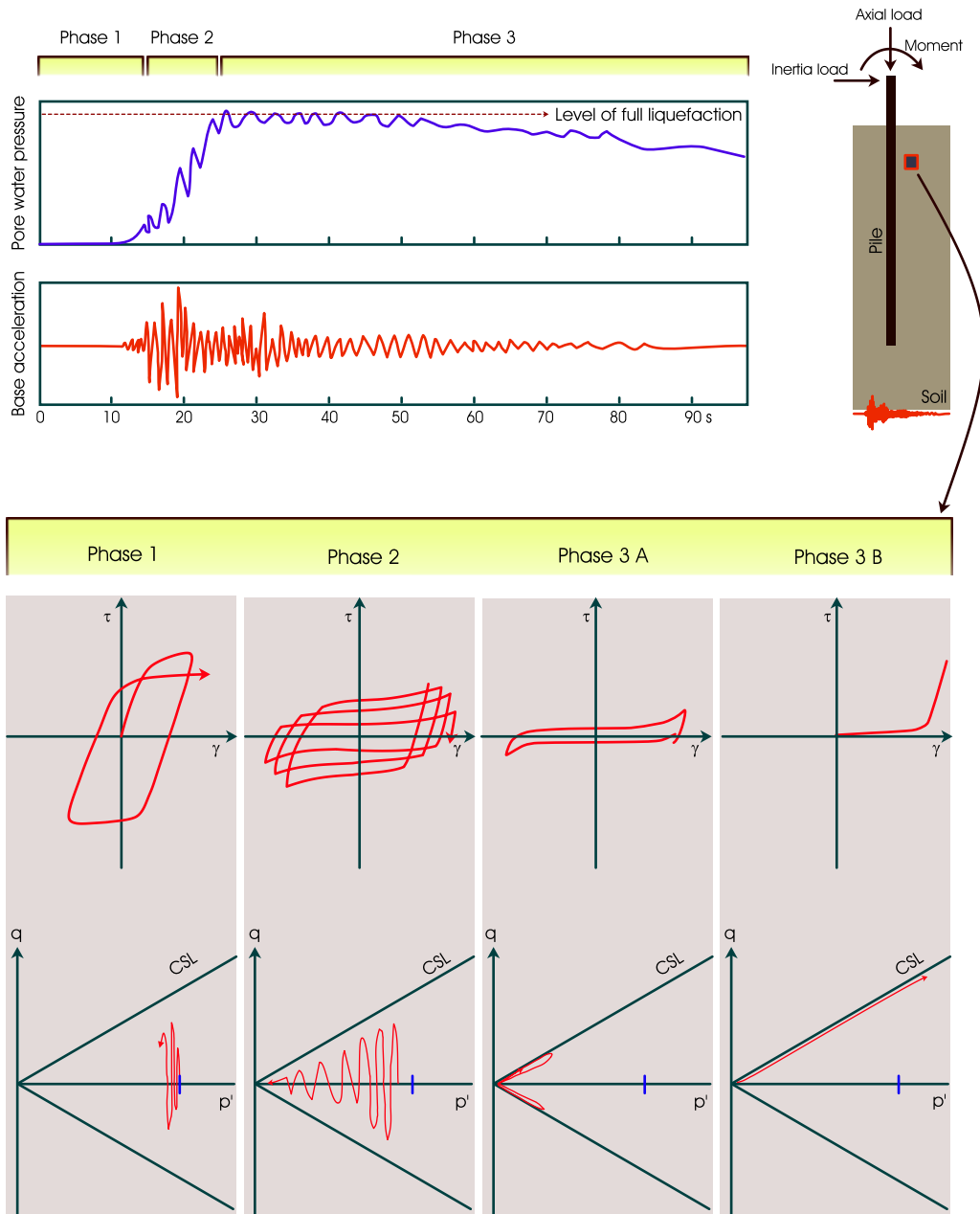
Figure 5.1: Different stages of the stress-strain behaviour of liquefiable soils during earthquakes.

The major observations (general and specific) from the collated data can be summarised as below.

1. The post liquefaction monotonic behaviour is always dilative but suppressed due to the undrained condition and the stress path $(q - p')$ follows a straight line close to the critical state line. The stress ratio remains constant regardless of its relative density.

144

2. The suppressed dilation in fully liquefied soil decreases the excess pore water pressure and consequently increases the effective overburden pressure in it.

3. Very large shear strain is required to mobilise any resistance. After a certain shear strain level, the shear modulus starts to increase and attains a constant value. With further increase in shear strain level, the shear modulus remains constant (Vaid & Thomas, 1995).

4. The post-liquefaction response represents continuously stiffening behaviour and an approach to any residual strength was not observed, regardless of density or effective stress conditions prior to cyclic loading (Vaid & Thomas, 1995).

5. During liquefaction, the small strain shear modulus of non-liquefied soil reduces to a very low value of about $1/100$ to $1/1000$ times the original, and this degradation is proportional to the excess pore water pressure developed (Yasuda *et al.*, 1987).

6. Large strain critical state shear modulus of liquefied soil (G_2) is significantly higher as compared to its small strain shear modulus. This higher stiffness at large strain can be attributed to suppressed dilation and re-locking of soil grains.

7. G_2 becomes stiffer with increase in initial confining stress (p'_{ini}) at low relative density, but, as the relative density increases, the effect of confining stress on G_2 is not so apparent.

8. G_2 is in the same order of magnitude as that of the pre-liquefied soil's large strain shear modulus.

9. G_2 increases with increase in relative density of the soil.

10. At a particular relative density, the compressional response is stiffer than the extensional response.

5.3.2 Present study on the effect of strain rate in liquefied soil

A collaborative study had been conducted at Yamaguchi University, Japan (Dash *et al.*, 2008) to understand the loading rate effect on post liquefied monotonic response of soil.

The tests were carried out by Yamada and Hyodo on Toyoura sand in an un-drained triaxial test setup. A brief introduction to the test setup and the test results are presented below.

5.3.2.1 Test procedure

Figure 5.2a shows the test facility used for this study. Toyoura sand, having mean diameter (D_{50}) of 0.2mm and maximum and minimum void ratios of 0.977 (e_{max}) and 0.597 (e_{min}), respectively, was used in this study. The soil sample was prepared at nearly 50% relative density (D_r). A uniform confining stress (σ_3) of 50kPa was applied to the sample from all directions (Figure 5.2b). During the test, σ_3 was kept constant. During all the tests except Test-6, the sample was subjected to cyclic axial stress (σ_1) to cause it to liquefy. Once the sample was fully liquefied, σ_1 was applied monotonically as axial compression with a predefined strain rate. The variation of deviatoric stress, q, with time is schematically shown in Figure 5.2c. In Test-6, the initial cyclic loading was not included and it was subjected only to monotonic compression. The schedule of tests are presented in Table 5.3. Test-1 is repeated with same strain rate, to observe the repeatability of the tests.

Table 5.3: Schedule of tests for strain rate effect study.

Test ID	γ_d (kN/m^3)	e	D_r (%)	SR (% /min)
Test-1(a)	14.35	0.805	49.8	0.1
Test-1(b)	14.32	0.808	48.8	0.1
Test-2	14.34	0.805	49.6	0.5
Test-3	14.27	0.814	47.0	1.0
Test-4	14.28	0.813	47.3	5.0
Test-5	14.31	0.809	48.5	10.0
*Test-6	14.35	0.804	50.0	0.1
* : Subjected only to monotonic compression without any prior cyclic loading. SR: Strain rate, γ_d: Dry unit weight of soil, e: Void ratio, D_r: Relative density				

5.3.2.2 Results and discussion

The stress-strain behaviour of the soil observed in Tests-1(a), 2, 3, 4 and 5 are plotted in Figure 5.3. The figure shows the effective stress path and the shear stress-strain behaviour. Note that the y axis of the stress path is τ, which is $(\sigma_1' - \sigma_3')/2$, instead of the conventional
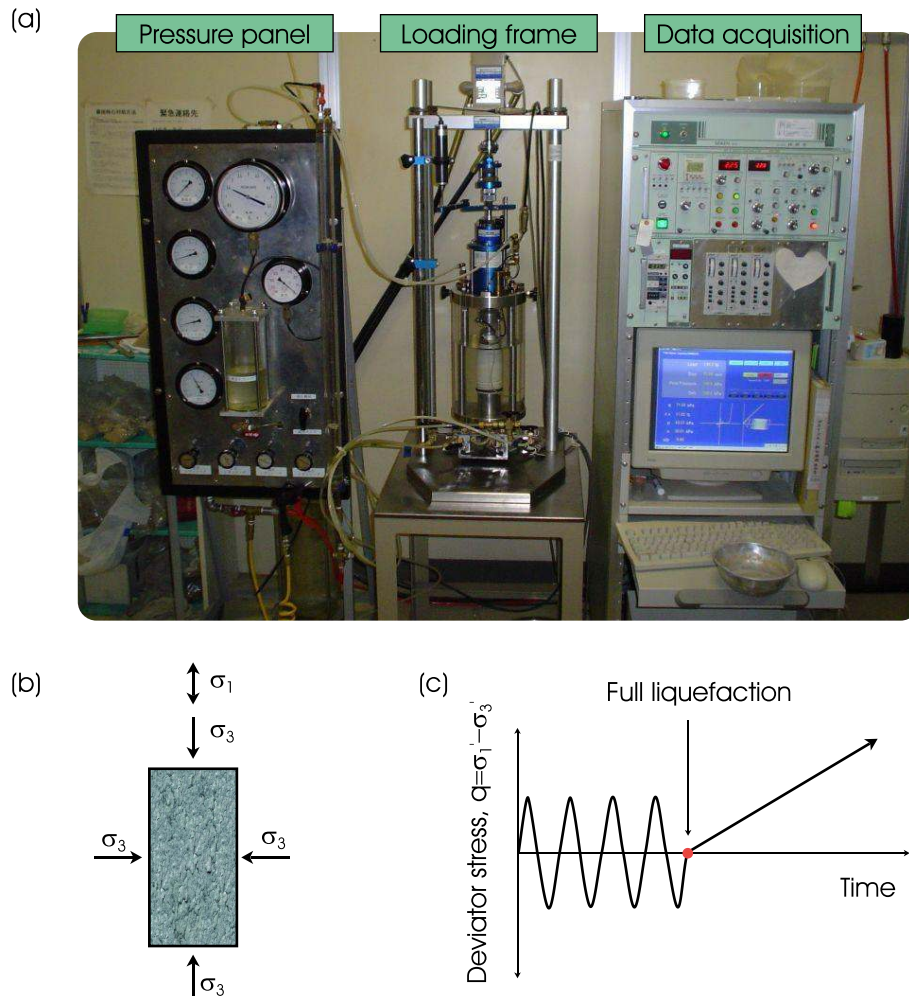
Figure 5.2: (a) Triaxial cyclic shear test apparatus at Yamaguchi University, Japan. (b) A schematic of the test specimen. (c) Loading sequence of the deviatoric stress with time.

notation q, which is $(\sigma_1' - \sigma_3')$. This figure is plotted in such a way to be consistent for the y-axis of the two plots.

All the test results have shown that the shear strain in the liquefied soil increased up to ~ 5 - 10% producing very low or negligible shear stress, after which the stress increased steadily. The tangent shear modulus of the liquefied soil (G_2) at large strain remained fairly constant and was not affected by different amount of strain rate. However, a small variation in G_2 can be seen between some tests (e.g., Test-1(a): SR=0.1% per minute and Test-5: SR = 10% per minute), which may be explained by the variation in initial relative density of the sample in the tests. These results were very promising in terms of the shape of the stress-strain curve as compared with the other experimental studies in liquefied sand (e.g., Yasuda *et al.*, 1999, 1998). The results did not show a definite

pattern in terms of rate of strain applied to the sample.
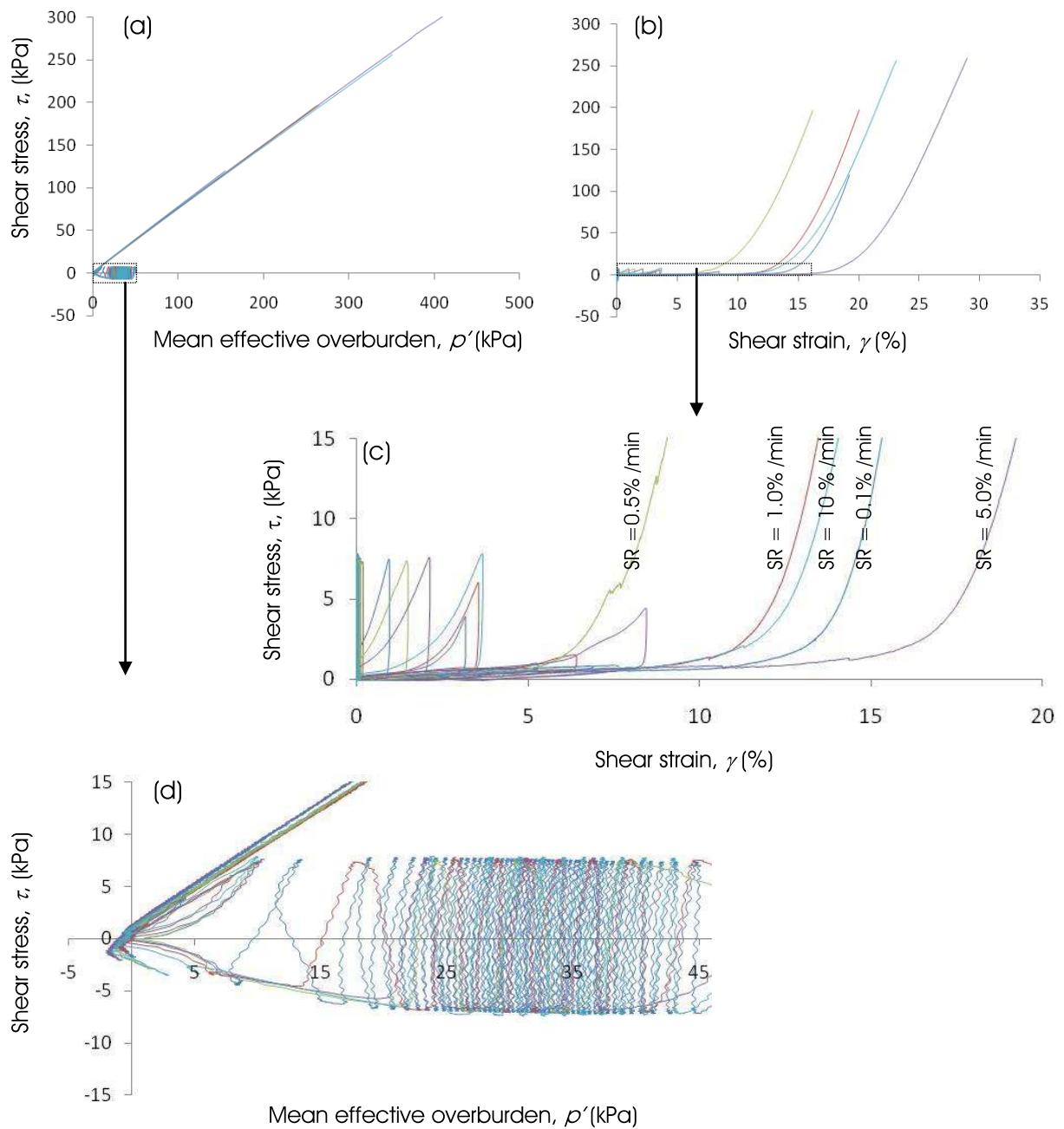
Figure 5.3: Effect of strain rate on stress-strain behaviour of liquefied soil (a) $\tau - p'$ stress path, (b) τ versus γ curve, (c) zoomed $\tau - \gamma$ curve, and (d) zoomed $\tau - p'$ path.

The behaviour of soil in Test-1(a) and 1(b), where the later test was a repetition of the earlier one with same strain rate, is presented in Figure 5.4. Though, same critical state shear modulus (G_2) was observed in both the cases, the difference in take-off strain (γ_{to}) was quite significant. The two tests did not show repeatability in terms of strain rate effect on γ_{to}.

A comparison has also been made between fully liquefied and non-liquefied Toyoura
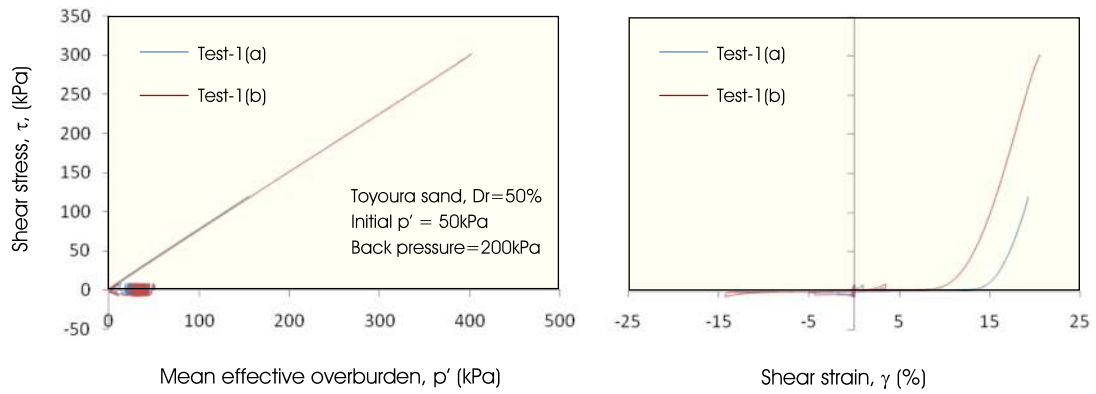
Figure 5.4: Stress-strain behaviour of Toyoura sand in Test-1(a) and Test-1(b).

sand subjected to large strain, as shown in Figure 5.5. The difference between initial stiffness is pronounced. However, the large strain stiffnesses in the critical state for both the tests are very similar. Similar observations were also made by Vaid & Thomas (1995) from the experiments carried out on Fraser river sand, as shown in Figure 5.6. Their results also showed that the large strain shear modulus is the same not only for fully liquefied soil and non-liquefied soil, but also for partially liquefied soil. In the pre-liquefied stage, large strain can be referred to as shear strain more than 1.0%, and the shear modulus at low strain (G_{max}) can be referred to as when shear strain is less than 10^{-5}% (see Figure 5.5b).
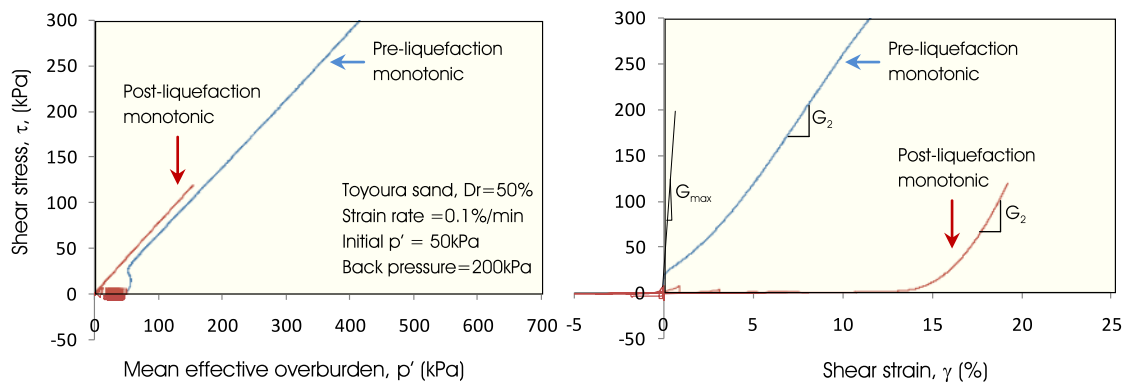
Figure 5.5: Comparison between pre-liquefaction (Test-6) and post liquefaction monotonic (Test-1(a)) stress-strain behaviour of Toyoura sand at $D_r = 50\%$.
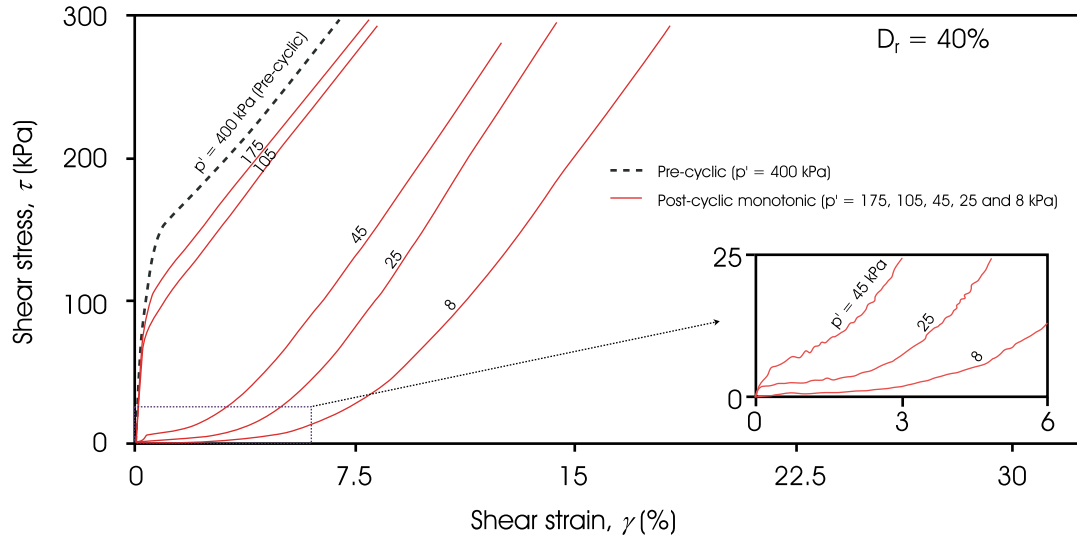
Figure 5.6: Pre and post liquefaction monotonic stress-strain behaviour of Fraser river sand (Redrawn after Vaid & Thomas, 1995). Different effective overburden pressure (p') represents the degree of liquefaction; e.g., 45kPa overburden pressure represents the state of soil that has 89% liquefied.

5.4 Factors affecting post liquefied stress strain behaviour

Various factors that may affect the stress-strain behaviour of liquefied soil are investigated. It is important to understand the effect of the parameters that affect the behaviour of a complex problem to be able to propose a simplified model. The insight gathered is used to understand the major active mechanism and the variables that have little impact in the behaviour are eliminated from the simplified model. The factors are discussed here keeping in mind the requirement of defining the four parameters (γ_{to}, G_1, G_2, τ_{max}) for the proposed simplified model, which will be discussed later in section 5.5.

5.4.1 Relative density (D_r)

Most of the studies on post liquefied behaviour of sand suggested that γ_{to} decreases with an increase in initial D_r of soil. This is supported by the fact that at take-off strain soil starts to become stiffer and offers considerable amount of strength which is due to the re-locking of sand particles that were in suspension during liquefaction. Hence, the correlation between D_r and γ_{to} has been explored in section 5.5.1 and a suitable relationship is proposed for further use.

G_1 and G_2 are not directly related to their initial relative density and hence excluded

150

from direct involvement in estimating these parameters, but, the initial D_r value is used indirectly to define G_2 as detailed in section 5.5.3.

5.4.2   Initial overburden pressure (p'_{ini})

It is well understood that the lateral resistance (or shear strength) of sandy soil is linearly proportional to the effective overburden pressure (p'), which increases with depth. This is based on the fact that the sandy soil obtains strength from its confinement. Based on this concept, API (2000) suggests a linear relation between the effective overburden pressure and ultimate lateral soil resistance both in shallow and deep soils (see Equation 3.2 and 3.3 in section 3.2.3). However, when the soil is fully liquefied the p' becomes zero. Hence, with the above assumption, the soil will offer no resistance to shear unless the overburden pressure is increased. However, the liquefied soil offers significant resistance at large strain and this shearing at large strain is associated with decrease in pore water pressure.

The full mobilization of strength happens at the lowest excess pore water pressure (EPWP) possible, which is dependent on the permeability and hydraulic gradient of the soil. Also, theoretically, the negative EPWP could reach the absolute minimum of 1bar (100kPa), however, this is very unlikely to happen in real field conditions. Hence, p'_{ini} is used directly to estimate the limiting shear resistance of liquefied soil (τ_{max}) as will be described later in section 5.5.4.

Also, the initial overburden pressure is normally used to define the stiffness of soil at small strain, and also has influence on G_2 at critical state. Hence p' is used to estimate G_2 as detailed in section 5.5.3.

Studies by Vaid & Thomas (1995) showed that the post liquefaction deformation in sandy soil occurs at a linear stress path in $q - p'$ plane (Figure 5.1) and is independent of its initial overburden. Sitharam *et al.* (2009) conducted a similar study on the behaviour of liquefied soil at three initial confining pressures at same relative density in a cyclic triaxial test setup. Their study showed that the monotonic strength of liquefied sand is not influenced by the initial confining pressure prior to liquefaction. Hence, the formulation of γ_{to} and G_1 excludes the direct involvement of p' in them.

5.4.3 Strain rate

For post liquefied monotonic behaviour of sand, the tests as discussed in section 5.3.2.2 could not suggest any definite relationship between strain rate and the take off strain. Kutter (1997) and Martin (1997) in the NSF workshop had also commented that the effect of strain rate on residual strength of granular soils is less substantial for a practical range of strain rate, however, it can be reasonable to expect the rate effect at very low or very high strain rate. It is also difficult to estimate the expected strain rate for a pile-soil interaction in liquefied soil during earthquakes. Hence, for this first level of simplified stress-strain model, effect of strain rate has not been included.

5.4.4 Severity of liquefaction (F_l)

The severity of liquefaction, F_l, in laboratory terms can be defined as the relative magnitude of stress/strain applied to produce initial liquefaction in the soil. F_l is 1 if the shear stress of τ_l causes the soil to liquefy in 20 cycles (Yasuda *et al.*, 1998). If either the number of cycle (N_{cy}) is not 20 or the applied shear stress (τ_p) is not τ_l, then F_l can be estimated by Equation 5.1 or Equation 5.2 (Yasuda *et al.*, 1998).

$$F_l = \left(\frac{N_{cy}}{20} \right)^b , \text{ where b = -0.17 for clean sand} \tag{5.1}$$

$$F_l = \frac{\tau_l}{\tau_p} \tag{5.2}$$

Studies by Yasuda *et al.* (1999) showed that the severity of liquefaction has significant influence on γ_{to} and G_2. Sitharam *et al.* (2009) also observed a similar effect in cyclic triaxial test and in DEM analysis where a difference of 60% between lower and upper take-off strain magnitude caused by a 2% variation in applied axial strain. In contrast to the above observations, studies by Vaid & Thomas (1995) showed that the post liquefaction response is essentially similar at each relative density regardless of the manner by which the state of liquefaction ($p' = 0$) is achieved. These observations suggest that further studies are required to describe the effect of severity of liquefaction on the stress-strain response of liquefied soil. Hence, for this simplified stress-strain model, the effect of the severity of liquefaction has been excluded.

5.4.5 Other factors

There are various other known factors that might have an influence on the stress-strain behaviour of liquefied soil, such as: fines content in soil, grain size distribution, stress path, pore pressure redistribution, consolidation stress, etc. However, these parameters require more in-depth studies to be able to propose a clear relationship with the simplified stress-strain parameters, and so are excluded in this first level of simplified model.

5.5 Proposed simplified monotonic stress-strain curve for liquefied soil

With the current understanding of the behaviour of liquefied soil and its influencing factors, a simplified model of monotonic stress strain curve is proposed that can be used later in constructing a $p - y$ curve. This model should ideally be simple and be a good representation of the actual behaviour of the soil. Figure 5.7 schematically shows the proposed model. The aim of this model is to provide the engineer/designer a firsthand approximation of a reasonable stress strain curve for liquefied soil from very basic soil properties, if the actual stress-strain curve is not readily available.

The proposed model can be defined with four parameters as listed below.

1. Take-off shear strain (γ_{to})

2. Initial shear modulus (G_1)

3. Critical state shear modulus (G_2)

4. Maximum shear stress (τ_{max})

The first three parameters can be obtained from element tests, but, the fourth parameter (τ_{max}) cannot generally be obtained from the tests. Element test results have shown that in post-liquefied monotonic shear there is no tendency of necking or residual stress state, and the shear stress goes on increasing with shear strain (Vaid & Thomas, 1995). This is because of the constraint in the laboratory test setup with higher applied back pressure. Hence, the magnitude of maximum negative pressure in a laboratory environment could

go up to nearly 100kPa more than the applied back pressure. However, this normally does not happen in a field condition, and a residual value may be attained at very large strain. Hence, to have a complete model of stress-strain behaviour that is compatible with very large strain as well, a limit to the maximum possible shear stress is imposed, depending on field condition as detailed in section 5.5.4.
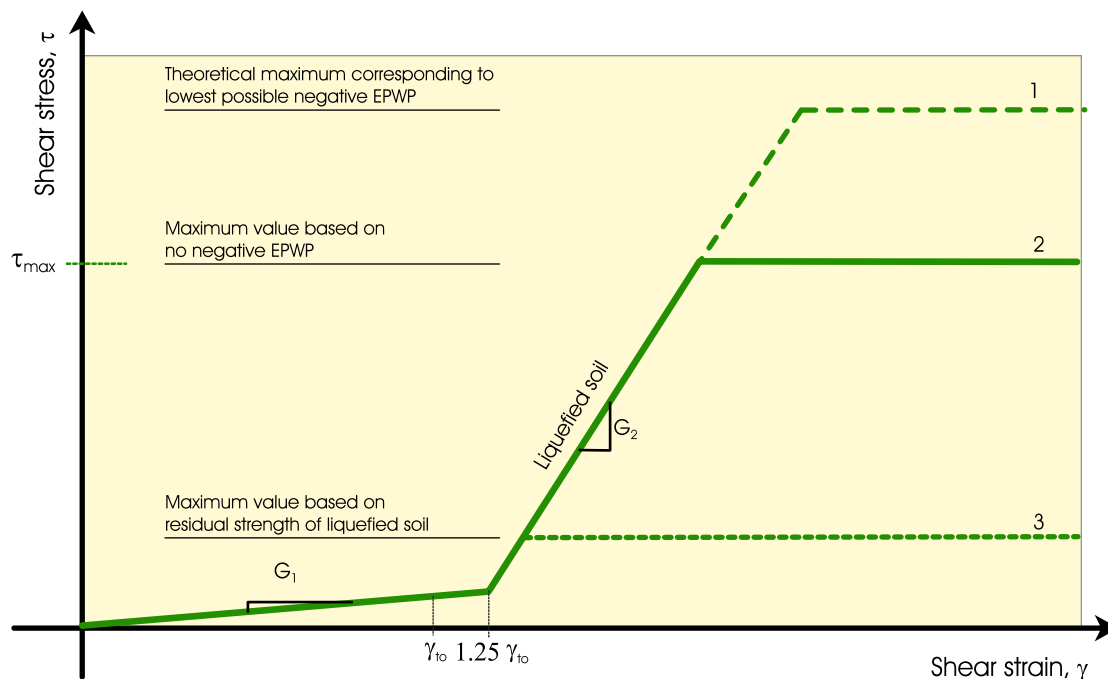
Figure 5.7: Simplified stress-strain model for liquefied soil.

5.5.1 Take-off shear strain (γ_{to})

From all the collated test data (Table B.1, Appendix B) on different soils, γ_{to} is plotted with respect to their initial D_r values as shown in Figure 5.8. The figure suggests that the take-off shear strain in liquefied soil decreases with increase in D_r even though the values are scattered a bit. Two global trend lines were fitted to all the test data at upper and lower bound values as given in Equations 5.3 and 5.4, where γ_{to} and D_r are in %.

$$\gamma_{to}^{ub} = 131 - 29 \ln D_r \tag{5.3}$$

$$\gamma_{to}^{lb} = 47 - 11 \ln D_r \tag{5.4}$$

A mean value relationship between γ_{to} and D_r was proposed for further use as given

in Equation 5.5.

$$\gamma_{to} = 89 - 20 \ln D_r \qquad (5.5)$$

In the actual observed shear stress - shear strain behaviour (for example see Figure 2.10), the transition between G_1 and G_2 is quite smooth and in some cases this transition zone mobilises up to 1-2% of shear strain. In contrast, the proposed simplified model does not include this smooth transition. Hence, to include this transition zone shear strain between G_1 and G_2, the value of γ_{to} has been increased by 25%. Hence the second linear segment of the stress-strain model starts from $1.25\gamma_{to}$, with a shear modulus of G_2.
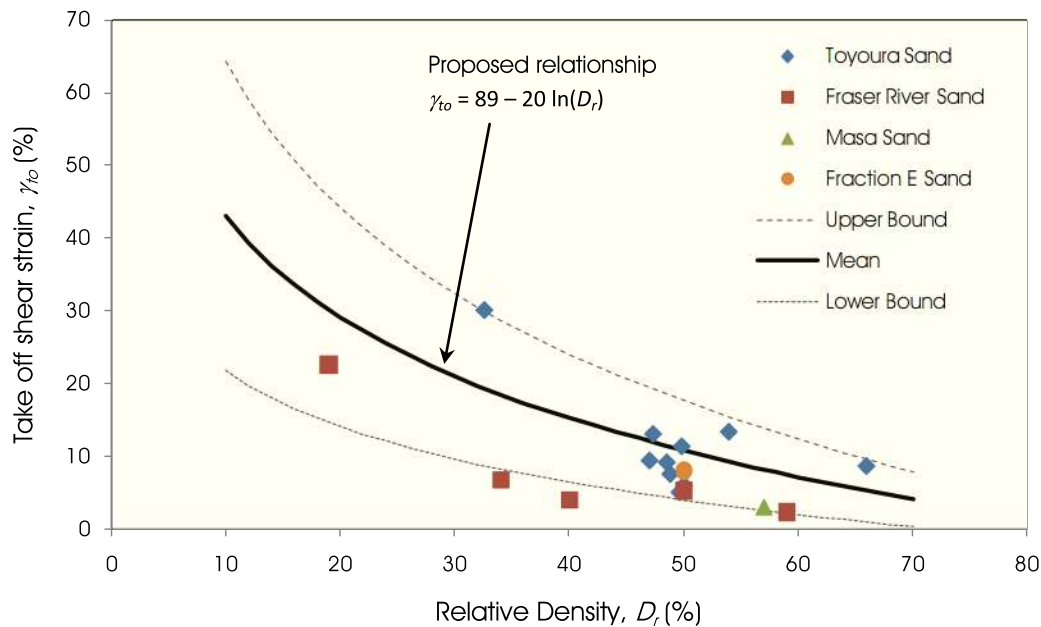
Figure 5.8: D_r versus γ_{to} of liquefied soils.

5.5.2 Initial shear modulus (G_1)

In the collated data, γ_{to} was defined corresponding to the shear stress value of 1kPa. Hence, for the simplified model, G_1 can be estimated based on γ_{to} as given in Equation 5.6. Figure 5.9 shows G_1 versus γ_{to} for the collated data points and plots the Equation 5.6.

$$G_1 = \frac{1}{\gamma_{to}} \text{ (in kPa)} \qquad (5.6)$$
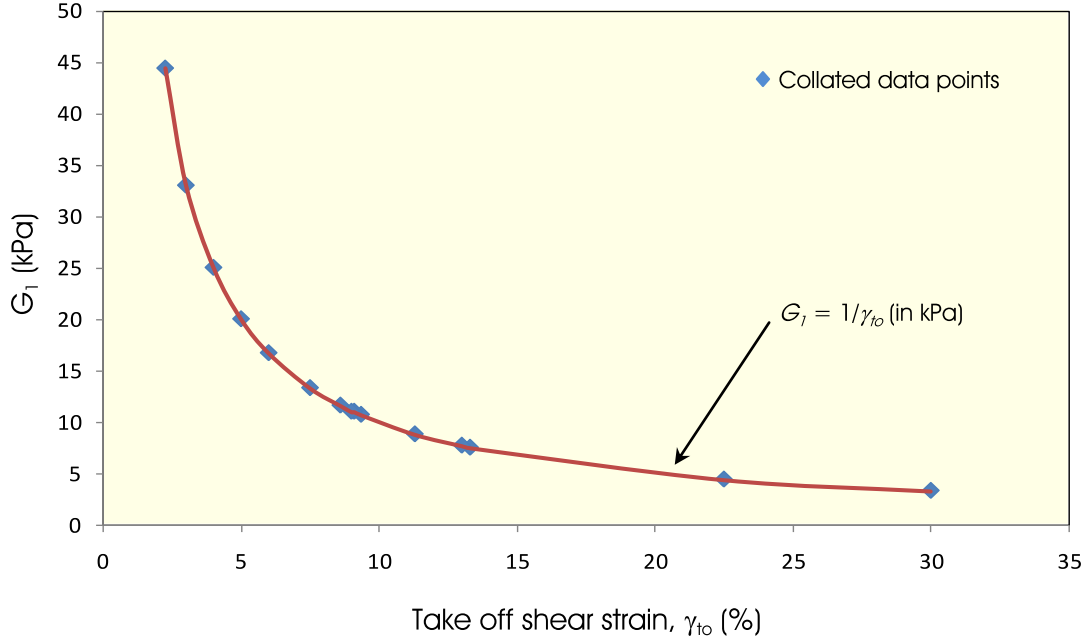
Figure 5.9: G_1 versus γ_{to} of collated element test data.

5.5.3 Critical state shear modulus (G_2)

As described earlier, the G_2 of liquefied soil exhibits a few typical characteristics such as:

1) G_2 is nearly same for various degrees of liquefaction,

2) G_2 is constant corresponding to the critical state of soil and does not depend on the shear strain value, and

3) G_2 is nearly same for pre-liquefied and post-liquefied soil.

In conventional practice, the shear modulus degradation curve is used to define shear modulus G at large strain. G is treated as a decreasing function with shear strain magnitude (γ), and is also dependent on mean effective confining pressure (p'). For example, the formulation for sand (PI= 0) as per Ishibashi & Zhang (1993), can be expressed as Equation 5.7, which is plotted in Figure 5.10.

$$\frac{G}{G_{max}} = K_g \times p'^{m}, \tag{5.7}$$

where, K_g and m are soil constants which depend on the level of shear strain, γ.

The above expression (Equation 5.7) is supported by experimental data with maximum shear strain level of 1%. Equation 5.7 being a continuous function cannot estimate

156
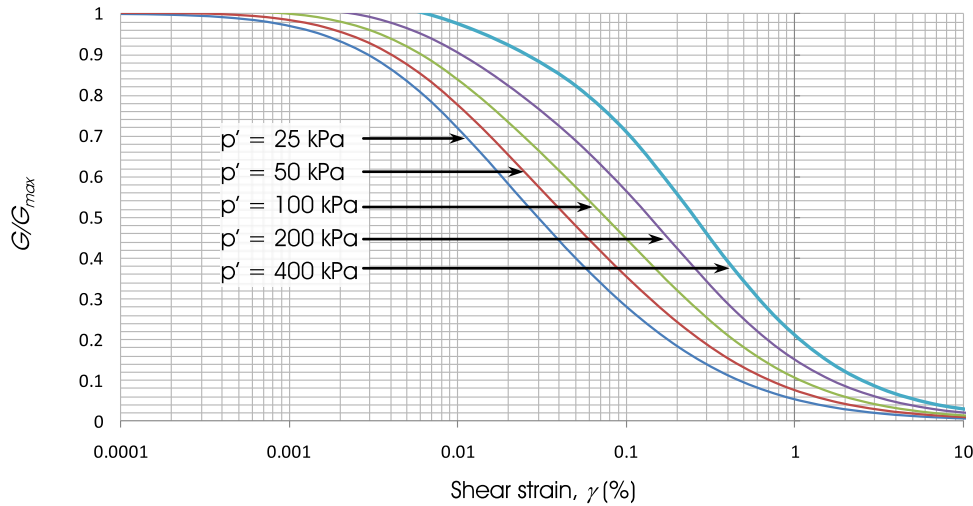
Figure 5.10: Shear modulus degradation curve for sand.

the critical state shear modulus G_2, which corresponds to large strain constant value. Hence, the traditional degradation curve may not be suitable for estimating G_2 for liquefied soil.

Looking for alternative correlations that may exist between G_2 and any other soil parameters, no expression was found in the literature. Neither is any theoretical concept available to estimate it. It seems, however, G_2 can be derived from theoretical critical state soil mechanics (CSSM) concepts including the rate of dilation effect in the soil, but this will involve rigorous mathematical derivation. Within the present scope of a first level simplified model, CSSM concept to obtain G_2 was not explored. Rather, experimental test results were used to relate G_2 with its G_{max} value. This is because G_{max} value is widely studied in the literature and can be obtained easily for a particular soil at particular depth and density. Some conventional expressions for G_{max} are presented in Appendix C.

There are some element test results available in literature which contains both pre- and post-liquefied soil behaviour. Here, the aim was to find out the relationship between the post-liquefied shear modulus at the critical state (G_2) and the pre-liquefied small strain shear modulus (G_{max}). However, it was practically impossible to obtain the G_{max} values (at a very low strain) from the figures/plots, where the author had not defined or presented it explicitly, and values can be subjected to individual interpretation. Hence, the G_{max} value was estimated from the available empirical expression (Equation C.2),

157

but the G_2 value was quite easy to read from the stress-strain plots of the element test data. The data set as tabulated in Table B.1 was used to get the G_2/G_{max} ratio. Three pre-cyclic monotonic test results by Thomas (1992) on Fraser River sand ($D_r = 40\%$, p'_{ini} = 400kPa, 800kPa, 1200kPa) were also included in the data set with the consideration that the G_2 for post-liquefied soil is similar to the slope of stress strain curve at critical state for pre-liquefied soil. The ratio of G_2/G_{max} for different values of D_r and p'_{ini} values from these tests are plotted in Figures 5.11 and 5.12.
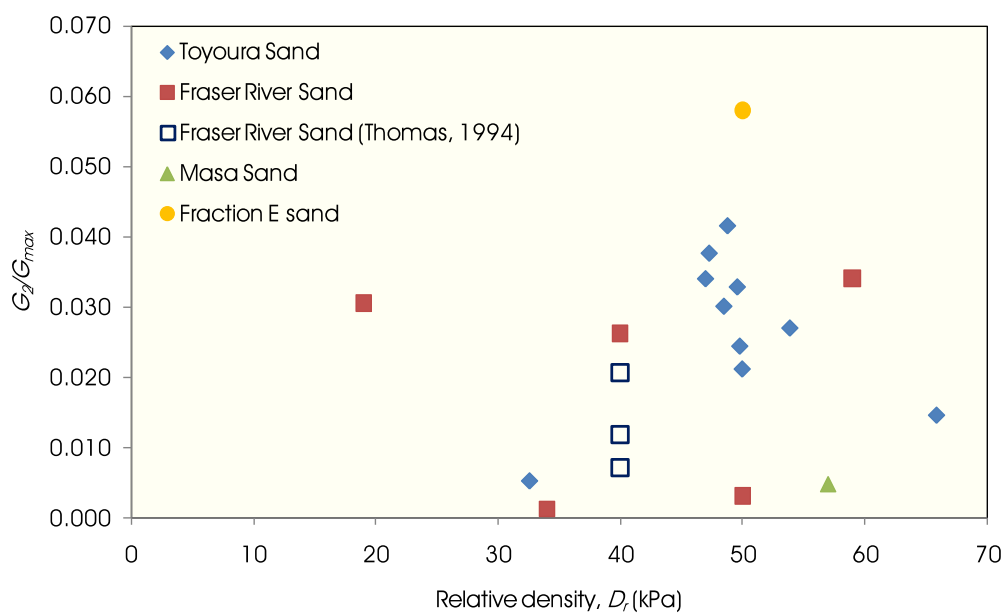
Figure 5.11: Relationship between G_2/G_{max} and D_r.

Although, it is not very clear from the figure about the dependency of the G_2/G_{max} ratio on D_r, the ratio is probably showing a quadratically decreasing trend for an increase in p'_{ini} value. It can be noted that the fitted trend line in the figure is highly dependent on the data points of the Fraser River sand by Thomas (1994) and the regression coefficient is 0.3 for the trend line. There is a possibility of artefacts in the plotted relationship due to the methods used to estimate G_{max} and G_2, where the former was obtained by empirical expressions and the latter was directly read from element test data. There could also be some other parameters which may have significant influence over this ratio, but, they were not explored here due to lack of available experimental data.

As a first level of assumption, the ratio G_2/G_{max} was considered to be inversely proportional to the square root of p'_{ini} (Equation 5.8).
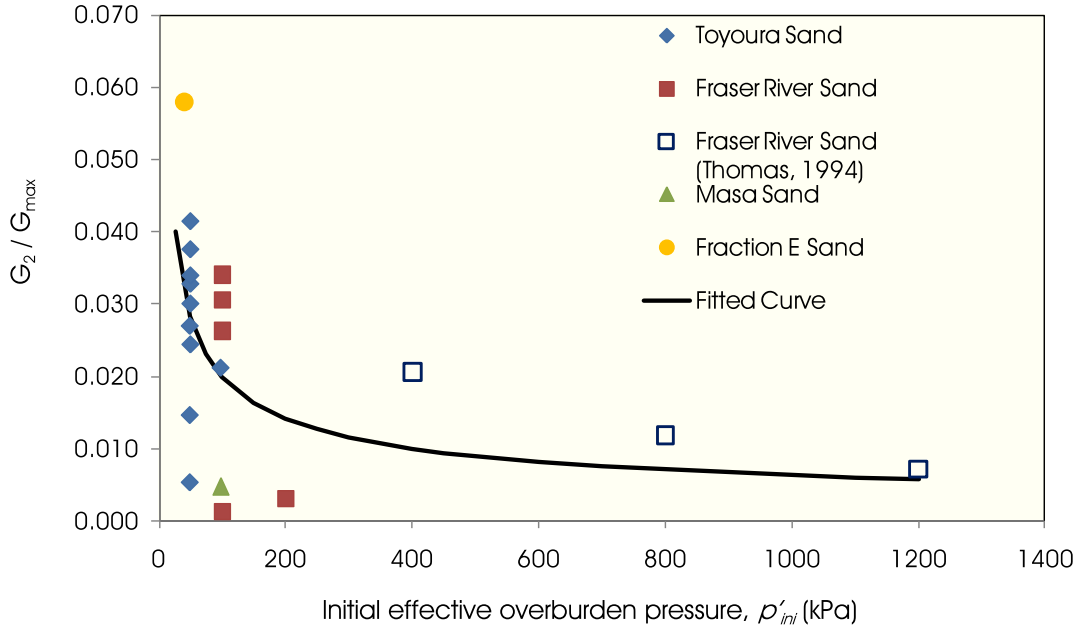
Figure 5.12: Relationship between G_2/G_{max} and p'_{ini}.

$$\frac{G_2}{G_{max}} \propto \frac{1}{\sqrt{p'_{ini}}} \qquad (5.8)$$

From the data set, the mean value of the proportionality factor for the above equation was found to be nearly 0.2. Hence the expression as given in Equation 5.9 was proposed to obtain G_2 value required for the simplified stress-strain model. However, further detailed experimental investigation is necessary to validate this expression.

$$G_2 = \frac{G_{max}}{5\sqrt{p'_{ini}}} \qquad (5.9)$$

5.5.4 Maximum shear stress (τ_{max})

The limiting value of maximum shear stress can be estimated in three ways, such as:

A - $\tau_{max}(1)$: Value corresponding to theoretically possible minimum EPWP (i.e., absolute vacuum condition).

B - $\tau_{max}(2)$: Value corresponding to minimum possible non negative PWP in post

liquefaction shearing .

C - $\tau_{max}(3)$: Residual strength of soil as obtained from back analysis of case histories in past earthquakes.

A typical field condition is presented in Figure 5.13, where different p' values corresponding to different stages of liquefaction (A, B, C and D) are presented. These stress state during A, B, C and D conditions are also shown in Figure 5.14 in $q - p'$ plot. The $q - p'$ relationship is linear on critical state line, where slope of the line is known as stress ratio. This stress ratio is different in both compression (M_c) and extension (M_e), and can be related to the critical angle of friction of the soil (ϕ_{cs}) as shown in Figure 5.14. Typical values of ϕ_{cs} can be referred to in Table 2.1. For a given value of p', the corresponding τ_{max} can be estimated as demonstrated in Figure 5.14. Generally the extensional strength of soil is not reliable in the field and hence avoided from consideration. With this assumption, only compressional shear stress value can be estimated using stress ratio M_c and this shear stress value can further be used to estimate lateral soil resistance (p).

5.5.4.1 $\tau_{max}(1)$

The theoretical maximum shear stress in compression can be written as Equation 5.10.

$$\tau_{max}(1) = \frac{M_c \left(p'_{ini} + 100 \text{ kPa} \right)}{2} \tag{5.10}$$

5.5.4.2 $\tau_{max}(2)$

Imposing the condition of non-negative excess pore water pressure, the maximum shear stress in compression can be written as Equation 5.11. This condition restricts the excess pore water pressure from cavitation.

$$\tau_{max}(2) = \frac{M_c p'_{ini}}{2} \tag{5.11}$$

5.5.4.3 $\tau_{max}(3)$

Several empirical relationships exist between the residual shear strength (s_u) of liquefied soil with standard penetration resistance (SPT value) derived by back calculations of liquefaction case histories. The shear stress that can be mobilized by an element of soil

Initial state before liquefaction

$$p_{tl} = \gamma_t h_1 + (\gamma_t - \gamma_w) h_2$$
$$u = \gamma_w h_2$$
$$u_{ex} = 0$$
$$p' = p_{tl} - u - u_{ex} (p'_{ini})$$

p_{tl} = Total lateral earth pressure
u = Hydrostatic PWP
u_{ex} = Excess PWP
p' = Effective overburden pressure
p'_{ini} = Initial Effective overburden pressure
γ_t = Total density of soil
γ_w = Density of water
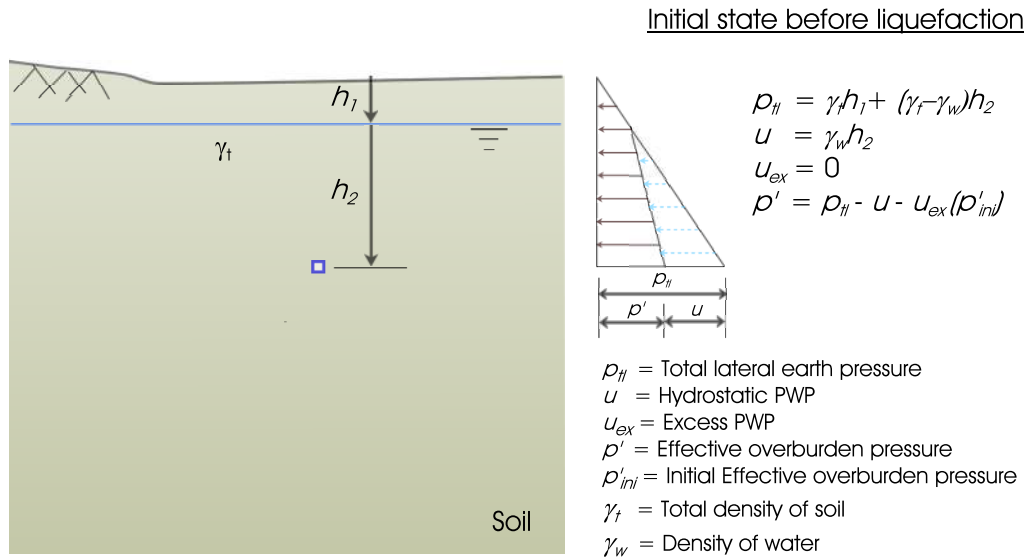
During earthquake shaking, u_{ex} changes due to pore water pressure generation/dissipation and changes p' but p_{tl} remains constant.

A: Before liquefaction, $p' = p'_{ini}$, $u_{ex} = 0$

B: Full liquefaction, $p' = 0$, $u_{ex} = p'_{ini}$

C: Post liquefaction without -ve u_{ex} (i.e., just before onset of cavitation) $p' = p'_{ini}$, $u_{ex} = 0$

D: Post liquefaction at lowest possible u_{ex}, $p' = p'_{ini} + 100$ kPa, $u_{ex} = -100$kPa

Figure 5.13: A typical field condition and the value of effective overburden pressure (p') at different stages of liquefaction.

when strained monotonically to very large strains is defined as the residual strength of soil. A summary of discussions on residual strength of soil can be found in section 2.4.2. Depending on the available soil parameter, s_u can be estimated. The maximum shear stress, hence, can be limited to the residual strength of that soil at liquefied state, as given in Equation 5.12.

$$\tau_{max}(3) = s_u \tag{5.12}$$

5.5.4.4 What τ_{max} value to use?

The $\tau_{max}(1)$ is a theoretical maximum possible value of shear stress, which corresponds to the case of absolute vacuum. However, this situation is not expected in normal field condition.

161
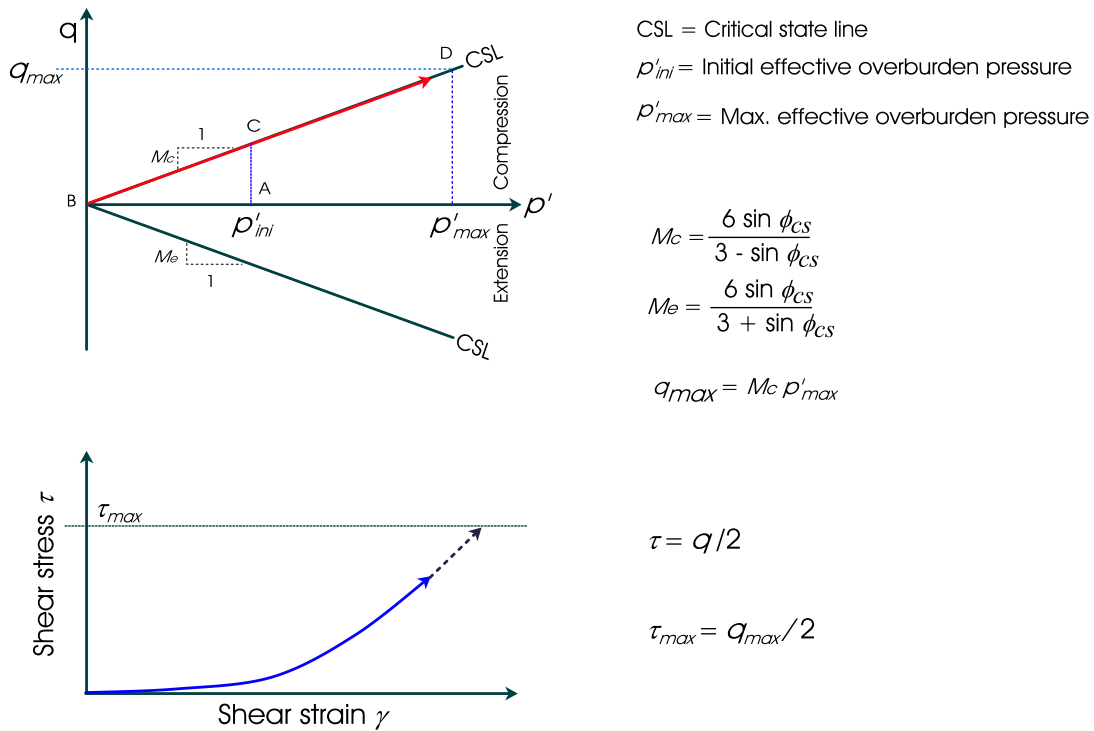
Figure 5.14: Critical state concept of getting maximum shear stress in liquefied soil.

The $\tau_{max}(3)$ is a back calculated value from the case histories of liquefied soil subjected to flow failure, which does not include the dilative behaviour of soil and is likely to underestimate the strength. However, this situation can well be assumed for soils at shallow depth without impermeable top crust, which is the similar field conditions (slope failures occurred during earthquakes) the residual strength formulations are based on.

On the other hand, at greater depths, where the dilative behaviour of soil is possible due to nearly undrained boundary condition, the case of non negative excess pore water pressure conditions in the field seem most appropriate to estimate the value of τ_{max}. A similar concept has also been used by Knappett & Madabhushi (2009) following a set of centrifuge tests.

Based on the above discussion, it is reasonable to assume maximum shear stress value of $\tau_{max}(2)$ at deeper depth and $\tau_{max}(3)$ at shallow depth, however, defining the condition of shallow or deeper soils could sometimes be difficult and will depend on the boundary condition and the specification of pile. While constructing a $p - y$ curve from this stress-strain curve, it is required to define a particular value of τ_{max}. Hence, in this situation the following guidelines can be used to define a single value of τ_{max}.

The failure pattern of the soil for a laterally loaded pile follows a wedge type failure at shallow depth, whereas at deeper depth a flow around failure mechanism governs (Klar & Randolph, 2008). Based on a similar concept, API guidelines (API, 2000) defines when to use the shallow estimation and the deeper estimation for ultimate lateral resistance of soil based on the angle of friction. Let us define the critical depth ratio which forms the boundary between shallow and deeper depth as β. The values of β for different relative densities of sand is plotted in Figure 5.15 as suggested by the API guidelines. For a particular soil, Figure 5.15 can then be used to obtain the value of β. For example, for a sandy soil with relative density 40%, $\beta = 13.5$. The value of β can then be compared to the h/D ratio at the depth of consideration (h) for a pile diameter of D. Depending on $\frac{h/D}{\beta}$ ratio, the maximum value of shear stress can then be interpolated between $\tau_{max}(2)$ and $\tau_{max}(3)$ as described below, which can then directly be scaled to obtain ultimate lateral soil resistance (p_u) of the $p - y$ curve.
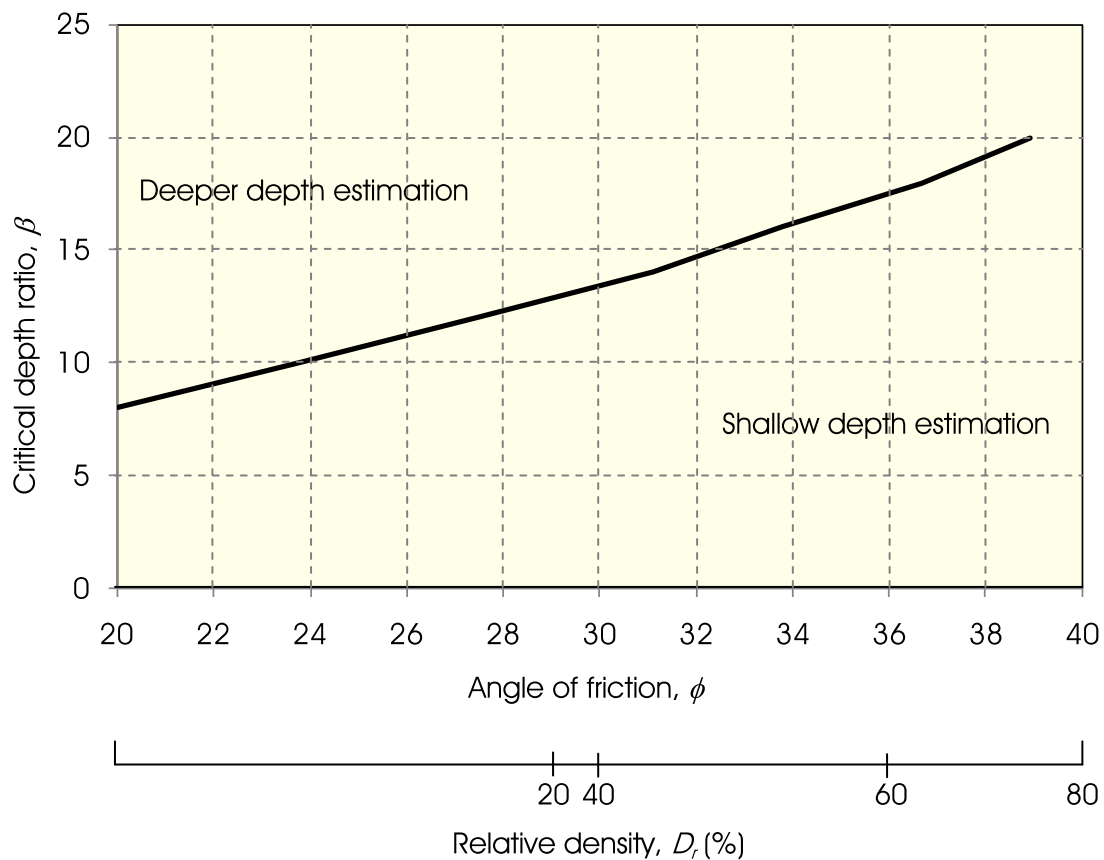
Figure 5.15: Value of critical depth ratio, β (formulated based on API guidelines).

Following the above discussion, the maximum shear stress for the simplified stress-

163

strain curve can be written as Equations 5.13 and 5.14.

$$\tau_{max} = s_u + \left(\frac{p'_{ini}M_c}{2} - s_u\right)\frac{h/D}{\beta}, \text{ if } \frac{h/D}{\beta} < 1 \text{ without impermeable top layer} \quad (5.13)$$

$$\tau_{max} = \frac{p'_{ini}M_c}{2}, \text{ if } \frac{h/D}{\beta} \geq 1 \text{ or with impermeable top layer} \quad (5.14)$$

When the τ_{max} of soil is less than 1kPa, it can be considered to be at its liquid limit and has no strength against shear deformation. For this soil, the lateral resistance of $p - y$ curve can be taken as zero.

5.5.5 Examples of simplified stress-strain curve for liquefied soil

Three sand samples from three different sets of element tests are considered to construct a simplified stress-strain curve and to compare it with the actual test results. The soil data used for three examples are given in Table 5.4. Four parameters are required to construct the stress-strain curve, γ_{to}, G_1, G_2 and τ_{max}. The procedure of obtaining these parameters is briefly presented below.

Step-1:   Input soil parameters are, D_r, p'_{ini} and ϕ_{cs} as given in Table 5.4.

Step-2:   The stress ratio for post-liquefied soil in triaxial compression (M_c) is estimated using Equation 2.6.

Step-3:   For the given D_r value, N_{1-60} is estimated using the correlations given in appendix C.

Step-4: γ_{to} is estimated using Equation 5.5.

Step-5: G_1 is estimated using Equation 5.6.

Step-6: G_2 is estimated using Equation 5.9, where G_{max} is estimated by Equation C.2 given in appendix C.

Step-7: $\tau_{max}(2)$ is estimated using Equations 5.11.

Step-8: $\tau_{max}(3)$ is estimated using Equation 5.12, where the residual shear strength, s_u, can be read from the Figure 2.18 for the N_{1-60} value obtained in Step-3.

The estimated parameters for the simplified stress strain model for three soil samples are presented in Table 5.4. These simplified stress-strain models are also plotted in Figure 5.16 along with their actual element test results. Two values of τ_{max} are used to define stress-strain behaviour at shallow depth and at deeper depth, which will be useful later in estimating the $p - y$ curve.

Table 5.4: Parameters for simplified stress-strain curve for fully liquefied soil.

	Example -1	Example - 2	Example - 3
Given Input Data			
Soil type	Toyoura sand	Toyoura sand	Toyoura sand
Relative density, D_r (%)	65.9	50	32.6
Initial effective overburden pressure, p'_{ini} (kPa)	49	98	49
Critical state angle of friction, ϕ_{cs} (°)	32.6	32.6	32.6
Estimated Data			
M_c	1.31	1.31	1.31
N_{1-60}	16.7	9.6	4.1
γ_{to} (%)	5.23	10.75	19.3
G_1 (kPa)	19.09	9.29	5.17
G_{max} (MPa)	83.8	99.6	54.4
G_2 (MPa)	2.40	2.01	1.55
$\tau_{max}(2)$ (kPa)	32.1	64.2	32.1
$\tau_{max}(3)$ (kPa)	7.35	9.8	2.94

It was not expected to get an exact match between the proposed simplified and experimental stress strain curve, however, the simplified stress-strain curves gave a reasonably acceptable shape and a similar order of magnitude as the experimental results. Most of the data used to arrive at this simplified stress strain curve were concentrated around 45-60% relative densities, and hence a better match was expected in this range of relative densities of the soil.
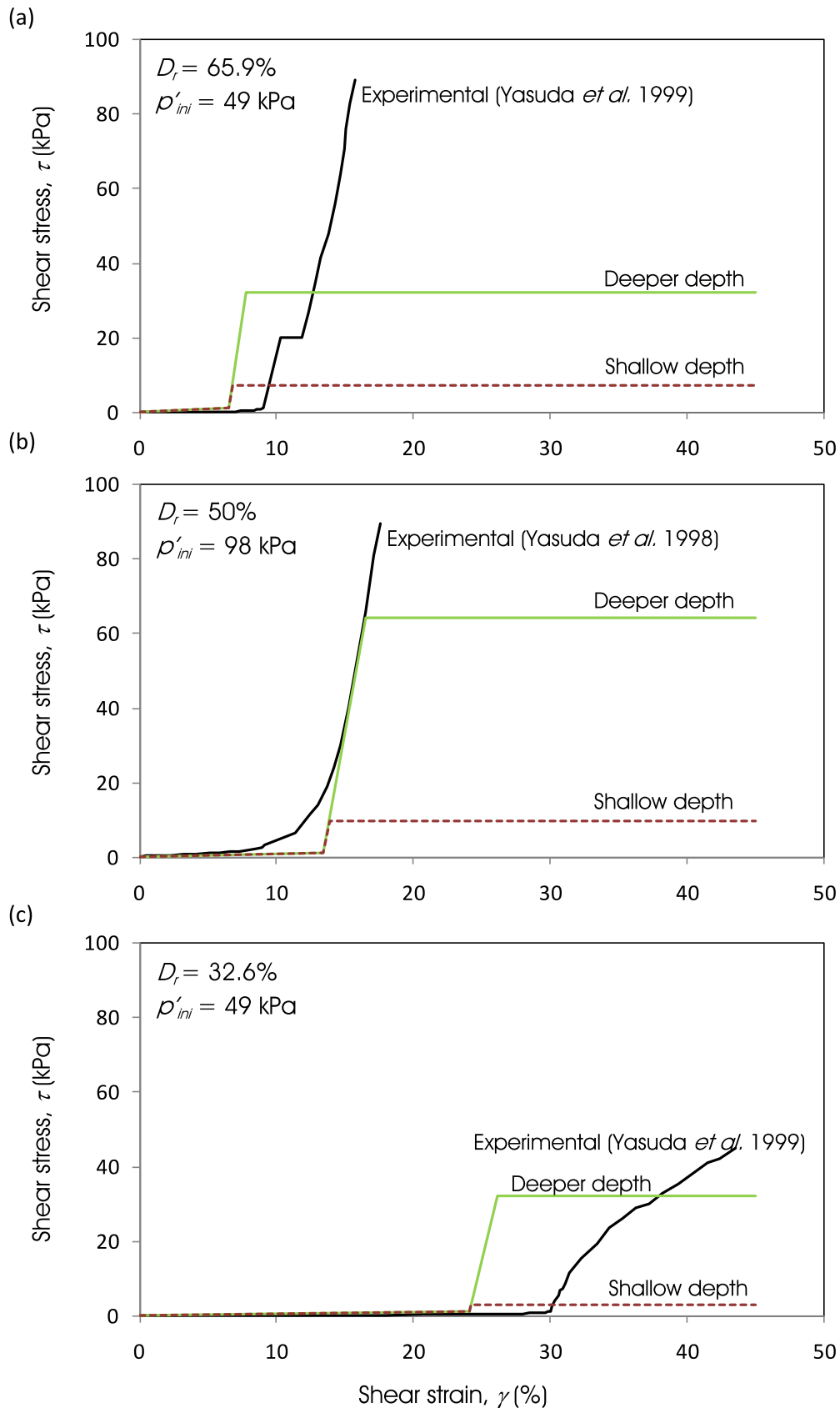
Figure 5.16: Proposed simplified stress-strain curve compared with element test results, (a) Example 1 (b) Example 2 and (c) Example 3 as discussed in section 5.5.5.

5.6 $p - y$ curve construction from stress-strain curve

5.6.1 Background

The technique of constructing a $p-y$ curve relies on the similarity between load-deformation characteristics of the pile with the stress-strain behaviour of the interacting soil (section 1.3.2, chapter 1). From a dimensional analogy of pile-soil interaction with flow type strain field, the strain distribution in soil due to pile deflection (y) is proportional to y/D, where D is the diameter of pile. The same analogy is also followed by Osman & Bolton (2005), Klar (2008) and Klar & Osman (2008) in evaluating the load-deformation solutions based on mobilised strength design approach. Following this analogy, the strain field in the soil is represented by a single value; the average engineering shear strain (γ_{ave}) over a definite deformation zone. The γ_{ave}, as given in Equation 5.15, acts as a link between the strain of the $\tau - \gamma$ curve and the deflection of the $p - y$ curve, and a scaling factor, M_s, equates γ_{ave} with y/D as given in Equation 5.16.

$$\gamma_{ave} = \frac{\int\limits_{vol} \gamma \mathrm{d}vol}{\int\limits_{vol} \mathrm{d}vol} \tag{5.15}$$

$$\gamma_{ave} = M_s \frac{y}{D} \tag{5.16}$$

The γ_{ave} for a field case can be correlated with the engineering shear strain (γ) of the element tests of the soil sample. In an element test, if the triaxial strain is represented by axial strain (ϵ_a) and radial strain (ϵ_r) and the test is undrained, γ can be obtained by Equation 5.17.

$$\gamma = \epsilon_a - \epsilon_r = \epsilon_a - (-0.5\epsilon_a) = 1.5\epsilon_a \tag{5.17}$$

Once the displacement field is related to the strain field, p is calculated from the stress in $\tau - \gamma$ curve of soil corresponding to γ_{ave} with a scaling factor, N_s, as given in Equation 5.18.

$$p = N_s \tau_{ave} D \tag{5.18}$$

where, τ_{ave} is the mobilised stress in the deformation zone as defined in Equation 5.19.

$$\tau_{ave} = \frac{\int\limits_{vol} \tau \, \mathrm{d}vol}{\int\limits_{vol} \mathrm{d}vol} \qquad (5.19)$$

The transformation of stress-strain to $p - y$ with the scaling factor N_s and M_s is shown schematically in Figure 5.17.
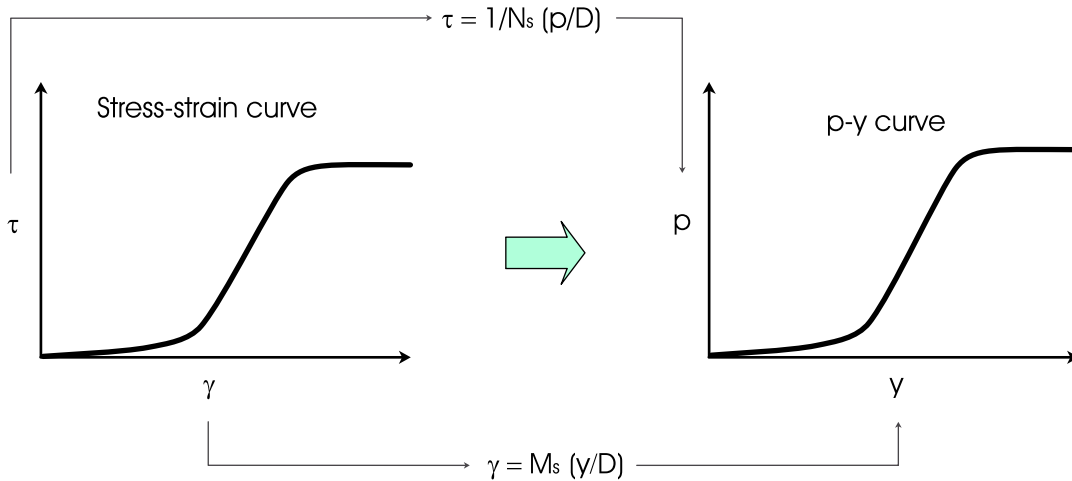
Figure 5.17: Schematic showing the scaling of the $p - y$ curve from the stress strain curve of the soil.

The scaling factor N_s is very similar to the lateral bearing capacity factor (N_c) used in pile design, where the ultimate lateral bearing capacity of the pile foundation is estimated as: $p_u = N_c s_u D$, where s_u is the undrained shear strength of the soil. M_s is also used in a similar way to relate a particular level of axial strain (ϵ_{50}) at half the maximum shear stress from the element test to define characteristic pile deflection (y_c) as $M_{ce}\epsilon_{50}D$, which is later used to construct $p - y$ curve in clay. It may be noted that the notation of M_{ce} is used instead of M_c as the later is used to define the critical stress ratio in triaxial compression. In comparison with M_{ce}, the derivation of M_s (Equation 5.16) relates y with the average engineering shear strain, γ, not the axial strain, ϵ. Various available values of N_c and M_{ce} are given in Tables 5.5 and 5.6 respectively. These relationships for N_c and M_{ce}, although justified in their own right, are not conclusive enough to be used for liquefiable soils. This can be corroborated given the limitation of the experimental techniques used to obtain them, and a strain softening type of material being considered

where the large strain response is governed by strength. Liquefied soil, on the other hand, is a strain hardening material with very low stiffness at smaller strain and higher stiffness at larger strain, and the large strain behaviour is governed by stiffness. The main aim behind the formulation of N_c and M_{ce} values was to obtain single values of p_u and y_c which may not be suitable for scaling of a stress-strain curve throughout to a obtain $p - y$ curve. Another major limitation of the suggested values of N_c and M_{ce} is that they are not interrelated, whereas in real situation the strain field is related to the nonlinear stress-strain response as well as loading stress history. Hence, N_s and M_s can be seen only as scaling parameters, different than N_c and M_{ce}, and hence studied in detail in the following section. The study was aimed to better understand the derivation of N_s and M_s and how to implement them for liquefied soil.

Table 5.5: Suggested values of bearing capacity factor N_c.

Reference(s)	N_c	Remarks
Matlock (1970)	$3 + \frac{\sigma_z}{s_u} + J\frac{z}{D}$ 3 at shallow depth 9 at deeper depth	Experimentally calibrated for different depth (z) $J=$ 0.25 for Lake Austin clay ,0.5 for Sabine clay and Offshore clays in gulf of Mexico
Reese *et al.* (1975)	$2 + \frac{\sigma'_v}{(s_u)_{ave}} + 2.83\frac{z}{D}$	Experimentally calibrated
Reese & Welch (1975)	$2 + \frac{(\sigma'_v)_{ave}}{(s_u)_{ave}} + 0.5\frac{z}{D}$	Experimentally calibrated
Gazioglu & O'Neill (1984)	$3 + 6\left(\frac{z}{3D\left(\frac{E_p I_p}{E_s D^4}\right)}\right)$	Relative soil pile stiffness considered
Randolph & Houlsby (1984)	9.14 (Smooth pile) 11.94 (perfectly rough pile) 10.5 (Suggested for practical use)	An exact solution based on plasticity theory for clayey soil
Kulhawy & Chen (1995)	9 (Driven pile) 12 (Drilled pile)	Suggested practical values
Einav & Randolph (2005)	18.566	A potential flow solution around a pile
Klar (2008)	14.52 (Rough pile) 10.06 (Smooth pile)	Analytical study based on mobilized strength design approach with elastic strain field around pile
Note: $\sigma_z=$ Total overburden at depth z, $s_u =$ undrained shear strength at depth z, $(\sigma'_z)_{ave}$ and $(s_u)_{ave}=$ Average value over depth z.		

Table 5.6: Suggested relationship between pile deflection (y) and soil strain.

Reference(s)	Axial soil strain (ϵ_a) to pile deflection, $y_c = M_{ce}\epsilon D$	Remarks
McClelland & Focht Jr (1958)	$y = 0.5\epsilon_a D$	Experimentally calibrated
Matlock (1970)	$y_{50} = 2.5\epsilon_{50}D$ (Soft clay)	Uses the relationship derived by Skempton (1951) for strip footing
Reese & Welch (1975)	$y_{50} = \epsilon_{50}D$ (Stiff clay without free water)	Skempton (1951) concept modified with field test values
Reese et $al.$ (1975)	$y_{50} = 2.5\epsilon_{50}D$ (Stiff clay with free water)	Uses Skempton (1951) relationship and verified with field test data
Stevens & Audibert (1979)	$y_c = 8.9\epsilon_{50}\sqrt{D}$	Calibrated with field test data with varying diameter
Gazioglu & O'Neill (1984)	$y_c = 0.8\epsilon_{50}\sqrt{D}\left(\frac{E_pI_p}{E_s}\right)^{0.125}$	Considering the relative soil pile stiffness
Dunnavant & O'Neill (1989)	$y_c = 0.0063\epsilon_{50}D\left(\frac{E_pI_p}{E_sL^4}\right)^{-0.875}$	Considering the relative soil pile stiffness
Klar (2008)	$y = \frac{1}{2.6}\gamma D$	Analytical study on fully plastic clay with an elastic strain field around pile

Note: y_c = Characteristic deflection, y_{50} = Deflection at half ultimate resistance, ϵ_a= Axial strain, ϵ_{50}= Axial strain at half maximum shear stress. γ = Engineering shear strain ($1.5\epsilon_a$ in a triaxial tests)

5.6.2 Proposed construction technique for the $p - y$ curve

The construction technique of a monotonic $p - y$ curve based on stress-strain scaling through N_s and M_s can be summarised in four major steps, such as:

Step-1: Obtain undrained monotonic τ-γ relationship for the soil.

The post liquefaction τ-γ relationship can be obtained from element testing of soil samples (for example: undrained cyclic triaxial test, or hollow cylinder test, etc). If the element test data are not readily available, the proposed simplified model of monotonic post liquefied stress-strain behaviour of soil as described section 5.5 can be chosen.

Step-2: Find pile displacements, y, using appropriate value of M_s (see section 5.7) with the shear strain values in the τ-γ curve.

Step-3: Relate τ to p using the appropriate value of N_s (see section 5.7).

Step-4: From the p and y values corresponding to the τ-γ values, construct a smoothed p - y curve.

5.7   Choosing scaling factors, N_s and M_s

5.7.1   Virtual work approach

A virtual work approach was used to obtain the scaling factors, N_s and M_s and to study their suitability for liquefiable soil. The soil-pile interaction at a particular depth was represented by a plane strain 2D model as shown in Figure 5.18.
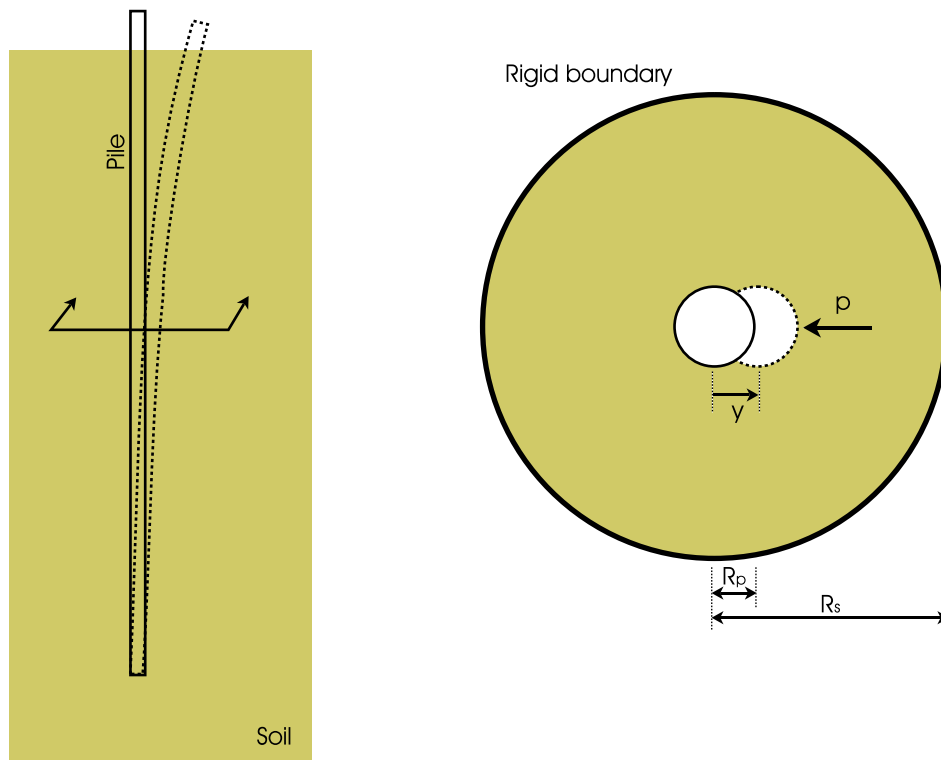
Figure 5.18: Consideration of soil-pile interaction at a particular depth in FE analysis.

Assuming the soil-pile system is initially in equilibrium, any incremental work done by pile movement will be equal to the incremental stain energy in the system. The pile was considered rigid with respect to the soil, so most of the strain energy was carried by the soil. The liquefied soil was considered to be fully undrained (i.e., Poisson's ratio = 0.5) and the plane strain condition was assumed. The following conditions were required to be satisfied in the system:

1. Pile deflection has to be compatible with the strain distribution in the soil.

2. The stresses in the soil have to be in equilibrium with the total reaction force on pile.

Considering Tresca yield criterion, the incremental work done due to the displacement of inner disk in terms of maximum shear stress and shear strain can be written as Equation 5.20.

$$\delta W = \int_{vol} (\mid \tau_{max} \mid \mid \delta\gamma_{max} \mid) dvol \tag{5.20}$$

where, the values of τ_{max} and $\delta\gamma_{max}$ can be defined as Equations 5.21 and 5.22 respectively. Please note that the incremental work done (δW) was computed for a unit slice thickness and hence has the unit of force.

$$\tau_{max} = \mid (\sigma_1 - \sigma_3) \mid /2 \tag{5.21}$$

$$\delta\gamma_{max} = \mid (\delta\epsilon_1 - \delta\epsilon_3) \mid \tag{5.22}$$

The equation for external and internal work done in the system can then be written as:

$$p\delta y = \delta W \tag{5.23}$$

where, p is the total reaction force over the boundary of the inner disk due to the incremental inner disk displacement of δy.

Combining Equations 5.23 and 5.18, N_s can then be written as:

$$N_s = \frac{\delta W}{\delta y \tau_{ave} D} \tag{5.24}$$

In Equation 5.24, τ_{ave} represents the average mobilised maximum shear stress representative of the stress field around pile.

The value of N_s depends on the extent of the fixed boundary chosen in the analysis. Displacements and stresses around a rigid disc have already been established by Baguelin *et al.* 1977. Unfortunately, displacements in both analytical and numerical analyses are

172

model size dependent. As can be seen later in the analysis (see Figure 5.27), the displacement to mobilise same lateral resistance increases with increasing soil boundary. For soil boundary tending to infinity the mobilised displacement will also tend to infinity. Consequently, there will be infinite values for N_s and M_s as they rely upon the mobilised displacements and lateral resistance developed in soil. Hence, to obtain rational values for N_s and Ms, it necessary to find a reasonable boundary distance which allows to determine unique values for these coefficients. Hence, using upper bound theorem, τ_{ave} is sought in the considered soil domain that minimizes the N_s value for a known displacement of y. The boundary at which the lowest value of N_s occurs can be considered as the effective deformation zone and the average shear strain mobilised (γ_{ave}) in the deforming soil due to pile deflection (y) can be from the FE analysis as given in Equation 5.16. Following the dimensional reasoning, M_s can then be obtained from γ_{ave} as given in Equation 5.25.

$$M_s = \frac{\gamma_{ave}}{(y/D)} \tag{5.25}$$

The virtual work method as described here is similar to the mobilised strength design (MSD) method used by Osman & Bolton (2005) to predict load settlement behaviour of shallow circular footing from stress-strain properties of a characteristic soil sample. The MSD method was further adopted by Klar (2008) to represent a pile-soil interaction problem analytically. In both the approaches, the first step is to choose a boundary for continuous displacement field, over which the deformation mechanism can be applied. Often, several boundary types and sizes need to be tested to obtain the lowest value of N_s. In a situation like pile vibration in liquefiable soil, it could be difficult to find the right mechanism and boundary. Hence, to study this problem, a finite element model with variable boundary sizes was prepared using COMSOL Multiphysics® (COMSOL, 2009) as discussed below.

5.7.2   Numerical analysis

A 2D pile-soil interaction was modelled in a plane strain environment in COMSOL. Mesh optimization and some initial parametric studies were performed to finalise the analysis procedure. A non-slip boundary was considered for the pile-soil interface, which corre-

sponds to a rough interface. Hence, the need of pipe material model was avoided and the inner boundary of the soil was considered as the pile surface. The pile displacement (y) was applied to the inner boundary of the soil. The exterior soil boundary was fixed. A triangular mesh was adopted (Figure 5.19) with Lagrange-quadratic elements. Three types of material models were used in the study:

a) Perfectly plastic material over an elastic strain field

b) Elastic material

c) Hyper-elastic material (like liquefied soil)
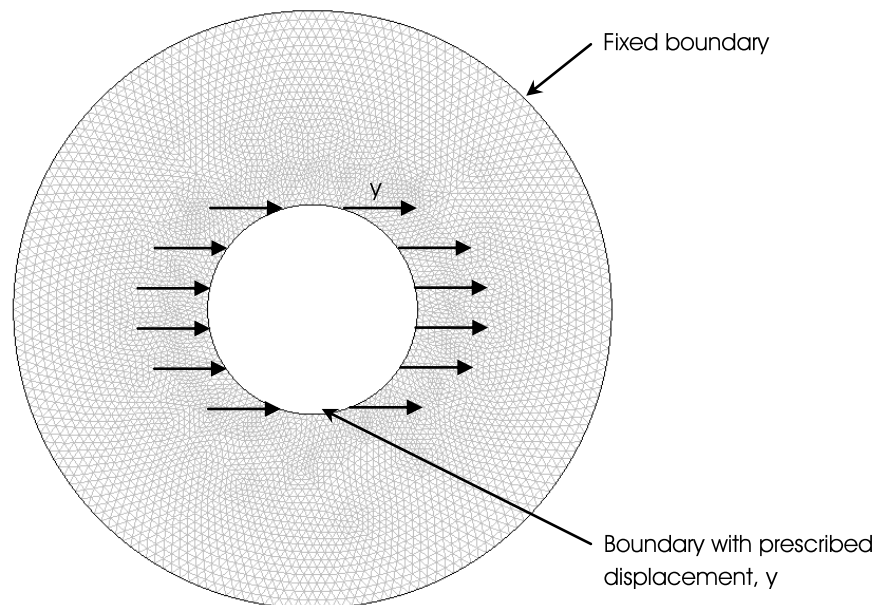
Figure 5.19: Pile-soil interaction mesh in FE model.

5.7.2.1 Perfectly plastic material over an elastic strain field

Generally the maximum resistance of clay is estimated using the perfectly plastic material theory. The analysis uses an elastic strain field around the pile and a perfectly plastic material with mobilizing shear strength of s_u. This analysis was carried out here in COMSOL to verify the FE model with available analytical solution by Klar (2008). The material properties assigned to the model were: Elastic Young's modulus (E_s) = 30MPa and Poisson's ratio = 0.499. A parametric solver was used in a plane strain static analysis

174

environment. The solution for N_s was estimated from the FE model results for the radius of soil (R_s) varying from 2 to 6 times that of the pile radius (R_p). An upper bound elastic solution was sought where N_s was evaluated for different soil boundaries and the boundary at which lowest N_s value was considered as the effective zone of influence.

The equation of virtual work (Equation 5.20) for a purely plastic material with an elastic strain field can be written as Equation 5.26, where the material has reached its plastic shear strength everywhere.

$$\delta W = s_u \int\limits_{vol} \delta \gamma_{max} \mathrm{d}vol \tag{5.26}$$

Combining Equations 5.24 and 5.26 for $\tau_{ave} = s_u$, N_s can be calculated as given in Equation 5.27.

$$N_s = \frac{\int\limits_{vol} \delta \gamma_{max} \mathrm{d}vol}{\delta y D} \tag{5.27}$$

Figure 5.20 plots the N_s value obtained from present FE model and compares that with Klar's (2008) analytical solution. Please note that the Klar's (2008) solution values are individual data points as read from the plot. As can be seen in the figure, both values are in close agreement. The lowest N_s value obtained was 14.525, which occurred at a soil boundary of $2.85R_p$. The mechanism of displacement and shear stress distribution at $R_s = 2.85R_p$ is shown in Figure 5.21 along with the Klar (2008) model. As expected, the pattern of the displacement field is same in both the models.

Once the solution for minimum N_s was obtained, γ_{ave} was estimated as a representative strain due to pile displacement for the soil boundary of $2.85R_p$. M_s was then estimated to be 2.6 (i.e., $\gamma_{ave} = 2.6\ (y/D)$) by using Equation 5.25, which is the same as obtained by Klar (2008). This verifies the concept of M_s, N_s and validates the present FE model with the available analytical solution.
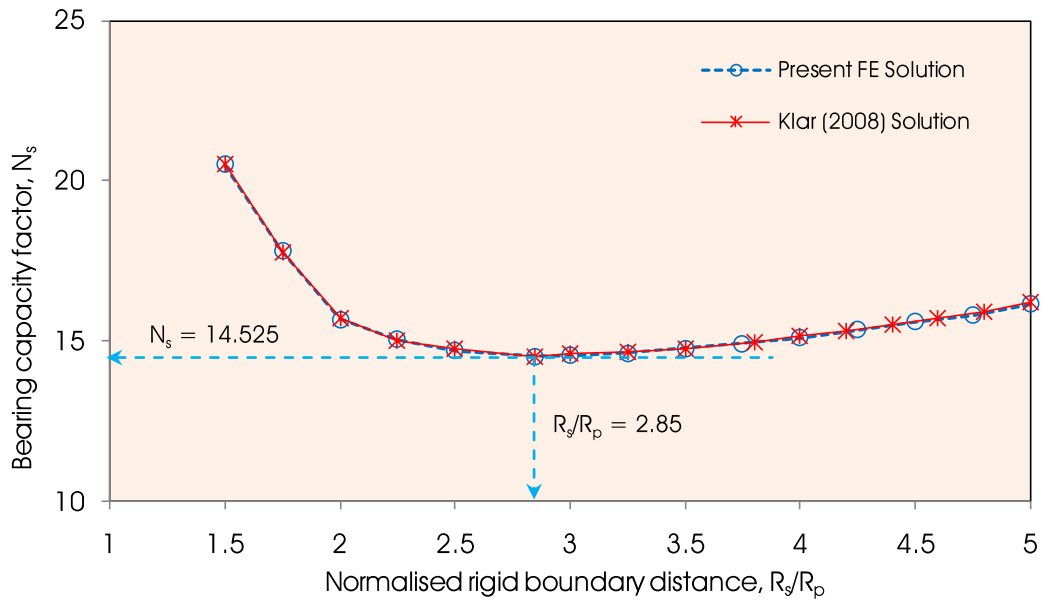
Figure 5.20: Solution of N_s for fully plastic soil as a function of soil boundary, comparison of present model and model by Klar (2008).
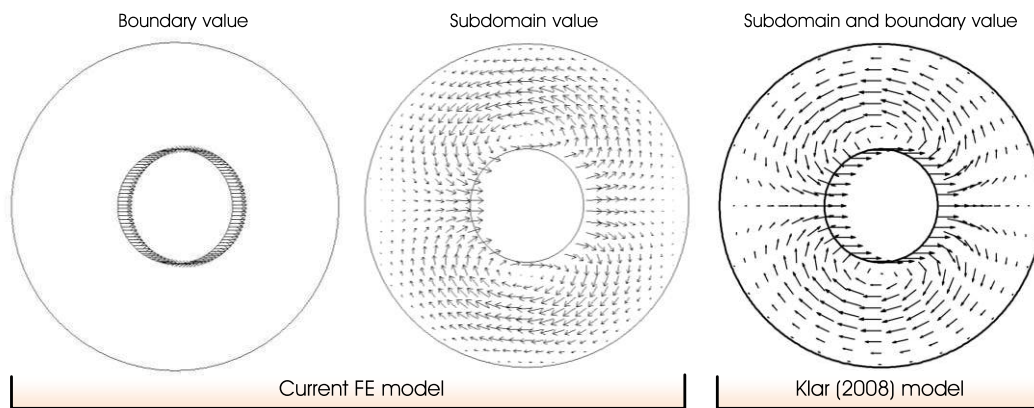
Figure 5.21: Comparison of deformation mechanism of this FE study and Klar (2008) analytical model.

5.7.2.2 Elastic material

The above numerical model was re-analysed with an elastic soil. The same material properties as assigned to the above model were also used in this model, where elastic Young's modulus $(E_s) = 30\text{MPa}$ and Poisson's ratio $= 0.499$.

Figure 5.22 plots the N_s values with respect to soil boundary. The N_s was lowest at the soil boundary of $2.85R_p$ with a value of 18.16, where τ_{ave} is the value as defined in Equation 5.19. In addition to the FE results, solutions by Einav & Randolph (2005)

and Randolph & Houlsby (1984) and Klar (2008) are also presented in Figure 5.22 for comparison. Please note that the present solution was for elastic soil, where as the solutions by Randolph & Houlsby (1984) and Klar (2008) were for perfectly plastic soil. On the other hand, the Einav & Randolph (2005) solution used an upper bound solution using the method of strain path in the flow field derived from classical fluid mechanics theories with strain softening behaviour of an incompressible material. The N_s value in the present FE solution was close to the potential flow solution by Einav & Randolph (2005) (N_s= 18.566) but higher than the exact solution by Randolph & Houlsby (1984) (N_s= 11.94). The value of M_s corresponding to $2.85R_p$ soil boundary was found to be 2.6, same as the solution obtained by Klar (2008). However this value is 6.5 times higher than the value suggested by Matlock (1970) for soft clay based on the experimental values on strip footing as obtained by Skempton (1951). The elastic strain field for $R_0 = 2.85R_p$ is shown in Figure 5.23, where the colour contours show the absolute engineering shear strain values and the arrows indicate the displacement vectors. As expected, the maximum shear strain was occurring at the pile soil boundary orthogonal to the direction of displacement loading.
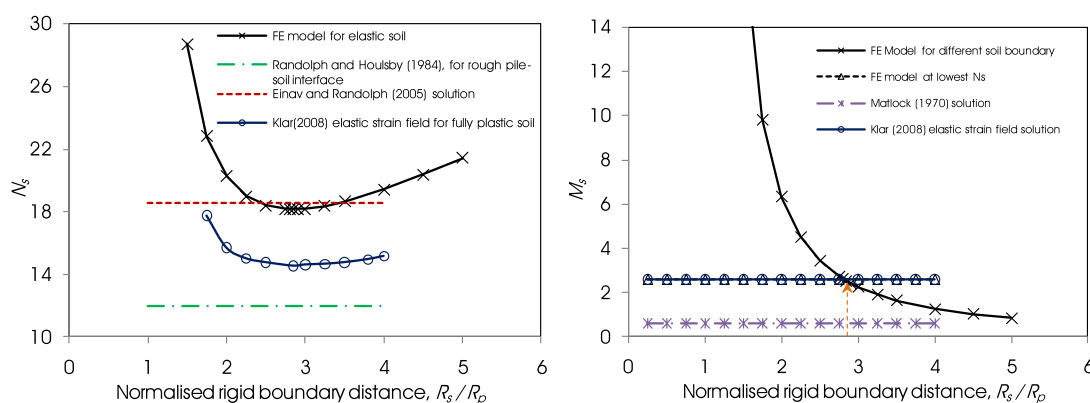
Figure 5.22: Scaling factors N_s and M_s for linear elastic soil with respect to the extent of outer rigid boundary of soil.

The FE model also gives the $p-y$ curve for the domain considered, where p can be obtained integrating the resistance over the inner boundary for different levels of y. The

Young's modulus (E) of the material = 30 MPa
Poisson's ratio of the material = 0.499

Applied displacement at inner ring = 0.01m
Boundary at outer ring: Fixed

1m
2.85m

Max: 0.0563

0.05

0.04

0.03

0.02

0.01

Min: 1.619e-4

Maximum Engineering
Shear Strain (ε_1-ε_3)
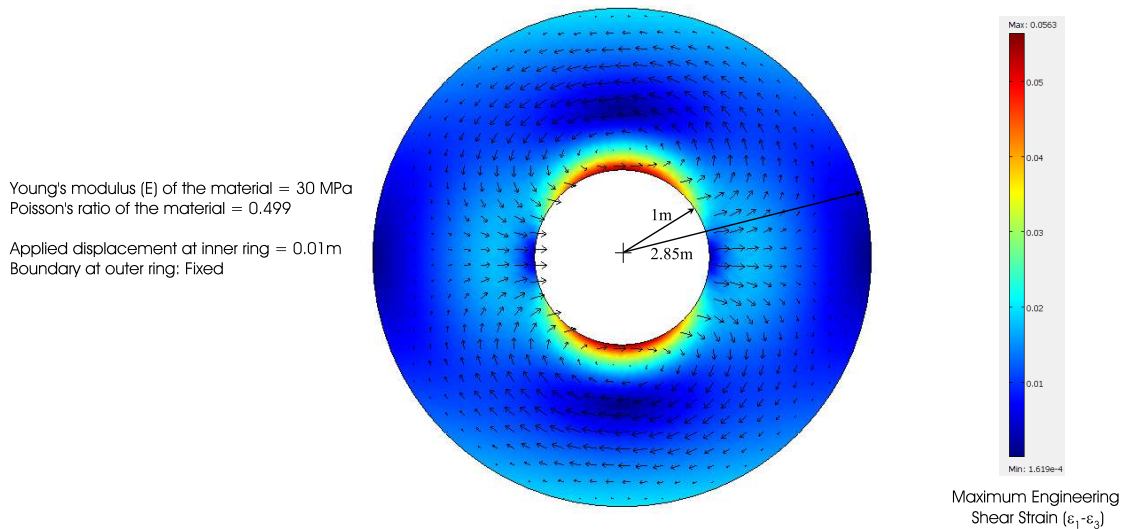
Figure 5.23: Elastic strain field distribution due to displacement of inner cylinder.

$p - y$ curve obtained from FE model for $R_s = 2.85 R_p$ was compared with the $p - y$ curve estimated using scaling factors for the elastic soil under consideration. The stress strain curve was scaled to the $p - y$ curve with N_s and M_s values of 18.16 and 2.6 respectively. With linear elastic material, the $p - y$ curve was also expected to be linear elastic. Figure 5.24 plots the results of this comparison, where both the methods yield same answer. It validates the $p - y$ curve construction procedure from stress strain behaviour for a linear elastic soil.

5.7.2.3   Hyperelastic material (Solution for M_s and N_s values for liquefied soil)

The above numerical model was re-analysed with its material model modified to represent the liquefied soil. Considering the fact that the liquefied soil behaves like an incompressible fluid, the same principle of obtaining M_s and N_s values as studied in section 5.7.2.1 was regarded applicable also to the liquefied soil. The simplified monotonic stress-strain curves of liquefied soil, which show a hyperelastic behaviour, were used. A parametric solver was used in a plane strain static analysis environment. To include the material nonlinearity, an equivalent linear elastic model was implemented in COMSOL, where the elastic modulus was assigned as a strain dependent parameter. As discussed in section 5.5, the ratio of G_2/G_1 for liquefied soils vary with different initial relative densities. For the listed
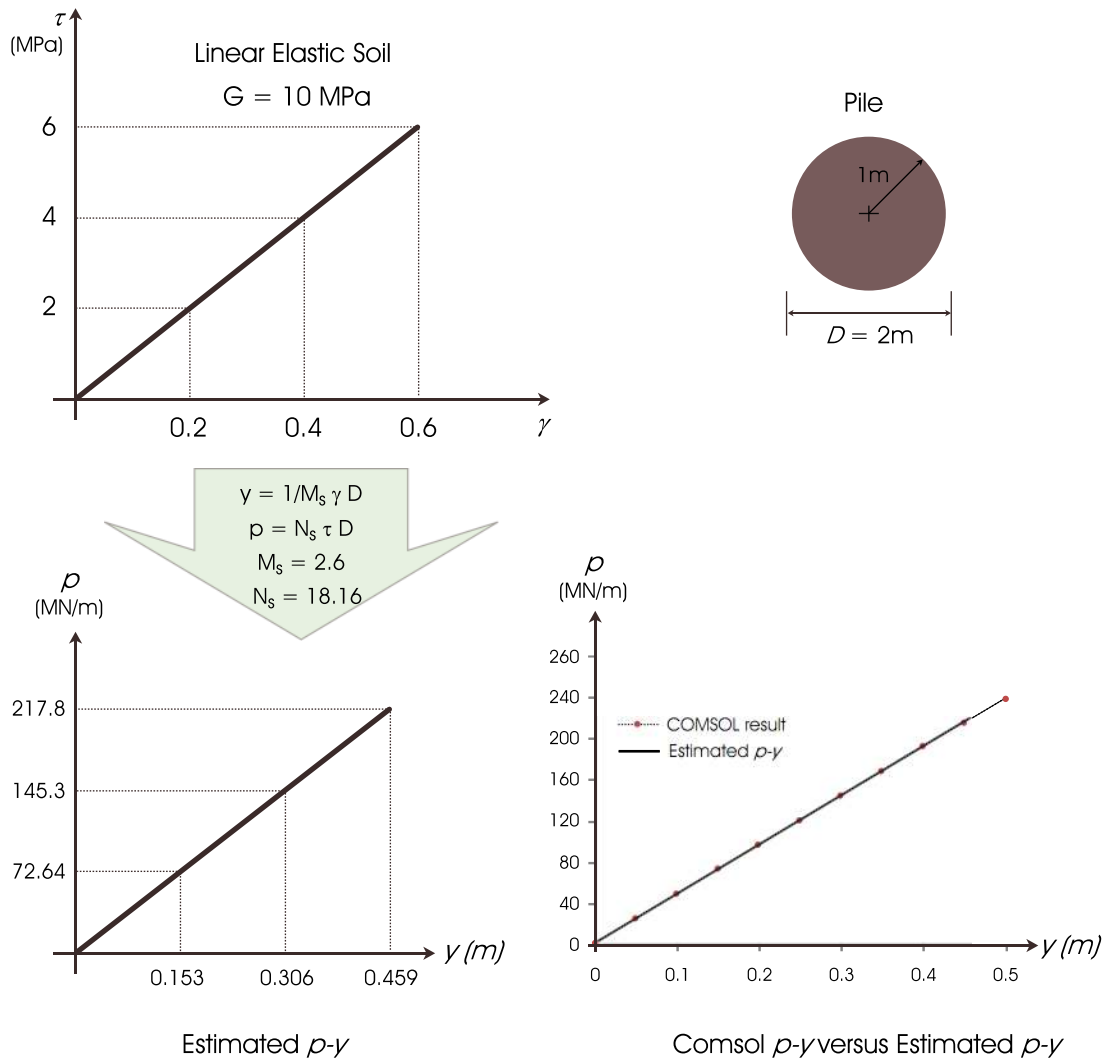
Figure 5.24: Comparison of estimated $p - y$ curve and $p - y$ curve from FE model for a linear elastic soil.

liquefied soil's monotonic behaviour in Table B.1, the G_2/G_1 ratio vary between 9 to 335. Hence, six stress-strain models were chosen for this analysis, where γ_{to}, τ_{max} and G_1 were fixed but the ratio of G_2/G_1 was varying from 10 to 500 ($G_2/G_1 = 10, 25, 50, 100, 200$ and 500). Figure 5.25 shows the six nonlinear material model used in COMSOL. The values of the fixed parameters in the model were as follows: $1.25\gamma_{to} = 0.075$, $\tau_{max} = 50$kPa and $G_1 = 1.25/0.075 = 16.7$kPa.

For all the models, material nonlinearity of the soil was defined as a backbone curve of Young's modulus (E_s) with respect to engineering shear strain (γ). This backbone curve was obtained from the $\tau - \gamma$ curve using a Poisson's ratio of 0.5 and $E_s = 3G$. In

(a)

(b)
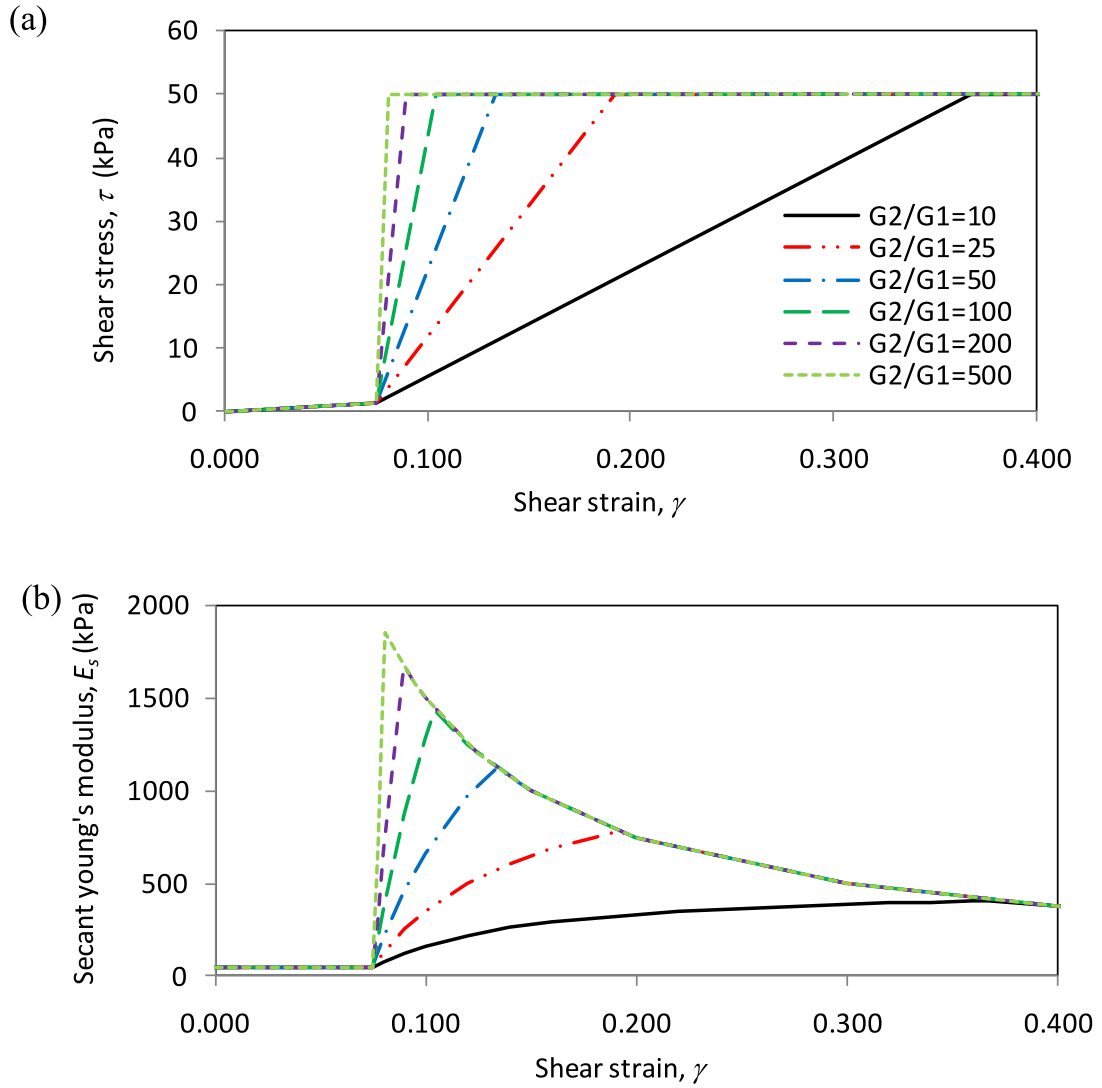
Figure 5.25: Simplified model of liquefied soil used as input to the FE model in COMSOL.

each step of the analysis, the maximum engineering shear strain was estimated according to Equation 5.28 and the material secant Young's modulus was then modified accordingly as per the pre-defined $E_s - \gamma$ curve.

$$\gamma = \sqrt{(\epsilon_x - \epsilon_y)^2 + 4\epsilon_{xy}^2} \tag{5.28}$$

Figure 5.26 compares the stress-strain path in a soil element near to pile surface followed by the FE model, where $G_2/G_1 = 100$, with the backbone stress-strain curve

assigned to the model in the form of $\gamma - E_s$ relationship. The figure shows that the stress-strain path in the soil during the FE analysis exactly followed the same stress-strain behaviour as assigned.
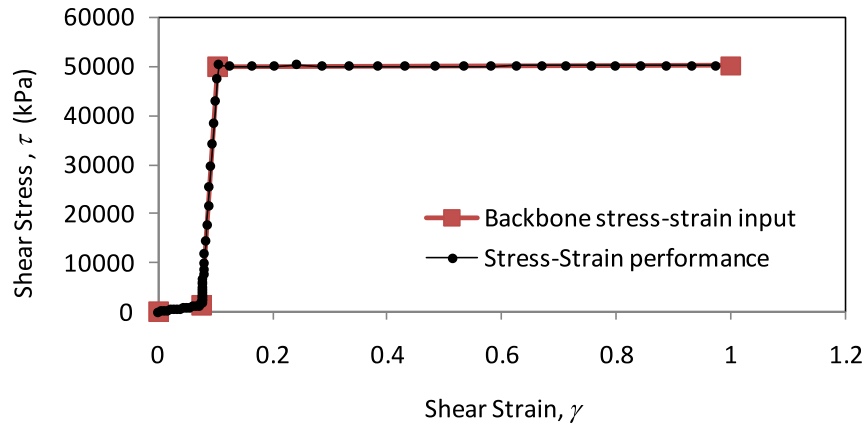
Figure 5.26: Stress strain performance of the FE model in COMSOL, and its comparison with the assigned backbone stress-stress curve.

The analyses were performed for a range of boundary sizes. The $p - y$ curve and corresponding N_s and M_s values for the liquefiable soil model of $G_2/G_1 = 100$, as obtained from the analysis for various boundaries, are plotted in Figure 5.27. The analysis did not converge over the full load path for each soil element, and hence the upper plateau is not apparent in the results. When the stress condition in most of the soil elements was approaching the τ_{max} value (see Figure 5.25), the analysis was getting unstable. In practice, however, τ_{max} is a hypothetical value assigned to limit the stress-strain behaviour of the soil (section 5.5). Hence, the convergence at this level does not significantly affect the results, as the zone of particular interest is the transition between G_1 to G_2. In the analysis, when the external fixed boundary was extended it took more pile displacement to mobilise the second shear modulus G_2 of the soil. The $p - y$ curves derived in this way were highly dependent on the extent of the chosen boundary, and consequently the scaling factors, N_s and M_s were also affected. Following the analogy of average shear strain representing the deformation field in soil, the $p - y$ curve, N_s and M_s values were also plotted with respect to the average shear strain, as shown in Figure 5.28. As can

181

be seen in the figure, $p-y$ curves for all the boundaries with respect to average shear strain values roughly stack together for all the boundaries. This shows that the average shear strain could probably be adequately used to represent the deformation state of the soil. The strain field for different levels of average shear strain is presented in Figure 5.29. As expected, with progressive displacement, the maximum engineering shear strain front progresses orthogonal to the displacement loading. N_s and M_s values were then studied with respect to average shear strain and plotted for different boundaries for the elastic soil model and for all six liquefiable soil models in Figures 5.30 and 5.31.
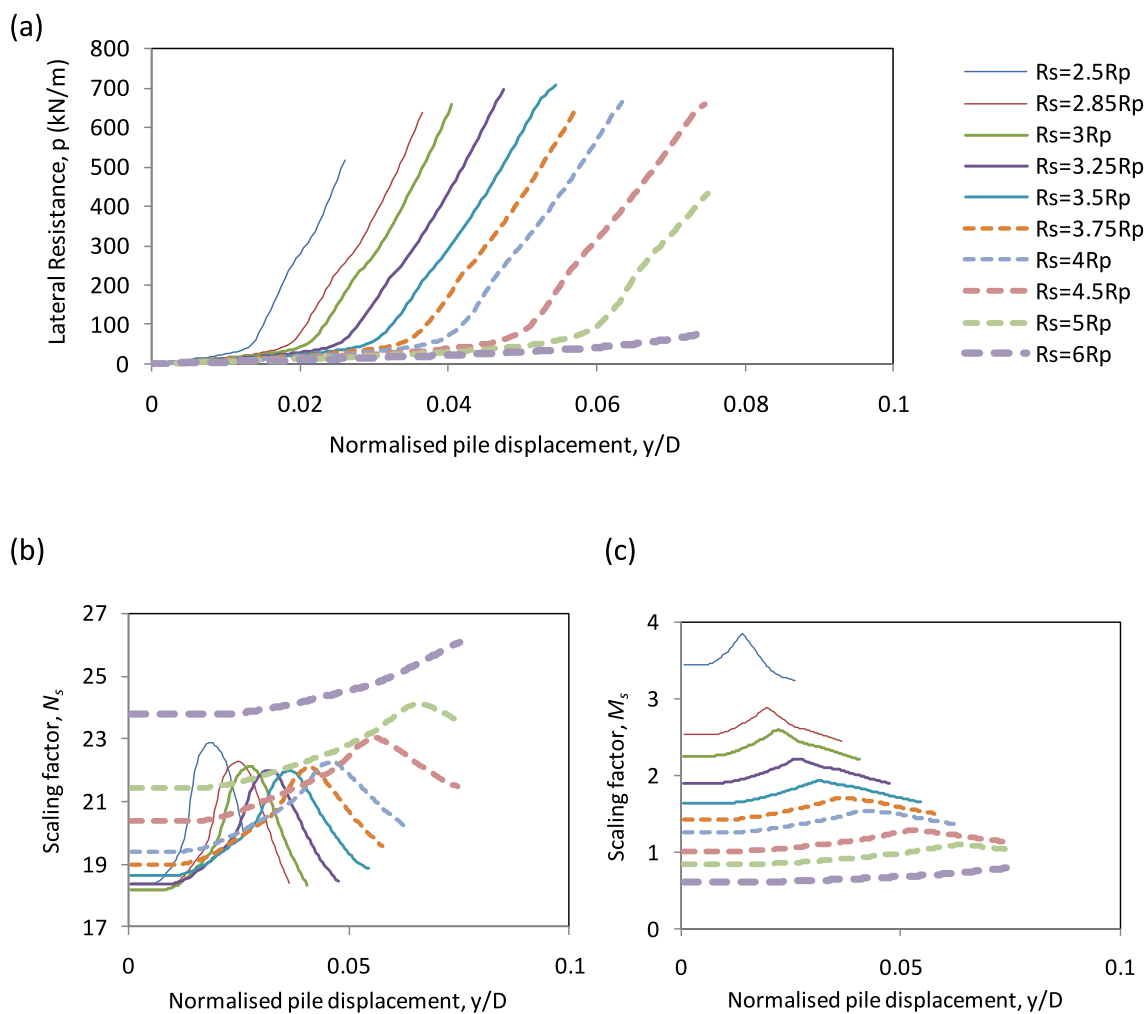
Figure 5.27: (a) $p-y$ curves for the liquefiable soil model of $G_2/G_1 = 100$ as obtained from numerical analysis by COMSOL for different soil boundary distances (R_s), and corresponding (b) N_s and (b) M_s values.
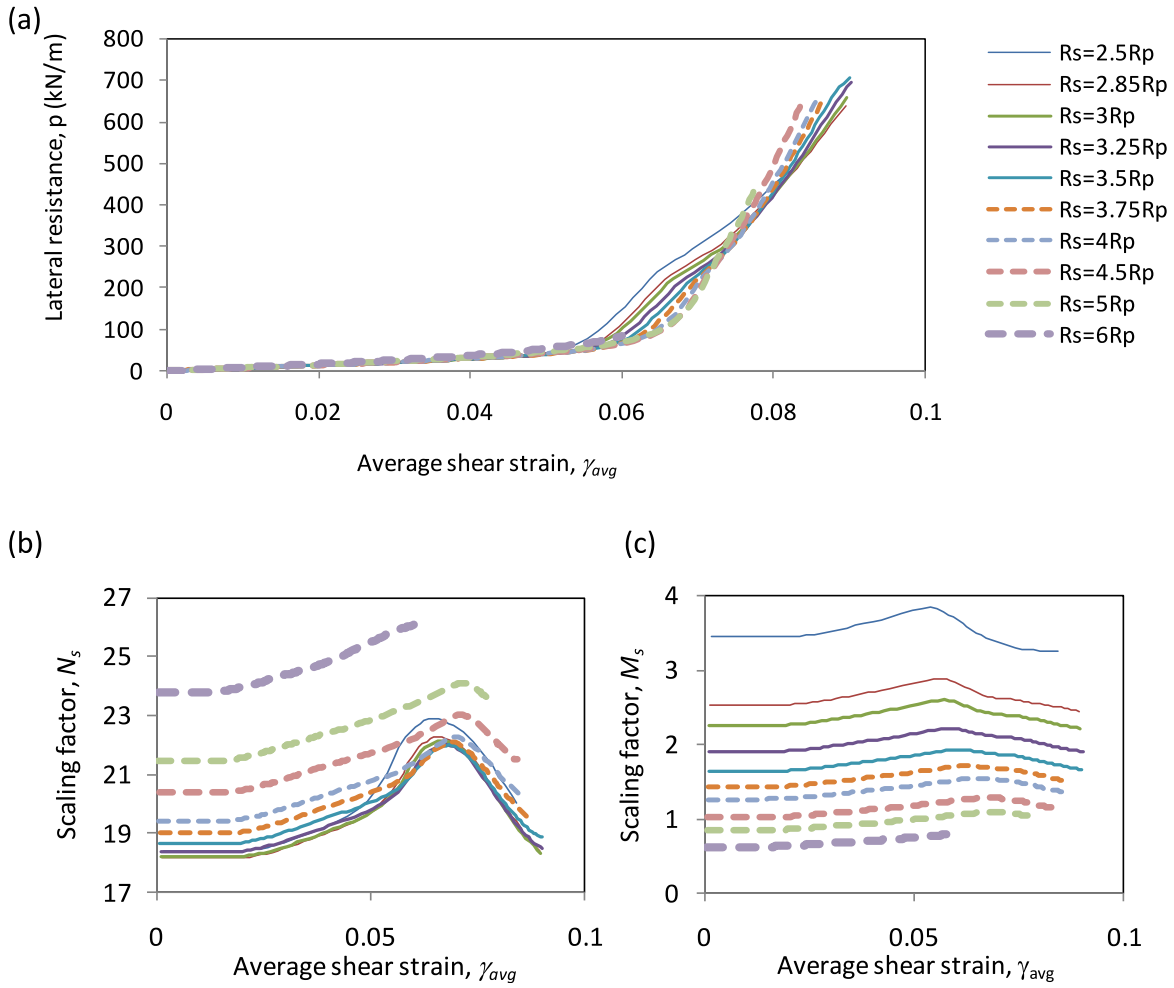
Figure 5.28: (a) $p - y$ curves for the liquefiable soil model of $G_2/G_1 = 100$ as obtained from numerical analysis by COMSOL for different soil boundary distances (R_s) plotted against the average shear strain in the soil, and corresponding (b) N_s and (b) M_s values.

Considering the upper bound theorem, the boundaries corresponding to minimum N_s values were considered as the effective zone of influence and the corresponding values of N_s and M_s were chosen as the scaling factors. As can be seen in the Figures 5.30 and 5.31, the effective zone is nonlinear and it increases with increase in nonlinearity in the system. When γ_{ave} was about 0.019 (i.e., about $\frac{1}{4}^{th}$ of the take off shear strain, 0.075), the nonlinearity in the system was noticeable. To note, although the average shear strain was still in initial elastic phase, some of the soil elements have already yielded and strained
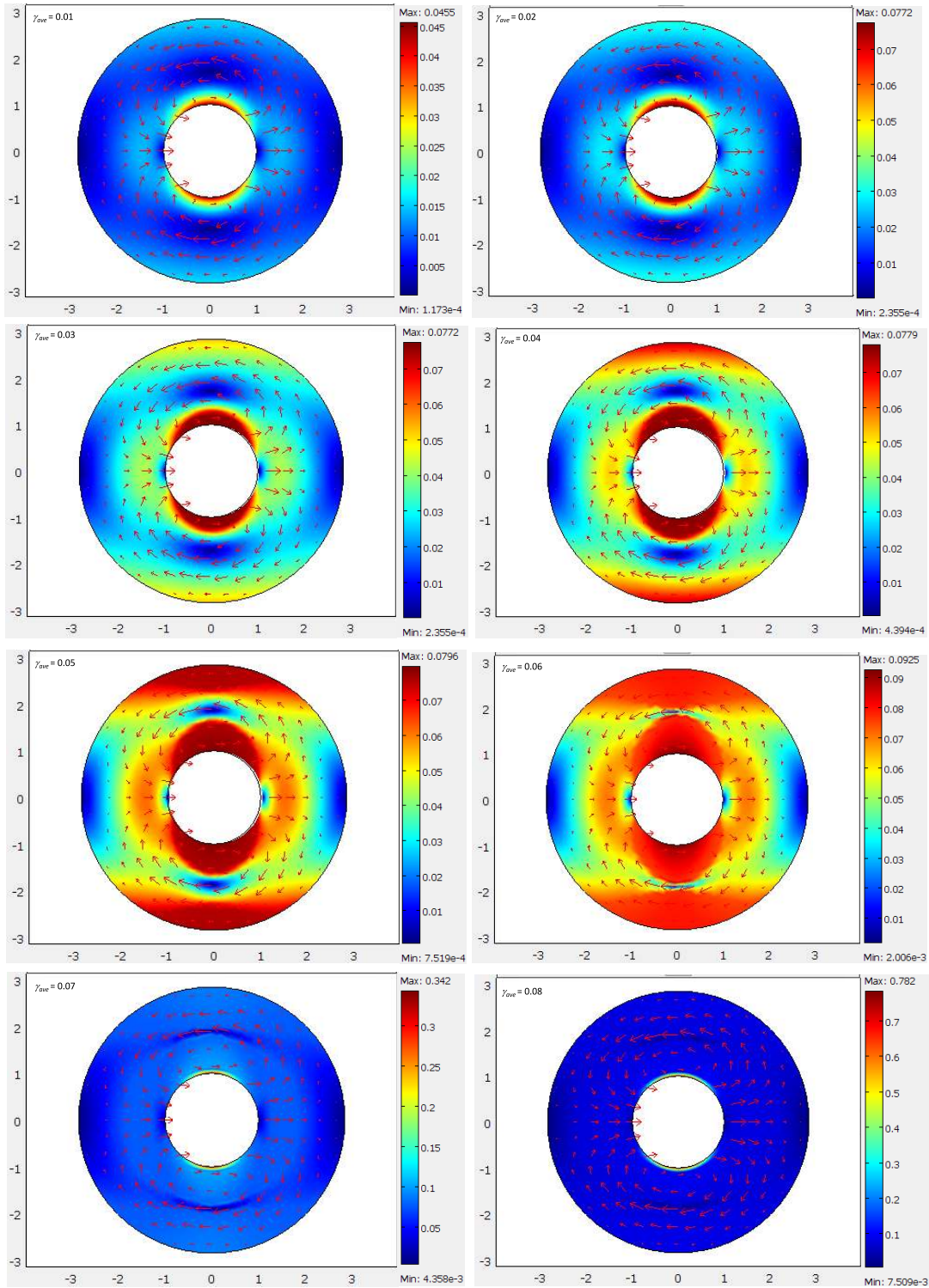
Figure 5.29: Strain field (engineering shear strain, γ) at different average engineering shear strain (γ_{ave}) levels for the liquefied soil model $G_2/G_1 = 100$ at $R_s = 2.85R_p$.

beyond 0.075 (7.5%) shear strain. In the very initial phase of straining, the soil boundary of $2.85R_p$ was acting as the effective zone, where most of the soil elements were linear elastic and strained below 0.075 shear strain. However, when γ_{ave} exceeded 0.019 shear
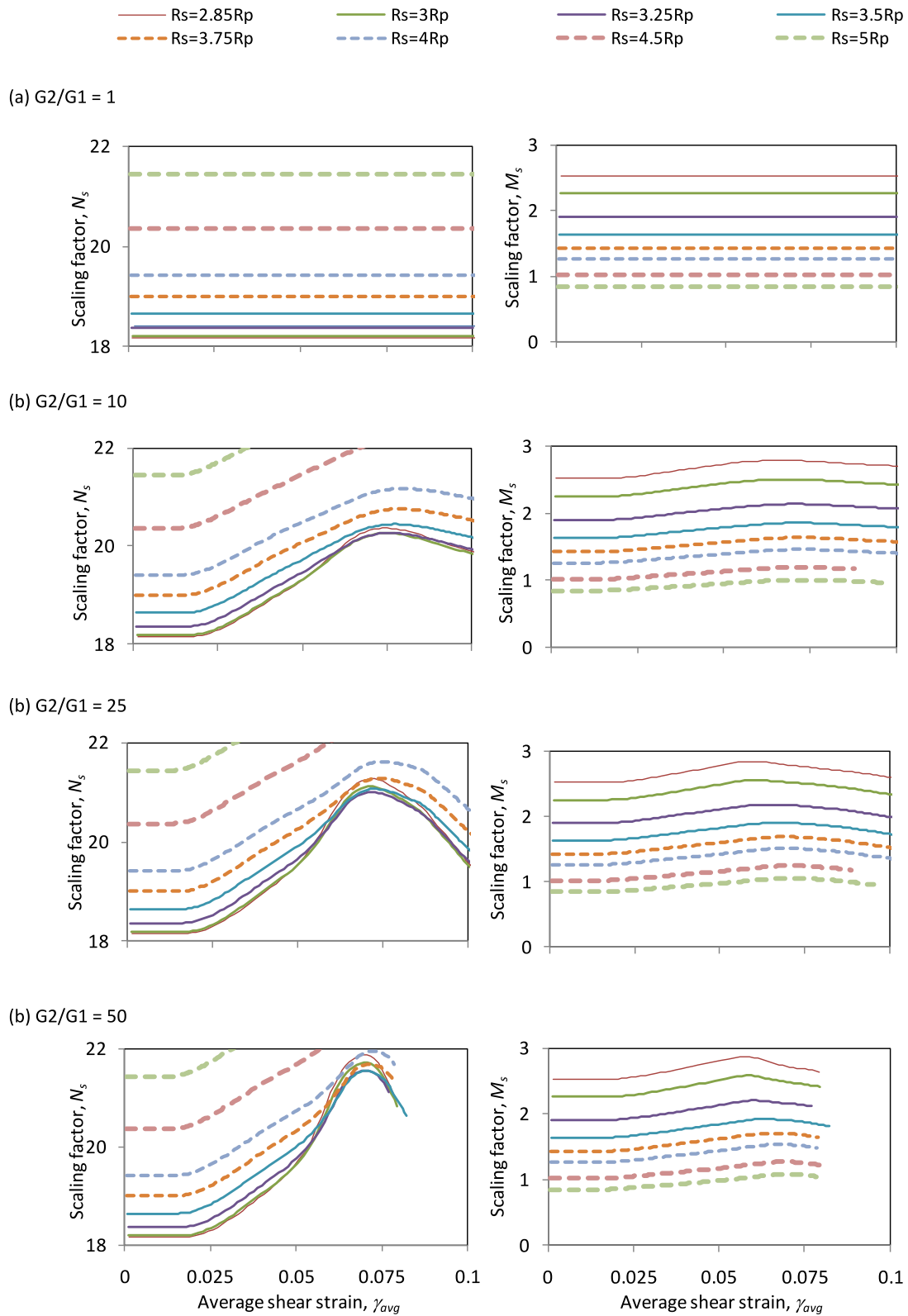
Figure 5.30: Scaling factors N_s and M_s for (a) elastic soil, $G_2/G_1 = 1$, (b) liquefied soil with $G_2/G_1 = 10$, (c) liquefied soil with $G_2/G_1 = 25$ and (d) liquefied soil with $G_2/G_1 = 50$.
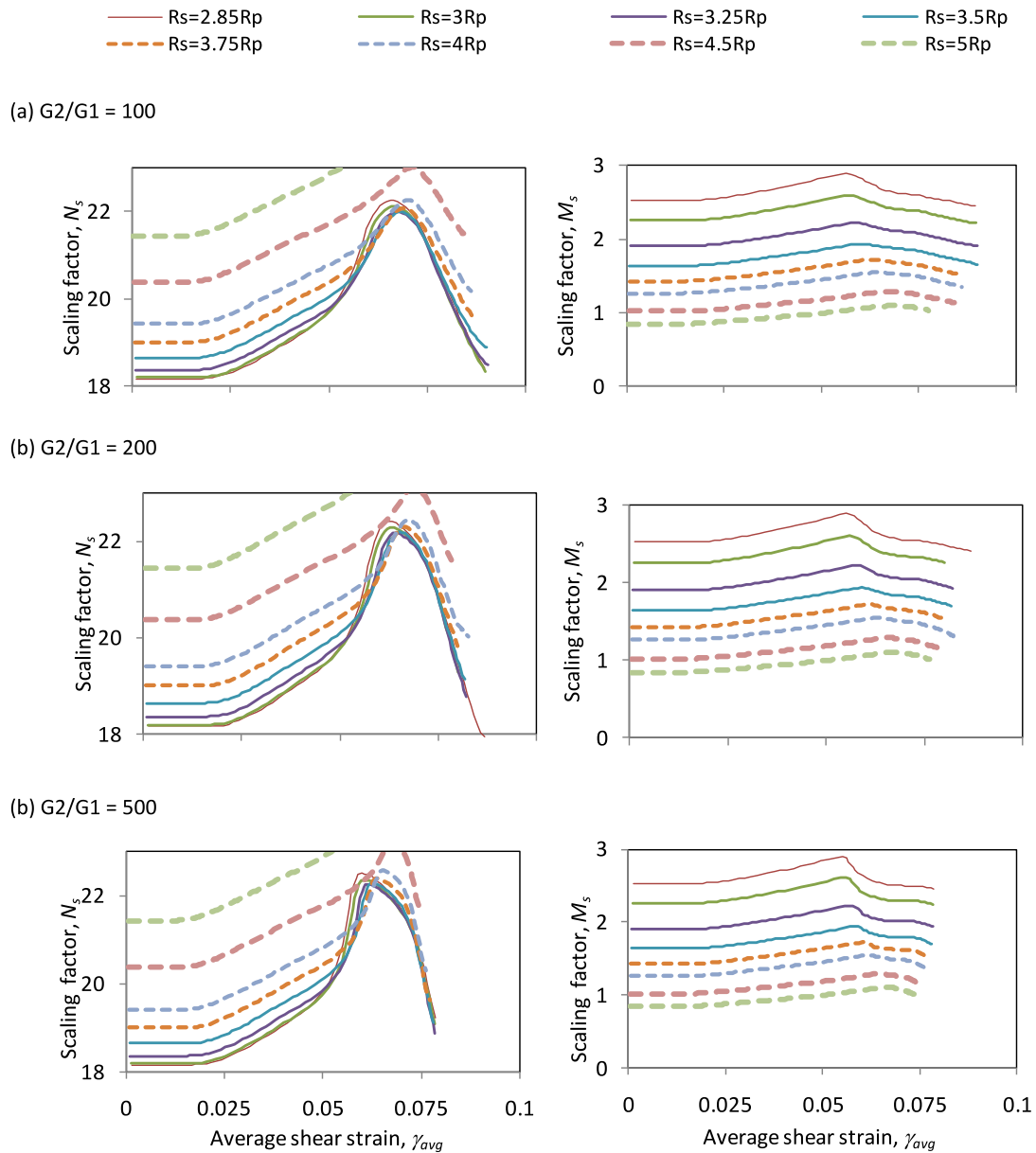
Figure 5.31: Scaling factors N_s and M_s for (a) liquefied soil with $G_2/G_1 = 100$, (b) liquefied soil with $G_2/G_1 = 200$ and (c) liquefied soil with $G_2/G_1 = 500$.

strain, the boundary of the effective zone of the soil corresponding to the minimum N_s shifted to a higher value. When γ_{ave} reached 0.075 ($1.25\gamma_{to}$), it can be considered that most of the soil elements have already yielded. As the effective zone and correspondingly the scaling factor M_s were changing during the nonlinear phase of the analysis. Hence, to obtain a single value of M_s, the state of the soil was considered to be at $\gamma_{ave} = 0.075$. Figure 5.32a shows the variation of the effective soil zone (as a ratio of $\frac{R_s}{R_p}$) for different G_2/G_1 ratios considered in the model. The figure shows a logarithmic increment of the

effective zone with respect to the G_2/G_1 ratio. For $G_2/G_1 = 1$, i.e., elastic soil, the effective zone of soil was at $2.85R_p$, however, for liquefied soil with higher G_2/G_1 ratio (i.e., stiffer G_2) the effective zone of soil was getting higher. For $G_2/G_1 = 50$, the effective zone of soil was at $3.25R_p$, which increased to $3.45R_p$ for $G_2/G_1 = 200$. Corresponding M_s values for the effective zone of soil is plotted in Figure 5.32c. The figure shows that $M_s = 2.6$ for elastic soil, which decreased to 2.1 for $G_2/G_1 = 50$ and 1.71 for $G_2/G_1 = 500$. The range of G_2/G_1 for liquefied soil as collated in Table B.1 is 9 to 335, for which the interpolated values of M_s were 2.32 and 1.87 respectively.

The values of N_s for the effective soil zones were also changing for different G_2/G_1 ratios and different stress state as can be seen in Figures 5.30, 5.31 and 5.30b. For example, in the liquefied soil model of $G_2/G_1 = 100$, N_s was 18.16 for the initial elastic straining till $\gamma_{ave} = 0.019$, which increased to 22 when $\gamma_{ave} = 0.066$, but then decreased to 21.2 when $\gamma_{ave} = 0.075$ and then after continued decreasing with further increase in strain. It can be argued that the value of N_s obtained from this FE upper-bound solution may not be the best solution to use because of the assumed symmetric boundary. The best known solution for bearing capacity factor, N_c, to date is 9.2 for smooth piles (e.g., steel piles) and 11.94 for rough piles (i.e., concrete piles) as suggested by Martin & Randolph (2006). Comparing the present FE solution with Martin and Randolph's (2006) closed form solution for rough pile soil interface, the FE solution overestimates the value of N_s by 52% for the elastic zone and 78% when $\gamma_{ave} = 0.075$.

Proposed N_s and M_s values for liquefied soils

For design consideration, the lower values of N_s and M_s can be considered as conservative as they give lesser strength and lesser stiffness to the $p - y$ curve, respectively. Hence, not to overestimate the strength of the soil, the the bearing capacity factor as suggested by Martin & Randolph (2006) can be used as the scaling factor N_s for design purpose, which is 9.2 for smooth pile-soil interface and 11.94 for rough pile-soil interface. The values of M_s obtained from the FE analysis for liquefied soils, on the other hand, were lower compared to the solution by Klar (2008) ($M_s = 2.6$) for a perfectly plastic soil. The
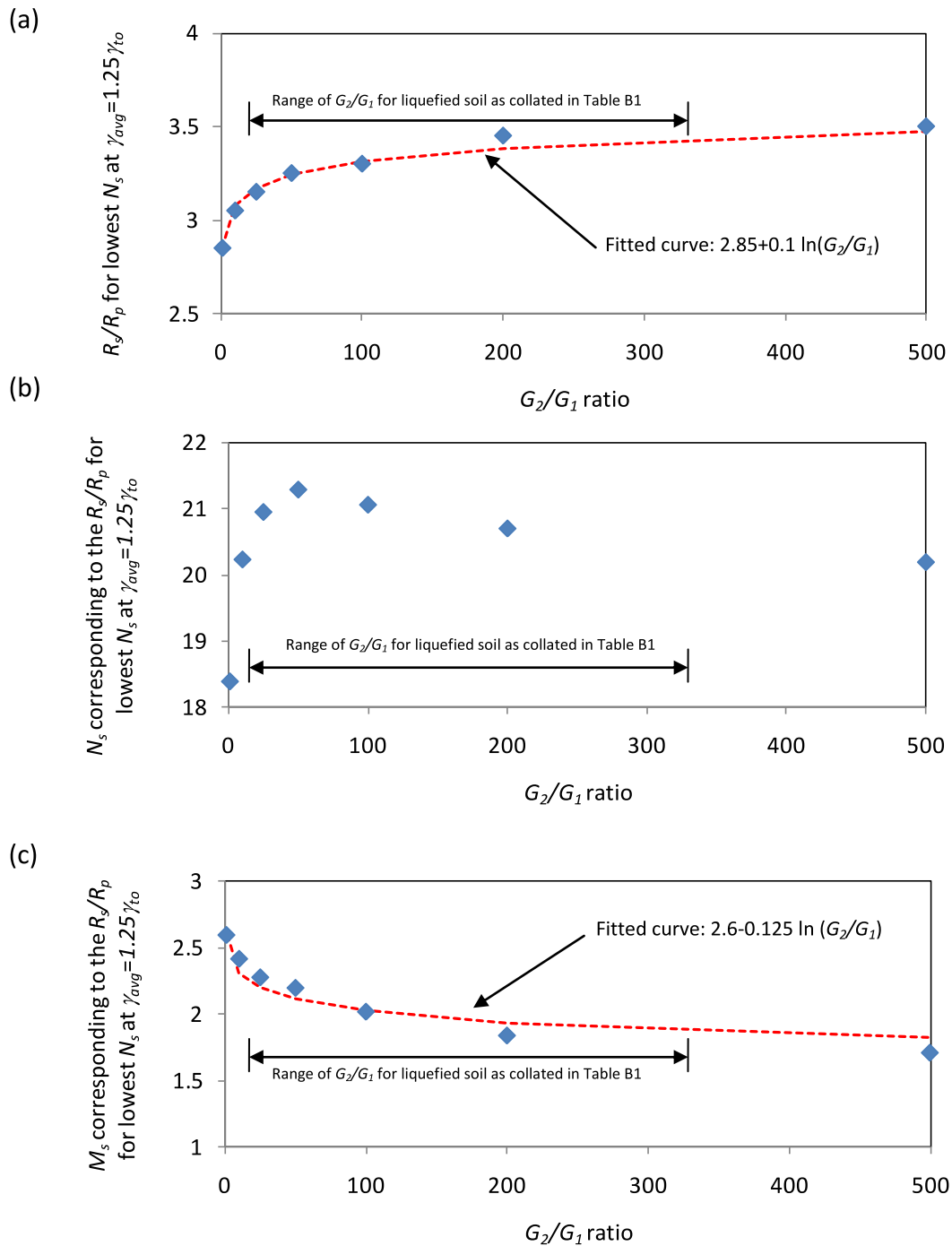
Figure 5.32: (a) Effective zone of soil corresponding to the lowest N_s values for different liquefied soil models when $\gamma_{ave} = 0.075$. (b) N_s values corresponding to the effective zone of soil for lowest N_s (c) M_s values corresponding to the effective zone of soil for lowest N_s.

use of $M_s = 2.6$ for liquefied soil could be unconservative as compared to the FE results. Although, M_s was found to be nonlinear from the FE analysis, for practical applications and to keep the transformation of stress-strain to $p-y$ curve linear, a single lowest value of

M_s, i.e., 1.87, was proposed for fully liquefied soil, corresponding to the highest recorded $G_2/G_1(335)$ value (i.e., $2.6 - 0.125\ln(335) = 1.87$), when $\gamma_{ave} = 1.25\gamma_{to}$. The value of M_s was also found to increase when the soil was strained beyond yielding and approached the ultimate strength (τ_{max}). However, the proposed value of M_s was kept same as 1.87 for the whole range of γ_{ave} to be in conservative side. Hence, for a fully liquefied soil with its monotonic stress-strain curve parameters γ_{to}, G_1, G_2 and τ_{max}, the parameters y_1, p_1, y_u and p_u required for the $p - y$ curve construction can be calculated as follows:

p_1= Initial lateral resistance corresponding to take off strain $= N_s 1.25\gamma_{to}G_1D$

y_1 = Initial lateral displacement corresponding to take off strain $= \frac{1.25\gamma_{to}D}{M_s}$

p_u= The ultimate lateral resistance $= N_s\tau_{max}D$

y_u= The ultimate lateral displacement $= \left(1.25\gamma_{to} + \frac{\tau_{max} - (G_1 1.25\gamma_{to})}{G_2}\right)\frac{D}{M_s}$

where,

N_s= Scaling factor for stress = 9.2 for smooth pile-soil interface and 11.94 for rough pile-soil interface

M_s= Scaling factor for strain = 1.87 for fully liquefied soil

D = Diameter of the pipe

As can be seen from the FE results in Figures 5.27 and 5.28, although the assigned stress-strain curve was having three linear segments, the development of lateral resistance with pile displacement (i.e., $p-y$ curve) was gradual. The linear scaling factors N_s and M_s, however, will give a tri-linear $p - y$ curve corresponding to the assumed tri-linear stress-strain curve (see the linearly scaled $p - y$ curve in Figure 5.33b). Hence, to accommodate the gradual development of the lateral resistance in the $p - y$ curves, Equation 5.29 was proposed using the parameters y_1, p_1, y_u and p_u. To note, Equation 5.29 gives positive values of p for positive increments of y with positive values of y_1, p_1, y_u and p_u. For negative increments of y, p should be estimated by using negative y_1, p_1, y_u and p_u.

$$p = \omega\frac{p_1}{y_1}y + A(1 - \omega)\left[\frac{p_u + p_1}{2} + \frac{p_u - p_1}{2}\tanh\frac{2\pi}{3(y_u - y_1)}\left(y - \frac{y_u + y_1}{2}\right)\right] \quad (5.29)$$

where,

$\omega = \text{A weight function} = \frac{1}{2}\left[1 - \tanh\left(\frac{6\pi}{y_u}\left(y - \frac{4y_1 + y_u}{6}\right)\right)\right]$

$A = \text{A constant} = 0 \text{ for } y = 0 \text{ and } 1 \text{ for } y \neq 0$

The above equation (Equation 5.29) was formulated to maintain the following boundary conditions:

1. At $y = 0$, $p = 0$.

2. Initial slope of $p - y$ curve $\left(\frac{p_1}{y_1}\right)$ is maintained till the displacement of $\frac{y_1}{3}$.

3. After $\frac{y_1}{3}$, the slope gradually increases and when the displacement is $y_1 + \frac{y_u - y_1}{3}$, the resistance is $p_1 + \frac{p_u - p_1}{3}$

4. The $p - y$ curve is same as the linearly scaled $p - y$ curve for middle $\frac{1}{3}^{rd}$ of the displacement between y_1 and y_u, i.e., from $y_1 + \frac{y_u - y_1}{3}$ till $y_1 + \frac{2(y_u - y_1)}{3}$.

5. At large displacement, full lateral resistance (p_u) is mobilised.

The linearly scaled model from a stress-strain curve was compared with the smooth proposed $p - y$ curve as shown in Figure 5.33 for a typical liquefied soil model. As can be seen in the figure, the smooth $p - y$ curve model avoids the sharp changes in stiffness, which is an undesirable feature in the linearly scaled model as compared to the FE results. The proposed smoothed $p - y$ curve was then compared with the actual $p - y$ curve obtained from the FE analysis for three liquefied soil models as shown in Figure 5.34. The figure shows that the proposed $p - y$ curves are in close agreement with the observed $p - y$ curves and can be considered as conservative, simple to estimate and easy to implement in a BNWF model.

The values of N_s and M_s thus provided the ability to scale a triaxial shear stress - shear strain curve to obtain the load-deformation $(p - y)$ curve which can then be used in a BNWF model to represent lateral pile soil interaction. However, the following few arguments must be made:

1) For nonlinear material, the scaling factors were nonlinear and were also varying with different G_2/G_1 ratios.
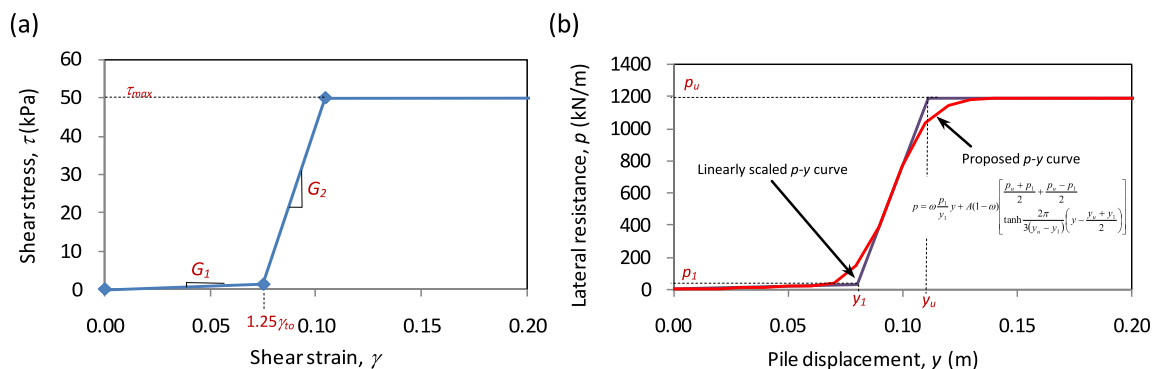
Figure 5.33: (a) A simplified stress-strain curve for liquefied soil, (b) and the corresponding $p - y$ curves.

2) The use of N_s values as obtained from the FE analysis would overestimate the strength and hence for a conservative design purpose the available best solution for bearing capacity factor was suggested.

3) The FE analysis was carried out only for rough pile-soil interface. For smooth pile-soil interface, the value of M_s may be different and further study is necessary to obtain an appropriate M_s.

4) The above study was based on plane strain idealisation of pile-soil interaction at deeper depth with flow type failure. However, at shallow depths a wedge type failure may govern and may affect the scaling factors.

5) This study was concentrated for fully liquefied soil only. For partially liquefied soil, it is questionable whether the use of linear scaling factors is appropriate or not.

It is clear from the above remarks that significant research is still necessary in this area and more field cases are needed to validate the proposed model.

5.8 Comparison of proposed $p - y$ curve with two experimentally observed $p-y$ curves for fully liquefied soils

The $p - y$ curve construction procedure, as proposed above, was used to construct two $p - y$ curves for fully liquefiable soils and compared with available experimental $p - y$
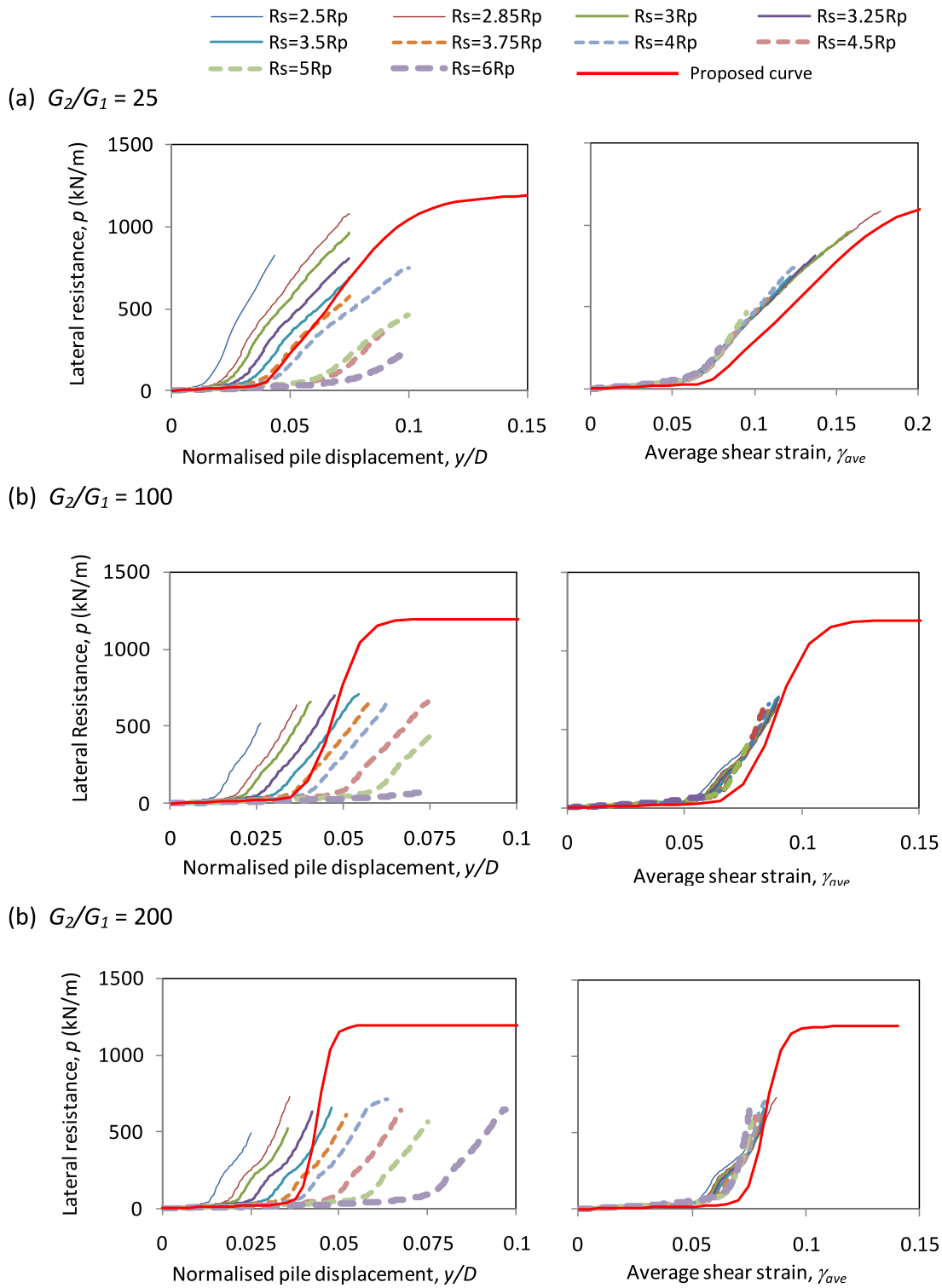
Figure 5.34: The $p-y$ curves as obtained from FE analysis and their comparison with the proposed $p-y$ curves.

curves. The procedure was involving two major steps, (a) preparing a simplified $\tau - \gamma$ model for the soil at the depth of consideration (Steps 1 to 7 as given below), (b) and scaling of the $\tau - \gamma$ curve to a $p-y$ curve (Steps 8 and 9 as given below). The procedure

followed in these examples is described as follows.

5.8.0.4   Example -1

The $p - y$ curve as observed by Rollins *et al.* (2005) from a full scale experimental test in liquefied soil was considered as an example. For the same site condition, the $p - y$ curve has been obtained using the proposed model and compared with the experimental $p - y$ curve. The test was conducted in a blast induced liquefied subsoil. Details of the test can be found in Rollins *et al.* (2005) and some specific results can be seen in section 2.8.3.2. The soil was at a relative density of 50% with an effective unit weight of 6kN/m^3. The test pile was 0.324m in diameter and made of steel. The depth of consideration for the $p - y$ curve was 4.57m and the water table was present at the ground level.

Input: soil parameters: Relative density, $D_r = 50\%$, Critical state angle of friction, $\phi_{cs} = 32°$(assumed)

Site parameters: Depth of consideration, $h = 4.57$m, Initial effective overburden pressure, $p'_{ini} = 6{\times}4.57 = 27.4$kPa

Input pile parameters: Pile type = Steel (smooth pile-soil interface), Outer diameter of pile, $D = 0.324$m

Calculations:

Step-1:   The stress ratio for post-liquefied soil in triaxial compression (M_c) was estimated using Equation 2.6, $M_c = \frac{6\sin 32°}{3-\sin 32°} = 1.29$

Step-2:   For D_r=50%, N_{1-60}=10.5, from the correlations given in appendix C.

Step-3:   Residual strength of soil, $s_u = 0.1p'_{ini} = 2.74$kPa, from Figure 2.18 for the $N_{1-60} = 10.5$.

Step-4:   For $D_r = 50\%$, the critical depth ratio $\beta = 16$, from Figure 5.15.

Step-5:   Actual to critical depth ratio $= \frac{h/D}{\beta} = \frac{4.25/0.324}{16} = 0.88$

Step-6:   For $D_r = 50\%$ and p'_{ini} =27.4kPa, $G_{max} = 52.7$MPa, estimated by Equation C.2 as given in appendix C.

193

Step-7:   For the simplified post liquefaction stress strain model of the soil (see Figure
            5.7), four parameters, G_1, G_2, γ_{to} and τ_{max} were estimated according to the
            section 5.5.5, such as:

$$\gamma_{to} = 89 - 20\ln(D_r) = 89 - 20\ln(50) = 10.76\%$$

$$G_1 = \tfrac{1}{\gamma_{to}} = \tfrac{1}{0.1076} = 9.29\text{kPa}$$

$$G_2 = \tfrac{G_{max}}{5\sqrt{p'}} = \tfrac{52700}{5\sqrt{27.4}} = 2013\text{kPa}$$

$$\tau_{max} = s_u + \left(\tfrac{p'_{ini}M_c}{2} - s_u\right)\tfrac{h/D}{\beta} = 2.74 + \left(\tfrac{27.4\times1.29}{2} - 2.74\right) \times 0.88 = 15.88\text{kPa},$$
$$\text{as } \tfrac{h/D}{\beta} < 1$$

Step-8:   For steel pile, a smooth pile-soil interface was assumed and the scaling factors
            N_s and M_s were chosen as 9.2 and 1.87 respectively. The parameters required
            for the $p-y$ curve construction were estimated as follows:

$$p_1 = N_s 1.25\gamma_{to}G_1 D = 9.2 \times 1.25 \times 0.1076 \times 9.29 \times 0.324 = 3.7\text{kPa}$$

$$y_1 = \tfrac{1.25\gamma_{to}D}{M_s} = \tfrac{1.25\times0.1076\times0.324}{1.87} = 0.0233\text{m} = 23.3\text{mm}$$

$$p_u = N_s\tau_{max}D = 9.2 \times 15.88 \times 0.324 = 47.33\text{kPa}$$

$$y_u = \left(1.25\gamma_{to} + \tfrac{\tau_{max}-(G_1 1.25\gamma_{to})}{G_2}\right)\tfrac{D}{M_s} = \left(1.25 \times 0.1076 + \tfrac{15.88-(9.29\times1.25\times0.1076)}{2013}\right)\tfrac{0.324}{1.87} =$$
$$0.0246\text{m} = 24.6\text{mm}$$

Step-9:   The $p-y$ curve was then estimated using Equation 5.29.

The $p-y$ curve estimated, as above, for fully liquefied soil was compared with the observed
$p-y$ curve at the site at 4.57m depth (Rollins et $al.$, 2005) as shown in Figure 5.35. Two
other $p-y$ curves for liquefied soil, one that was proposed by Rollins et $al.$ (2005) from all
their tests and one that is based on 10% strength of the API $p-y$ curve are also plotted in
the figure. The proposed $p-y$ curve matches fairly well in the initial part of the observed
$p-y$ curve, but, it over-predicts the strength and stiffness at higher displacement. In
theory, there should be mobilisation of strength in the soil at large displacement, however,
the same was not observed in the field tests. This difference in the strength of the $p-y$
curve could be due to the difference in the type of soil actually present in the site and
the assumed simplified stress-strain curve for estimating the $p-y$ curve. To note, the

simplified stress-strain curve uses available element test data of clean sand, which could be different from the naturally occurring soil at site. In the proposed $p - y$ curve, the second stiffer part represents suppressed dilation of the soil in front of pile, which might not have happened in the field test due to pore pressure dissipation in axial direction along the pile. More field tests with different site conditions are certainly required to validate the proposed $p - y$ curve model.
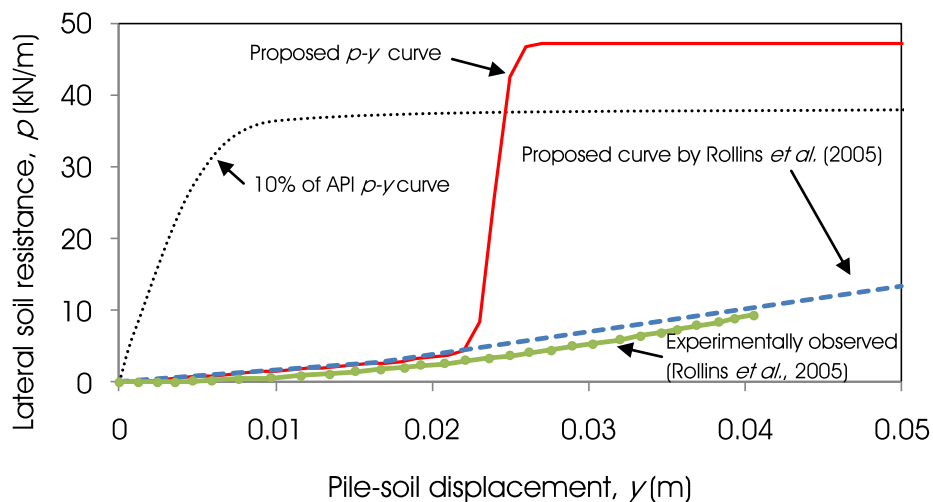
Figure 5.35: Proposed $p - y$ curve compared with full scale experimental test results of Rollins *et al.* (2005).

5.8.0.5 Example-2

The centrifuge test models as described in chapter 3, where $p - y$ curves were back calculated from the pile strain measurements, were taken as another example to compare the proposed $p - y$ curve model. Soil condition for three representative centrifuge tests in prototype scale (see chapter 3, tests CT5-A, CT7-A and CT8-A) were considered. The soil was at a relative density of 50% and fully liquefied during the test. A single cycle of the back-calculated $p - y$ curves at the middle of the liquefied soil (i.e., at a depth of 4.05m) was chosen in this example. A similar procedure as described for example-1 was repeated here to construct the proposed $p - y$ curve.

The proposed $p - y$ curve was compared with the $p - y$ curves obtained from the

centrifuge tests at full liquefaction as shown in Figure 5.36. In the initial part of the $p-y$ curve, the proposed model provides a qualitative match with the pattern and magnitude of $p-y$ curve. The proposed curve is close to the lower bound values of the observed $p-y$ curves, however, the 10% API $p-y$ curve gives very high initial stiffness. A high initial stiffness may be very unconservative in terms of dynamic and buckling response of the pile. The proposed model, although not exactly predicting the $p-y$ curve and the mobilising plateau is not observed in the experiments, does retain the shape and characteristics of the stress-strain behaviour of liquefied soil and represents it within a practical limit of acceptance. The discrepancy between proposed and observed $p-y$ curves could partly be attributed to two major causes, a) the assumed simplified stress-strain behaviour of the soil for proposed $p-y$ curve construction and b) the limitations of $p-y$ curve estimation from centrifuge tests. More experimental studies are necessary to validate the proposed $p-y$ curve and its wide usability.
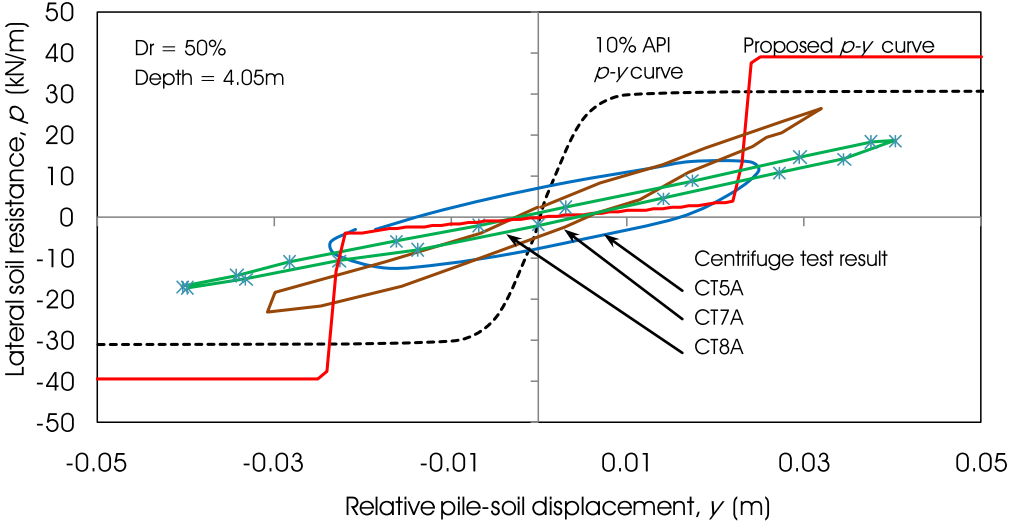
Figure 5.36: Proposed $p-y$ curve compared with centrifuge test results (tests CT5-A, CT7-A and CT8-A) as described in chapter 3.

5.9 Summary of conclusions

The current understanding of the stress-strain behaviour of liquefied soil has facilitated to propose a simplified stress-strain model of it, which can be obtained from its basic properties and can be used in the absence of actual laboratory test data. A tri-linear shear-stress versus shear-strain curve was proposed for fully liquefied soil with four parameters, such as: γ_{to}, G_1, G_2 and τ_{max}.

The study of strain rate effect on the stiffness of soil suggested that the $p - y$ curve can be modelled as a pseudo-static curve and the effect of strain rate, which becomes significant during dynamic analysis, can be related to the damper properties in a BNWF model. For a soil at a particular relative density, the tests have shown that the strain rate dependency on critical state shear modulus (G_2) is not apparent.

The $p - y$ curve construction procedure from stress-strain properties of the soil has been explored in this chapter. The stress and strain of the soil was scaled to obtain the parameters of the $p - y$ curve using two scaling factors, N_s and M_s. Appropriate values of N_s and M_s have been proposed through FE analysis. A smooth $p - y$ curve was then proposed which maintains the characteristics of the stress-strain behaviour of liquefied soil, and is yet simple to define and implement in a BNWF model.

The proposed $p - y$ curve model was compared with two experimental $p - y$ curves from (a) the full scale field test results by Rollins *et al.* (2005) and (b) the centrifuge test models as described in chapter 3. The proposed and observed $p - y$ curves were in close agreement in the initial part, however, at large displacement the magnitude of the proposed $p - y$ curves were higher. Although, an exact match between proposed and observed $p - y$ curves was not found because of the assumed simplifications in stress-strain behaviour of soil and the $p - y$ curve model definition, the proposed $p - y$ curve was providing qualitatively similar strength and initial stiffness values as compared to the experimental observations. Considering the complexity of the problem, the proposed procedure may be regarded as a reasonably simplified model for constructing a pseudo-static $p - y$ curve, however, the user must be aware of its limitations. The proposed $p - y$ curve is applicable only for fully liquefied soil subjected to monotonic loading. This may represent field conditions when the liquefied soil flows past pile or the pile

deflects monotonically in the liquefied soil. The proposed model does not include the cyclic behaviour of the soil. However, for a dynamic loading scenario, this model may be used for initial simplified pseudo-static analysis. Significant research is still necessary to compensate the limitations of the proposed $p - y$ curve model and more field cases are necessary to validate it.

Chapter 6

Study of a case history of pile failure using the proposed $p - y$ curve

6.1   Introduction

The failure of piles in liquefiable soils can be governed by the coupling of failure mechanisms rather than by a single mechanism. The possible interactions of these mechanisms have already been discussed in section 2.5. Two major combinations of the failure mechanisms in liquefiable soils were studied by Dash *et al.* (2009) (bending + settlement), and Dash *et al.* (2010a) (bending + buckling) by using a beam on non-linear Winkler foundation (BNWF) model. The analyses have shown that the pile-soil interaction can ideally be represented by an appropriate BNWF model which can also incorporate the interaction of different mechanisms. Dash *et al.* (2010a) showed the inconsistency that lies in defining lateral resistance of liquefied soil in current practice while modelling LPSI in liquefied soil in a BNWF model. In chapter 5, a new $p - y$ curve was proposed, which can give a better representation of LPSI in liquefiable soils. In this chapter, the proposed $p - y$ curve has been implemented in a BNWF model to study a case history of pile failure in liquefiable soil.

6.1.1   Outline of the chapter

The failure of Showa Bridge piles during 1964 Niigata earthquake has been taken as an example of pile failure in liquefiable soils and analysed using a BNWF model. The reasons for choosing this particular case study has been mentioned in section 6.2. The current hypothesis of bridge failure and its controversies are detailed. The proposed $p - y$ curve

for liquefied soil has been implemented in a BNWF model and important inferences from the results are discussed.

6.2   Analysis of the case history of Showa Bridge pile failure

The Showa Bridge was a simple steel girder bridge with pile foundations crossing the Shinano River, Japan. The bridge collapsed just one month after its construction during the 1964 Niigata earthquake as shown in Figure 6.1. This case history of pile failure has received significant attention from the research community and is considered in the present study for the following three reasons.

1. The bridge was almost new when collapsed, and had steel tubular piles. This ensures less uncertainty of material strength as degradation of piles due to corrosion is not expected.

2. The failure pattern of a bridge pile and the soil profile are available from post earthquake investigations (Figures 6.2 and 6.3).

3. This case history is well documented in many technical papers and reports; see for example Takata *et al.* (1965); Fukuoka (1966); Iwasaki (1984); Hamada (1992a); Ishihara (1993); Kramer (1996); Bhattacharya *et al.* (2005); Yoshida *et al.* (2007).

6.2.1   Post earthquake observations

During the 1964 Niigata earthquake, the Showa Bridge site was subjected to extensive liquefaction and lateral spreading. Five of the twelve spans fell off the pile heads in the earthquake (Figure 6.2). Figure 6.3 gives the soil and pile data obtained from post earthquake investigation of a recovered pile. From detailed soil investigation, Hamada & O'Rourke (1992) estimated that the soil liquefied to a maximum depth of 10 m below the riverbed. The liquefaction soil profile under the bridge is shown in Figure 6.4.

Yoshida *et al.* (2007) collated many eyewitness statements and established the chronology of the bridge failure. They mentioned that the bridge started to fail about
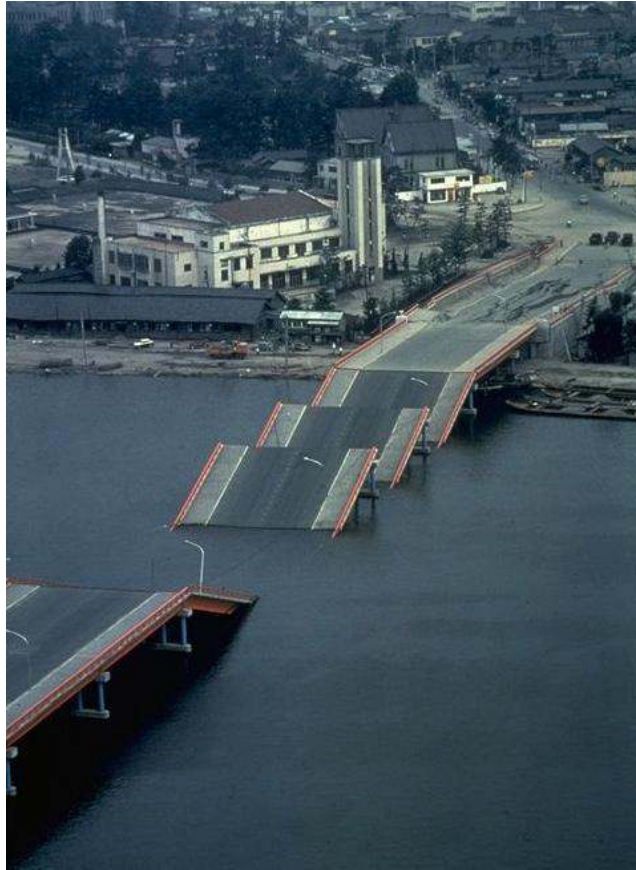
Figure 6.1: Showa Bridge Collapse during 1964 Niigata Earthquake (JGS, 1964).

60s after the first shock of the earthquake. The progressive collapse of the bridge took about 20s, and started with the falling of bridge deck G6. Based on eyewitness reports, Kazama *et al.* (2008) reported that the collapse of bridge girders proceeded as G6→G7→G5→G4→G3.
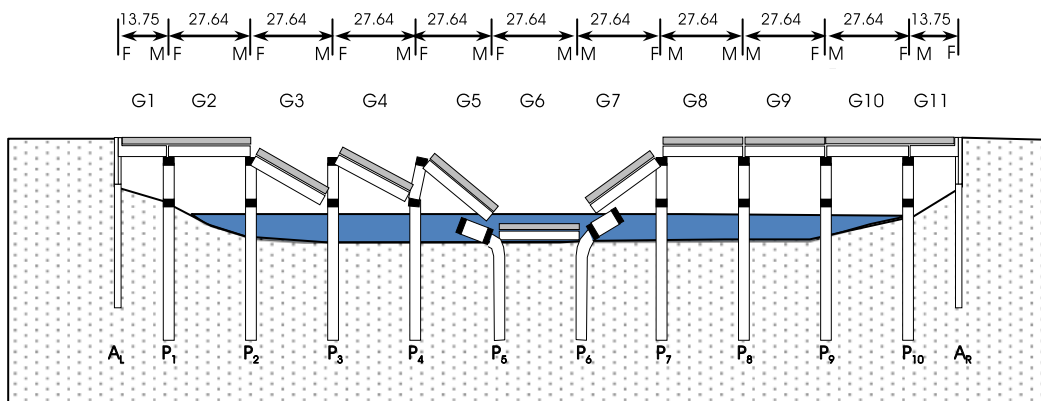
Figure 6.2: Failed Showa Bridge after 1964 Niigata earthquake (redrawn after Yoshida *et al.* (2007)). [M: Movable bearing, F: Fixed bearing]
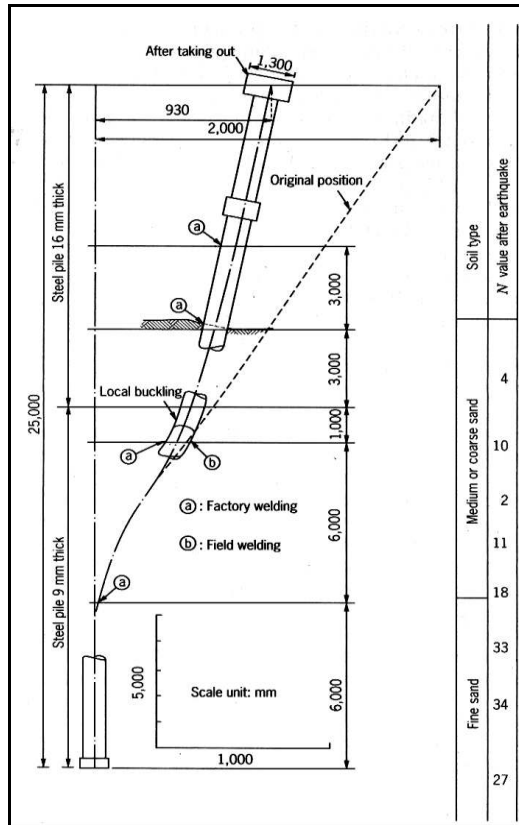
Figure 6.3: Structural and surrounding soil data of one Showa Bridge pile (see pile P4 in Figure 6.2) after post earthquake recovery (Fukuoka, 1966).
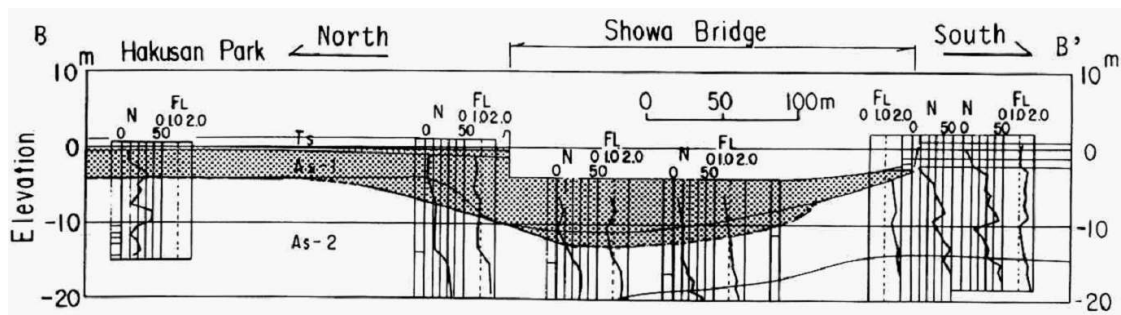
Figure 6.4: Soil Liquefaction profile (in grey) at Showa Bridge site (Hamada & O'Rourke, 1992).

There was no measurement of ground motion during the earthquake very close to the bridge site. The nearest available measurement was taken at Kawagishicho apartment, 2km away from the bridge, which is not very far from a practical point of view unless a significant change in soil profile was expected. Figure 6.5 shows the time history of

the Niigata earthquake in both North-South and East-West directions recorded at the basement of the apartment. Due to the absence of a ground motion recording close to the bridge, the measured ground motion 2km away from bridge was used as representative ground motion at the bridge site. The ground motion recorded at the basement of the building was assumed not to have significant SSI (Soil Structure Interaction) effect. The magnitude of the earthquake recorded (N-S component) at the basement of Kawagishicho apartment was about $0.1g$ at ~ 0.16Hz frequency of vibration during the time of bridge collapse. The longitudinal axis of the bridge was about 30° North-West (Yoshida *et al.*, 2007), hence the acceleration magnitude in the longitudinal axis of the bridge was expected to be a combination of both N-S and E-W components of the measured ground motion.
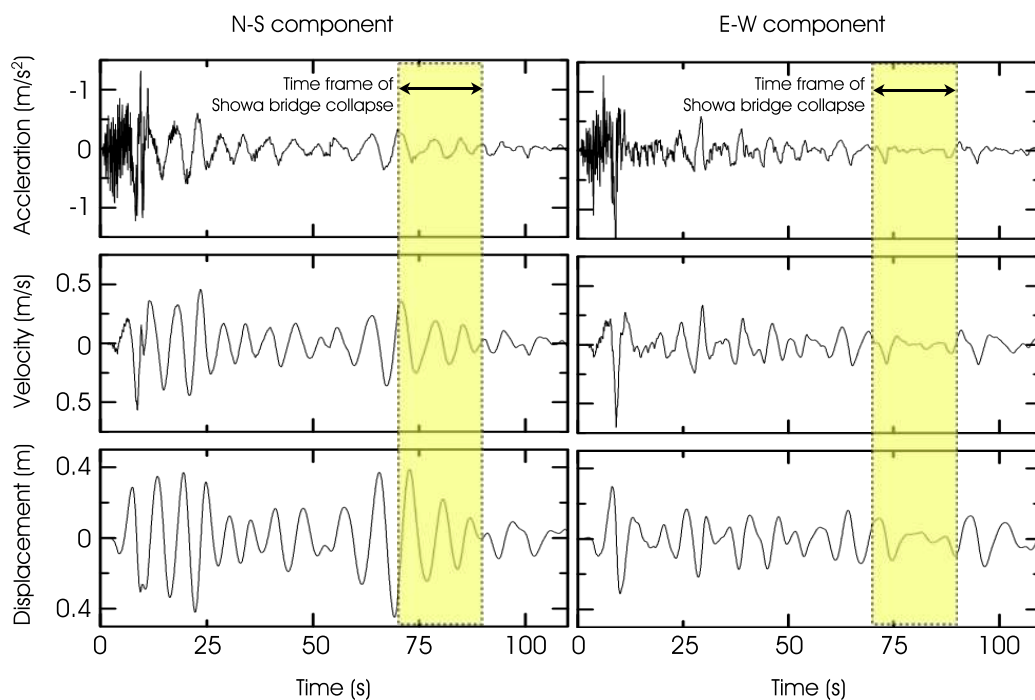
Figure 6.5: Time frame of the Showa Bridge collapse shown over the acceleration time history recorded at the basement of Kawagishicho apartment (after Kudo *et al.*, 2000).
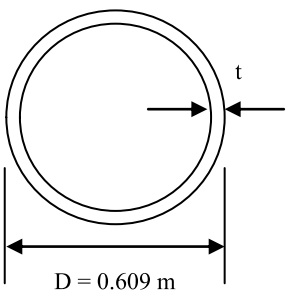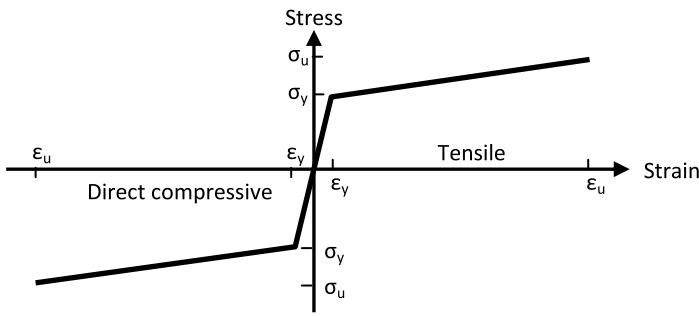
6.2.2 Structural details of the bridge pile

The bridge was 304m long, 24m wide with 12 spans (Fukuoka, 1966). The foundation of each supporting pier was a single row of 9 tubular steel piles connected laterally by a pile cap. Each pile was 25m long with outer diameter of 0.609m. The wall thickness of the upper 12m of the pile was 16mm and the bottom 13m thickness was 9mm. The axial load

(P) carried by each pile from a dead load analysis was estimated by Bhattacharya (2003) as 740kN, and the same value was used in the present study. The design live loads were ignored as there was no significant traffic on the bridge during its failure.

The material of the Showa Bridge piles, as per the Japanese standard JIS-A:5525 (JSA, 2004), was assumed to be SKK490 grade steel pipe with the yield strength (σ_y) and ultimate strength (σ_u) of 315MPa and 490MPa respectively. The stress-strain behaviour and sectional properties of the pile are presented in Table 6.1.

Table 6.1: Structural properties of the Showa Bridge pile section.

Sectional details of the pile	Axial Capacity (kN)	Bending Capacity (kNm)
t = 16mm	P_y = 9405	M_y = 1354 (for P = 0kN) = 1286 (for P = 740kN)
	P_u = 14630	M_p = 2675 (for P = 0kN) = 2415 (for P = 740kN)
t = 9mm	P_y = 5355	M_y = 790 (for P = 0kN) = 680 (for P = 740kN)
D = 0.609 m	P_u = 8330	M_p = 1567 (for P = 0kN) = 1385 (for P = 740kN)

Note: P_y = Axial yield capacity
P_u = Ultimate axial capacity
M_y = Yield moment capacity
M_p = Plastic moment capacity

ε_y = 0.00157 ε_u = 0.089
σ_y = 315 MPa σ_u = 490 MPa

6.3   Current hypothesis of the Showa Bridge failure and controversies

The case history of the Showa Bridge failure has been used extensively by many researchers to study the response of piles in liquefiable soils including Dobry & Abdoun (2001), Hamada (1992a); Ishihara (1993); Kramer (1996); Bhattacharya (2003); Bhattacharya *et al.* (2005) and Dash *et al.* (2010a). The major hypotheses have been suggested by the

researchers can be classified in three categories as described below.

6.3.1 Bending hypothesis

Many researchers including Dobry & Abdoun (2001); Hamada (1992a); Ishihara (1993) and Kramer (1996) illustrated that the Showa Bridge failure was due to the effects of lateral spreading on piles. Hamada (1992a) quotes a reliable eyewitness report, "*The girders began to fall somewhat later, perhaps about 0 to 1 minute after the earthquake motion ceased*" and goes on to describe the current conventional theory of the failure as:

"*The ground on the left bank and in the riverbed liquefied as a result of the earthquake motion and moved toward the river centre. The ground displacements continued even after the earthquake motion ceased, until the excess pore pressure dissipated. The permanent ground displacement on the left bank reached several meters, substantially deforming the foundation piles and causing the girders to fall*".

This hypothesis suggests that the pile failed due to bending (see bending philosophy as discussed in section 2.5.1) due to the force experienced by lateral spreading. Based on this hypothesis, plenty of research has been carried out to propose a limiting force that the liquefied soil can apply during lateral spreading (e.g., He *et al.*, 2006, Brandenberg, 2005 Abdoun & Dobry, 2002). JRA guideline (JRA, 2002) also suggests a limiting force model for laterally spreading liquefied soil following this hypothesis.

6.3.2 Buckling hypothesis

In contrast to the bending hypothesis, Bhattacharya (2003); Bhattacharya *et al.* (2005) demonstrated that the lateral spreading force of liquefied soil is quite small and it also cannot fully explain the mode of failure of the bridge. The argument was that as the bridge failed after the period of strong shaking the failure must be the result of some secondary action of the earthquake. If the pile failure had been due to lateral spreading, the piers would have displaced in the same direction down the slope (left to right). In contrast, the piles of pier P5 displaced towards the left and the piles of pier P6 displaced towards the right as shown in Figure 6.2. The piers close to the riverbank did not fail despite the lateral spreading there being severe. They, hence, hypothesised that the failure was due

to buckling instability (see buckling philosophy as discussed in section 2.5.1) owing to the loss of lateral strength of soil due to liquefaction. Assuming no lateral stiffness of liquefied soil, Bhattacharya *et al.* (2005) estimated the theoretical Euler buckling load for the pile to be 1030kN, quite close to the allowable load of the pile (965kN) from geotechnical consideration, which could have caused the bridge to fail with small lateral loading or practical imperfection.

6.3.3   Bending-buckling hypothesis

Designing pile foundations for bending as opposed to buckling failure criteria requires different approaches. Bending failure depends on the bending strength (moment at yield, M_y, and plastic moment capacity, M_p) of the pile, whereas, buckling represents a sudden instability of the pile when the axial load, P, reaches the buckling load. However, in reality, piles are subjected to both axial and lateral loads during an earthquake and hence act like beam-column members. Dash *et al.* (2010a) carried out a detailed investigation using this case history of pile failure and demonstrated the bending-buckling interaction as a possible mechanism of pile failure in liquefiable soils.

Six models that are used in practice for bending analysis in liquefiable soils were considered in the analysis (as shown in Figure 6.6), modelling details of which can be found in Dash *et al.* (2010a). Conventional bending analysis, simplified buckling analysis and coupled bending-buckling analysis (considering both axial and lateral load) were performed. The major conclusions drawn from the analyses are given below.

1. The lateral load on piles due to the flow of liquefied soil varies widely according to various design guidelines and researchers (see Figure 6.7). For displacement based models, the maximum lateral force was taken as the maximum resistance of $p-y$ springs for the liquefiable soil layer (i.e., αp_u of the $p-y$ spring as in Figure 2.29a).

2. The conventional bending analyses (without considering the axial load) showed that 3 out of 6 models did not predict the pile failure. The simplified buckling analysis gave a factor of safety (FOS) of 1.33 against theoretical elastic buckling and could not describe the failure of a bridge pile alone.

3. The analyses, while not indicating failure under bending analysis, could predict failure when bending-buckling interaction was taken into account. Figure 6.8 shows the results of the coupled analysis for a force based model (model c) and a displacement based model (model e). For example, the model-c, which could not predict failure when no axial load was applied, predicted failure when the axial loads were incorporated in the analysis. The pile failed at 60% of the lateral load when an axial load of 370kN was used. This reduced further to only about 11% when full axial load of 740kN was applied.

4. The analysis showed that while in some cases the pile can be considered safe if designed for bending and buckling criteria in isolation, it can, however, be seen to fail when both the criteria are taken together.

5. The coupled bending-buckling hypothesis was able to predict structural failure of the pile, but it could not ascertain why the plastic hinge formed at 3.5m below ground level. The locations of maximum bending moment predicted by all these models were within the bottom non-liquefied soil.

6.3.4 Controversies

The major observations of the bridge failure that any theory has to explain include:

- Pile failed structurally with visible cracks and local buckling at a depth of 3.5m from ground level.

- The bridge failed about 60sec after the main earthquake shock.

- The failure started at the middle of the bridge.

None of the three hypotheses described above (i.e., bending, buckling and bending-buckling interaction as given in Section 6.3) was able to describe these observations. Table 6.2 summarises the results of different analyses performed to study the Showa Bridge failure observations. Although some of the models were able to predict the structural failure of the pile, none of the models were able to predict the location of the plastic hinge in the pile.

Figure 6.6: Six models (3 force based and 3 displacement based) of Showa Bridge pile subjected to lateral force from soil flow (Modified after Dash *et al.*, 2010a).

All of these hypotheses discussed consider that the bridge had failed after the earthquake, and ignore the inertia load at top of the pile. Although some bending analysis and some coupled bending-buckling analysis models predicted structural failure of the pile, the source of lateral loading considered in these studies is still under question. It is clear that lateral spreading occurred around the left riverbank, however, there is no evidence that the riverbed (directly underneath the bridge) experienced lateral spreading. Recent studies by Yoshida *et al.* (2007) suggested that the bridge failed before the lateral spreading had begun. The argument made by Kerciku *et al.* (2007) showed that the liquefied soil under the middle of the bridge (under pile P5 and P6) was already at its lowest position
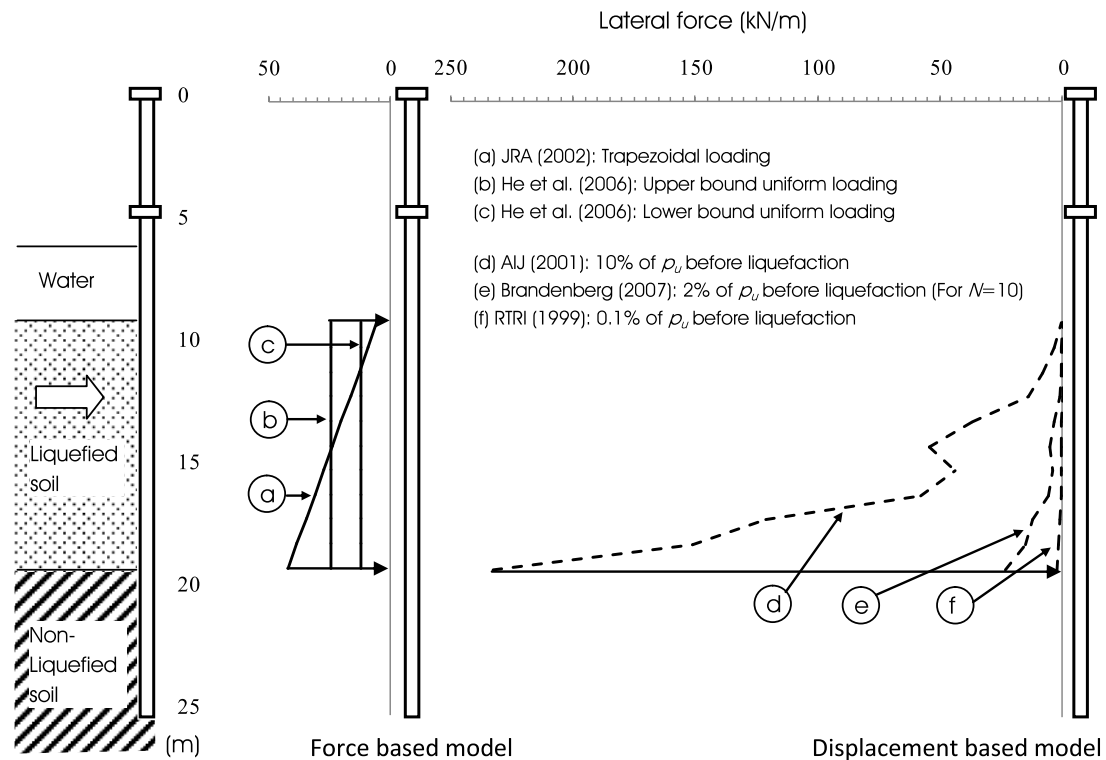
Figure 6.7: Comparison of maximum lateral force on pile due to the flow of liquefied soil; force based models (models a, b, c as in Figure 6.6) versus displacement based models (model d, e, f as in Figure 6.6) (Dash *et al.* (2010a)).

of potential energy and would not be expected to flow. This is also supported by the fact that piers P5 and P6 collapsed in opposite directions. These arguments thus discard the lateral spreading being the reason for Showa Bridge collapse.

In contrast, the ground motion recorded near the bridge site shows that the earthquake was still continuing with a small magnitude low frequency vibration during the failure of the bridge (Figure 6.5). None of the models considers the dynamic characteristics of the bridge pile, which is expected to change during liquefaction of the subsoil.

Hence, the bridge pile was re-analysed here by a BNWF model to incorporate the inertia effect in the analysis. The model was similar to the displacement based model studied by Dash *et al.* (2010a), but the $p - y$ curves for liquefied soils were replaced by the proposed new $p - y$ curves (section 5.6.2). A coupled bending-buckling interaction analysis was carried out considering the possible interaction between inertia force and axial load in pile.
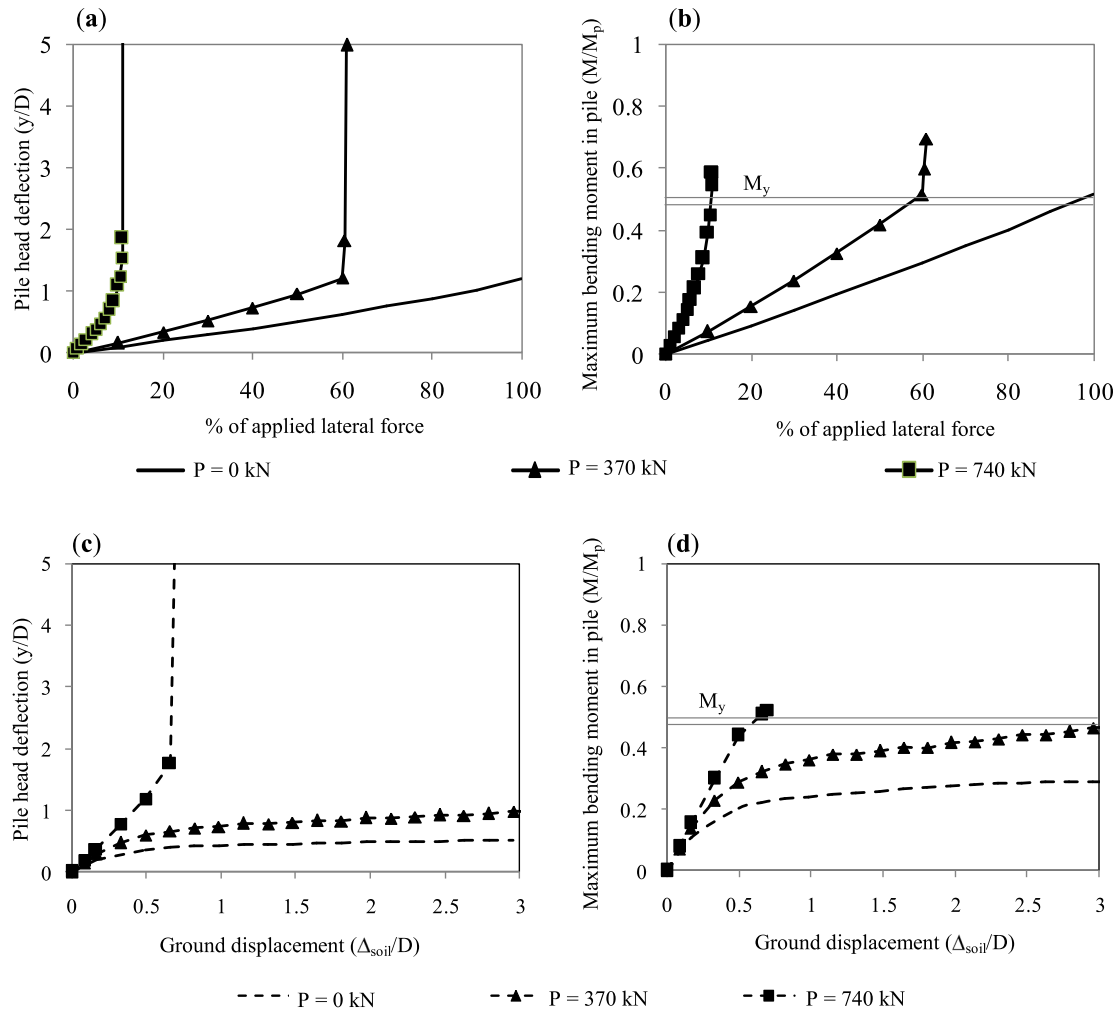
Figure 6.8: For P = 0kN ,370kN and 740kN: Normalised (a) pile head displacement and (b) maximum bending moment in pile w.r.t % of applied force (model-c as in Figure 6.6), Normalised (c) pile head displacement and (d) maximum bending moment with increase in ground displacement (model e as in Figure 6.6) (Dash *et al.* (2010a)).

6.4 Analysis of bridge pile using the proposed $p - y$ curve model

6.4.1 BNWF Model details

6.4.1.1 Structural model

The 25m long Showa Bridge pile was passing through a four-layer system of air, water, liquefied soil and non-liquefied soil (Figure 6.3). It was restrained over the bottom 6m of non-liquefied soil and carried an inertia force and an axial load at its head. The bridge pile was modelled as a Beam on a Nonlinear Winkler Foundation (BNWF) using the finite

Table 6.2: Showa Bridge failure prediction by different analysis models.

Field observations →	Pile had visible cracks and local buckling	Bridge started to fail at the middle span (G6)	Cracks (plastic hinge) in the pile was 3.5m below GL	Bridge failed 60sec after the main shock
Model predictions				
Simplified bending analysis (Bhattacharya *et al.*, 2005)	No	No	–	–
Simplified buckling analysis (Dash *et al.*, 2010a)	No	No	–	No
Bending analysis (DB models a and b, Figure 6.7)	Yes	No	12.5m below GL	Yes
Bending analysis (FB model c, Figure 6.7)	No	No	12.5m below GL	Yes
Bending analysis (DB model d, , Figure 6.7)	Yes	No	9.75m below GL	Yes
Bending analysis (DB model e, Figure 6.7)	No	No	12.25m below GL	Yes
Bending analysis (DB model f, Figure 6.7)	No	No	11.75m below GL	Yes
Bending -buckling analysis (FB model-c, Figure 6.7)	Yes	No	12.5m below GL	Yes
Bending -buckling analysis (DB model e, Figure 6.7)	Yes	No	12.25m below GL	Yes
Note: FB: Force based, DB: Displacement based, GL: Ground level				

element program SAP 2000 (CSI, 2008), where the pile was modelled as beam-column elements and the soil-pile interaction was modelled as lateral soil springs ($p - y$ springs) lumped at 0.5m intervals. The structural properties of the pile can be found in section 6.2.2. The pile was assumed to be free at top and has a roller support at the bottom, similar to the Dash *et al.* (2010a) model.

6.4.1.2 Soil model

The length of the pile embedded in the soil was 16m, of which the top 10m had liquefied during the earthquake. For non-liquefied soil layer, nonlinear $p-y$ spring properties are estimated as per API guidelines (API, 2000). The calculation of $p-y$ curves as per API guidelines required the *in-situ* relative density (D_r) values, which were estimated from the available SPT N values using Equation C.4 (Appendix C). During liquefaction, the effective stress in the liquefied soil layer becomes nearly zero, and hence, for estimating the $p-y$ springs for the bottom 6m of non-liquefied soil, the effective stress was considered zero at its surface, that increased with depth. The effective unit weight of the soil was taken to be 10kN/m^3.

For the 10m liquefied soil layer, the $p-y$ curve as proposed in section 5.6.2 was used. A step by step calculation procedure can be referred in section 5.8. The proposed $p-y$ curves at four depths are presented in Figure 6.9. Few salient features of the model can be seen in the plot. The ultimate strength of the $p-y$ curve increases with depth, which is a function of initial effective overburden pressure. The initial stiffness, however, is a function of relative density of the soil. As the soil profile in this case had a very soft layer, at 5m to 8m from GL, the initial low stiffness of the $p-y$ curve at $h = 6.25$m was higher than that of the $p-y$ curve at $h = 4.25$m as can be seen in Figure 6.9a. The proposed $p-y$ curve at a particular depth is compared to the API $p-y$ curve for non-liquefied soil, and its reduced 10% value for liquefied soil in Figure 6.9b. The figure clearly shows that the initial stiffness in the proposed model is very low (about 25 times lower) as compared to the initial stiffness of 10% API $p-y$ curve. For the top 1m of liquefied soil the maximum shear strength (τ_{max}) was estimated to be less than 1kPa (see Step-7 of section 5.8), and hence the $p-y$ curve was not modelled for this part of the liquefied soil.

The proposed $p-y$ curves for liquefiable soils are compared with the $p-y$ curves of one of the widely used BNWF models (model-d as given in Figure 6.6). In model-d, the $p-y$ curves in liquefied soils were modelled as 10% of the API $p-y$ curve for non-liquefied soils. The comparison is shown in Figure 6.10 at four depths. Although, the model-d proposes a lesser value of ultimate lateral resistance, the initial stiffness is quite
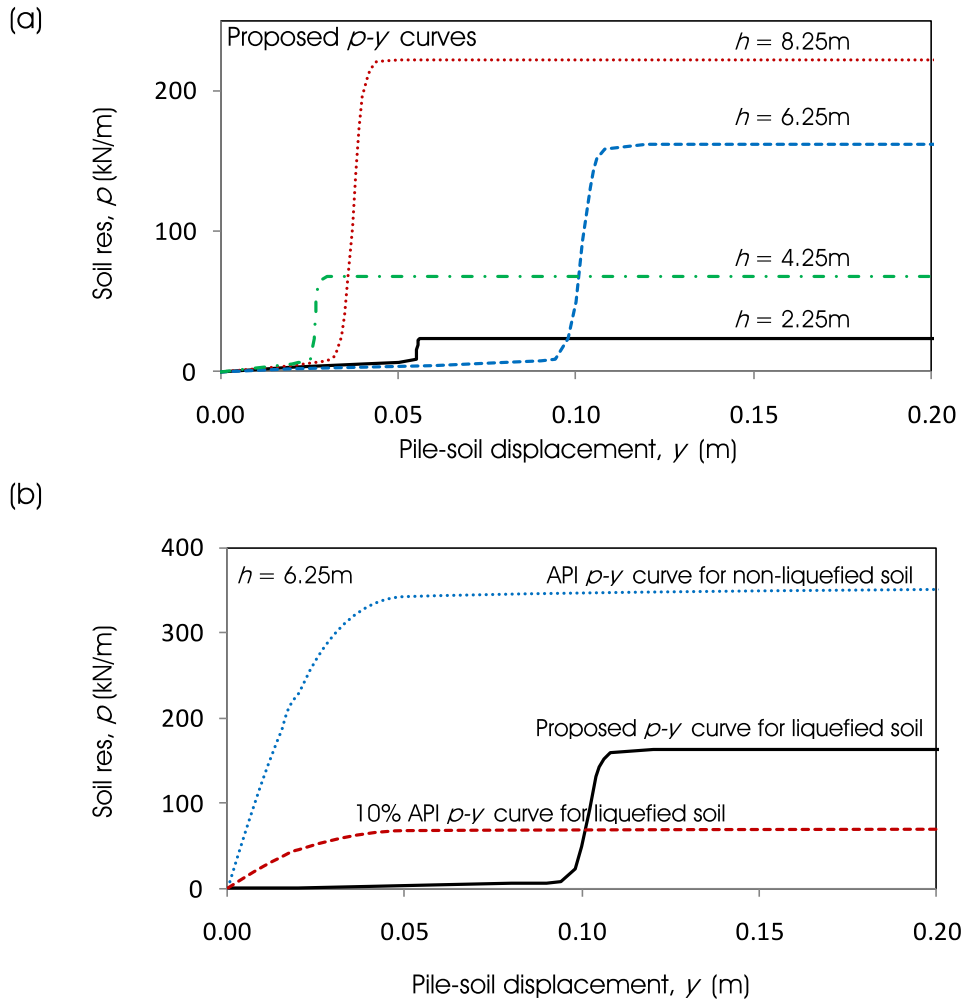
Figure 6.9: (a) The proposed $p - y$ curves at four depths in the fully liquefied soil layer. (b) Comparison of the proposed $p - y$ curve at a particular depth with API $p - y$ curve for non-liquefied soil and 10% of it for liquefied soil.

high compared to the proposed $p - y$ curve model. K_i^n and K_i^c are defined as the initial stiffness of the proposed and the conventional $p - y$ curves as shown in Figure 6.10. For the Showa Bridge soil profile, K_i^n was about 7 to 92 times smaller than K_i^c at different depths in the liquefied soil.

6.4.1.3 Analysis type

The BNWF model was used to perform three analyses, such as:

    1) elastic buckling analysis

    2) modal analysis to estimate dynamic characteristics of bridge pile before and after liquefaction
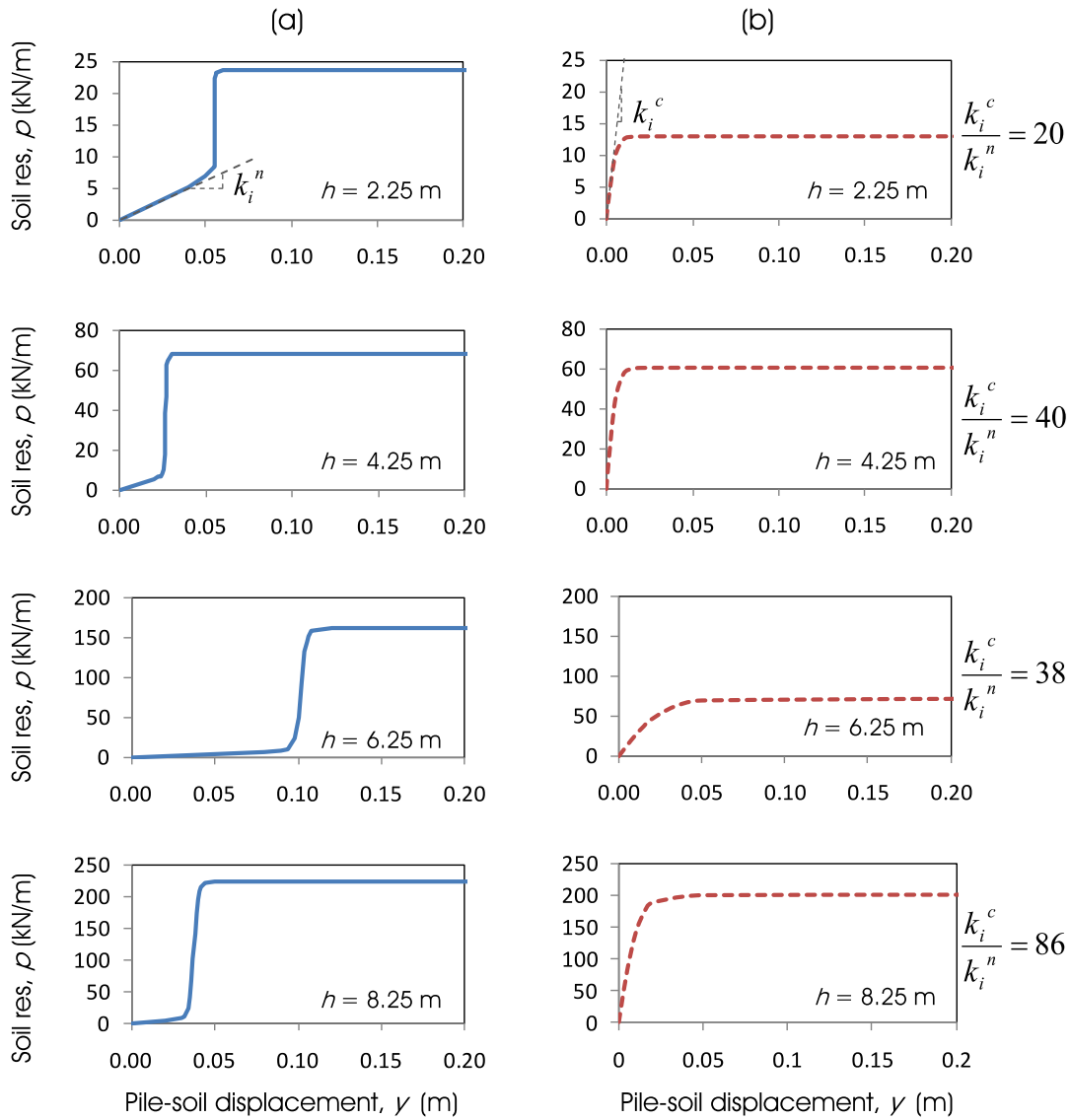
Figure 6.10: $p - y$ curves of based on (a) proposed model and its comparison with (b) 10% of API $p - y$ curves (see model-d in Figure 6.6) at four depths in the liquefied soil layer (h = depth from ground level).

3) coupled bending-buckling analysis considering inertia and axial load on pile

Each of the analysis and its results are discussed below.

6.4.2   Analysis results

6.4.2.1   Elastic buckling analysis

An elastic buckling analysis of the bridge pile was carried out under three different conditions as shown in Figure 6.11. Elastic buckling loads obtained for these cases are presented in Table 6.3. In service condition (Figure 6.11a), the buckling load, P_{cr}, for the pile (as

a fixed-free column) was extimated to be 4459kN. For the fully liquefied condition, considering zero stiffness of the liquefiable soil layer, the buckling load was estimated to be 985kN. The proposed $p-y$ curve model for the liquefiable soil layer predicted the buckling load to be 1495kN. Hence, if the buckling criterion is taken alone for design, the factor of safety is more than one for all the three cases considered, which suggests that the pile can be treated as safe against elastic buckling.
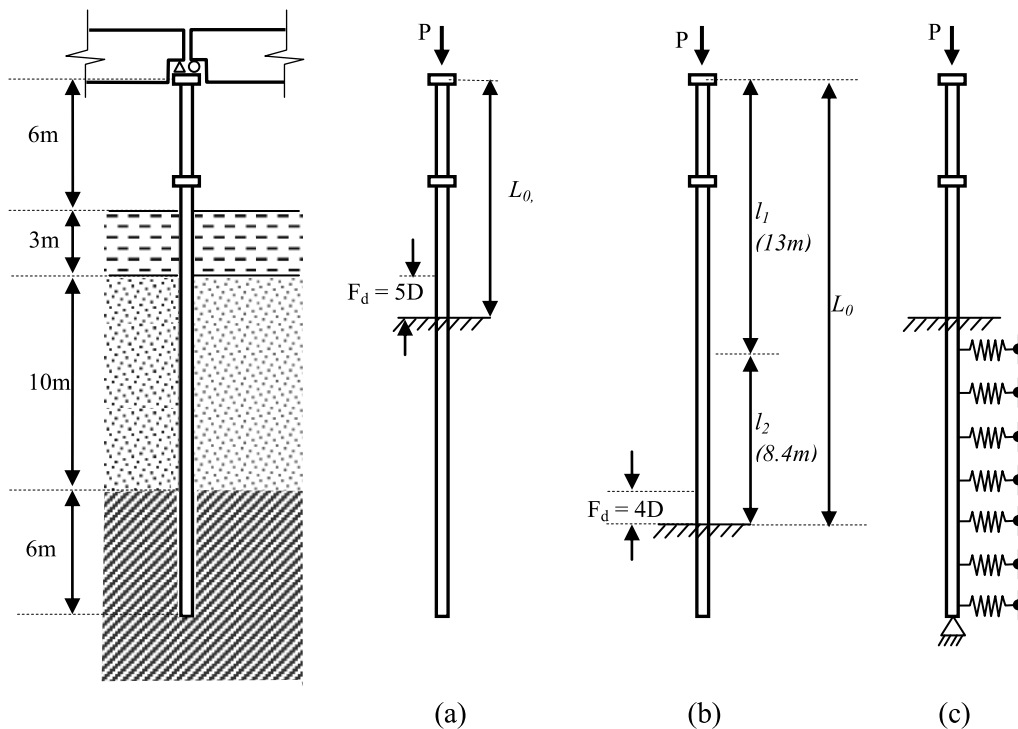
Figure 6.11: Showa Bridge pile configuration for buckling load estimation. (a) Service condition, (b) Fully liquefied case with zero stiffness of soil in the liquefied soil zone, (c) BNWF model with proposed $p-y$ curve for liquefiable soil.

Table 6.3: Elastic buckling load of bridge pile as estimated for different models.

Type of model (Refer to Figure 6.11)	Elastic buckling load	Factor of safety against buckling
Before liquefaction (service condition)	4459kN	4459 / 740 = 6.03
At full liquefaction without any soil stiffness for liquefied soil	985kN	985 / 740 = 1.33
Proposed $p-y$ curve for liquefied soil	1495kN	1495/ 740 = 2.02

6.4.2.2 Modal analysis to estimate dynamic characteristics of bridge pile before and after liquefaction

Usually, fundamental frequency of vibration of a pile-supported structure is estimated based on formulas which are derived from internationally calibrated data (Chopra & Goel, 2000), which do not account for the supporting soil, and the structural length of the pile is taken as the length of pile above the ground and a depth of fixity (usually $3D$ to $5D$). This could be a fair assumption for piles in competent soil. However, during liquefaction the piles in liquefiable soils lose its lateral confinement and become an integral part of the structure. The frequency of the structure may alter substantially and in most cases will reduce. Reduction in fundamental frequency of the structure will increase its flexibility and the structure may suffer more lateral deformation. The bending moment in the piles may increase significantly if the altered natural frequency of the structure comes close to the driving frequency of the earthquake.

Considering the piles as the integral part of the bridge, fundamental frequencies of the bridge for various soil conditions were estimated. The mass of the superstructure was applied as a lumped mass to the pile head. For each pile a mass of 74Ton was applied at its head. Table 6.4 summarises the first fundamental frequencies, f_n of the pile before and after liquefaction obtained from the BNWF model. The analyses gave f_n of 0.367Hz before liquefaction (i.e., time period, $T_n = 2.72$s), which decreased to 0.176Hz after full liquefaction (i.e., $T_n = 5.68$s). A simplified estimation considering zero stiffness of the liquefied soil gave f_n of 0.126Hz (i.e., $T_n = 7.95$s) at full liquefaction. It is worth noting that the estimated fundamental frequency of the Showa Bridge at full liquefaction (0.176Hz) is quite close to the driving frequency of the earthquake ($\sim$0.16Hz) at the time of the bridge collapse, which could have increased the bending moment in the piles leading towards failure.

6.4.2.3 Coupled bending-buckling analysis considering both inertia and axial load on pile

The ground motion record available near the Showa Bridge site during 1964 Niigata earthquake is given in Figure 6.5. For a liquefiable site, it is expected that the ground

216

Table 6.4: First fundamental period of pile for different models.

Type of model	First fundamental frequency, f_n (Hz)	First fundamental period, T_n (s)
Before liquefaction (service condition), from the analysis of the BNWF model using API $p - y$ curves	0.367	2.72
At full liquefaction, considering zero stiffness of the soil	0.126	7.95
At full liquefaction, from the analysis of the BNWF model with proposed $p - y$ curve	0.176	5.68

motion will be higher at the base of the liquefied soil layer than the recorded motion at ground level, because most of the shear waves of ground motion cannot travel through liquefied soil. Hence, predicting the actual magnitude of ground motion at the bottom of the pile from the measured ground motion at the surface is particularly difficult as the basic information in the data is missing.

In a very simplified seismic design consideration for a SDOF system, about 10% of the weight is taken as inertia force. As the amount of inertia for the present case during bridge failure is unknown, the analysis was carried out for a range of inertia forces at the pile head, varying from 0 to $0.1P$ (i.e., $F_i = 0$ to 74kN). The pile was first subjected to the full static axial load ($P = 740$kN), and then the lateral inertia load was applied gradually keeping the axial load constant. The analysis included P-delta and large displacement effects. A nonlinear pseudo-static analysis was carried out in SAP (CSI, 2008), which was essentially a modified time-history analysis to incorporate the bending-buckling interaction. The damping and mass of the system was forced to be near zero value and a very slow loading function was applied for axial and lateral load as shown in Figure 6.12. Time values at A, B and C in the figure were defined as 0s, 100s and 200s for both axial and lateral loading.

Figure 6.13 plots the normalised pile head deflection and normalised maximum bending moment in the pile due to lateral inertia load. The results in the figure are presented for two levels of axial load in pile, 0kN and 740kN. It is clear from the figure that the lateral deflection is amplified due to the inclusion of axial load in the analysis. Without considering the effect of axial load in the analysis, the yielding in pile was occurring
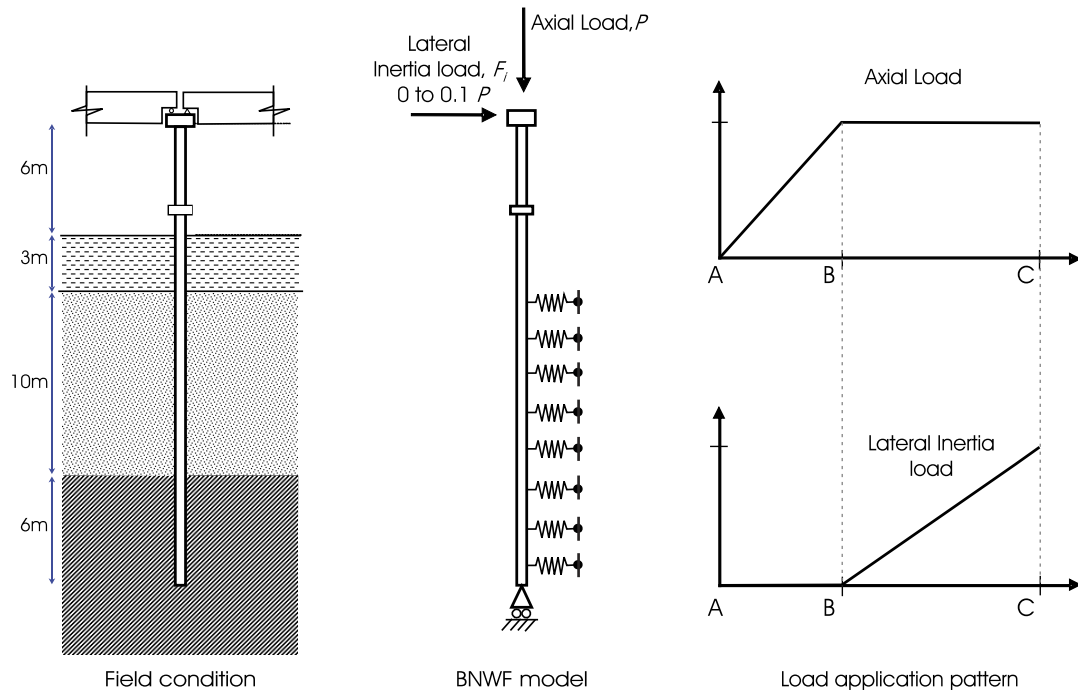
Figure 6.12: Loading function used in the analysis for axial and inertia load.

at about $0.09P$ (66.6kN) of inertia load (i.e, bending moment $= M_y$), which reduced to $0.041P$ (30.34kN, about 54% less as compared with 66.6kN), when the axial load of 740kN was included in the analysis. The sharp deflection of the pile head in the figure shows the instability in the pile due to 30.34kN of inertia (lateral) load in presence of 740kN of axial load at the pile head.

The analysis showed that at $0.041P$ of inertia load and 740kN of axial load, the first yielding of the pile was occurring at a location 3.5m below the ground level (see Figure 6.14a). The soil reaction profile along the pile length and lateral pile deflection for this level of loading is presented in Figure 6.14b and Figure 6.14c. Looking at these results along with Figure 6.10 suggests that the top 5m of soil in the liquefied zone has mobilised beyond the initial low stiffness part, but the soil layer below this depth did not and the resistance was quite low. In the bottom non-liquefied soil layer, higher lateral resistance was observed even for very small deflection as it uses soil springs with API $p-y$ curves for non-liquefied soils. This resistance distribution along the pile also impelled the bending moment in the pile to be maximum in the top 5m of the liquefied soil layer.

The bending moment distribution along the pile length for two levels of inertial force ($0.025P$ and $0.041P$) is presented in Figure 6.15. As shown in the figure, the location of

218
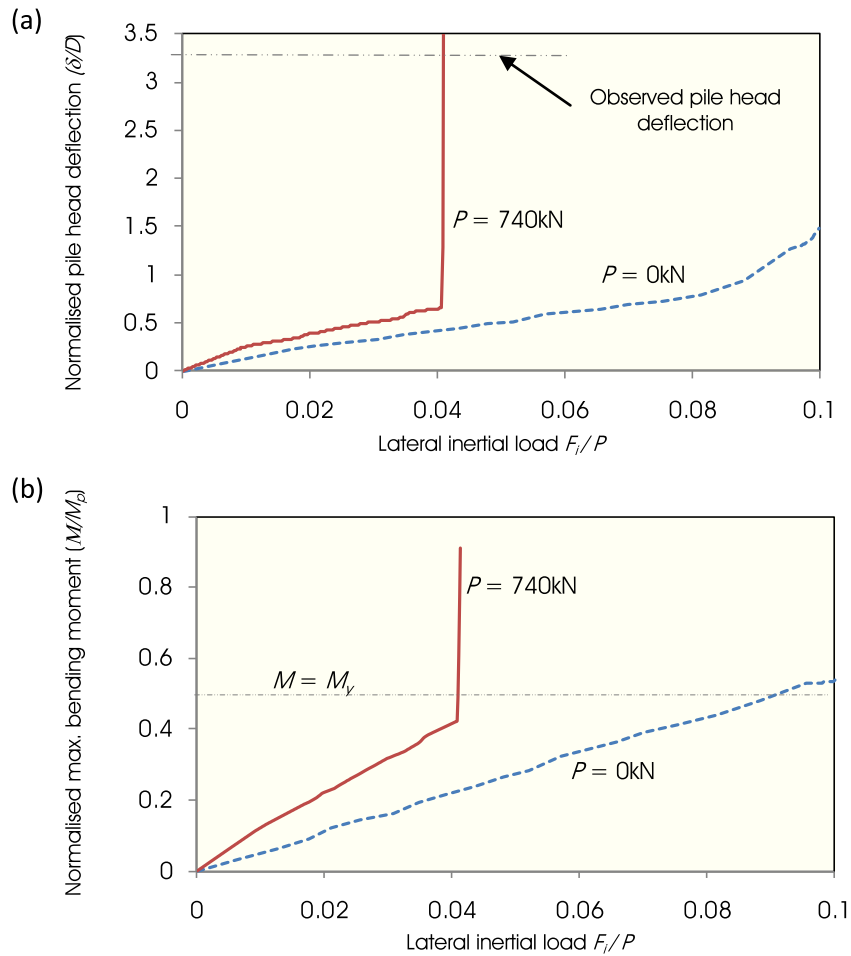
Figure 6.13: (a) Normalised pile head displacement and (b) normalised maximum bending moment due to lateral inertia force (F_i), with and without axial load (P).

first yielding was occurring at 3.5m below ground level, corresponding to the maximum bending moment location. This matches well with the field observation. The proposed $p - y$ curve model with coupled bending-buckling analysis was thus able to predict the structural failure of the pile and the location of the plastic hinge.

6.5 Discussion of results

The present analysis with the new proposed $p - y$ curve model showed structural failure of the pile and could also predict the location of hinge formation in the pile, which matches with the observation. However, it could not justify why the bridge failed after 60s of earthquake and not during the maximum inertia force. Also this analysis could not justify why only few piles failed when every pile was subjected to a similar inertia force.
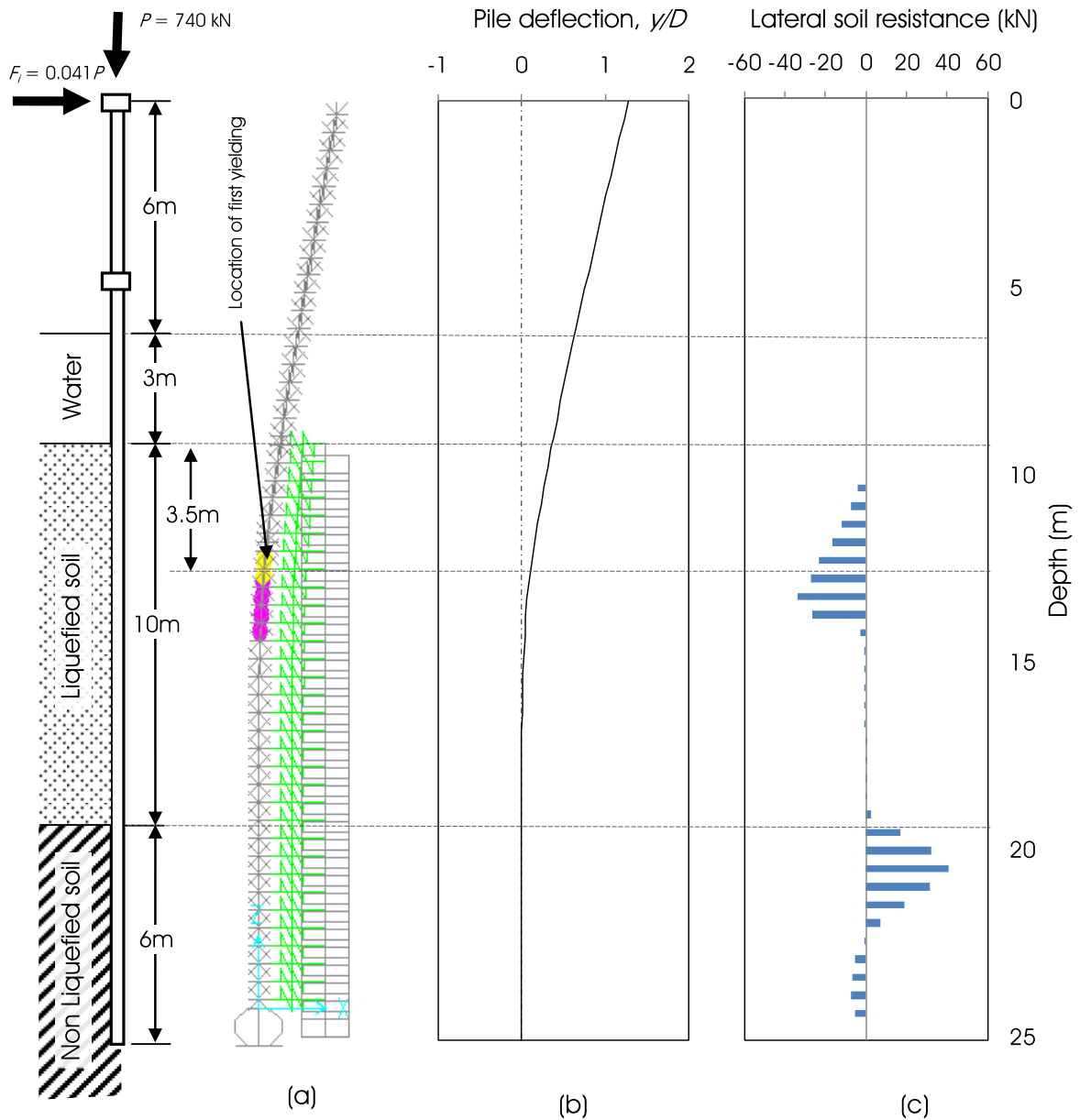
Figure 6.14: (a) Deflected pile showing the location of first yielding, (b) Lateral pile deflection, and (c) soil resistance along the length of the pile from proposed $p - y$ curve model for $0.041P$ of lateral inertia force with an axial load (P) of 740kN.

The dynamic characteristics of the bridge pile during full liquefaction may explain it.

The above analysis was carried out for pile P4, whose post earthquake details were available. However, the bridge collapse initiated with the falling of girder G6, one end of which was seating on pile P6. Figure 6.16 shows the seating arrangement of girders over pile P4 and P6.

Generally a bridge has maximum lateral flexibility at its centre and it reduces towards the end (Kerciku *et al.*, 2007). Added to this, the liquefaction caused the pile to
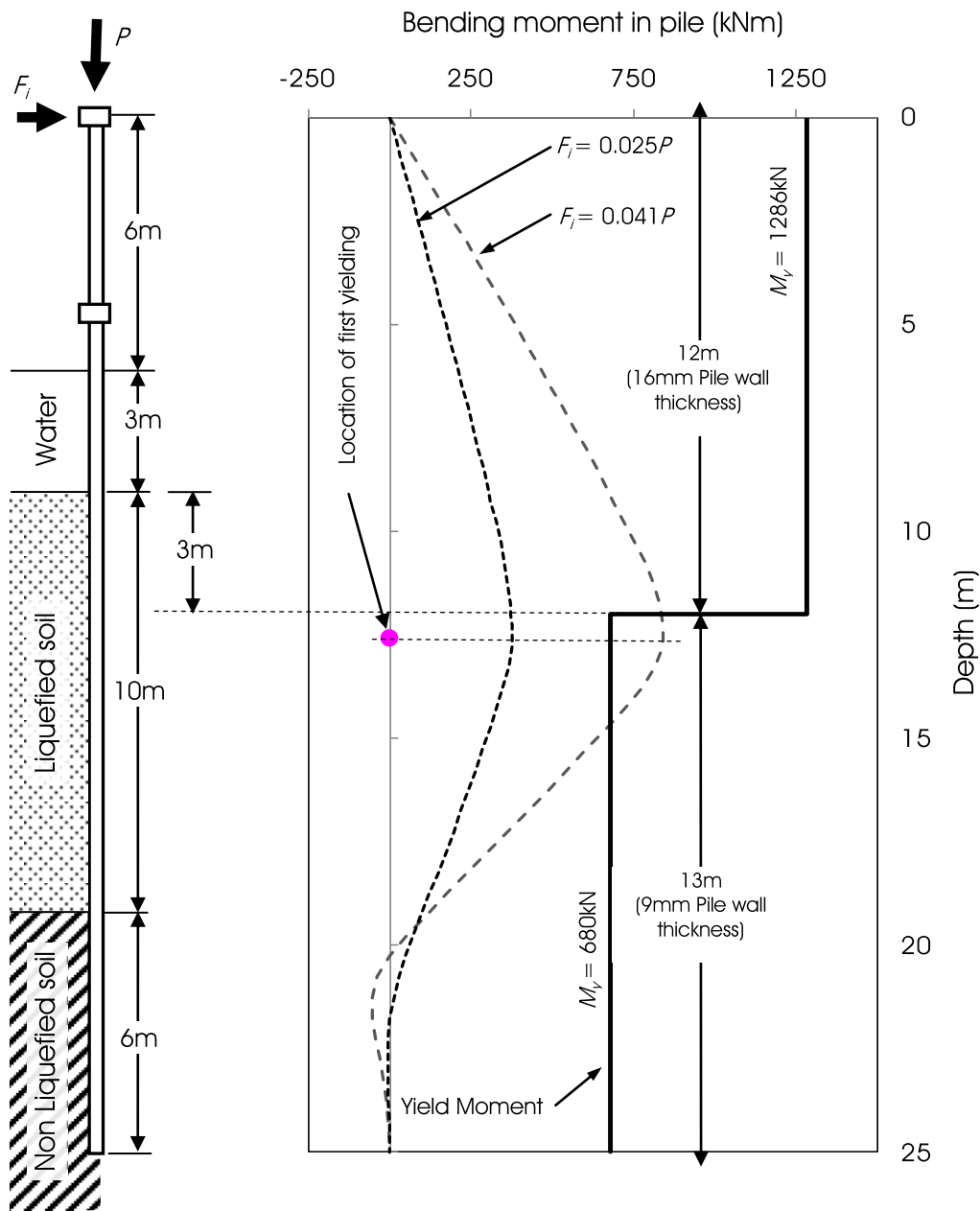
Figure 6.15: Bending moment distribution along the depth of the pile at $0.025P$ and $0.041P$ lateral inertia force.

be nearly unsupported for about double the length of its original unsupported length, which effectively increased the flexibility of the bridge pile. Unfortunately, the central pile had two sliding bearings that supported girders G6 and G7. The pseudo-static analysis showed large pile head deflection for an inertia load of $0.041P$ (30.34kN) along with 740kN of axial load. If the soil profile near to the pile P6 is considered to be same as near to pile P4, the girder might have fallen from the seating due to this loading. Also, the increased flexibility of the pile at full liquefaction could have induced higher deflection to
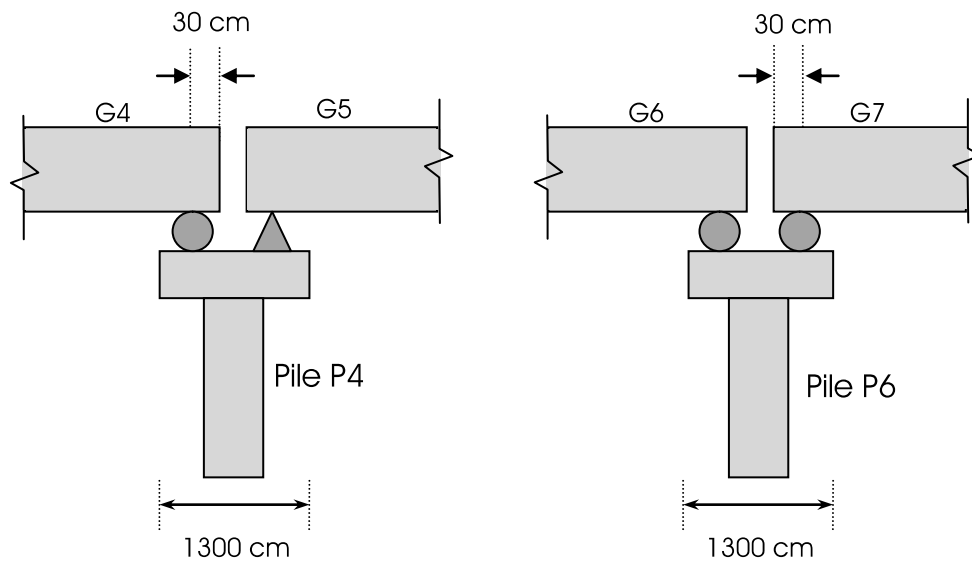
Figure 6.16: Seating arrangement at pile head of the Showa Bridge pile P4 and P6.

the pile head when the large ground displacement occurred at about 60sec after the main shock (see Figure 6.5). It can be hypothesised that during the main shock, the soil did not liquefy fully, but by the time a second jolt came at about 60sec from the main jolt the soil was fully liquefied.

Based on the above discussion, it is reasonable to assume that the increased lateral flexibility and the combined action of axial and inertia load have caused girder G6 to fall from the pile head. Once the girder is out of the pile head it will start to fall down due to its own weight, which will apply additional lateral force on the pile. This lateral force can be considered very similar to the inertia force as considered in the present analysis. Hence, the new $p - y$ curve model still retains the validity of predicting structural failure and location of hinge formation even if the cause of the Showa Bridge failure was initiated due to the fall of girder from the top.

6.6 Summary and conclusions

From the above numerical studies of the Showa Bridge pile failure, the following conclusions can be drawn.

- In BNWF model, liquefied soil can be represented by the new proposed $p - y$ curve, which is based on the mechanics of pile-soil interaction and a direct derivation from

the fundamental stress-strain behaviour of the soil. However, the proposed $p - y$ curve is only applicable for fully liquefied soil and for a monotonic or pushover type analysis.

- It is important for designers to take into account the bending-buckling interaction during seismic design of piles in liquefiable soils, which can be easily incorporated in a BNWF model and applying axial loads along with other seismic loading (e.g., lateral spreading force, inertia force, etc.).

- The inertia force can be a feasible source of lateral loading for the Showa Bridge pile, which in combination with axial load and degraded soil stiffness at full liquefaction could predict the structural failure of the pile.

- The analysis predicted the location of maximum bending moment in the Showa Bridge pile at 3.5m below GL, which matches well with the observation. The failure of the bridge after full liquefaction also discards the possibility of hinge formation at intermediate depths during the top-down progression of liquefaction, which is discussed in section 3.9 as another possible reason of plastic hinge formation at intermediate depths.

- Although, the aim of this study was not to find the actual cause of Showa bridge pile failure, the analysis captured some major field observations of the failure by using the proposed $p - y$ curve model such as the location of the plastic hinge formation.

Chapter 7

Conclusions

This thesis investigates the lateral pile soil interaction (LPSI) in liquefiable soils. The modelling technique of LPSI using $p-y$ curves in a beam on non-linear Winkler foundation (BNWF) model and its present shortcomings for modelling liquefiable soil are highlighted. A set of 13 centrifuge pile group test results were analysed in detail to obtain $p-y$ curves in liquefied soil. To further understand the LSPI close to the pile, a series of $1-g$ tests was performed and the $p-y$ curves at different degrees of liquefaction with various rates of loading were studied. Considering the similarity between the experimentally observed $p-y$ curves and the stress-strain behaviour in liquefied soil, element tests available in literature that give the stress-strain behaviour of liquefied soils are collated. Based on these element test results and a numerical analysis, a very simplified monotonic $p-y$ curve has been proposed that preserves the characteristics of experimentally observed $p-y$ curves as well as the stress-strain behaviour of liquefied soil. Finally the proposed $p-y$ curve was used to study the case history of Showa Bridge pile failure and the important observations were highlighted.

7.1 Specific conclusions

Each chapter in this thesis ends with the summary of conclusions from that chapter. The specific conclusions obtained from the present study can be summarised as follows.

7.1.1 Resistance of liquefied soil

Based on the experimental studies, both centrifuge and $1-g$ tests, and already available field test (see section 2.8.3) and element test data (see section 2.3.3), it may be inferred

that liquefied soil can offer significant lateral resistance to a pile if sufficiently sheared in an undrained condition. The origin of this lateral resistance to a pile has been hypothesised as suppressed dilation of liquefied soil that causes the decrease in excess pore water pressure during post liquefied monotonic shearing. For a medium dense sand ($\sim 50\%$ relative density), centrifuge tests have shown that at full liquefaction the resistance can normally range from 1-10% of the API suggested resistance for non-liquefied soil. The $1 - g$ tests have also shown similar reduced resistance for partially liquefied soil, for example, at 50% liquefaction, the maximum lateral resistance was about 1/2 of the API suggested resistance for non-liquefied soil.

7.1.2 Shape of the $p - y$ curves

Most of the centrifuge tests have suggested that the shape of the $p - y$ curve is a strain hardening type, offering very low stiffness for initial relative pile-soil displacement but higher stiffness at large displacement. The $1 - g$ tests have shown that the initial stiffness of the $p - y$ curve reduces with increasing degree of liquefaction. However, the stiffness at larger displacement does not depend on degree of liquefaction. This is in contrast to the present practice of strain softening type $p - y$ curve. The $1 - g$ tests have also shown that the $p - y$ curve can reach a maximum resistance value when subjected to large displacement of about 0.4-0.5D. Hence, the shape of a monotonic $p - y$ curve for liquefied soil can be visualised as a sigmoid curve.

7.1.3 Damping in liquefied soil

The cyclic $p - y$ curves as back calculated from centrifuge tests were used to estimate equivalent viscous damping ratio. The results have shown that the damping ratio in liquefied soil could be very high, up to 50% in some cases. The higher damping ratio was associated with small strain vibration as the proportionate energy dissipated at small strain vibration was large as compared to large strain vibration. This was due to the cyclic strength degradation of the soil and change in shape of the hysteresis loop with strain.

7.1.4 Bending moment in pile during the process of liquefaction

The centrifuge test results have shown that before liquefaction of the soil, the pile had sufficient lateral confinement and the depth of fixity lies within the top non-liquefied soil layer. This, then, causes the bending moment to be maximum near to the pile head. As the liquefaction progresses from shallow depth to deep depth, the location of maximum bending moment shifts from the top to the bottom of the liquefied soil layer, where the rate of shifting depends on the development of liquefaction at the site. Once the soil is fully liquefied the depth of fixity moves down further to the non-liquefied layer below. This top-down effect of the maximum bending moment location can be recognized as one of the reasons for the formation of one or more plastic hinges at intermediate depths of pile in liquefiable soils during earthquakes, which has been observed in many cases of pile failure in past earthquakes.

7.1.5 Pore pressure distribution: near to the pile *versus* far field

Centrifuge test results have shown that higher lateral resistance is associated with the decrease in excess pore water pressure (EPWP) near to the pile. Though, excess pore pressure near to the pile could be more appropriate to define soil resistance, it is hard to characterise the expected value in a field condition, as it depends on many parameters including the shear loading, pile dimension, gap formation near to pile that facilitates easy dissipation of EPWP. Hence, the lateral resistance of liquefied soil at soil-pile interface is normally characterised by the degree of liquefaction expected in the soil at the site without considering the influence of pile. Also the observations suggest that the pore pressure dissipation near to pile is quicker than in the free field due to the availability of a vertical path for EPWP dissipation at the pile-soil interface.

7.1.6 Proposed $p-y$ curve model based on stress-strain behaviour of the soil

Based on the shear stress - shear strain $(\tau - \gamma)$ behaviour of liquefied soil, the parameters for $p - y$ curve construction were proposed using two scaling factors, N_s and M_s. N_s

scales τ to p whereas M_s scales strain to y. Appropriate values of N_s and M_s have been investigated through FE analysis and design values were suggested for fully liquefied soil. The value of M_s was proposed to be 1.87 for conservative design. The value of N_s was proposed to be the same as the bearing capacity factor used in current practice, which is 9.2 for a smooth pile-soil interface and 11.94 for a rough pile-soil interface. A smooth continuous $p - y$ curve was proposed which uses the scaled $p - y$ curve parameters (y_1, p_1, y_u and p_u). The proposed $p - y$ curve model maintains the characteristic stress-strain behaviour of liquefied soil, and is yet simple to define and implement in a BNWF model. Although, the model was developed for generalised field condition, it has few limitations and its application should be limited to fully liquefied soil in monotonic loading situations only. This model does not include the cyclic behaviour of soil. A rough pile-soil interface was assumed in the finite element analysis carried out to obtain the scaling factors N_s and M_s. Further study is required to validate the applicability of these factors for smooth pile-soil interface. Significant amount of research is still necessary in this area and more field cases are needed to validate the proposed model for its wide adaptability.

7.1.7 Application of the proposed $p - y$ curve model

To demonstrate the application of the proposed $p - y$ curve model for fully liquefied soil, a well known case history of Showa Bridge pile failure in liquefiable soils was considered, which failed during the 1964 Niigata earthquake. The proposed $p - y$ curve was used in a BNWF model to represent lateral pile-soil interaction. A monotonic pushover analysis was performed considering both axial and lateral loads on pile. Pile foundations in liquefiable soils subjected to seismic shaking may fail either due to a) excessive settlement, b) shear c) bending, d) static instability, or e) dynamic instability. It is important for the designers to take into account the appropriate pile-soil interaction representation to be able to choose right failure mechanism of pile for safe design. In design, either a single failure mechanism or an interaction of one or more mechanisms governs. The analyses have shown that the bending-buckling interaction is a more probable mechanism of pile failure rather than the individual bending or buckling mechanisms. The characteristics of the proposed $p - y$ curve were compared with the $p - y$ curve in conventional practice and its implication in

capturing the failure mechanisms for pile design has been demonstrated. Although, the aim of this study was not to find the actual cause of Showa bridge pile failure, the analysis captured some major field observations of the failure by using the proposed $p - y$ curve model such as the location of the plastic hinge formation.

7.2 Limitations of the present research and scope for further work

The following items can be considered limitations in this research and should be investigated further.

1. The proposed $p - y$ curve from the stress-strain behaviour of the soil was based on clean sand element test results and plane strain FE analysis. More full scale tests are required to verify the proposed $p - y$ curve model for soils in the field conditions.

2. For the next level of improvements, the $p - y$ curve model should incorporate the effect of different degrees of liquefaction and cyclic loading.

3. Piled foundations are most often designed in a group configuration, and piled foundations that support long span bridges are no exception. Such a foundation configuration typically contains a large number of closely spaced piles cast into a substantial pile cap. In case of a large pile group, the individual responses of piles within the group are certainly influenced by the presence of neighboring piles if they are spaced very closely, about less than 3 times pile diameter. Although the centrifuge tests considered in this study had pile groups, the piles were spaced more than 3D. The $1 - g$ model tests also considers the case of a single pile while obtaining the $p - y$ response. Hence, the effect of closely spaced piles on $p - y$ curve in liquefiable soils should be studied further.

4. The experimental setup used in $1 - g$ tests needs further improvement in terms of deeper depth to simulate higher stress level in soil and a better base actuator system that can generate and sustain full liquefaction in soil for longer time. This

may provide more experimental evidence to support/improve the proposed $p - y$ curve model.

5. The major focus of this thesis was on lateral pile-soil interaction. During earthquakes the pile-soil interaction in axial direction and at end bearing may also influence the overall performance of pile foundation. However, the literature is very limited on these interactions in liquefied soil. Hence, the axial and end bearing response of piles in liquefied soils should also be studied.

References

Abdoun, T., & Dobry, R. 2002. Evaluation of pile foundation response to lateral spreading. *Soil Dynamics and Earthquake Engineering*, **22(9-12)**, 1051–1058.

AIJ. 2001. *Recommendations for Design of Building Foundations*. Architectural Institute of Japan, Japan.

Andrews, D.C.A., & Martin, G.R. 2000. Criteria for liquefaction of silty soils. *In: 12th World Conference on Earthquake Engineering, Auckland, New Zealand*.

API. 2000. *Recommended Practice for Planning, Designing, and Constructing Fixed Offshore Platforms - Working Stress Design*. American Petroleum Institute, USA.

Arulmoli, K., Muraleetharan, KK, Hossain, MM, & Fruth, LS. 1992. Velacs: Verification of liquefaction analyses by centrifuge studies, laboratory testing program, soil data report. *Research Report*.

Ashour, M., Norris, G., & Pilling, P. 1998. Lateral loading of a pile in layered soil using the strain wedge model. *Journal of Geotechnical and Geoenvironmental Engineering*, **124**(4), 303–315.

Atkinson, J.H. 1993. *An introduction to the mechanics of soils and foundation through critical state soil mechanics*. McGraw-Hill London.

Baguelin, F., Frank, R., & Said, YH. 1977. Theoretical study of lateral reaction mechanism of piles. *Geotechnique*, **27**(3), 405–434.

Banerjee, P.K., & Davies, T.G. 1978. The behavior of axially and laterally loaded single pile embedded in non-homogeneous soils. *Geotechnique*, **21(3)**, pp. 309–326.

Bhattacharya, S. 2003. *Pile instability during earthquake liquefaction*. Ph.D. thesis, University of Cambridge, UK.

Bhattacharya, S. 2005. *Cyclic tri-axial test on liquefied Fraction E sand*. Unpublished experimental data, (From personal communication).

Bhattacharya, S., Madabhushi, S. P. G., & Bolton, M. D. 2004. An alternative mechanism of pile failure in liquefiable deposits during earthquakes. *Geotechnique*, **54**(3), 203–213.

Bhattacharya, S., Bolton, M. D., & Madabhushi, S. P. G. 2005. A reconsideration of the safety of the piled bridge foundations in liquefiable soils. *Soils and Foundations*, **45**(4), 13–26.

Bhattacharya, S., Blakeborough, A., & Dash, S. R. 2008. Learning from collapse of piles in liquefiable soils. *ICE Special Issue 2: Learning from failures*, **161**(November), 54–60.

Bolton, M.D. 1986. The strength and dilatancy of sands. *Geotechnique*, **36**(1), 65–78.

Boulanger, R.W., & Idriss, IM. 2006. Liquefaction susceptibility criteria for silts and clays. *Journal of Geotechnical and Geoenvironmental Engineering*, **132**, 1413.

Brandenberg, S. J. 2005. *Behavior of pile foundations in liquefied and laterally spreading ground.* Ph.D. thesis, University of California at Davis, Davis, California, USA.

Brandenberg, S.J., Boulanger, R.W., Kutter, B.L., Chang, D., *et al.* 2005. Behavior of pile foundations in laterally spreading ground during centrifuge tests. *Journal of Geotechnical and Geoenvironmental Engineering*, **131**, 1378.

Brennan, A. J., Govindaraju, L., & Bhattacharya, S. 2007. Liquefaction: Susceptibility, Assessment and Remediation. *In:* Bhattacharya, S. (editor) (ed), *Design of Foundations in Seismic Areas: Principles and Applications, Bhattacharya (ed)*, vol. ISBN: 81-904190-1-3. NICEE.

Brennan, AJ, Thusyanthan, NI, & Madabhushi, SPG. 2005. Evaluation of shear modulus and damping in dynamic centrifuge tests. *Journal of Geotechnical and Geoenvironmental Engineering*, **131**, 1488.

Casagrande, A. 1971. On Liquefaction phenomena. *Geotechnique*, **21**(3), 197–202.

Castro, G. 1987. *On the Behavior of Soils During Earthquakes-Liquefaction.* Soil dynamics and liquefaction, Elsevier.

Castro, G, & Poulos, S.J. 1977. Factors affecting Liquefaction and Cyclic Mobility. *ASCE Journal of Geotechnical Engineering*, **103**(GT 6), 501–516.

Chakraborty, T., & Salgado, R. 2010. Dilatancy and Shear Strength of Sand at Low Confining Pressures. *Journal of Geotechnical and Geoenvironmental Engineering*, **136**(3), 527–532.

Chandrasekaran, VS. 2001. Numerical and centrifuge modelling in soil structure interaction. *Indian Geotechnical Journal*, **31**(1), 1–59.

Chanerley, AA, & Alexander, NA. 2007. Correcting data from an unknown accelerometer using recursive least squares and wavelet de-noising. *Computers & Structures*, **85**(21-22), 1679–1692.

Chopra, A.K., & Goel, R.K. 2000. Building period formulas for estimating seismic displacements. *Earthquake Spectra*, **16**, 533.

COMSOL, A.B. 2009. *COMSOL multiphysics user guide.* Version - 3.5a edn. COMSOL AB Stockholm, Sweden.

CSI. 2008. *SAP 2000: V11.0 - Integrated Software for Structural Analysis and Design.* Berkeley, California, USA.: Computer and Structures Inc (CSI).

Cubrinovski, M., Haskell, JJM, & Bradley, BA. 2009. The effect of shear strength normalisation on the response of piles in laterally spreading soils. *In: Earthquake Geotechnical Engineering Satellite Conference and XVIIth International Conference on Soil Mechanics & Geotechnical Engineering, Alexandria, Egypt.*

Dash, S. R., & Bhattacharya, S. 2007. Criteria for design of piled foundations in seismically liquefiable deposits. *In: Proceedings of 4th International Conference on Earthquake Geotechnical Engineering.*

Dash, S. R., Govindaraju, L., & Bhattacharya, S. 2009. A case study of damages of the Kandla Port and Customs Office tower supported on a mat–pile foundation in liquefied soils under the 2001 Bhuj earthquake. *Soil Dynamics and Earthquake Engineering*, **29**(2), 333–346.

Dash, S.R., Bhattacharya, S., Blakeborough, A., & Hyodo, M. 2008 (October 12-17). p-y curve to model lateral response of pile foundations in liquefiable soils. *In: 14th World Conference on Earthquake Engineering (14WCEE)*.

Dash, S.R., Bhattacharya, S., & Blakeborough, A. 2010a. Bending-buckling interaction as a failure mechanism of piles in liquefiable soils. *Soil Dynamics and Earthquake Engineering*, **30**(1-2), 32–39.

Dash, SR., NK, S., Blakeborough, A., & Bhattacharya, S. 2010b. Characterisation of ERT as a new non-invasive monitoring method of liquefaction process. *In: Proc. of 7th International Conference on Urban Earthquake Engineering (7CUEE) & 5th International Conference on Earthquake Engineering (5ICEE), March 3-5.* Tokyo Institute of Technology, Tokyo, Japan.

Dobry, R., & Abdoun, T. 2001. Recent Studies on Seismic Centrifuge Modeling of Liquefaction and Its Effect on Deep Foundations. *Pages 1–30 of: Proc. 4th International Conference on Recent Advances in Geotechnical Earthquake Engineering and Soil Dynamics.*

Dobry, R., Taboada, V., & Liu, L. 1995. Centrifuge modeling of liquefaction effects during earthquakes. *Pages 14–16 of: Proc. 1st Intl. Conf. On Earthquake Geotechnical Engineering, IS-Tokyo.*

Dodds, A. M., & Martin, G. R. 2007. *Modeling pile behavior in large pile groups under lateral loading.* Tech. rept. MCEER 07-0004. Multidisciplinary Center for Earthquake Engineering Research, Buffalo, NY.

Dou, H., & Byrne, P.M. 1996. Dynamic response of single piles and soil–pile interaction. *Canadian Geotechnical Journal*, **33**(1), 80–96.

Dungca, JR, Kuwano, J., Takahashi, A., Saruwatari, T., Izawa, J., Suzuki, H., & Tokimatsu, K. 2006. Shaking table tests on the lateral response of a pile buried in liquefied sand. *Soil Dynamics and Earthquake Engineering*, **26**(2-4), 287–295.

Dunnavant, TW, & O'Neill, MW. 1989. Experimental p-y model for submerged, stiff clay. *American Society of Civil Engineers. Journal of Geotechnical Engineering*, **115**(1), 95–114.

EERI. 2002. *Bhuj, India Earthquake of January 26, 2001 Reconnaissance Report, Supplement A to volume 18.* Earthquake Engineering Research Institute.

Einav, I., & Randolph, M.F. 2005. Combining upper bound and strain path methods for evaluating penetration resistance. *International Journal for Numerical Methods in Engineering*, **63**(14), 1991–2016.

Eurocode. 1998. *Design provisions for earthquake resistance of structures- foundations, retaining structures and geotechnical aspects.* European Committee for standardization.

Ferritto, J.M. 1997. *Seismic Design Criteria for Soil Liquefaction.* Tech. rept. Naval Facilities Engineering Service Center, Port Hueneme, CA, USA.

Finn, W. D. L. 2005. A Study of Piles during Earthquakes: Issues of Design and Analysis. *Bulletin of Earthquake Engineering*, **3**, 141–234.

Finn, W. D. L., & Fujita, N. 2002. Piles in liquefiable soils: seismic analysis and design issues. *Soil Dynamics and Earthquake Engineering*, **22(9-12)**, 731–742.

Fukuoka, M. 1966. Damage to civil engineering structures. *Soils and Foundations*, **6**(2), 45–52.

Gazioglu, S.M., & O'Neill, M., W. 1984. Evaluation of p-y Relationships in Cohesive Soils. *Pages 192–213 of: Analysis and design of pile foundations: proceedings of a symposium sponsored by the ASCE Geotechnical Engineering Division, San Francisco, California, October 1-5, 1984.* American Society of Civil Engineers.

Ghosh, B. 2003. *Behavior of Rigid Foundation in Layered Soils during Seismic Liquefaction.* Ph.D. thesis, University of Cambridge.

Goh, S., & O'Rourke, T. D. 1999. Limit state model for soil–pile interaction during lateral spread. *Pages 237–260 of: Proc. 7th US–Japan Workshop on Earthquake Resistant Design of Lifeline Facilities and Countermeasures Against Soil Liquefaction.*

Guo, T., & Prakash, S. 1999. Liquefaction of silts and silt-clay mixtures. *Journal of geotechnical and geoenvironmental engineering*, **125**, 706.

Ha, I.S., Olson, S.M., Seo, M.W., & Kim, M.M. 2011. Evaluation of reliquefaction resistance using shaking table tests. *Soil dynamics and earthquake engineering*, **31**(4), 682–691.

Hadush, S., Yashima, A., & Uzuoka, R. 2000. Importance of viscous fluid characteristics in liquefaction induced lateral spreading analysis. *Computers and Geotechnics*, **27**(3), 199–224.

Haigh, S.K. 2002. *Effects of Liquefaction on Pile Foundations in Sloping Ground.* Ph.D. thesis, University of Cambridge.

Hamada, M. 1992a. *Large ground deformations and their effects on lifelines: 1964 Niigata earthquake. Case studies of liquefaction and lifelines performance during past earthquake.* Tech. rept. Technical Rep: NCEER-92-0001. National Center for Earthquake Engineering Research, Buffalo, NY.

Hamada, M. 1992b. *Large ground deformations and their effects on lifelines: 1983 Nihonkai-Chubu earthquake. Case studies of liquefaction and lifelines performance during past earthquake.* Tech. rept. Technical Rep. NCEER-92-0001. National Center for Earthquake Engineering Research, Buffalo, NY.

Hamada, M., & O'Rourke, T.D. 1992. Case studies liquefaction and lifeline performance during past earthquakes: Japanese case studies. *Technical Report NCEER-92-0001.*

Han, S. 2003. Retrieving the time history of displacement from measured acceleration signal. *Journal of Mechanical Science and Technology*, **17**(2), 197–206.

Hazen, A. 1920. Hydraulic-fill dams. *Transactions of the American Society of Civil Engineers*, **83**(1), 1713–1745.

He, L., Elgamal, A., Abdoun, T., Abe, A., Dobry, R., Meneses, J., Sato, M., & Tokimatsu, K. 2006 (April). Lateral load on piles due to liquefaction-induced lateral spreading during one-g shake table experiments. *In: Proceedings of 8th U.S. National Conference on Earthquake Engineering.*

Hetenyi, M. 1946. *Beams on elastic foundation.* The Univ. of Michigan Press.

Holscher, P., van Tol, A.F., & Huy, N.Q. 2008. Influence of rate effect and pore water pressure during Rapid Load Test of piles in sand. *Rapid Load Testing on piles,* 59.

Hwang, J.I., Kim, C.Y., Chung, C.K., & Kim, M.M. 2006. Viscous fluid characteristics of liquefied soils and behavior of piles subjected to flow of liquefied soils. *Soil Dynamics and Earthquake Engineering,* **26**(2-4), 313–323.

Hyodo, M., Hyde, AFL, & Aramaki, N. 1998. Liquefaction of crushable soils. *Geotechnique,* **48**(4), 527–543.

Imai, T., & Tonouchi, K. 1982. Correlation of N-value with S-wave velocity and shear modulus. *Pages 67–72 of: Proc. 2nd European Symposium on Penetration Testing, Amsterdam,* vol. 1.

Imam, S.M.R., Morgenstern, N.R., Robertson, P.K., & Chan, D.H. 2005. A critical-state constitutive model for liquefiable sand. *Canadian Geotechnical Journal,* **42**(3), 830–855.

IS-1893. 2000. *Part-1: Criteria for earthquake resistant design of structures.* Bureau of Indian Standard, New Delhi, India.

Ishibashi, I., & Zhang, X. 1993. Unified dynamic shear moduli and damping ratios of sand and clay. *Soils and Foundations,* **33**(1), 182–191.

Ishihara, K. 1993. Liquefaction and flow failure during earthquakes. *Geotechnique,* **43**(3), 351–415.

Ishihara, K. 1997. Terzaghi oration: geotechnical aspects of the 1995 Kobe earthquake. *Pages 2047–2073 of: Proc. 14th International Conference on Soil Mechanics and Foundation Engineering, Hamburg,* vol. 4.

Ishihara, K., Tatsuoka, F., & Yasuda, S. 1975. Undrained deformation and liquefaction of sand under cyclic stresses. *Soils and Foundations,* **15**(1), 27.

Iwasaki, T. 1984. *A case history of bridge performance during earthquakes in Japan.* Tech. rept. Keynote lecture at the International Conference on Case histories in Geotechnical Engineering, University of Missouri Rolla.

Jeanjean, P. 2009. Re-assessment of PY curves for soft clays from centrifuge testing and finite element modeling. *In: Offshore Technology Conference.*

Jefferies, M, & Been, K. 2006. *Soil liquefaction: A critical state approach.* Taylor & Francis.

JGS. 1964. *CD with Photographs and Motion Pictures of the Niigata City Immediately after the Earthquake in 1964.* Japanese Geotechnical Society, Japan.

JRA. 2002. *Specifications for Highway Bridges, Part V. Seismic Design.* Japanese Road Association, Tokyo, Japan.

JSA. 2004. *JIS A 5525: Steel pile pipe.* Japanese Standards Association, Japan.

Kagawa, T., & Kraft, LM. 1980. Lateral load-deflection relationships of piles subjected to dynamic loadings. *Soils and Foundations*, **20**(4), 19–36.

Kamijo, N., Saito, H., Kusama, K., Kontani, O., & Nigbor, R. 2004. Seismic tests of a pile-supported structure in liquefiable sand using large-scale blast excitation. *Nuclear Engineering and Design*, **228**(1-3), 367–376.

Kawakami, T., Suemasa, N., Hamada, M., Sato, H., & Katada, T. 1994. Experimental study on mechanical properties of liquefied sand. *Pages 285–99 of: Proc. 5th US–Japan Workshop on Earthquake Resistant Design of Lifeline Facilities and Countermeasures against Soil Liquefaction. Technical Report NCEER-94-0026, Salt Lake City, USA*.

Kazama, M., Sento, N., Uzuoka, R., & Ishimaru, M. 2008. Progressive Damage Simulation of Foundation Pile of the Showa Bridge Caused by Lateral Spreading During the 1964 Niigata Earthquake. *Geotechnical Engineering for Disaster Mitigation and Rehabilitation*, 171–176.

Kerciku, A.A, Bhattacharya, S., & Burd, H. J. 2007. Why do pile-supported bridge piers and not abutments collapse in liquefiable soils during earthquakes? *In: Proc. 2nd Japan-Greece Workshop on Seismic Design, Observation, and Retrofit of Foundations, Tokyo, Japan*.

Kimura, Y., & Tokimatsu, K. 2005. Buckling stress of steel pile with vertical load in liquefied soil. *Journal of Structural and Construction Engineering*, **595**, 73–78.

Klar, A. 2008. Upper Bound for Cylinder Movement Using Elastic Fields and Its Possible Application to Pile Deformation Analysis. *International Journal of Geomechanics*, **8**, 162.

Klar, A., & Osman, AS. 2008. Load-displacement solutions for piles and shallow foundations based on deformation fields and energy conservation. *Geotechnique*, **58**(7), 581–590.

Klar, A., & Randolph, MF. 2008. Upper-bound and load-displacement solutions for laterally loaded piles in clays based on energy minimisation. *Geotechnique*, **58**(10), 815–820.

Knappett, J.A., & Madabhushi, S.P.G. 2006. Modelling of liquefaction-induced instability in pile groups. *Geotechnical Special Publication*, **145**, 255–267.

Knappett, JA, & Madabhushi, SPG. 2009. Influence of axial load on lateral pile response in liquefiable soils. Part II: numerical modelling. *Geotechnique*, **59**(7), 583–592.

Kokusho, T., Hara, T., & Hiraoka, R. 2004. Undrained Shear Strength of Granular Soils with Different Particle Gradations. *Journal of Geotechnical and Geoenvironmental Engineering*, **130**(6), 621–629.

Koo, KK, Chau, KT, Yang, X., Lam, SS, & Wong, YL. 2003. Soil-pile-structure interaction under SH wave excitation. *Earthquake Engineering & Structural Dynamics*, **32**(3), 395–415.

Kramer, S.L. 1996. *Geotechnical earthquake engineering.* Prentice-Hall, Civil Engineering and Engineering Mechanics Series.

Kudo, K., Uetake, T., & Kanno, T. 2000. Re-evaluation of nonlinear site response during the 1964 Niigata earthquake using the strong motion records at Kawagishi-cho, Niigata City. *Proc. 12the World Conference on Earthquake Engineering, Auckland, New Zealand*, **969**.

Kuhlemeyer, R.L. 1979. Static and dynamic laterally loaded floating piles. *Journal of the Geotechnical Engineering Division*, **105**(2), 289–304.

Kulhawy, FH, & Chen, Y. 1995. A thirty year perspective of Broms' lateral loading models, as applied to drilled shafts. *In: Bengt Broms Symposium in Geotechnical Engineering*.

Kutter, B. L. 1997 (April 18-19). Strength of liquefied soil is not a material constant; liquefaction is a boundary value problem. *In: NSF workshop proceedings on Post Liquefaction Shear Strength of Granular Soils*.

Liao, SSC, & Whitman, RV. 1986. Overburden correction factors for SPT in sand= Facteurs de correction dus à la couverture pour les essais de pénétration standard dans du sable. *Journal of Geotechnical Engineering*, **112**(3), 373–377.

Liu, L., & Dobry, R. 1995. Effect of liquefaction on lateral response of piles by centrifuge model tests. *National Center for Earthquake Engineering Research (NCEER) Bulletin*, **9**(1), 7–11.

Luong, M.P., & Sidaner, J.F. 1981. Undrained behaviour of cohesionless soils under cyclic and transient loading. *In: Proc. International Conference on Recent Advances in Geotechnical and Earthquake Engineering and Soil Dynamics*.

Madabhushi, G., Knappett, J., & Haigh, S. 2009. *Design of Pile Foundations in Liquefiable Soils*. Imperial College Press.

Makris, N. 1994. Soil-pile interaction during the passage of Rayleigh waves: an analytical solution. *Earthquake Engineering & Structural Dynamics*, **23**(2), 153–167.

Martin, C.M., & Randolph, M.F. 2006. Upper bound analysis of lateral pile capacity in cohesive soil. *Geotechnique*, **56-2**, 141–145.

Martin, R. G. 1997 (April 18-19). Post liquefaction shear strength from laboratory and field tests. *In: NSF workshop proceedings on Post Liquefaction Shear Strength of Granular Soils*.

Matlock, H. 1970. Correlation for design of laterally loaded piles in soft clay. *In: Offshore Technology Conference*.

Matlock, H., & Ripperger, EA. 1956. Procedures and instrumentation for tests on a laterally loaded pile. *In: Proceedings, Eighth Texas Conference on Soil Mechanics and Foundation Engineering*.

Matsumoto, H., Sasaki, Y., & Kondo, M. 1987. Coefficient of Subgrade Reaction on Pile in Liquefiable Ground. *In: Proc. Second National Conference on Soil Mechanics and Foundation Engineering, (in Japanese)*.

McClelland, B., & Focht Jr, J.A. 1958. Soil modulus for laterally loaded piles. *Transactions, ASCE*, **123**(1049-1063).

Meyerhof, G. G. 1957. Discussion on soil properties and their measurement. *In: Proc. 4th International Conference on Soil Mechanics and Foundation Engineering*, vol. 3.

Meymand, P.J. 1998. *Shaking table scale model tests of nonlinear soil-pile-superstructure interaction in soft clay*. Ph.D. thesis, University of California, Berkeley.

Mizuno, H. 1987. Pile Damage during Earthquake in Japan (1923-1983). *Page 53 of: Dynamic response of pile foundations–experiment, analysis, and observation: proceedings of a session of the Geotechnical Engineering Division of the ASCE in conjunction with the ASCE Convention in Atlantic City, New Jersey, April 27*. Amer Society of Civil Engineers.

Mondal, G., & Rai, D.C. 2008. Performance of harbour structures in Andaman Islands during 2004 Sumatra earthquake. *Engineering Structures*, **30**(1), 174–182.

Muhunthan, B., & Schofield, AN. 2000. Liquefaction And Dam Failures. *Page 266 of: Slope stability 2000: Proc. Geo-Denver 2000: August 5-8, 2000, Denver, Colorado*. Amer Society of Civil Engineers.

MuirWood, D. 1990. *Soil behaviour and critical state soil mechanics*. Cambridge Univ Pr.

NEHRP. 2000. NEHRP recommended provisions for seismic regulations for new buildings and other structures. *In: Rep. Nos. FEMA 368 (Provisions) and 369 FEMA (Commentary)*. Council, B.S.S.

NGDC. 2010. *National Geographic Data Center, www.ngdc.noaa.gov.*

NICEE. 2010. *National Information Center of Earthquake Engineering, www.nicee.org.*

NISEE. 2010. *National Information Services for Earthquake Engineering, http://nisee.berkeley.edu/.*

Olson, S.M., & Stark, T.D. 2002. Liquefied strength ratio from liquefaction flow failure case histories. *Canadian Geotechnical Journal*, **39**(3), 629–647.

O'Neill, MW, & Murchison, JM. 1983. An evaluation of py relationships in sands. *Report to American Petroleum Institute, University of Texas at Austin.*

O'Rourke, M.J., & Liu, X. 1999. Response of buried pipelines subject to earthquake effects. *MCEER Monograph-3*. Multidisciplinary Center for Earthquake Engineering Research.

Osman, AS, & Bolton, MD. 2005. Simple plasticity-based prediction of the undrained settlement of shallow circular foundations on clay. *Geotechnique.*, **55**(6), 435–447.

Park, K.T., Kim, S.H., Park, H.S., & Lee, K.W. 2005. The determination of bridge displacement using measured acceleration. *Engineering structures*, **27**(3), 371–378.

Poulos, H.G. 1971. Behavior of laterally loaded piles: I-single piles. *Journal of the Soil Mechanics and Foundations Division*, **97**(5), 711–731.

Poulos, S.J., Castro, G., & France, J.W. 1985. Liquefaction evaluation procedure. *Journal of Geotechnical Engineering*, **111**, 772.

Randolph, MF. 1981. Response of flexible piles to lateral loading. *Geotechnique*, **31**, 247–59.

Randolph, M.F., & Houlsby, GT. 1984. Limiting pressure on a circular pile loaded laterally in cohesive soil. *Geotechnique*, **34**(4), 613–623.

Reese, L., Cox, W., & Koop, F. 1974. Analysis of laterally loaded piles in sand. *In: Offshore Technology Conference.*

Reese, L., Cox, W., & Koop, F. 1975. Field Testing and Analysis of Laterally Loaded Piles in Stiff Clay. *In: Offshore Technology Conference.*

Reese, L.C., & Welch, R.C. 1975. Lateral loading of deep foundations in stiff clay. *Journal of the Geotechnical Eengineering Division*, **101**(7), 633–649.

Rollins, K.M., Gerber, T.M., Lane, J.D., & Ashford, S.A. 2005. Lateral resistance of a full-scale pile group in liquefied sand. *Journal of Geotechnical and Geoenvironmental Engineering*, **131**, 115–125.

Roscoe, KH, Schofield, AN, & Wroth, CP. 1958. On the yielding of soils. *Geotechnique*, **8**(1), 22–53.

RTRI. 1999. *Design Standard for Railway Facilities-Seismic Design.* Railway Technical Research Institute, Japan.

Sato, H., Hamada, M., & Doi, M. 1994. An experimental study of effects of laterally flowing ground on in-ground structures. *Pages 405–414 of: Proc. 5th Japan–US Workshop on Earthquake Resistant Design of Lifeline Facility and Countermeasures against Soil Liquefaction, Technical Report NCEER-94-0026.*

Sato, M. 1994. A new dynamic geotechnical centrifuge and performance of shaking table tests. *In: Proc. Centrifuge 94, Leung, Lee and Tan (eds), Balkema, Rotterdam, ISBN 9054103523.*

Schofield, A., & Wroth, P. 1968. *Critical state soil mechanics.* McGraw-Hill London.

Schofield, A. N. 1981. Dynamic and Earthquake Geotechnical Centrifuge Modelling. *Pages 1081–1100 of: Proc. International Conference Recent Advances in Geotechnical Earthquake Engineering and Soil Dynamics*, vol. Vol. 3.

Seed, H., & Harder, L.F. 1990. SPT-based analysis of cyclic pressure generation and undrained residual strength. *Pages 351–376 of: Proc. H. Bolton Seed Memorial Symposium.*

Seed, H. B., & Lee, K. L. 1966. Liquefaction of Saturated Sands During Cyclic Loading. *Journal of the Soil Mechanics and Foundation Division*, **92**(SM6), 105–134.

Seed, H.B. 1979. Soil liquefaction and cyclic mobility evaluation for level ground during earthquakes. *Journal of the Geotechnical Engineering Division*, **105**(2), 201–255.

Seed, H.B. 1987. Design Problems in Soil Liquefaction. *Journal of Geotechnical Engineering*, **113**(8), 827–845.

Seed, H.B., & Idriss, IM. 1970. Soil moduli and damping factors for dynamic response analysis. *Report No. EERC 70-10, Earthquake Engineering Research Center, University of California, Berkeley.*

Shamoto, Y., Zhang, J.M., & Goto, S. 1997. Mechanism of large post-liquefaction deformation in saturated sand. *Soils and Foundations*, **37**(2), 71–80.

Shanker, K., Basudhar, P.K., & Patra, N.R. 2007. Buckling of piles under liquefied soil conditions. *Geotechnical and Geological Engineering*, **25**(3), 303–313.

Sitharam, TG, GovindaRaju, L., & Sridharan, A. 2004. Dynamic properties and liquefaction potential of soils. *Current Science*, **87**(10), 1370–1378.

Sitharam, TG, Vinod, JS, & Ravishankar, BV. 2009. Post-liquefaction undrained monotonic behaviour of sands: experiments and DEM simulations. *Geotechnique*, **59**(9), 739–749.

Sivathyalan, S. 1994 (December). *Static, Cyclic and Post Liquefaction Simple Shear Response of Sands*. MSc Thesis, University of British Columbia.

Skempton, A.W. 1951. The Bearing Capacity of Clays. *Proc. Building Research Congress*, **1**, 180–189.

Spillers, WR, & Stoll, RD. 1964. Lateral response of piles. *Journal of the Soil Mechanics and Foundation Division*, **90**(6), 1–9.

Stark, T.D., & Mesri, G. 1992. Undrained shear strength of liquefied sands for stability analysis. *Journal of Geotechnical Engineering*, **118**, 1727–1727.

Stevens, JB, & Audibert, JME. 1979. Re-examination of py curve formulations. *Page 397 of: Proc. 11th Annual Offshore Technology Conference.*

Takada, S., Tanabe, K., Yamajyo, K., & Katagiri, S. 1987. Liquefaction Analysis for Buried Pipelines. *In: Proc. 3rd International Conference on Soil Dynamics and Earthquake Engineering.*

Takahashi, A. 2002. *Soil-Pile-Interaction in Liquefaction induced lateral spreading of soils*. Ph.D. thesis, Tokyo Institute of Technology, Japan.

Takata, T., Tada, Y., Toshida, I., & Kuribayashi, E. 1965. *Damage to bridges in Niigata earthquake (in Japanese)*. Tech. rept. Report no-125-5. Public Works Research Institute (PWRI), Japan.

Take, WA, & Bolton, MD. 2002. A new device for the measurement of negative pore water pressures in centrifuge models. *Pages 89–94 of: International Conference Physical Modelling Geotechnics.*

Tanabe, K. 1988. *Fundamental Study on Seismic Assessment and Design of Bruried Pipelines Subjected to Ground Failure during Earthquake*. Ph.D. thesis, Kobe University.

Tazoh, T. 2007. Earthquake engineering research on pile foundations with emphasis on pile foundations subjected to large ground deformations. *In:* Bhattacharya, Dr. S. (ed), *Design of Foundations in Seismic Areas: Principles and Applications*, vol. ISBN: 81-904190-1-3. NICEE (National Information Center of Earthquake Engineering).

Tazoh, T., Sato, M., & Gazetas, G. 2005. Centrifuge Tests on Pile Foundation Structure Systems Affected by Liquefaction Induced Soil Flow after Quay Wall Failure. *In: Proc. 1st Greece-Japan workshop: Seismic Design, Observation, and Retrofit of Foundations, Athens.*

Thavaraj, T., Liam Finn, WD, & Wu, G. 2010. Seismic Response Analysis of Pile Foundations. *Geotechnical and Geological Engineering*, **28**(3), 275–286.

Thomas, J. 1992 (October). *Static, Cyclic and Post Liquefaction Undrained Behaviour of Fraser River Sand.* MSc Thesis, University of British Columbia.

Ting, J.M. 1987. Full scale cyclic dynamic lateral pile response. *Journal of Geotechnical Engineering*, **113**(1), 30–45.

Tokimatsu, K., & Suzuki, H. 2004. Pore water pressure response around pile and its effects on PY behavior during soil liquefaction. *Soils and foundations*, **44**(6), 101–110.

Tokimatsu, K., Hiroshi, O. O., Satake, K., Shamoto, Y., & Asaka, Y. 1998. Effects of lateral ground movements on failure patterns of piles in the 1995 Hyogoken-Nambu earthquake. *Pages 1175–1186 of: Proceedings of a speciality conference, Geotechnical Earthquake Engineering and Soil Dynamics III, ASCE Geotechnical Special Publication.*

Towhata, I., Sasaki, Y., Tokida, K., Matsumoto, H., Tamari, Y., & Yamada, K. 1992. Prediction of permanent displacement of liquefied ground by means of minimum energy principle. *Soils and Foundations*, **32**(3), 97–116.

Towhata, I., Vargas-Monge, W., Orense, RP, & Yao, M. 1999. Shaking table tests on subgrade reaction of pipe embedded in sandy liquefied subsoil. *Soil Dynamics and Earthquake Engineering*, **18**(5), 347–361.

Tsuchida, H. 1970. Prediction and countermeasure against the liquefaction in sand deposits. *In: Seminar in the Port and Harbor Research Institute (in Japanese).*

USGS. 2010. *Earthquake Facts.* U.S. Geological Survey, www.usgs.gov.

Uzuoka, R., Yashima, A., Kawakami, T., & Konrad, J.M. 1998. Fluid dynamics based prediction of liquefaction induced lateral spreading. *Computers and Geotechnics*, **22**(3-4), 243–282.

Vaid, YP, & Thomas, J. 1995. Liquefaction and post liquefaction behavior of sand. *Journal of Geotechnical Engineering*, **121**(2), 163–173.

Welch, P. 1967. The use of fast Fourier transform for the estimation of power spectra: a method based on time averaging over short, modified periodograms. *IEEE Transactions on Audio and Electroacoustics*, **15**(2), 70–73.

Wilson, D.W. 1998. *Soil-pile-superstructure interaction in liquefying sand and soft clay.* Ph.D. thesis, University of California, Davis, USA.

Wilson, D.W., Boulanger, R.W., & Kutter, B.L. 2000. Observed seismic lateral resistance of liquefying sand. *Journal of Geotechnical Engineering, ASCE*, **126**(10), 898–906.

Wu, G., & Finn, W.D.L. 1997. Dynamic nonlinear analysis of pile foundations using finite element method in the time domain. *Canadian Geotechnical Journal*, **34**(1), 44–52.

Xenaki, VC, & Athanasopoulos, GA. 2003. Liquefaction resistance of sand-silt mixtures: an experimental investigation of the effect of fines. *Soil Dynamics and Earthquake Engineering*, **23**(3), 1–12.

Yang, Z., Elgamal, A., & Parra, E. 2003. Computational Model for Cyclic Mobility and Associated Shear Deformation. *Journal of Geotechnical and Geoenvironmental Engineering*, **129**(12), 1119–1127.

Yasuda, S., Saito, K., & Suzuki, N. 1987. Soil Spring Constant on Pipe in Liquefied Ground. *Pages pp. 189–192 of: Proc. 19th JSCE Conference on Earthquake Engineering (in Japanese)*.

Yasuda, S., Kiku, H., & Yosida, T. 1989. Shaking table tests on the friction force between the buried pipelines and the ground during liquefaction. *Pages pp. 759–760 of: Proc. 24th National Conference, JSSMFE (in Japanese)*.

Yasuda, S., Terauchi, T., Morimoto, M., Erken, A., & Yoshida, N. 1998. Post liquefaction behavior of several sands. *In: Proc. 11th European Conference on Earthquake Engineering*. Balkema, Rotterdam.

Yasuda, S., Yoshida, N., Kiku, H., Adachi, K., & Gose, S. 1999. A simplified method to evaluate liquefaction-induced deformation. *Pages 555–566 of:* e Pinto, P. Sêco (ed), *Proc. Earthquake Geotechnical Engineering, Balkema, Rotterdam*, vol. 2.

Yoshida, N., & Hamada, M. 1991. Damage to foundation piles and deformation pattern of ground due to liquefaction-induced permanent ground deformations. *Pages 147–161 of: 3rd US-Japan Workshop on Earthquake-Resistant Design of Lifeline Facilities and Countermeasures for Soil Liquefaction, Technical Repon NCEER-91-0001. NCEER, Buffalo, NY*.

Yoshida, N., Tazoh, T., Wakamatsu, K., Yasuda, S., Towhata, I., Nakazawa, H., & Kiku, H. 2007. Causes of Showa Bridge Collapse in the 1964 Niigata Earthquake Based on Eyewitness Testimony. *Soils and Foundations*, **47**(6), 1075–1087.

Yoshida, T., & Uematsu, M. 1978. Dynamic Behavior of a Pile in Liquefiable Sand. *Pages pp. 657–663 of: Proc. 5th Japan Earthquake Engineering Symposium (in Japanese)*.

Zhao, M., Liu, D., Zhang, L., & Jiang, C. 2008. 3D finite element analysis on pile-soil interaction of passive pile group. *Journal of Central South University of Technology*, **15**(1), 75–80.

Appendices

Appendix A

Evaluation of first fundamental frequency

A.1 Dynamic Amplification Factor (DAF) method

The DAF method was used to determine the first fundamental frequency of the soil-pile-footing-structure system from the centrifuge test data as presented in chapter 3.

A frequency domain analysis was carried out and the amplification factor for the input signal (base acceleration time history) and output signal (acceleration time history on top of the footing or superstructure) was estimated for the centrifuge test results. Matlab® command "tfestimate" was used to evaluate the transfer function between input and output signal. From the transfer function, the dynamic amplification factor was calculated as the ratio of the transfer function (T_f) at each time step divided by the transfer function at initial time step (T_{fi}). T_{fi} can be referred to as the static response of the system.

$$DAF = \frac{T_f}{T_{fi}} \tag{A.1}$$

Figure A.1 shows the dynamic amplification for base acceleration to footing acceleration and base acceleration to superstructure acceleration for test CT6-A. This is essentially the amplification between input signal and output signal in frequency domain, and the frequency at which maximum amplification is observed is regarded as the fundamental frequency of the system. The DAF analysis was carried out in prototype scale. In figure A.1, Phase I and Phase II denotes the signal during non-liquefied and liquefied state of the soil. The analysis has shown that the first fundamental frequency for both non-liquefied and liquefied cases for test case CT6-A as 6.83Hz and 1.17Hz respectively.

A.2 Verification of the DAF results using simplified analytical method

The pile group with footing and superstructure was modelled as a simplified lumped mass 2DOF system and it was assumed that the pile head near the footing was free to translate but constrained against rotation. The same boundary condition was also assumed for the superstructure column head. The effect of lateral restraint from soil was modelled by fixing the pile at a certain depth (depth of fixity) from the surface. The depth of fixity in initial phase of vibration (before liquefaction state) was considered as 5times the
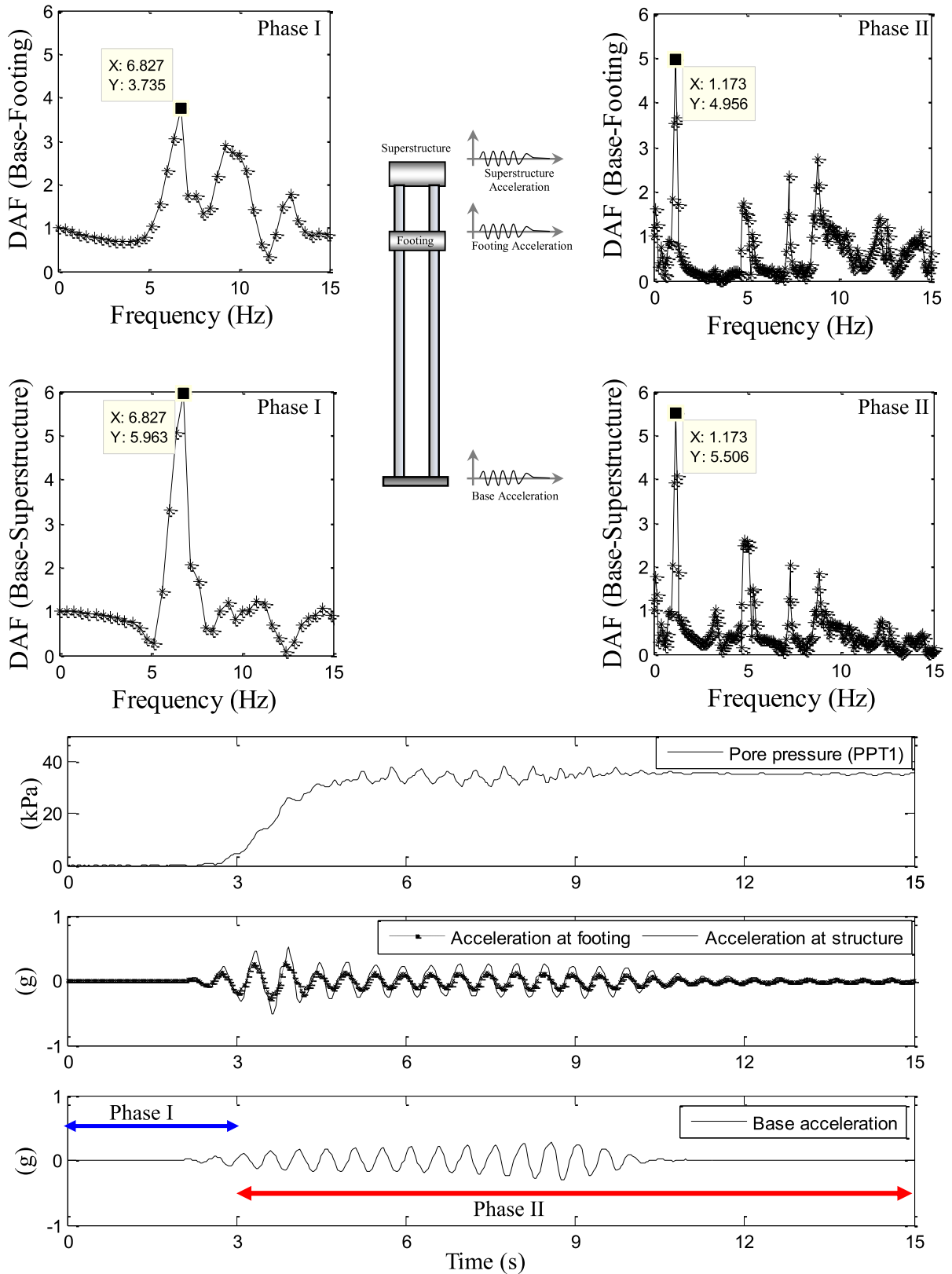
Figure A.1: Dynamic amplification factor for soils before liquefaction (1 - 3sec) and during liquefaction (3 - 15sec) in the test CT6-A.

diameter of pile (5×0.3m = 1.5m). For the fully liquefied condition, the total depth of fixity was considered as the summation of top non-liquefiable soil layer (1.8m), liquefiable soil layer (3.9m) and a fixity depth in non-liquefiable soil layer below liquefiable soil layer (1.5m). Hence the total depth of fixity estimated to be 7.2m for fully liquefiable condition. A traditional lumped mass model was considered where the mass was lumped at two heights, footing level and superstructure level. At the superstructure level, it included half of the mass of column and at floor level it included half of the column and pile mass. The 2DOF model is shown in figure A.2 with its mass and stiffness parameters. The mass and stiffness matrix of the model can be written as Equations A.2 and A.3 for both non-liquefied and liquefied cases respectively.

$$M_{NL} = \begin{bmatrix} m1_{NL} & 0 \\ 0 & m2 \end{bmatrix} \quad K_{NL} = \begin{bmatrix} k1_{NL} + k2 & -k2 \\ -k2 & k2 \end{bmatrix} \quad \text{(A.2)}$$

$$M_L = \begin{bmatrix} m1_L & 0 \\ 0 & m2 \end{bmatrix} \quad K_L = \begin{bmatrix} k1_L + k2 & -k2 \\ -k2 & k2 \end{bmatrix} \quad \text{(A.3)}$$

The Eigen solution of the equation of motion ($M\ddot{x} + K\dot{x} = 0$) was carried out using the generated mass and stiffness matrix. The first natural frequency obtained for both non-liquefied and liquefied cases were 7.69Hz and 1.22Hz respectively.
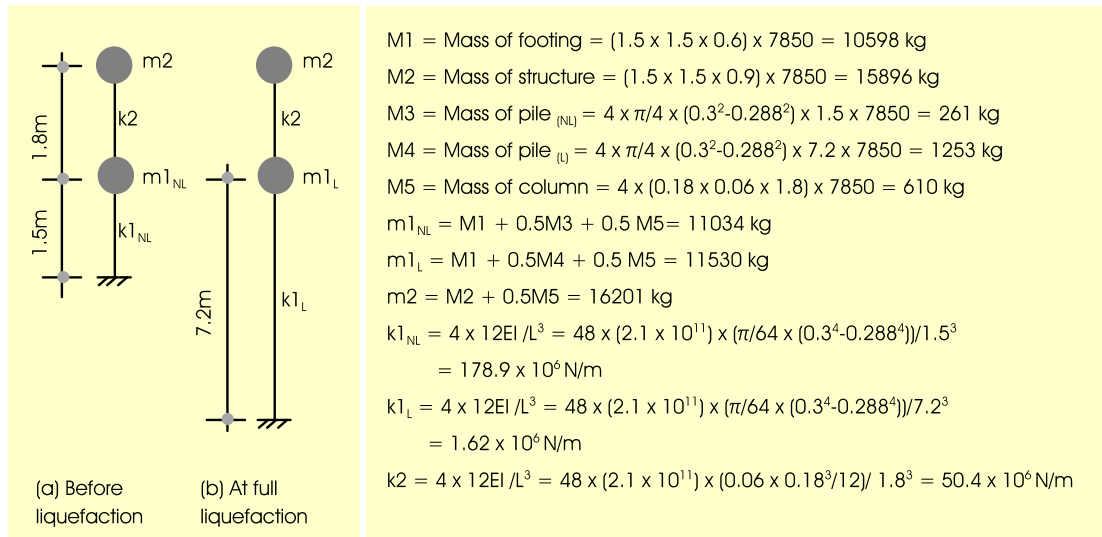
Figure A.2: Simplified 2 DOF model for soil-pile-footing-structure system of test case CT6-A (Refer Figure 3.8 and Table 3.6), (a) before liquefaction, and (b) at full liquefaction.

A.3   Verification of the DAF results using numerical method

To get a better estimation of fundamental frequency than the analytical solution as carried out above, the pile group with footing and structure was modelled in SAP2000 V11 (CSI, 2008) in prototype scale. Modal analysis was carried out with the pile base fixed and the pile head and column head were assigned with a horizontal diaphragm constraint. Same depth of fixity was considered here as assumed in analytical solution above. The

first fundamental frequencies of the system before liquefaction and during full liquefaction were estimated to be 6.45Hz and 1.09Hz respectively (figure A.3).

Figure A.3: First fundamental period of the pile-footing-structure system (a) before liquefaction and (b) at full liquefaction obtained from numerical analysis in SAP2000.
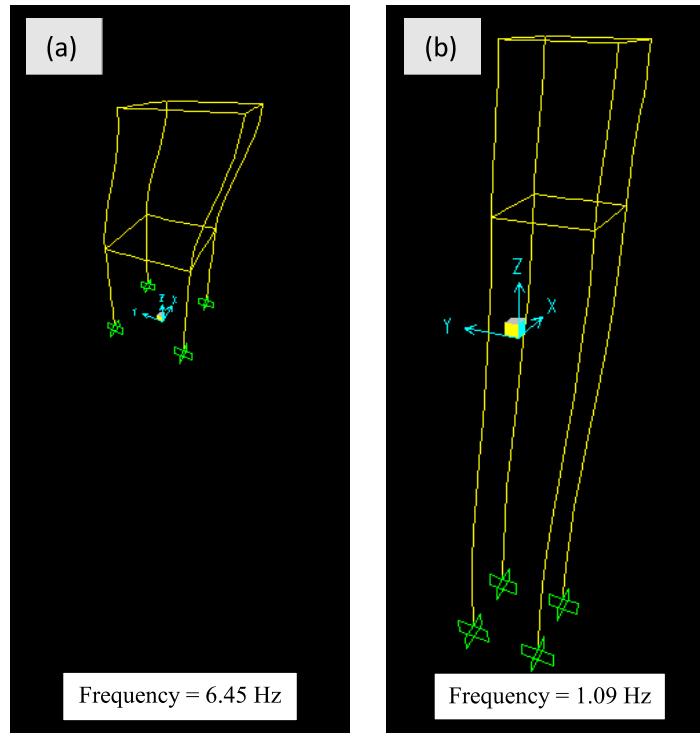
A.4 Results

The results of DAF analysis is compared with the results from analytical and numerical solutions and presented in table A.1. As expected, the results of numerical and analytical solution differ from DAF solution due to the inherit shortcoming of these methods to include the nonlinear soil behaviour. Still, the estimated value of fundamental frequency by DAF analysis was in close agreement with the calculated numerical and analytical values. DAF analysis also showed the same fundamental frequency of the system for both base-to-footing analysis and base-to-structure analysis, although, the amount of amplification was different in both the cases. This gave confidence in DAF analysis to find out the fundamental frequency of the system before and at full liquefaction. Further, the fundamental frequencies for other test cases were estimated by DAF analysis and the results are summarized in Table A.2.

Table A.1: Comparison of first fundamental frequency of the soil-pile-footing-structure system obtained from different analysis methods for centrifuge test CT6-A.

Soil condition	First fundamental frequency of the system		
	DAF analysis	Analytical method	Numerical method
Before liquefaction	6.83 Hz	7.69 Hz	6.43 Hz
At full liquefaction	1.17 Hz	1.22 Hz	1.09 Hz

Table A.2: Fundamental frequencies of the soil-pile-footing-structure system in all the thirteen centrifuge test cases before liquefaction and at full liquefaction as obtained from DAF analysis.

Sl No.	Test ID	First Fundamental frequency of the soil-pile-footing-structure system (Hz)	
		Before liquefaction	At full liquefaction
1	CT1-A	7.14	1.00
2	CT1-B	7.03	0.92
3	CT2-A	7.29	1.17
4	CT2-B	8.02	1.08
5	CT3-A	7.04	1.04
6	CT3-B	7.16	1.30
7	CT4-A	7.04	1.11
8	CT4-B	6.49	1.12
9	CT5-A	6.83	1.17
10	CT6-A	6.77	1.17
11	CT7-A	6.63	1.10
12	CT8-A	6.47	1.19
13	CT9-A	6.32	1.18

Appendix B

Post liquefaction monotonic stress–strain parameters from element test data

Index for table B.1 :

 TS - Torsional shear apparatus
 CT - Cyclic triaxial apparatus
 SS - Simple shear apparatus

Table B.1: Parameters of post liquefied monotonic behaviour of different sands.

Name of sand	Type of sand	Relative density	p' (kPa)	Type of instrument used	γ_{to} (%)	G_1 (kPa)	G_2 (kPa)	Reference (s)
Toyoura sand	sub-angular	32.6	49	TS	30	3.3	291	Yasuda et al. (1999)
Toyoura sand	sub-angular	53.9	49	TS	13.3	7.5	2000	Yasuda et al. (1999)
Toyoura sand	sub-angular	65.9	49	TS	8.6	11.6	1229	Yasuda et al. (1999)
Toyoura sand	sub-angular	49.8	50	CT	11.3	8.8	1735	Test-1(a), Section 5.3.2
Toyoura sand	sub-angular	48.8	50	CT	7.5	13.3	2906	Test-1(b), Section 5.3.2

Toyoura sand	sub-angular	49.6	50	CT	5.0	20	2325	Test-2, Section 5.3.2
Toyoura sand	sub-angular	47.0	50	CT	9.35	10.7	2325	Test-3, Section 5.3.2
Toyoura sand	sub-angular	47.3	50	CT	13	7.7	2583	Test-4, Section 5.3.2
Toyoura sand	sub-angular	48.5	50	CT	9.1	11	2100	Test-5, Section 5.3.2
Toyoura sand	sub-angular	50.0	98	TS	6	16.7	2113	Yasuda et al. (1998)
Fraser River sand	sub-angular to sub-rounded	19	100	CT	22.5	4.4	1437	Vaid & Thomas (1995)
Fraser River sand	sub-angular to sub-rounded	40	100	CT	4	25	2300	Vaid & Thomas (1995)
Fraser River sand	sub-angular to sub-rounded	59	100	CT	2.25	44.4	3833	Vaid & Thomas (1995)
Fraser River sand	sub-angular to sub-rounded	34	100	SS	6.75	11.1	100	Sivathyalan (1994)
Fraser River sand	sub-angular to sub-rounded	50	200	SS	5.25	14.3	437	Sivathyalan (1994)
Masa sand	Gravely sand with fines	57	98	TS	3	33	520	Yasuda et al. (1998)
Fraction E sand	Uniformly graded fine silica sand	50	40	CT	8	11	3688	Bhattacharya (2005)

Appendix C

Geotechnical Correlations

C.1 Estimation of G_{max} for a particular soil

The value of G_{max} can be determined from a range of soil parameters depending on site condition and field/laboratory tests conducted. For example, as in most of the seismic geophysical tests the shear strain level stays lower than $3 \times 10^{-4}\%$ the measured shear wave velocities can be used to estimate G_{max} as:

$$G_{max} = \rho v_s^2 \tag{C.1}$$

A brief note on different methods of obtaining G_{max} can be found in Kramer (1996). For instance, either of the following equations (Equation C.2 by Seed & Idriss (1970) or Equation C.3 by Imai & Tonouchi (1982)) can be used to obtain G_{max} (in kPa) of the soil.

$$G_{max} = 219k_{2,max}\sqrt{p'} \tag{C.2}$$

$$G_{max} = 14400N^{0.68} \text{ (in kPa)} \tag{C.3}$$

For Equation C.2, p' is in kPa and $k_{2,max}$ can be obtained from D_r value of the soil as given in Table C.1.

Table C.1: Values of soil modulus coefficient $k_{2,max}$. (Seed & Idriss, 1970)

D_r (%)	30	40	45	60	75	90
$k_{2,max}$	34	40	43	52	59	70

C.2 Correlation between SPT value (N) and relative density (D_r) of the soil

The *in-situ* relative density, D_r, of the soil and SPT value, N, can be correlated using equation C.4 (Meyerhof, 1957) for a given overburden pressure (σ_v').

$$D_r = 21\sqrt{\frac{N}{0.7 + \frac{\sigma_v'}{98}}} \tag{C.4}$$

The SPT value, N, can be corrected for effective overburden pressure, which is generally denoted as N_1. The correlation between N and N_1 can be written as Equation C.5, as proposed by Liao & Whitman (1986).

$$N_1 = \frac{N}{\sqrt{\frac{\sigma'_v}{98}}} \tag{C.5}$$

As the standard of SPT field testing procedure in different parts of the world vary, the obtained value of N must be corrected for effective overburden pressure and a number of site specific factors including SPT hammer energy. However, for a soil of given relative density, D_r, and effective overburden pressure, σ'_v, the value of N_1 estimated using equation C.4 and C.5 does not require energy correction, and it can be considered as N_{1-60}.